

National and Kapodistrian University of Athens

School of Science

Department of Physics

PhD Thesis

Piezoelectric/ferromagnetic hybrid nanostructures: bidirectional control of their properties by means of the heteroconjugate, externally applied fields

Georgia Vertsioti

Supervisor: Dimosthenis Stamopoulos

Advisory Committee: Michael Pissas & Shujun Zhang

Athens 2020

Εθνικό και Καποδιστριακό Πανεπιστήμιο Αθηνών

Σχολή Θετικών Επιστημών

Τμήμα Φυσικής

Διδακτορική Διατριβή

Πιεζοηλεκτρικές/σιδηρομαγνητικές υβριδικές νανοδομές: αμφίδρομος έλεγχος των ιδιοτήτων τους από τα ετεροσυζυγή, εξωτερικά εφαρμοζόμενα πεδία

Γεωργία Βερτσιώτη

Επιβλέπων καθηγητής: Δημοσθένης Σταμόπουλος
Συμβουλευτική επιτροπή: Μιχαήλ Πίσσας & Shujun Zhang

Αθήνα 2020

Seven-member examination committee

Dimosthenis Stamopoulos

Assoc. Professor
Physics Department
National and Kapodistrian University of Athens

Shujun Zhang

Professor
Australian Institute of Innovative Materials
University of Wollongong

Michael Pissas

Research Director
Institute of Nanoscience and Nanotechnology
National Center of Scientific Research 'Demokritos'

Nikolaos Stefanou

Professor
Physics Department
National and Kapodistrian University of Athens

Ioanna Zergioti

Professor
School of Applied Mathematics and Physical Sciences
National Technical University of Athens

Konstantina Mergia

Research Director
Institute of Nuclear and Radiological Science, Energy, Technology and Safety
National Center of Scientific Research 'Demokritos'

Antonios Papathanasiou

Assist. Professor
Physics Department
National and Kapodistrian University of Athens

To my family, Panos, Maria & Vaso

Prologue

At this point I take the opportunity to extend my sincere gratitude and appreciation to all those who made this PhD Thesis possible.

First and foremost, I wish to express my deepest gratitude to my supervisor Assoc. Prof. Dimosthenis Stamopoulos for giving me the chance to work on this PhD Thesis. His consistent guidance, support and patience during the running of the Thesis are invaluable to me. I am grateful for transmitting his immense knowledge in the fields of piezoelectrism and magnetism and for introducing me in detail to a variety of experimental techniques. Through his integral view of experimental research and his mission to provide high-quality work, I learnt how to approach a problem with critical and systematic thinking. What is more, his precious advice in the writing of our research papers provided me important knowledge on how to efficiently communicate the obtained experimental data. Beyond the scientific part, I am also grateful for the conversations, advice and encouragement on a friendly level that gave me power and spirit. Due to all these facts, I sincerely want to thank him for making my PhD experience stimulating and productive, leading to a thorough understanding of the physics beyond the specific subject of my Thesis.

Apart from my supervisor, I express my gratitude to the other two members of my advisory committee, Prof. Shujun Zhang and the Research Director Michael Pissas, for their insightful comments and constructive recommendations on my Thesis. I would like to offer my special thanks to Prof. Shujun Zhang for providing us the PMN-PT single crystals and for performing the global electric polarization and global strain measurements. Also, I want to thank Dr. Michael Pissas for giving me access to the 'Magnetic and Physical Properties Laboratory' of INN in NCSR 'Demokritos'.

In addition, I wish to express my appreciation to the other four members of the Jury, Prof. Nikolaos Stefanou, Prof. Ioanna Zergioti, Research Director Konstantina Mergia, and Assist. Prof. Antonios Papathanasiou for the critical reading of the Thesis and their fruitful comments.

Furthermore, I want to acknowledge the personel of the Machinery Department of NCSR 'Demokritos', namely Spyros Mpakalis, Serafeim Zogas and Giorgos Kokkinis, for their valuable technical contribution in the construction of the devices that were developed during this PhD Thesis. In addition, I want to express my heart-felt gratitude to my fellow lab mate Dr. Emmanouil Zeibekis for the excellent cooperation and assistance.

In addition, I would sincerely like to thank the Research Director Vassilios Psycharis for giving me access to the laboratory of X-ray Diffraction and the Research Director Nikolaos Boukos and Dr. Anastasios Travlos for giving me access to the laboratory of Scanning Electron Microscopy.

Furthermore, I wish to acknowledge A. G. Leventis Foundation and the National Research project 'NanoTher' for providing me financial support. Regarding the latter, I owe my special thanks to Prof. Ioanna Zergioti that was the coordinator of the project.

Last but not least, I want to thank my dear family and friends. Their great spiritual support, love and encouragement have always kept me going ahead and accomplish my personal goals.

Abstract

Natural materials, whether in elemental or compound form, are generally restricted to exhibit a single ‘ferroic’ behavior; ferroelectricity and ferromagnetism are two ‘immiscible’ ingredients since the underlying order parameters are not coupled. Accordingly, a ferroelectric/magnetic material is practically unresponsive to the heteroconjugate externally applied magnetic/electric field.

Under circumstances, the above mentioned limitations can be surpassed by employing hybrid nanostructures, composed of distinct ferroelectric (FE) and ferromagnetic (FM) constituents; these metamaterials can be designed at will to exhibit a multiferroic behavior associated with an underlying *magnetolectric* (ME) coupling. Among other mechanisms, the latter is usually mediated through the strain that is induced when FE -and thus piezoelectric (PE)- and FM -and thus magnetostrictive- constituents are combined, in a variety of topologies. Details on the theoretical background referring to FE-PE, FM-magnetostrictive and on multiferroic materials are presented on Chapter 1 of the Thesis.

In this spirit, the present PhD Thesis aims to study PE/FM composites, with respect to their response under application of the heteroconjugate external electric (E_{ex}) and magnetic (H_{ex}) fields. Two different topologies were investigated: (i) FM nanofilms of Co (thickness of 30-50 nm) deposited on both sides of bulk PE single crystals of $Pb(Mg_{1/3}Nb_{2/3})O_3-xPbTiO_3$ (PMN-0.30PT) in a planar configuration FM/PE/FM, that is Co/PMN-0.30PT/Co and (ii) FM nanoparticles of Fe_3O_4 (diameter 50-100 nm) embedded into a bulk PE matrix of $Pb(Zr_{0.52}Ti_{0.48})O_3$ (PZT), that is PZT- xFe_3O_4 , where x is the weight percentage concentration of Fe_3O_4 . Regarding the former, the ultra-high PE response of PMN-0.30PT, along with the noticeable magnetostriction of Co, render Co/PMN-0.30PT/Co a planar hybrid structure that is favorable for both basic science investigation and applications, such as ME memory devices. Regarding the latter, we stress that, although both PZT and Fe_3O_4 are two thoroughly studied compounds, well known to possess significant piezoelectric and magnetostrictive properties, curiously, the corresponding bulk ME composite has not been investigated systematically. Since the fabrication of this system is relatively simple and low cost, a possibly notable ME performance at room temperature could make it a strong candidate for potential applications.

The aforementioned hybrid nanostructures were prepared by means of magnetron sputtering and sintering and studied systematically with a variety of experimental techniques, including simulations. Specifically, we performed measurements referring to X-ray diffraction, electric polarization, strain under electric-field, $S_{zz}(E_{ex})$ via a classic technique of bulk character, electric current-voltage characteristics, scanning electron microscopy, magnetization via a superconducting quantum interference device magnetometer and strain under electric-field, $S_{zi}(E_{ex})$ ($i=x,y$) via a local optical microscopy (OM) based PE technique. Most important, regarding the specialized magnetization measurements, we employed a home-made sample rod so that, in addition to the standard external magnetic field, H_{ex} , that is applied over the sample surface, an external electric field, $E_{ex,z}$, could also be applied along the sample thickness. In this scheme, the sample magnetization can be measured under the simultaneous application of two external fields, a magnetic, H_{ex} , and an electric, $E_{ex,z}$. Referring to the specialized local

OM based PE technique, we constructed a home-made platform that enables us to simultaneously apply two external fields, an electric, $E_{ex,z}$, and a magnetic, $H_{ex,z}$ (both along the sample thickness) under real time observation with an OM. In this scheme, the in-plane PE response can be measured under the simultaneous application of two external fields, $H_{ex,z}$ and $E_{ex,z}$. Subsequently, from these data, we can estimate the in-plane strain as function of electric field, $S_{zi}(E_{ex,z})$, $i=x,y$, under the application of $H_{ex,z}$. Accordingly, from the $S_{zi}(E_{ex,z})$ data we can estimate the corresponding in-plane PE coefficients, $d_{zi}=dS_{zi}(E_{ex,z})/dE_{ex,z}$. Details on the basic principles of the above mentioned experimental techniques are presented on Chapter 2 of the Thesis.

The main results of this PhD Thesis summarize as following.

Regarding the first topology, Co/PMN-0.30PT/Co, the Co nanolayer had thickness ranging within 30-50 nm; we focused on Co nanolayers with thickness 30 nm, since, due to shape anisotropy reasons, for the specific value the magnetization changes orientation from in-plane to out-of-plane, thus probably being susceptible to modulation by an external control parameter. The corresponding results are shown below:

- *Influence of an external electric field, $E_{ex,z}$, on the magnetic coercive field, H_c .* At cryogenic temperature conditions, e.g. $T=10$ K, H_c exhibits modulation under application of an external electric field, $E_{ex,z}$, with a notable percentage variation of H_c on the order of 47%, at maximum. This modulation is ascribed to two mechanisms; the first is the pinning of the magnetic domain walls by surface/interface roughness or ‘bulk’ static disorder and the second is the change of domain wall population, associated with the underlying modulation of the Co nanofilm thickness. These effects can both be promoted by the strain experienced by the FM Co nanofilms due to their contact with the PE PMN-0.30PT single crystal. The modulation of H_c gets weaker as we increase the temperature. Ultimately, at room temperature conditions, e.g. $T=300$ K, H_c is almost unresponsive to $E_{ex,z}$, due to the dominance of thermal energy over the aforementioned mechanisms.
- *Influence of an external electric field, $E_{ex,z}$, on the remanent magnetization, m_{rem} .* At room temperature conditions, e.g. $T=300$ K, m_{rem} of Co nanolayers displays degradation under application of an external electric field, $E_{ex,z}$, in the form of distinct suppression events that we term electric field-induced magnetic instabilities (EMIs). Except from electric-field induced, these instabilities are also thermally activated, while they completely cease below 170 K. From the comparison of the magnetization data -referring to Co/PMN-0.30PT/Co- with PE ones -associated with PMN-0.30PT- we conclude that the EMIs are motivated by the strain induced to the PMN-0.30PT single crystals by $E_{ex,z}$.

Regarding the second topology, PZT-xFe₃O₄, after thorough electric and magnetic characterization of the samples with different weight percentage Fe₃O₄ concentration ($x=0\%$, 1%, 3%, 5%, 10%, 20%, 30%, 50%) we focused on the ones with $x=5\%$; the specific samples are strongly insulating (leakage current lower than 1 μ A) within the electric field range applied in our measurements (-10 kV/cm $\leq E_{ex,z} \leq +10$ kV/cm) and also adequately ferromagnetic. The corresponding results are shown below:

- *Influence of an external electric field, $E_{ex,z}$, on the relaxation of remanent magnetization, m_{rem} .* At room temperature, $T=300$ K, m_{rem} of PZT-5%Fe₃O₄ displayed

modulation of relaxation under application of an external electric field, $E_{ex,z}$, in the range $-9 \text{ kV/cm} \leq E_{ex,z} \leq +9 \text{ kV/cm}$. All $m_{rem}(t)$ relaxation data were well fitted by an exponential law. The initial m_{rem} value, $m_{rem}(0)$, exhibited maxima located at $E_{ex,z} = \pm 6 \text{ kV/cm}$, being practically independent of the time window that was used for the fitting. In addition, the relaxation constant (better termed as ‘relaxation function’ in this Thesis, since it depends on $E_{ex,z}$) exhibited maxima at the exact same points, $E_{ex,z} = \pm 6 \text{ kV/cm}$, a proof of slower relaxation of m_{rem} around this characteristic values. From independent polarization data, $P(E_{ex,z})$, for the same category of samples, PZT-5% Fe_3O_4 , we found out that the nucleation fields -which associate with the relaxation of electric polarization- occur at $E_{nuc} = \pm 6 \text{ kV/cm}$. Comparing the polarization, $P(E_{ex,z})$, and piezoelectric, $S(E_{ex,z})$, data with the aforementioned magnetization ones, $m_{rem}(E_{ex,z})$, we conclude that the relaxation of m_{rem} is affected by the relaxation of electric polarization.

- *Influence of an external magnetic field, $H_{ex,z}$, on the in-plane PE coefficients, d_{zi} .* At room temperature, $T=300 \text{ K}$, d_{zi} of PZT-5% Fe_3O_4 displayed dramatic decrease on the order of 50-60% when applying a relatively low $H_{ex,z}=1 \text{ kOe}$. Most important, the initial value of d_{zi} is completely recovered upon removal of $H_{ex,z}$, thus the process is entirely reversible. The comparison of electrical polarization data, $P(E_{ex,z})$, referring to plain PZT with the ones referring to composite PZT-5% Fe_3O_4 , showed that the addition of Fe_3O_4 nanoparticles render PZT ferroelectrically harder, as they introduce static structural disorder. By combining this fact to the magnetic-field control of d_{zi} , we conclude that the FM Fe_3O_4 nanoparticles do not simply serve as static structural disorder, but also introduce an additional control parameter that we term reconfigurable magnetic disorder.

- The results presented above regarding the PZT-5% Fe_3O_4 samples clearly prove the presence of ME coupling between their PE and FM constituents. The underlying mechanism of this coupling is attributed to strain transfer, since the elastic properties of the two constituents, the magnetostriction of the Fe_3O_4 nanoparticles and the PE strain of PZT, have comparable values. Details on the corresponding results, along with the respective discussion, are presented in Chapter 3 of the Thesis.

In addition, we performed simulations, aiming to evaluate the applicability and limitations of the OM-based PE technique that was extensively used in this Thesis. By means of these simulations, we validated the reliability of this experimental technique. Two additional characteristics of this technique, the ease of use and the versatility of application in a series of questions, render it suitable for standard PE characterization for a wide range of materials used in current technological applications. Details on these simulations are presented in Chapter 4 of the Thesis.

The conclusions and perspectives of this PhD Thesis are presented in detail in Chapter 5.

Περίληψη

Τα φυσικά υλικά, είτε σε στοιχειακή μορφή είτε σε μορφή χημικής ένωσης, γενικώς περιορίζονται σε μία μοναδική 'σιδηρική' συμπεριφορά: ο σιδηροηλεκτρισμός και ο σιδηρομαγνητισμός είναι δύο 'μη-αναμείξιμα' συστατικά καθώς οι υποκείμενες παράμετροι τάξης δεν συζεύγγονται. Επομένως, ένα σιδηρο-ηλεκτρικό/μαγνητικό υλικό πρακτικά δεν ανταποκρίνεται στα ετεροσυσζυγή εξωτερικά εφαρμοζόμενα μαγνητικά/ηλεκτρικά πεδία.

Υπό συνθήκες, οι περιορισμοί οι οποίοι αναφέρθηκαν πιο πάνω μπορούν να ξεπεραστούν χρησιμοποιώντας υβριδικές νανοδομές, αποτελούμενες από διακριτά σιδηροηλεκτρικά (ferroelectric, FE) και σιδηρομαγνητικά (ferromagnetic, FM) συστατικά· αυτά τα μεταλλικά μπορούν να σχεδιαστούν κατά βούληση ώστε να επιδεικνύουν μία πολυσιδηρική συμπεριφορά, συσχετιζόμενη με μία υποκείμενη μαγνητοηλεκτρική (magnetoelectric, ME) σύζευξη. Μεταξύ άλλων μηχανισμών, αυτή η σύζευξη πραγματοποιείται μέσω της μηχανικής τάσης που επάγεται όταν FE -επομένως και PE- και FM -επομένως και μαγνητοσυστελόμενα- συστατικά συνδυάζονται σε διάφορες τοπολογίες. Λεπτομέρειες για το θεωρητικό υπόβαθρο σχετικά με FE-PE, FM-μαγνητοσυστελόμενα και πολυσιδηρικά υλικά παρουσιάζονται στο Κεφάλαιο 1 της Διατριβής.

Σε αυτό το πνεύμα, η παρούσα Διδακτορική Διατριβή έχει ως στόχο να μελετήσει σύνθετα PE/FM υλικά, σε σχέση με την απόκρισή τους υπό των ετεροσυσζυγών, εξωτερικά εφαρμοζόμενων ηλεκτρικών (external electric field, E_{ex}) και μαγνητικών (external magnetic field, H_{ex}) πεδίων. Μελετήθηκαν δύο διαφορετικές τοπολογίες: (i) FM νανοϋμένια Co (πάχους 30-50 nm) εναποτεθειμένα πάνω στις δύο πλευρές ογκικών PE μονοκρυστάλλων $Pb(Mg_{1/3}Nb_{2/3})O_3-xPbTiO_3$ (PMN-0.30PT) σε επίπεδη διάταξη, FM/PE/FM, δηλαδή Co/PMN-0.30PT/Co και (ii) FM νανοσωματίδια Fe_3O_4 (διαμέτρου 50-100 nm) διεσπαρμένα μέσα σε ογκική PE μήτρα $Pb(Zr_{0.52}Ti_{0.48})O_3$ (PZT), δηλαδή PZT- xFe_3O_4 , όπου x είναι η επί τοις εκατό κατά βάρος συγκέντρωση του Fe_3O_4 . Σχετικά με την πρώτη, η εξαιρετικά υψηλή PE απόκριση του PMN-0.30PT, μαζί με την αξιοσημείωτη μαγνητοσυστολή του Co, καθιστούν το Co/PMN-0.30PT/Co μία επίπεδη υβριδική δομή, η οποία είναι κατάλληλη τόσο για τη βασική επιστημονική μελέτη όσο και για εφαρμογές, όπως συσκευές ME μνήμης. Σχετικά με τη δεύτερη, τονίζουμε ότι, παρόλο που τα PZT και Fe_3O_4 είναι δύο καλά μελετημένες ενώσεις για τις σημαντικές PE και μαγνητοσυστολικές τους ιδιότητες, παραδόξως, το αντίστοιχο ME σύνθετο υλικό δεν έχει μελετηθεί συστηματικά. Καθώς η παρασκευή αυτού του συστήματος είναι σχετικά απλή και χαμηλού κόστους, μία πιθανώς αξιόλογη ME επίδοση σε θερμοκρασία δωματίου θα το καθιστούσε επιλέξιμο για ενδεχόμενες εφαρμογές.

Οι προαναφερθείσες υβριδικές νανοδομές παρασκευάστηκαν μέσω μαγνητικά υποβοηθούμενης καθοδικής ιοντοβολής και πυροσυσσωμάτωσης και μελετήθηκαν με ποικίλες πειραματικές τεχνικές, συμπεριλαμβανομένων και προσομοιώσεων. Συγκεκριμένα, πραγματοποιήσαμε μετρήσεις περιθλασιμετρίας ακτίνων X, ηλεκτρικής πόλωσης, μηχανικής τάσης υπο την εφαρμογή ενός ηλεκτρικού πεδίου, $S_{zz}(E_{ex})$, μέσω μίας κλασσικής τεχνικής ογκικού χαρακτήρα, χαρακτηριστικών ηλεκτρικού ρεύματος-τάσης, ηλεκτρονικής μικροσκοπίας σάρωσης, μαγνήτισης με χρήση μαγνητόμετρου υπεραγωγίμης κβαντικής συμβολής και μηχανικής τάσης υπο την εφαρμογή ενός ηλεκτρικού πεδίου, $S_{zi}(E_{ex})$ ($i=x,y$), μέσω μίας τοπικής PE τεχνικής που βασίζεται στην οπτική μικροσκοπία (OM). Κυρίως,

σχετικά με τις εξειδικευμένες μετρήσεις μαγνήτισης, χρησιμοποιήσαμε έναν τροποποιημένο δειγματοφορέα, έτσι ώστε, σε συνδιασμό με το καθιερωμένο εξωτερικό μαγνητικό πεδίο που εφαρμόζεται παράλληλα στην επιφάνεια του δείγματος, H_{ex} , να μπορεί να εφαρμοσθεί και ένα εξωτερικό ηλεκτρικό πεδίο, $E_{ex,z}$, κατα μήκος του πάχους του δείγματος. Σε αυτή τη διάταξη, η μαγνήτιση του δείγματος μπορεί να μετρηθεί υπό την ταυτόχρονη εφαρμογή δύο πεδίων, ενός μαγνητικού, H_{ex} , και ενός ηλεκτρικού, $E_{ex,z}$. Όσον αφορά την εξειδικευμένη τοπική PE τεχνική που βασίζεται στην ΟΜ, κατασκευάσαμε μία πλατφόρμα η οποία μας δίνει τη δυνατότητα ταυτόχρονης εφαρμογής δύο πεδίων, ενός ηλεκτρικού, $E_{ex,z}$, και ενός μαγνητικού, $H_{ex,z}$, (και τα δύο κατα μήκος του πάχους του δείγματος) με παρατήρηση μέσω ΟΜ, σε πραγματικό χρόνο. Σε αυτή τη διάταξη, η παράλληλα-στο-επίπεδο παραμόρφωση του δείγματος μπορεί να παρατηρηθεί υπό την ταυτόχρονη εφαρμογή δύο πεδίων, $H_{ex,z}$ και $E_{ex,z}$. Στη συνέχεια, από αυτά τα δεδομένα, μπορούμε να εκτιμήσουμε την παράλληλα-στο-επίπεδο μηχανική τάση, $S_{zi}(E_{ex})$, $i=x,y$, υπό την εφαρμογή ενός $H_{ex,z}$. Επομένως, από τα δεδομένα $S_{zi}(E_{ex,z})$ μπορούμε να εκτιμήσουμε τους αντίστοιχους παράλληλα-στο-επίπεδο PE συντελεστές $d_{zi}=dS_{zi}(E_{ex,z})/dE_{ex,z}$. Λεπτομέρειες για τις βασικές αρχές των πειραματικών τεχνικών που αναφέρθηκαν πιο πάνω, παρουσιάζονται στο Κεφάλαιο 2 της Διατριβής.

Τα κύρια αποτελέσματα της Διδακτορικής Διατριβής συνοψίζονται ακολούθως.

Σχετικά με την πρώτη τοπολογία, Co/PMN-0.30PT/Co, τα νανοϋμένια Co είχαν πάχος που κυμαίνεται εντός 30-50 nm. Εστίασαμε σε αυτή την περιοχή τιμών καθώς για λόγους ανισοτροπίας σχήματος για τη συγκεκριμένη τιμή η μαγνήτιση αλλάζει προσανατολισμό από παράλληλη-στο-επίπεδο σε κάθετη-στο-επίπεδο, έτσι ώστε πιθανά να είναι επιδεκτική σε μεταβολή από μία εξωτερική παράμετρο ελέγχου. Τα αντίστοιχα αποτελέσματα φαίνονται πιο κάτω:

- *Επίδραση ενός εξωτερικού ηλεκτρικού πεδίου, $E_{ex,z}$, στο μαγνητικό συνεκτικό πεδίο (coercive field, H_c). Σε συνθήκες κρογενικών θερμοκρασιών, π.χ. $T=10$ K, το H_c δείχνει μεταβολή υπό την εφαρμογή ενός εξωτερικού ηλεκτρικού πεδίου, $E_{ex,z}$, με μία αξιοσημείωτη ποσοστιαία μεταβολή του H_c της τάξης του 47%, κατά μέγιστο. Αυτή η μεταβολή αποδίδεται σε δύο μηχανισμούς: ο πρώτος είναι η παγίδευση (pinning) των τοιχωμάτων των μαγνητικών περιοχών από την τραχύτητα των επιφανειών/διεπιφανειών ή των ‘ογκικών’ στατικών κρυσταλλικών ατελειών και ο δεύτερος είναι η αλλαγή του πληθυσμού των τοιχωμάτων των μαγνητικών περιοχών, η οποία σχετίζεται με την υποκείμενη αλλαγή του πάχους των νανοϋμενίων Co. Τα φαινόμενα αυτά μπορούν να ευνοηθούν από την μηχανική τάση που υφίστανται τα FM νανοϋμένια Co εξαιτίας της επαφής τους με τον PE PMN-0.30PT μονοκρυστάλλο. Η μεταβολή του H_c εξασθενεί καθώς αυξάνουμε τη θερμοκρασία. Τελικά, σε συνθήκες θερμοκρασίας δωματίου, π.χ. $T=300$ K, το H_c δεν έχει σχεδόν καθόλου εξάρτηση από το $E_{ex,z}$, λόγω της επικράτησης της θερμικής ενέργειας έναντι των προαναφερθέντων μηχανισμών.*
- *Επίδραση ενός εξωτερικού ηλεκτρικού πεδίου, $E_{ex,z}$, στην παραμένουσα μαγνήτιση (remanent magnetization, m_{rem}). Σε συνθήκες θερμοκρασίας δωματίου, π.χ. $T=300$ K, η m_{rem} των νανοϋμενίων Co δείχνει μείωση υπό την εφαρμογή ενός εξωτερικού ηλεκτρικού πεδίου, $E_{ex,z}$, με τη μορφή βηματικών διακριτών συμβάντων τα οποία καλούμε μαγνητικές αστάθιες επαγόμενες από ηλεκτρικό πεδίο (electric-field induced*

magnetic instabilities, EMIs). Εκτός από το ότι είναι επαγόμενες από ηλεκτρικό πεδίο, αυτές οι αστάθειες είναι επίσης θερμικά ενεργοποιούμενες, ενώ σταματούν πλήρως κάτω από τους 170 K. Από τη σύγκριση των δεδομένων της μαγνήτισης -τα οποία αναφέρονται στο Co/PMN-0.30PT/Co- με PE δεδομένα -τα οποία σχετίζονται με το PMN-0.30PT- συμπεραίνουμε ότι οι EMIs υποκινούνται από τη μηχανική τάση που επάγεται στους μονοκρυστάλλους PMN-0.30PT από το $E_{ex,z}$.

Σχετικά με τη δεύτερη τοπολογία, PZT- $x\text{Fe}_3\text{O}_4$, μετά από ενδελεχή ηλεκτρικό και μαγνητικό χαρακτηρισμό των δειγμάτων με διαφορετική επι τοις εκατό κατά βάρος συγκέντρωση Fe_3O_4 ($x=0\%$, 1%, 3%, 5%, 10%, 20%, 30%, 50%) εστίασαμε σε αυτά με $x=5\%$, δεδομένου ότι τα συγκεκριμένα δείγματα είναι ισχυρά μονωτικά (ρεύμα διαρροής μικρότερο από 1 μA) εντός του εύρους ηλεκτρικών πεδίων που εφαρμόσαμε στις μετρήσεις μας ($-10 \text{ kV/cm} \leq E_{ex,z} \leq +10 \text{ kV/cm}$) και επίσης ισχυρά σιδηρομαγνητικά. Τα αντίστοιχα αποτελέσματα παρουσιάζονται πιο κάτω:

- *Επίδραση ενός εξωτερικού ηλεκτρικού πεδίου, $E_{ex,z}$ στον εφησυχασμό της παραμένουσας μαγνήτισης (remanent magnetization, m_{rem}).* Σε θερμοκρασία δωματίου, $T=300 \text{ K}$, η m_{rem} του PZT-5% Fe_3O_4 έδειξε μεταβολή του εφησυχασμού υπό την εφαρμογή εξωτερικού ηλεκτρικού πεδίου, $E_{ex,z}$, για εύρος $-10 \text{ kV/cm} \leq E_{ex,z} \leq +10 \text{ kV/cm}$. Σε όλα τα δεδομένα εφησυχασμού $m_{rem}(t)$ έγινε εκθετική προσαρμογή. Η αρχική τιμή της m_{rem} , $m_{rem}(0)$, έδειξε μέγιστα εντοπισμένα στις τιμές $E_{ex,z} = \pm 6 \text{ kV/cm}$, τα οποία είναι πρακτικά ανεξάρτητα από το χρονικό παράθυρο που χρησιμοποιήθηκε στην προσαρμογή. Επιπρόσθετα, η σταθερά εφησυχασμού (καλύτερα οριζόμενη ως 'συνάρτηση εφησυχασμού' σε αυτή τη Διατριβή, καθώς εξαρτάται από το $E_{ex,z}$) έδειξε μέγιστα στα ίδια ακριβώς σημεία, $E_{ex,z} = \pm 6 \text{ kV/cm}$, απόδειξη του αργού εφησυχασμού της m_{rem} γύρω από αυτές τις χαρακτηριστικές τιμές. Από ανεξάρτητα δεδομένα ηλεκτρικής πόλωσης, $P(E_{ex,z})$, για την ίδια κατηγορία δειγμάτων, PZT-5% Fe_3O_4 , βρήκαμε ότι τα πεδία πυρηνοποίησης (nucleation fields, E_{nuc}) -τα οποία συσχετίζονται με τον εφησυχασμό της ηλεκτρικής πόλωσης- εμφανίζονται στις τιμές $E_{nuc} = \pm 6 \text{ kV/cm}$. Συγκρίνοντας τα δεδομένα πόλωσης, $P(E_{ex,z})$, και τα πιεζοηλεκτρικά δεδομένα, $S(E_{ex,z})$, με τα προαναφερθέντα δεδομένα μαγνήτισης, $m_{rem}(E_{ex,z})$, συμπεραίνουμε ότι ο εφησυχασμός της παραμένουσας μαγνήτισης, m_{rem} , επηρεάζεται από τον εφησυχασμό της ηλεκτρικής πόλωσης.

- *Επίδραση ενός εξωτερικού μαγνητικού πεδίου, $H_{ex,z}$ στους παράλληλα-στο-επίπεδο PE συντελεστές, d_{zi} .* Σε θερμοκρασία δωματίου, $T=300 \text{ K}$, οι d_{zi} του PZT-5% Fe_3O_4 έδειξαν δραματική μείωση της τάξης του 50-60% όταν εφαρμόζουμε ένα σχετικά χαμηλό μαγνητικό πεδίο, $H_{ex,z}=1 \text{ kOe}$. Πιο σημαντικά, η αρχική τους τιμή ανακάτται πλήρως όταν αφαιρέσουμε το $H_{ex,z}$, συνεπώς η διαδικασία είναι εντελώς αντιστρεπτή. Η σύγκριση των δεδομένων ηλεκτρικής πόλωσης, $P(E_{ex,z})$, που αναφέρονται στο απλό PZT, με εκείνα που αναφέρονται στο σύνθετο PZT-5% Fe_3O_4 , έδειξαν ότι η προσθήκη των νανοσωματιδίων Fe_3O_4 καθιστούν το PZT σιδηροηλεκτρικά πιο σκληρό, καθώς εισάγουν στατική δομική αταξία. Συνδυάζοντας αυτό το γεγονός με την ελεγχόμενη μεταβολή των PE συντελεστών d_{zi} από ένα εξωτερικό μαγνητικό πεδίο, $H_{ex,z}$, συμπεραίνουμε ότι τα FM νανοσωματίδια Fe_3O_4 δεν χρησιμεύουν απλώς ως στατική δομική αταξία, αλλά επίσης εισάγουν μία επιπρόσθετη παράμετρο ελέγχου την οποία καλούμε επαναδιαχειρίσιμη μαγνητική αταξία.

- Τα αποτελέσματα που παρουσιάστηκαν πιο πάνω σχετικά με τα δείγματα PZT-5%Fe₃O₄ αποδεικνύουν ξεκάθαρα την παρουσία ΜΕ σύζευξης μεταξύ των ΡΕ και FM συστατικών. Ο υποκείμενος μηχανισμός αυτής της σύζευξης αποδίδεται στη μεταφορά μηχανικής τάσης, καθώς οι ελαστικές ιδιότητες των δύο συστατικών, η μαγνητοσυστολή των νανοσωματιδίων Fe₃O₄ και η ΡΕ μηχανική τάση του PZT, έχουν συγκρίσιμες τιμές. Λεπτομέρειες για τα αντίστοιχα αποτελέσματα, μαζί με την σχετική συζήτηση, παρουσιάζονται στο Κεφάλαιο 3 της Διατριβής.

Επιπλέον, πραγματοποιήσαμε προσομοιώσεις, με στόχο να αξιολογήσουμε την εφαρμογή και τους περιορισμούς της ΡΕ τεχνικής βασιζόμενης στην ΟΜ, η οποία χρησιμοποιήθηκε εκτενώς σε αυτή τη Διατριβή. Μέσω αυτών των προσομοιώσεων, επικυρώσαμε την αξιοπιστία αυτής της πειραματικής τεχνικής. Δύο επιπλέον χαρακτηριστικά της, η ευκολία στη χρήση της και η ευελιξία στη εφαρμογή της σε μία σειρά προβλημάτων, την καθιστούν κατάλληλη για τυπικό ΡΕ χαρακτηρισμό ενός μεγάλου εύρους υλικών που χρησιμοποιούνται σε τεχνολογικές εφαρμογές. Λεπτομέρειες για αυτές τις προσομοιώσεις παρουσιάζονται στο Κεφάλαιο 4 της Διατριβής.

Τα συμπεράσματα και οι προοπτικές αυτής της Διαδακτορικής Διατριβής παρουσιάζονται αναλυτικά στο Κεφάλαιο 5.

Table of Contents

Chapter 1: Introduction	1
1.1 Fundamentals of ferroelectric and piezoelectric materials	1
1.1.1 Definitions	1
1.1.2 Linear constitutive relations of the direct and converse piezoelectric effect	2
1.1.3 General properties of ferroelectric and piezoelectric materials	3
1.1.4 Ferroelectric materials of different types and compositions	6
I. The archetypal system of $\text{Pb}(\text{Zr}_{1-x}\text{Ti}_x)\text{O}_3$	6
II. The synchronous system of $(1-x)\text{Pb}(\text{Mg}_{1/3}\text{Nb}_{2/3})\text{O}_3-x\text{PbTiO}_3$	7
1.2 Fundamentals of ferromagnetic, magnetostrictive and piezomagnetic materials	8
1.2.1 Definitions	8
1.2.2 Constitutive relations of the direct and converse magnetostrictive effect	9
1.2.3 General properties of ferromagnetic and magnetostrictive materials	10
1.2.4 Ferromagnetic materials of different types and geometries	13
I. Thin metallic films	13
II. Transition metal oxides in bulk and nanoparticle form	14
1.3 Fundamentals of multiferroic materials	16
1.3.1 The direct and converse magnetoelectric effect	16
1.3.2 Review in multiferroic materials	17
I. Single phase multiferroic magnetoelectric materials	18
II. Composite magnetoelectric materials	18
1.4 Motivation of the Thesis	23
Chapter 2: Sample Preparation, characterization and research experimental techniques	31
2.1 Sample preparation experimental techniques	31
2.1.1. Magnetron sputtering	31
2.1.2. Solid-state sintering	34
2.2 Characterization experimental techniques	35
2.2.1 X-Ray Diffraction	35
2.2.2 Current-voltage characteristics	36
2.2.3 Local measurement of magnetic field by means of a Gaussmeter	36
2.2.4 Global polarization and strain measurements	37
2.3 Research experimental techniques	39
2.3.1 Optical microscopy	39

2.3.2 Superconducting Quantum Interference Device	53
2.3.3 Scanning Electron Microscope	58
2.4 Sample categories	63
2.4.1 Ferromagnetic Co thin films on PMN-xPT single crystals	63
A. PMN-xPT single crystals	63
B. Co thin films	63
2.4.2. Fe ₃ O ₄ nanoparticles embedded in a PZT matrix	64
2.4.3. Main sample series	65
Chapter 3: Experimental results and discussion	67
3.1 Ferromagnetic Co thin films on PMN-0.30PT single crystal substrates	67
3.1.1 Characteristic physical properties	68
I. Crystallographic data	68
III. Magnetization data	69
3.1.2 Magnetization measurements protocol under E _{ex,z}	70
3.1.3 Magnetization data under E _{ex,z} application	70
I. m(H _{ex}) measurements at T=10 K and T=300 K under E _{ex,z} application	70
II. m _{rem} (T) measurements under E _{ex,z} application	75
3.2 Fe ₃ O ₄ nanoparticles embedded in a PZT matrix	78
3.2.1 Characteristic physical properties	79
I. Electrical resistance and current-voltage characteristics	79
II. Magnetization data	80
III. Crystallographic data	83
IV. Polarization and out-of-plane strain data	85
V. In-plane strain data	87
VI. Microstructure data	91
VII. Elemental analysis and homogeneity investigation	93
3.2.2 Electric-field control of the magnetic properties for a PZT-5%Fe ₃ O ₄ composite	96
I. Magnetization measurement protocol under E _{ex,z}	96
II. Fitting of m _{rem} (t) data	97
III. In-plane strain and polarization data	100
IV. Comparison of the magnetization, in-plane strain and polarization data	102
3.2.3 Magnetic-field control of the piezoelectric properties for a PZT-5%Fe ₃ O ₄ composite	103
I. Piezoelectric data for PZT-5%Fe ₃ O ₄ samples in the absence/presence of an H _{ex,z}	103
II. Polarization and leakage current data for both PZT and PZT-5%Fe ₃ O ₄ samples	106

III. Comparison of in-plane strain and polarization data	108
3.2.4 Underlying mechanism of the ME coupling in the PZT-5%Fe ₃ O ₄ composite	108
Chapter 4: Applicability and limitations of the OM-based local experimental technique for the estimation of the in-plane strain-electric field curves and piezoelectric coefficients	112
4.1. Empirical model	112
4.2. Simulations data	113
Chapter 5: Conclusions and perspectives	122
List of Publications	129
List of Conferences	129
Appendix A	A.1-A.7
Appendix B	B.1-B.4
Appendix C	C.1-C.11
Appendix D	D.1-D.8

Table of Abbreviations

A

Alternating current (AC)

Atomic Force Microscopy (AFM)

B

Backscattered electrons (BSE)

Beamsplitter (BS)

C

Characteristic point (CP)

D

Direct current (DC)

E

Electric-field Induced MIs (EMIs)

Energy Dispersive X-Ray Spectroscopy (EDS)

Equations (Eqs.)

F

Ferroelectric (FE)

Ferromagnetic (FM)

Field cooling (FC)

Figure (Fig.)

M

Magnetic instabilities (MIs)

Magnetoelectric (ME)

Magnetic domains (MDs)

Magnetic domain walls (MDWs)

Morphotropic Phase Boundary (MPB)

Monoclinic phase (M)

Multiferroic (MF)

N

Nanoparticle (NP)

Numerical aperture (NA)

O

Optical frame (OF)

Optical microscope (OM)

P

Physical Vapor Deposition (PVD)

Piezoelectric (PE)

$\text{Pb}(\text{Zr}_{1-x}\text{Ti}_x)\text{O}_3$ (PZT_x)

$\text{Pb}(\text{Zr}_{0.52}\text{Ti}_{0.48})\text{O}_3$ (PZT)

$\text{Pb}(\text{Mg}_{1/3}\text{Nb}_{2/3})\text{O}_3$ (PMN)

PbTiO_3 (PT)

$(1-x)\text{Pb}(\text{Mg}_{1/3}\text{Nb}_{2/3})\text{O}_3-x\text{PbTiO}_3$ (PMN-xPT)

R

Relaxor ferroelectrics (RFEs)

Rhombohedral (R)

Radio frequency (RF)

S

Sawyer-Tower (S-T)

Scanning Electron Microscope (SEM)

Secondary electrons (SE)

Secondary electrons imaging (SEI)

Superconducting (SC)

Superconducting Quantum Interference Device (SQUID)

Symmetry Axis (SA)

T

Tetragonal (T)

X

X-Ray Diffraction (XRD)

Z

Zero-field cooling (ZFC)

Table of Symbols

A/ α

α : mean field exchange parameter

$\alpha^{H \rightarrow E}$: direct ME coefficient

$\alpha^{E \rightarrow M}$: converse ME coefficient

B

B: ions' mobility

C

c: concentration per unit volume of ions

C_0 : linear capacitor

D/ Δ, δ

D : dielectric displacement

d : film thickness

δ : phase difference

Δx : displacement of a CP

d_{ij} : charge PE coefficient, or simply PE coefficient

d_{zi} ($i=x,y$): in-plane (i.e. over the sample surface) PE coefficients upon application of an $E_{ex,z}$

d_{zz} : out-of-plane (i.e. along the sample thickness) PE coefficients upon application of an $E_{ex,z}$

d_{ij}^m : magnetostrictive coefficients

d_{hkl} : interplanar spacing

d_{min} : the minimum distance of two points which can be still observed separately with OM

E

E : electric field

e: electron charge

E_{ex} : external electric field

$E_{ex,z}$: external electric field applied out-of-plane (i.e. over the sample thickness)

E_c : electric coercive field

E_{nuc} : nucleation field

E_{domain} : energy of a magnetic domain

E_{exch} : exchange energy

E_Z : Zeeman energy

E_{ms} : magnetostatic energy

E_{mc} : magnetocrystalline energy

E_{me} : magnetoelastic energy

F/ Φ

Φ : magnetic flux

Φ_0 : magnetic flux quantum

H/ χ

H: magnetic field

H : Hamiltonian

\hbar : reduced Planck's constant

H_{ex} : external magnetic field

H_c : magnetic coercive field

H_M : molecular field

hkl: Miller indices

χ_m : magnetic susceptibility

χ_e : dielectric susceptibility

I

I: electric current

I_l : electric leakage current

I_m : light intensity for the measured beam

I_r : light intensity for the reference beam

I_{max} : maximum interference light intensity

I_{min} : minimum interference light intensity

I_s : supercurrent

I_c : critical current

J

J_{ij} : exchange integral

J: flux of the diffusing ions

K

K: magnetocrystalline anisotropy

K : relative dielectric constant

k_B : Boltzmann's constant

L/ λ

λ : wavelength

$\lambda_{\text{X-rays}}$: X-rays wavelength

λ : magnetostriction constant

L: length

M/ μ

M: Magnetization

M_s : spontaneous magnetization

M_{rem} : remanent magnetization

μ : chemical potential

μ_0 : magnetic permeability of free space

N

n: refractive index of a medium

N: integer representing the order of reflection

P

P: polarization

P_S: spontaneous electric polarization

P_{sat}: saturation polarization

P_{rem}: remanent polarization

Q/θ

θ: angle between the incident beam and the reflecting lattice

θ_{ap}: half of the aperture angle of the objective lens of an OM

R

R: electrical resistance

R_L: Low-temperature rhombohedral phase

R_H: High-temperature rhombohedral phase

r_m: optical path for measured beam

r_r: optical path for reference beam

R_{OM}: resolution corresponding to a processed OM image

S/σ

S: mechanical strain

S_{zi} (i=x,y): in-plane (i.e. over the sample surface) strain upon application of an E_{ex,z}

S_{zz}: out-of-plane (i.e. along the sample thickness) strain upon application of an E_{ex,z}

S: Atomic spin

σ_w: energy of a DW

s_{ij}: elastic compliance coefficient

T

T: mechanical stress

T_{ex}: external mechanical stress

T_T: transition temperature from R_L to R_H phase

T_{RT}: transition temperature from R to T phase

T: temperature

T_V: temperature of Verwey transition

T_{sin}: sintering temperature

T_{inf}: inflection temperature

T_{ces}: cessation temperature

T_c: Curie temperature

t: time

t : sample thickness

V

V : voltage

V_{ex} : external voltage

V_{sample} : sample volume

W

w : magnetic domain size

X

x_i : initial in-plane position of a CP from the sample's center of symmetry

x_f : final in-plane position of a CP from the sample's center of symmetry

x : Fe_3O_4 concentration

Z

Z : atomic number

Chapter 1: Introduction

This Chapter presents the theoretical background of the Thesis. The subchapters 1.1 and 1.2 present the basic principles of ferroelectric (FE)-piezoelectric (PE) and ferromagnetic (FM)-magnetostrictive materials, respectively. We focus our discussion on the corresponding categories of materials employed in this PhD research: the FE-PE $\text{Pb}(\text{Zr}_{1-x}\text{Ti}_x)\text{O}_3$ and $(1-x)\text{Pb}(\text{Mg}_{1/3}\text{Nb}_{2/3})\text{O}_3-x\text{PbTiO}_3$, and the FM-magnetostrictive metallic Co and iron oxides, Fe_3O_4 , Fe_2O_3 . Most important, subchapter 1.3 discusses the concept of multiferroic (MF) materials and magnetoelectric (ME) effect. Two different categories of MF ME materials (or simply called ME materials) are presented, that is the single phase and composite ones; emphasis is paid on the latter, providing detailed information about their physical mechanism, ME properties and architectures. Also, a review on bulk composite ME materials is provided. Finally, in the subchapter 1.4, the motivation of the Thesis is briefly discussed.

1.1 Fundamentals of ferroelectric and piezoelectric materials

1.1.1 Definitions

Piezoelectricity (or, according to the Greek word piezo, “electricity generated from pressure”) was discovered by Jacques and Pierre Curie in 1880 [1]. In their experiments on a number of crystals, such as tourmaline, quartz and topaz, they observed the presence of dielectric displacement, D , under the application of external mechanical stress, T_{ex} , that is the *direct piezoelectric, PE, effect*. One year later, the *converse PE effect* -i.e. the presence of mechanical strain, S , under presence of an external electric field, E_{ex} - was predicted theoretically by G. Lippmann [2] and was soon after confirmed experimentally by Curie brothers [3].

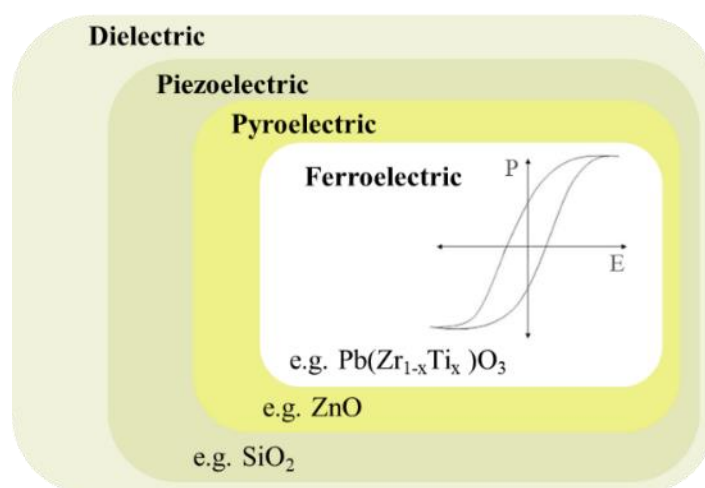


Fig. 1.1: Schematic illustration of the subclasses of dielectric materials, with a representative example for each class; for ferroelectric materials, the characteristic polarization-electric field loop, $P(E)$, is also shown.

In a microscopic level, piezoelectricity originates from the lack of the center of symmetry in the unit cell of the crystal. Among the 32 crystal classes of dielectric materials, the 20 ones are non-centrosymmetric and exhibit piezoelectricity.

With a further subdivision, 10 of these PE classes exhibit a finite and permanent value of polarization, known as spontaneous electric polarization, P_S , which exists even in the absence of an E_{ex} or T_{ex} . Crystals with the respective behavior are called *pyroelectric* crystals [4,5], with P_S varying as a function of temperature. Additionally, when the direction of P_S can also be changed by E_{ex} , the crystal is called *ferroelectric*, FE. The term FE is derived from the analogy with ferromagnetic materials in that both types of materials possess domains, exhibit hysteresis loops and show Curie-Weiss behavior near their phase transition temperatures (see subchapters 1.1.3 and 1.2.3, below). Figure (Fig.) 1.1 summarizes the aforementioned subclasses of dielectric materials.

1.1.2 Linear constitutive relations of the direct and converse piezoelectric effect

The constitutive relations for the direct and converse PE effect are presented below in tensor form. The PE coupling is described by a linear relation between a first-rank tensor (D or E) and a second-rank tensor (T or S). Thus, the corresponding coupling coefficient d_{kij} (charge PE coefficient, or simply PE coefficient) is a third-rank tensor. Accordingly, the constitutive relations can be written as [5]:

$$D_k = d_{kij}T_{ij} \quad (1.1)$$

$$S_{ij} = d_{kij}E_k \quad (1.2)$$

where $i, j, k=1, 2, 3$. The Equations (Eqs.) (1.1) and (1.2) are the linear constitutive relations which describe the direct and the converse PE effect, respectively. What is more, they can be further expressed by using the reduced matrix notation, d_{km} ; index k denotes the direction of the D and E with $k=1, 2, 3$. In addition, index m denotes the mode of T and S tensors, with $m=1-3$ for normal modes and $m=4-6$ for shear modes. Hence, Eqs. (1.1) and (1.2) can be expressed as:

$$D_i = d_{ij}T_i \quad (1.3)$$

$$S_j = d_{ij}E_i \quad (1.4)$$

with $i=1-3$ and $j=1-6$.

Figs. 1.2(a.i) and 1.2(a.ii) present the most simple cases, that can be easily illustrated, of the direct and converse PE effect for a plate-shaped sample; the externally applied tensors ($T_{ex,z}$ and $E_{ex,z}$) are denoted by blue color, while the induced tensors (i.e. their responses D_z and S_x, S_y) are denoted by red color. Fig. 1.2(b) shows the Cartesian coordinate corresponding to the possible tensor directions.

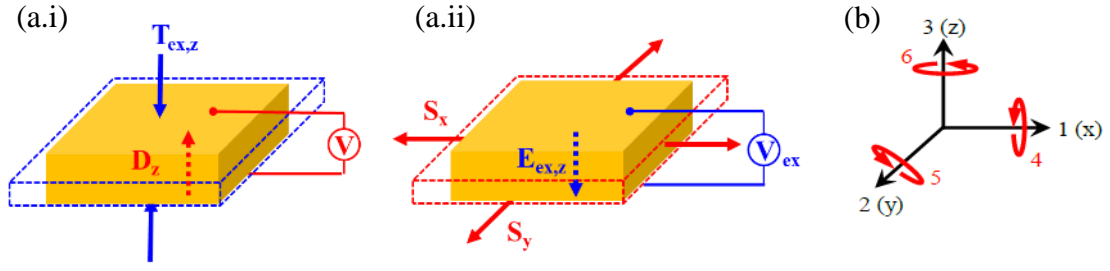


Fig. 1.2: (a) Schematic illustration of a plate-shaped sample under the (a.i) direct and (a.ii) converse PE effect. (a.i) External stress along z -axis, $T_{ex,z}$ induces electric displacement, D_z (or measurable electric voltage, V). (a.ii) External electric field along z -axis, $E_{ex,z}$ (or external electric voltage, $V_{ex,z}$) induces strain along x , S_x , and y , S_y , axes. (b) Cartesian coordinate system that describes the possible directions of the externally applied (blue colored) and the induced (red colored) tensors; numbers 1-3 correspond to the normal modes, while numbers 4-6 correspond to the shear modes.

Regarding the PE coefficients, d_{ij} , they represent the polarization charge generated per unit of mechanical stress, T , (direct PE effect) or the mechanical strain induced per unit of electric field, E , (converse PE effect) [6]. Accordingly, d_{ij} is given by the relations:

$$d_{ij} = \left(\frac{\partial D_i}{\partial T_j} \right)^E \quad (1.5)$$

$$d_{ij} = \left(\frac{\partial S_j}{\partial E_i} \right)^T \quad (1.6)$$

where upper index in Eqs. (1.5) and (1.6) denotes constant electric and stress field, respectively. We should note that, in this Thesis, the strain tensors will be referred to as S_{zi} , $i=x, y, z$ (instead of S_x, S_y and S_z shown above) in order to clarify in which direction the external electric field is applied and the mechanical strain is induced; the first subscript denotes the direction of the external electric field (always applied along z -axis in this Thesis), while the second one denotes the direction of induced strain (along x, y, z axis).

The aforementioned linear relations shown in Eqs. (1.3) and (1.4) correspond to PE materials, a particular class of dielectric materials. We should note that, even in the general case of the latter, the application of an E_{ex} also induces strain, due to the so-called electrostrictive effect. In this case, the change of strain is a quadratic function of the applied electric field. In realistic strain-electric field curves, $S(E_{ex})$, of PE materials both effects, piezoelectric and electrostrictive, contribute.

1.1.3 General properties of ferroelectric and piezoelectric materials

At a microscopic level, the driving force for ferroelectricity is the off-center displacement of the ions of the solid and their corresponding electrons under the so-called Curie temperature (T_c). For example, the non-centrosymmetric perovskite structure of the unit cell shown in Fig. 1.3(b) (discussed in detail in the subchapter 1.1.4) is reached by shifting of the B^+ cation off-center relative to the oxygen O^{2-} anions; as a consequence, a spontaneous polarization, P_s , derives from the electric dipole moment created by this shift. In this case P_s exists in the

absence of an external electric field, E_{ex} . In addition, a material is classified as FE when the P_S may be altered at will by the application of an E_{ex} . It should be noted that, at a macroscopic level the FE material does not exhibit spontaneous polarization, under the absence of E_{ex} , due to the presence of the FE domains- microscopic areas where the electric dipoles are aligned (see below).

Some subcategories of FE materials, based on the structure of their unit cell, are the tungsten-bronze group, the pyrochlore group, the bismuth-layer structure group, and the oxygen octahedral group [7]. Among them, the latter -also known as ABO_3 perovskite type- possesses the most important properties. Specifically, the ABO_3 unit cell, shown in Fig. 1.3(a) consists of a cubic structure ($a=b=c$), with the ions A (A^+ or A^{2+}), O^{-2} and B (B^{4+} or B^{5+}) occupying the edges, face centers and cube center, respectively. This configuration corresponds to the ideal perovskite structure; it can be taken as the high symmetry reference structure of the high temperature paraelectric phase, where there is no available direction for the development of P_S . The paraelectric phase is present above a T_c , where the dielectric susceptibility, χ_e , follows the Curie-Weiss law:

$$\chi_e = \frac{C}{T - T_c} \quad (1.7)$$

where C is a constant.

Upon cooling below T_c , FE materials undergo a structural phase transition. Accordingly, the development of P_S is caused by the displacement of the relative position of O^{-2} octahedra and the B^+ ions leading to a tetragonal structure ($a=b \neq c$), as shown in Fig. 1.3 (b). The direction of P_S can be switched between the six equivalent polarization directions shown by dashed arrows in Fig. 1.3(b). This transition happens so that the system minimizes the electrostatic energy generated due to surface charge at T_c (depolarizing field) and the accompanying elastic energy associated with mechanical constraints to which the FE material is subjected [7,8].

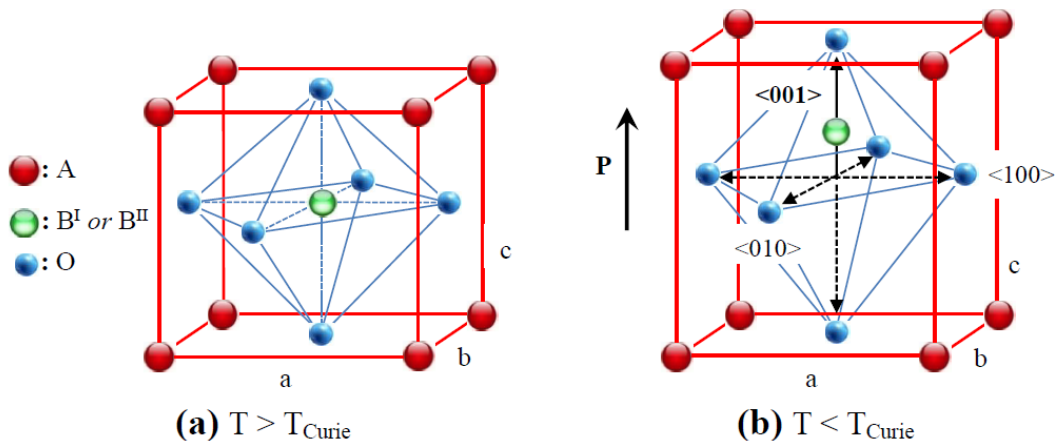


Fig. 1.3: Schematic illustration of the unit cell of a FE oxide with general perovskite type ABO_3 at (a) $T > T_c$ and (b) $T < T_c$. The six equivalent polarization directions are shown in (b) with the dashed arrows inside the octahedron; the solid arrows denotes the direction of polarization, P , and the simultaneous displacement of the central B^+ ion.

The interface between two FE domains is delimited by a FE domain wall (DW). The DW which separates two adjacent domains can be classified into two main categories: 180° DW, which separate two domains with opposed polarization, P , directions, and non- 180° DW, which separate the domains with P angle different than 180° [8]. The latter is the most significant contributor to piezoelectricity (strain production), especially for bulk FE materials [9, 10].

The most interesting properties of FEs are unveiled when they are subjected to E_{ex} . Thus, Figs. 1.4(a) and 1.4(c) present the electric polarization, P , and PE strain, S , as a function of E_{ex} , that is $P(E_{ex})$ and $S(E_{ex})$, respectively. Below, we discuss the basic characteristics of these loops.

Specifically, Fig. 1.4(a) shows a representative hysteresis loop $P(E_{ex})$ upon varying E_{ex} from point A to H. At first (point A), for an unpolarized FE material ($P=0$ at $E_{ex}=0$), the FE domains are randomly oriented. By increasing E_{ex} , P increases in a non-linear way, at first slowly (segment AB), and subsequently abruptly (segment BC), until saturation of polarization ($+P_{sat}$) is reached (point D). During this process the domains get reoriented towards the direction of E_{ex} ; once they are finally aligned with E_{ex} (point D), a single-domain state is formed (P is homogeneous throughout the entire sample). By decreasing E_{ex} (segment DE), some DWs will back-switch, while at $E_{ex}=0$ (point E), P attains a non-zero value, called remanent polarization ($+P_{rem}$), where some FE domains are still oriented towards E_{ex} . Subsequently, by increasing E_{ex} in the opposite direction (segment EF), P decreases down to zero (point F). The corresponding electric field at which P regains zero value is called *electric coercive field*, E_c^- (point F); at $E_{ex}^- = E_c^-$ a multi-domain state occurs, where P is randomly distributed all over the volume of the material so that its net value is zero. It should be noted that the point F', just before F is reached, corresponds to another characteristic electric field, referred to as *nucleation field*, E_{nuc}^- (the definition of E_{nuc} will be discussed below, in the last paragraph of this subchapter). Subsequent increase of E_{ex} in the opposite direction (segment FG) causes reversal and ultimate alignment of the FE domains with E_{ex} (point G), signifying the respective saturation of electric polarization ($-P_{sat}$). By decreasing E_{ex} back to zero (point K), $-P_{rem}$ is reached, while by increasing it once again (segment KH) $P(E_{ex})$ traces the points H' and H, which correspond to E_{nuc}^+ and E_c^+ , respectively.

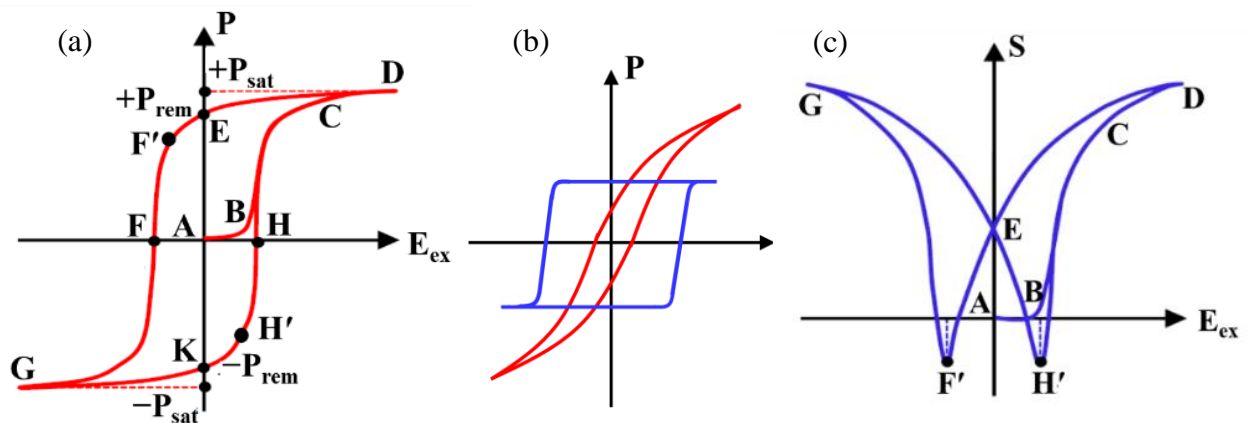


Fig. 1.4: (a), (b) Typical electric polarization-electric field hysteresis loops for ferroelectric (FE) materials, $P(E_{ex})$. (a) The characteristic segments/points of $P(E_{ex})$ loop are denoted by symbols (see text for details). (b) Different $P(E_{ex})$ loops of 'hard' and 'soft' FE materials are denoted by blue and red curves, respectively. (c) Typical PE strain hysteresis loop for FE materials, $S(E_{ex})$. The characteristic segments/points of $S(E_{ex})$ loop corresponding to the ones of $P(E_{ex})$ are denoted by the same capital letters.

Depending on the form of the $P(E_{ex})$ loop, two basic types of FE materials exist, the so-called ‘hard’ and ‘soft’ ones. The former have higher E_c and P_{rem} values and under specific circumstances, lower dielectric losses than the latter. Regarding their PE properties, ‘soft’ FE materials display higher PE coefficients than the ‘hard’ ones. Typical $P(E_{ex})$ for ‘hard’ and ‘soft’ FE materials are shown in Fig. 1.4(b) with blue and red lines, respectively.

Along with $P(E_{ex})$ hysteresis loop, the respective $S(E_{ex})$, loop can be also recorded upon E_{ex} application, the so-called butterfly loop, as shown in Fig. 1.4(c). The origin of this hysteresis loop is both the converse PE effect (referring to the linear segments of the loop), and the switching/movement of the non- 180° DWs (referring to the non-linear segments of the loop) [8]. The segments/points of $S(E_{ex})$ corresponding to the ones of $P(E_{ex})$ are denoted by the same capital letters. At this point we should note three basic characteristics of the $S(E_{ex})$ curves. First, $S(E_{ex})$ takes both positive and negative values, which corresponds to tensile and compressive S , respectively. Second, the variation of S , from tensile to compressive and vice versa, takes place approximately at the nucleation fields, E_{nuc}^\pm (points F', H'), that occur at electric fields that are slightly smaller than the coercive ones E_c^\pm , mentioned above; E_{nuc}^\pm denote the onset of polarization reversal, i.e. where the FE domains appear and start to move/rotate, ultimately dictating complete reversal of polarization [10-12]. Third, $S(E_{ex})$ consists of both non-linear and linear or linear-like segments. In any case we can always estimate the PE coefficients d_{ij} based on Eq. (1.6) whether we refer to linear, linear-like or non-linear behavior of the $S(E_{ex})$ curves.

1.1.4 Ferroelectric materials of different types and compositions

Subchapters 1.1.4.I and 1.1.4.II examine the basic properties of bulk Pb-based PE materials with high performance which highly depends on their composition. Specifically, we focus our discussion on the archetypal $Pb(Zr_{1-x}Ti_x)O_3$ and the synchronous $(1-x)Pb(Mg_{1/3}Nb_{2/3})O_3$ - $xPbTiO_3$, since they are the PE constituents of the multiferroic composites studied in this Thesis.

I. The archetypal system of $Pb(Zr_{1-x}Ti_x)O_3$

The FE material $Pb(Zr_{1-x}Ti_x)O_3$ (PZT_x) is the most widely studied thanks to its outstanding electromechanical properties and relatively low production cost, which render it extensively applied in actuators, sensors and transducers [13,14]. The typical perovskite structure of PZT_x (in the paraelectric phase) is shown in Fig. 1.3(a), with A and B sites occupied by Pb^{2+} and Zr^{4+}/Ti^{4+} respectively. Depending on the desirable properties, PZT_x ceramics can be modified with different dopants, exhibiting ‘hard’ characteristics with acceptor dopants (such as Fe^{3+} , Mn^{+3} , Mn^{+2} on B sites) or ‘soft’ characteristics with donor dopants (such as Nb^{5+} , Sb^{5+} on B sites and La^{3+} on A sites) [15, 16].

The temperature-composition phase diagram is presented in Fig. 1.5(a). Above Curie temperature, PZT_x is in the cubic crystallographic phase and it exhibits paraelectric behaviour. At room temperature, Ti concentration increases, causing a structural phase transition from the Zr-rich rhombohedral (R) region to the Ti-rich tetragonal (T) region, both exhibiting FE behavior. The former, consists of two FE rhombohedral phases, the low-temperature rhombohedral phase, R_L , with tilted oxygen octahedra, and the high-temperature rhombohedral

phase, R_H , with regular non-tilted octahedra; temperature T_T corresponds to the transition from R_L to R_H phase. The R and T phases are separated by the morphotropic phase boundary (MPB) at $x \approx 0.48$, where the maximum piezoelectric and dielectric responses are met [17-24]. More specifically, indicative values of the PE constants and strain for $Pb(Zr_{0.52}Ti_{0.48})O_3$ (PZT) are $d_{31} \approx 260$ pm/V, $d_{33} \approx 600$ pm/V [25, 26] and $S_{31} = 5 \times 10^{-4}$, $S_{33} = 1 \times 10^{-3}$, respectively [27]. The maximization of PE properties mainly stems from the existence of an intermediate monoclinic phase (M_A), discovered by Noheda et al., [17] in a narrow area around the composition $x \approx 0.48$, as shown in Fig. 1.5(a). In M_A phase the spontaneous polarization, P_S , (denoted by the thick magenta arrow) is allowed to rotate continuously between R and T phases (Fig. 1.5(c.i)), as shown by the magenta-shaded space. Accordingly, the accessible reorientation of P_S with E_{ex} application among multiple available directions gives rise to high PE performance at MPB, a feature known as the polarization-rotation model. Due to the complex nature of monoclinic phase, alternative mechanisms have also been proposed, involving the role of domains [28-30]. Though it is still a matter of debate, both mechanisms probably contribute to the PE response at the MPB of PZT_x . These mechanisms are also at play for other Pb-based materials, such as the $(1-x)Pb(Mg_{1/3}Nb_{2/3})O_3-xPbTiO_3$ that will be discussed right below.

II. The synchronous system of $(1-x)Pb(Mg_{1/3}Nb_{2/3})O_3-xPbTiO_3$

The FE system $(1-x)Pb(Mg_{1/3}Nb_{2/3})O_3-xPbTiO_3$ (PMN-xPT) is a solid solution of $Pb(Mg_{1/3}Nb_{2/3})O_3$ (PMN) with $PbTiO_3$ (PT), which has been extensively investigated the last decades thanks to its ultra-high values of PE coefficients. The initial compound (PMN) belongs to class of materials named as relaxor ferroelectrics (RFEs), with chemical formula $Pb(B', B'')O_3$, where B' is a low valence cation and B'' is a high valence cation. Their main characteristic that distinguishes them from the most common FE materials, like PZT, is the diffusive phase transition and the frequency dependence of their dielectric properties that establishes the term relaxor [31-33]. The ferroelectric-paraelectric transition and all the related properties are characterized not by abrupt changes, but rather by gradual ones that extend in a relatively broad range of temperature [34]. The origin of these features is the existence of local, randomly oriented polar clusters, referred as polar nanoregions [35, 36].

The solid solution of the PMN, which is the RFE part, with PT, which is the conventional FE part, forms the phase diagram presented in Fig. 1.5(b). In temperatures $T > T_c$ the system is in the cubic phase and exhibits paraelectric behavior. At room temperature, the system is in the FE phase and obtains the following crystallographic phases: R/M_B (M_B monoclinic with pseudorhombohedral features) for $x \leq 0.27$, M_B for $0.27 \leq x \leq 0.30$, M_C for $0.31 \leq x \leq 0.40$ and T for $x > 0.40$. The configuration of P_S in M_B and M_C phases is shown in Figs. 1.5(c.ii) and 1.5(c.iii), respectively; P_S (denoted by the thick magenta arrow) can rotate and switch continuously between the R and orthorhombic (O) phases for M_B (Fig. 1.5(c.ii)) and T and O phases for M_C (Fig. 1.5(c.iii)), as shown by the corresponding magenta-shaded space [37].

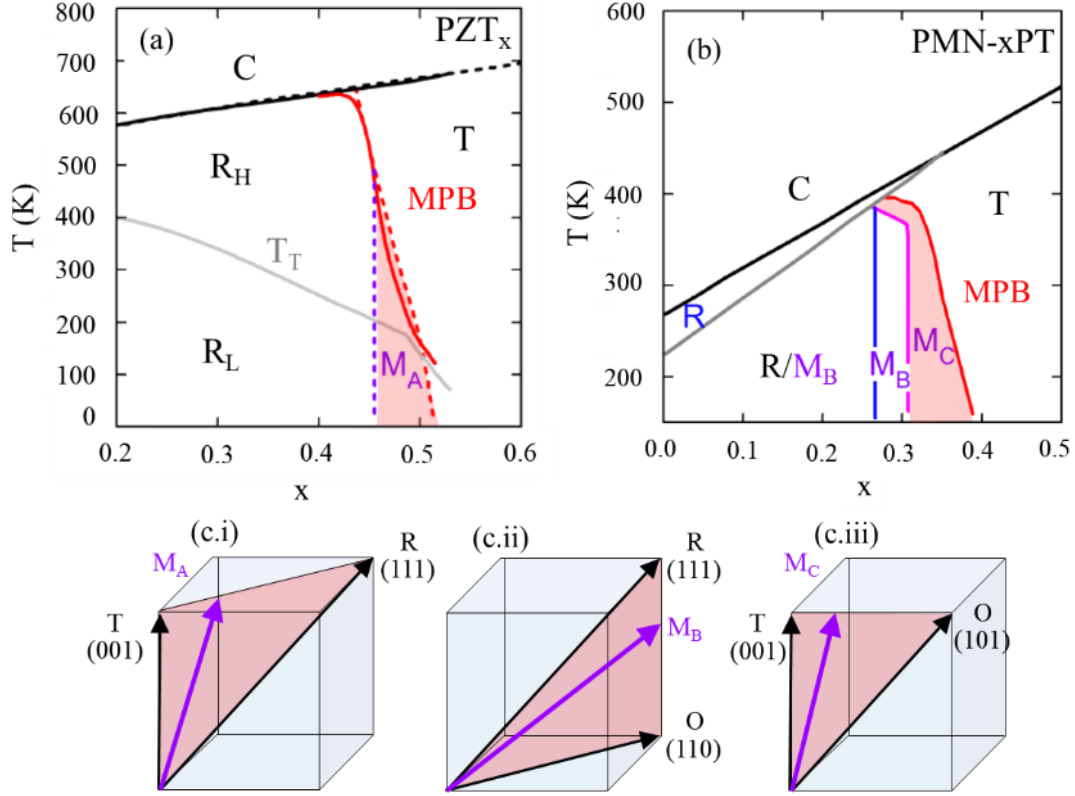


Fig. 1.5: Phase diagrams of (a) $Pb(Zr_{1-x}Ti_x)O_3$ (PZT_x) and (b) $(1-x)Pb(Mg_{1/3}Nb_{2/3})O_3-xPbTiO_3$ ($PMN-xPT$). (c) The thick magenta arrow and the corresponding magenta-shades spaces show the directions in which the spontaneous polarization, P_s , can rotate and switch continuously in the (c.i) M_A , (c.ii) M_B and (c.iii) M_C monoclinic phases [18, 19].

As we can see in Fig. 1.5 (b), in the compositional range $0.30 \leq x \leq 0.37$ there is a steep and sharp line that separates M_B and M_C phases, which corresponds to the MPB of PMN-xPT. Specifically, at $x \approx 0.30$ the maximum piezoelectric response occurs, with $d_{33} \approx 700$ pm/V for polycrystalline PMN-0.30PT [38], while ultra-high values are encountered for PMN-0.30PT single crystals with $d_{33} \approx 2500$ pm/V and $S_{33} \approx 5 \times 10^{-3}$ [39,40]. Concerning the origin of this ultra-high PE response, the most widely accepted approach is the polarization rotation in monoclinic phases M_B and M_C ; these monoclinic phases serve as ‘structural bridge’ between the different crystallographic R, T and O phases [36]. In addition, according to recent studies [41-44], another key factor for the ultra-high PE coefficients of PMN-xPT, in particular, and of PT-based RFEs, in general, is the endogenous existence of polar nanoregions [35, 36].

1.2 Fundamentals of ferromagnetic, magnetostrictive and piezomagnetic materials

1.2.1 Definitions

Ferromagnetism comes from the word ‘ferrous’ meaning iron, which is the first type of metal discovered to exhibit attraction to magnetic fields. The characteristic feature of a ferromagnetic

(FM) material is the existence of a spontaneous magnetization, M_S that can be altered at will by an external magnetic field, H_{ex} . Detailed description of FM materials is presented in the subchapter 1.2.3.

In addition, almost all FM materials change their shape under the influence of an H_{ex} , that is the *direct magnetostrictive effect (or else Joule effect)*. This effect originates from the rotation and reorientation of the magnetic domains (MDs) of the FM material (see subchapter 1.2.3) under the influence of an H_{ex} . Usually, magnetostriction (or magnetostrictive strain, S^m) is defined as the relative change in length of the FM material, $\Delta L/L$, and it may be positive (i.e. expansion) or negative (i.e. contraction). Often, this strain is also termed *magnetostriction constant*, λ , and it is used to denote magnetostriction measured from coercivity to saturation [45]; typical λ values range within 10^{-6} - 10^{-4} [46]. Complementary to the direct effect, the *converse magnetostrictive effect (or else Villari effect)*, that is the change of magnetic flux density (B) when T_{ex} is applied, is also observed in FM materials. In analogy to electrostriction, magnetostriction describes a change in strain as a quadratic function of H_{ex} .

Except from the magnetostrictive effect -that is typically a quadratic effect- there is also the piezomagnetic effect -that is a linear effect- referring to the induction of a magnetic flux density by applying T_{ex} , or the induction of strain by applying H_{ex} . Its occurrence is attributed to the fact that the structure of crystals which possess a magnetic moment is not invariant under time reversal [47]. This effect is closely connected with the appearance of weak ferromagnetism in non ideal antiferromagnets [48]. Investigations of magnetostrictive materials inevitably involve their elastic and magnetic properties (non linear effects), as well as their piezomagnetic response (linear effect); when these properties coexist they cannot be distinguished experimentally. This is in direct analogy with the case of ferroelectric materials, in which the elastic and dielectric properties (non linear effects) cannot be distinguished from piezoelectricity (linear effect). In this context, polarized magnetostrictive materials may be treated as effectively piezomagnetic over linear ranges of operation, in the same manner as has been done for the analogous piezoelectric materials [49]. For the sake of completeness, both the specific linear piezomagnetic equations and the general magnetostrictive constitutive ones are shown below, in analogy to the respective piezoelectric ones, presented above, in this chapter.

1.2.2 Constitutive relations of the direct and converse magnetostrictive effect

Analogously to Eqs. (1.3) and (1.4) corresponding to the PE effect, the constitutive Eqs. of the direct and converse linear magnetostrictive effect (piezomagnetic effect) in tensor form are:

$$S_j^m = d_{ij}^m H_i \quad (1.8)$$

$$B_i = d_{ij}^m T_j \quad (1.9)$$

with $i=1-3$, $j=1-6$ (for the respective Cartesian coordinate system see Fig. 1.2(b)) and B_i the stress-induced magnetic field. Eqs. (1.8) and (1.9) correspond to the direct and converse linear magnetostrictive effect, respectively. The superscript ‘m’ is used to distinguish the linear

magnetostrictive (piezomagnetic) coefficients, d_{ij}^m , and strain, S_j^m , from their piezoelectric analogs.

In the general case magnetostriction can exhibit a non-linear behavior. Regarding the piezomagnetic coefficients, d_{ij}^m , they represent the magnetic induction generated per unit of mechanical stress, T , or the mechanical strain induced per unit of magnetic field, H . Accordingly, d_{ij}^m is given by the relations:

$$d_{ij}^m = \left(\frac{\partial B_i}{\partial T_j} \right)^H \quad (1.10)$$

$$d_{ij}^m = \left(\frac{\partial S_j}{\partial H_i} \right)^T \quad (1.11)$$

where upper index in Eqs. (1.10) and (1.11) denotes constant magnetic and stress field, respectively.

1.2.3 General properties of ferromagnetic and magnetostrictive materials

At a microscopic level, the driving force for ferromagnetism is the existence of the electrons' net angular momentum. This can arise from either the orbital angular momentum, or the spin component (if there are unequal numbers of 'up' and 'down' spin electrons) or both. Assuming atoms with localized electrons, the exchange energy that causes the alignment of spins in the case of ferromagnetism is described by the Heisenberg Hamiltonian:

$$H = - \sum_{ij} J_{ij} \mathbf{S}_i \cdot \mathbf{S}_j \quad (1.12)$$

where J_{ij} is the exchange integral and \mathbf{S}_i , \mathbf{S}_j are the atomic spins, with $J_{ij} > 0$.

Similarly to FE materials, this ordering takes place under a characteristic Curie temperature T_c ; in a FM domain, a spontaneous magnetization, M_S , derives from the ordered spins per unit volume, even in the absence of an external magnetic field, H_{ex} . It should be noted that, at a macroscopic level the FM material does not exhibit spontaneous magnetization, under the absence of H_{ex} , due to the presence of the FM domains (see below).

The mechanism for the appearance of M_S , was first clarified by Pierre Ernest Weiss in 1907 who suggested the existence of MDs in FM materials. A MD obtains uniform M_S below T_c , while the magnetization in different MDs may point to different directions, with the interfaces separating MDs called magnetic domain walls (MDWs). To explain the ferromagnetism within a MD, Weiss introduced the concept of a mean molecular field [50]. Accordingly, the interactions between localized magnetic moments are equivalent to the existence of an additional internal magnetic field, the so-called molecular field H_M that is a function of the M_S :

$$H_M = \alpha M_S \quad (1.13)$$

where α is the mean field exchange parameter. Weiss theory accounts satisfactorily for the variation of the M_S with temperature and for the fact that a Curie-Weiss law (see Eq. 1.14, below) is obeyed, at least approximately, above T_c . In addition, this model can well describe systems with localized spins, such as EuO. However, it cannot explain the existence of ferromagnetism in metals [51].

In accordance to FE materials discussed in the subchapter 1.1.4, above T_c , thermal fluctuations destroy the magnetic ordering and the material becomes paramagnetic. From Weiss mean field theory, it can be deduced that the magnetic susceptibility in the paramagnetic phase follows the Curie-Weiss law:

$$\chi_m = \frac{M}{H_{ex}} = \frac{C}{T - T_c} \quad (1.14)$$

where M is the magnetization, H_{ex} is the external magnetic field and C is a constant.

The energy of a MD is determined by the following competing energy terms [52-54]:

$$E_{domain} = E_{exch} + E_z + E_{ms} + E_{mc} + E_{me} \quad (1.15)$$

where

- E_{exch} is the exchange energy, i.e. the energy that dominates the alignment of magnetic dipoles at small length scales,
- E_z is the Zeeman energy, i.e. the energy that describes the interaction between magnetization and H_{ex} ,
- E_{ms} is the magnetostatic energy, i.e. the energy referring to the stray field of the magnetic domain,
- E_{mc} is the magnetocrystalline energy, i.e. the energy needed to deflect the magnetic dipoles from ‘easy’ (the nearest to the H_{ex} direction) to the ‘hard’ crystallographic axis,
- E_{me} is the magnetoelastic energy, i.e. the energy associated with the magnetostrictive strain and stress.

Similarly to Figs. 1.4(a) and 1.4(c), which show the behavior of electric polarization, P , and PE strain, S , of FE materials under E_{ex} , Figs. 1.6(a) and 1.6(c) present the behavior of magnetization, M , and magnetostrictive strain, S^m , of FM materials under H_{ex} , respectively.

Specifically, Fig. 1.6(a) shows a representative hysteresis loop $M(H_{ex})$ upon varying H_{ex} from point A to I. At first (point A), for an unmagnetized FM material ($M=0$ at $H_{ex}=0$) the MDs are randomly oriented. By increasing H_{ex} , M increases, at first slowly (segment AB), and subsequently abruptly (segment BC), until saturation of magnetization ($+M_{sat}$) is reached (point D). During this process, many interesting phenomena occur. At first, domain wall motion, where the MDs which are aligned favorably to H_{ex} grow at the expense of the unfavorably aligned ones. At higher fields, domain rotation can occur, where magnetocrystalline anisotropy can be outweighed; M can suddenly rotate away from its original direction towards the ‘easy’ axis. In the highest H_{ex} , coherent domain rotation towards H_{ex} occurs, irrespectively of the ‘easy’ and ‘hard’ axes [53]. By decreasing H_{ex} (segment DE) some MDWs will back-switch, while at $H_{ex}=0$ (point E), M attains a non-zero value, called remanent magnetization ($+M_{rem}$), where some MDs are still oriented towards H_{ex} . By increasing H_{ex} in the opposite direction, M decreases down to zero (point F). The corresponding magnetic field at which M regains zero value is called magnetic coercive field, H_c^- (point F); at $H_{ex}^- = H_c^-$ the moments of the individual MDs are randomly oriented and sum to zero. With further increase of H_{ex} in the opposite direction (segment FG), the MDs get reversed and ultimately aligned with H_{ex} (point G), signifying the respective saturation of magnetization ($-M_{sat}$). By decreasing H_{ex} back to zero (point K), $-M_{rem}$ is reached, while by increasing it once again (segment KI) $M(H_{ex})$ traces the point H, which corresponds to H_c^+ .

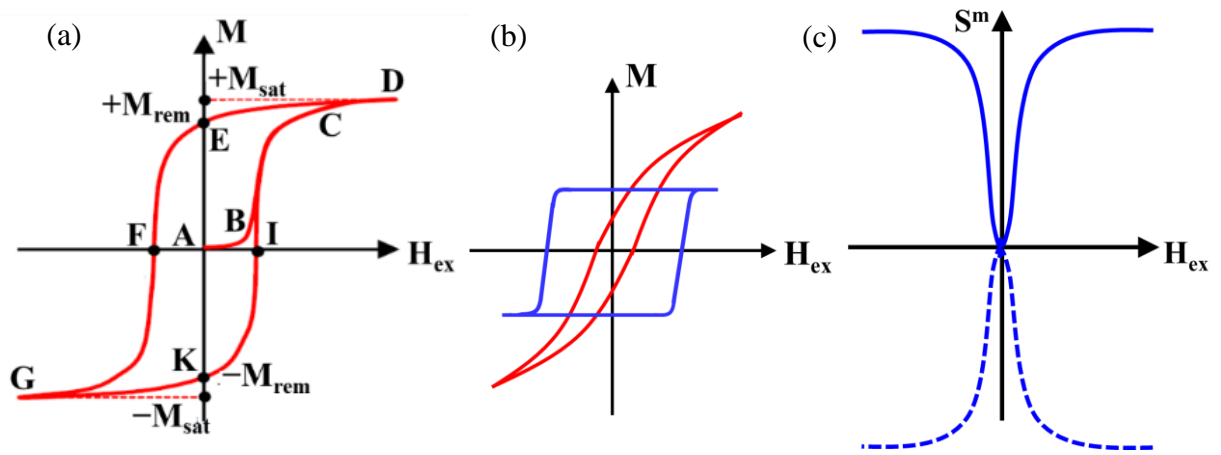


Fig. 1.6: (a), (b) Typical magnetization-magnetic field hysteresis loops for ferromagnetic, FM, materials, $M(H_{ex})$. (a) The characteristic segments/points of $M(H_{ex})$ loop are denoted by symbols (see text for details). (b) Different $M(H_{ex})$ loops of ‘hard’ and ‘soft’ FM materials are denoted by blue and red curves, respectively. (c) Typical magnetostrictive strain curve for FM materials, $S^m(H_{ex})$. The solid and dashed lines correspond to positive (expansion) and negative (contraction) magnetostriction, respectively.

Similarly to FE materials, FM materials can also be categorized as ‘hard’ and ‘soft’. The former ones are characterized by high H_c (difficulty in the reversal of MDs) and high M_{rem} , while the latter ones by a much smaller H_c and M_{rem} , as it is shown in Fig. 1.6(b), by the blue

and red curves, respectively. Typical ‘hard’ FM materials are Co, Ni and their alloys, while typical ‘soft’ FM (or ferrimagnetic) materials are iron oxides (Fe_3O_4 , Fe_2O_3), NiO, and MgO.

Fig. 1.6(c) shows the variation of magnetostrictive strain, $S^m = \Delta L/L$, with H_{ex} , that is $S^m(H_{\text{ex}})$, for positive and negative magnetostriction, denoted by the solid and dashed blue lines, respectively. For relatively small H_{ex} values, $S^m(H_{\text{ex}})$ is almost linear, while for high H_{ex} values $S^m(H_{\text{ex}})$ has quadratic behavior, reaching saturation.

1.2.4 Ferromagnetic materials of different types and geometries

Subchapters 1.2.4.I and 1.2.4.II survey the basic properties of FM thin metallic films and of FM transition metal oxides, respectively. We focus our discussion on Co thin films and, mostly, on iron oxides (Fe_3O_4 and Fe_2O_3 in bulk and nanoparticle (NP) form), since these are the magnetic constituents of the composite materials that were studied in this Thesis (see subchapters 3.1 and 3.2).

I. Thin metallic films

Regarding ferromagnetism in metals, in general, the aforementioned Weiss theory fails to describe it, as already mentioned in the subchapter 1.2.3. Alternatively, the band theory is a successful approach. According to the latter, the electrons responsible for ferromagnetism are considered to belong to the crystal as a whole and to be capable of moving from one atom to another, rather than being localized at the positions of the atoms. This theory explains fairly well the relative magnitudes of magnetic moment per atom in Fe, Ni and Co and the value of the average magnetic moment per atom in certain alloys [51].

Concerning thin film magnetism, in particular, the development of spintronics from the early 1990s onwards has been a considerable motive for its extensive investigation [57-59]. Specifically the thin films of the transition metals Fe, Ni, Co and their alloys are the most important for applications, thanks to their large magnetic moments and high tunability [60]. A remarkable characteristic of these systems is that they are dominated by strong magnetic (shape) anisotropy [61]. As the film thickness increases, Kittel predicted that, due to competition between wall and shape energy, the magnetization switches from in-plane (i.e. along the plane of the film) to out-of-plane (along the film thickness, d) [62]. The predicted value of d for which the magnetization switches from in-plane to out-of-plane was calculated to be [62,63]:

$$d \approx 6.8\sigma_w \left(\frac{M_{\text{sat}}}{K} \right) \quad (1.16)$$

where σ_w is the energy of the DW and K the magnetocrystalline anisotropy.

When this condition is applied to polycrystalline Co thin films the crossover is predicted to occur at 30 nm [64], while according to experimental studies, the critical thickness ranges between 30-50 nm. Also, the formation of MDs may depend on the film thickness. For $d < 30$ -50 nm, MDs, if exist, are relatively large with irregular form and in-plane configuration of

magnetization, while for $d > 30\text{-}50$ nm MDs have the form of relatively narrow stripes with alternating out-of-plane orientation of magnetization [65].

It is worth mentioning that among pure metallic FM materials (like Fe and Ni) Co has the highest magnetostriction constant with $\lambda \sim 60 \times 10^{-6}$ [46].

II. Transition metal oxides in bulk and nanoparticle form

Transition metal oxides constitute one of the most interesting classes of materials, exhibiting a wide range of electronic and magnetic properties, which are attributed to the nature of their outer d-electrons [66]. Regarding the magnetic ordering, both antiferromagnetism and ferromagnetism can be observed in transition metal oxides. Antiferromagnetism originates from the interaction between the unpaired d-electrons of two neighbor cations mediated by the bonded oxygen anion (superexchange interaction) [67,68], while ferromagnetism is favored when metal ions with mixed valence are involved (double exchange interaction) [69].

Among other FM transition metal oxides, Fe_3O_4 (magnetite) and the polymorphs of Fe_2O_3 , $\alpha\text{-Fe}_2\text{O}_3$ (hematite) and $\gamma\text{-Fe}_2\text{O}_3$ (maghemite), have been long-term investigated due to their significant magnetic properties. Specifically, the iron oxide NPs have attracted great interest, as they meet tremendous applications in various fields, such as in biomedicine [70-72] and data storage [73-76].

A. Fe_3O_4 , Fe_2O_3 in bulk form

In Figs. 1.7(a)-(c) the crystal structures of the iron oxides Fe_3O_4 , $\gamma\text{-Fe}_2\text{O}_3$ and $\alpha\text{-Fe}_2\text{O}_3$ are presented. Magnetite, Fe_3O_4 , has a cubic inverse spinel structure at room temperature, with Fe^{2+} ions (black spheres) occupying half of the octahedral sites and the Fe^{3+} ions (green spheres) the remaining octahedral and tetrahedral sites (Fig. 1.7(a)).

Bulk magnetite is ferromagnetic at room temperature, with $M_{\text{sat}} \approx 95$ emu/g, and it becomes paramagnetic at $T_c = 850$ K [77-79]. The spins of the octahedral and tetrahedral cations ($\text{Fe}^{3+}/\text{Fe}^{2+}$ and Fe^{3+} , respectively) form two FM sublattices via double exchange interactions, which are coupled antiferromagnetically to one another via superexchange interactions [80]. The electrical conductivity of Fe_3O_4 is higher than other ferrites of the same form ($10^2\text{-}10^3$ $\text{Ohm}^{-1}\text{cm}^{-1}$), displaying an almost metallic character [79]. At $T_V \approx 120$ K, the so-called Verwey transition takes place [81], in which the electrical conductivity decreases by two orders of magnitude and the lattice distorts from cubic to monoclinic structure. This low-temperature metal-insulator transition has been originally attributed to charge ordering for $T < T_V$, although its nature still remains controversial, with some experiments implying that Verwey transition is driven by electron-phonon interactions [82-84].

Figs. 1.7(b) and 1.7(c) present the crystal structures of the $\gamma\text{-Fe}_2\text{O}_3$ and $\alpha\text{-Fe}_2\text{O}_3$, two polymorphs that can be formed by oxidation of Fe_3O_4 in air at $T \geq 500$ K [85].

Specifically, the metastable $\gamma\text{-Fe}_2\text{O}_3$ can be considered as the intermediate form of Fe_3O_4 and $\alpha\text{-Fe}_2\text{O}_3$ [86]. Likewise to Fe_3O_4 , it has a cubic spinel ferrite structure with Fe^{2+} vacancies on the cation sublattice. Thus, only Fe^{3+} cations exist in $\gamma\text{-Fe}_2\text{O}_3$, which are arbitrarily distributed in octahedral and tetrahedral sites, as shown in Fig. 1.7(b). At room temperature, $\gamma\text{-Fe}_2\text{O}_3$ is FM with $M_{\text{sat}} = 76$ emu/g, while its Curie temperature is difficult to be measured, since,

due to its thermal instability, $\gamma\text{-Fe}_2\text{O}_3$ conventionally converts to $\alpha\text{-Fe}_2\text{O}_3$ above $T=550$ K [87-89].

In Fig. 1.7(c) the crystal structure of the most stable $\alpha\text{-Fe}_2\text{O}_3$ is shown, with Fe^{3+} ions occupying two-thirds of the octahedral sites that are confined by the nearly ideal hexagonal close-packed oxygen lattice. The magnetic structure of $\alpha\text{-Fe}_2\text{O}_3$ is canted-antiferromagnetic at

room temperature, with $M_{\text{sat}}\approx 0.4$ emu/g and $T_c=950$ K. At $T_M\approx 260$ K, $\alpha\text{-Fe}_2\text{O}_3$ undergoes a spin-reorientation transition, known as Morin transition [90], from canted antiferromagnetic to pure antiferromagnetic phase.

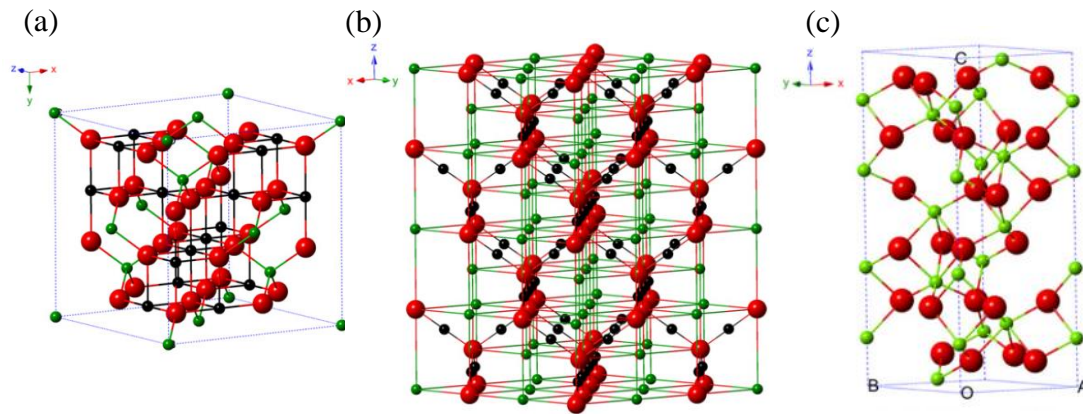


Fig. 1.7: Crystal structure of (a) magnetite, Fe_3O_4 , (b) maghemite, $\gamma\text{-Fe}_2\text{O}_3$ and (c) hematite, $\alpha\text{-Fe}_2\text{O}_3$, at room temperature. The green, black and red spheres correspond to Fe^{3+} , Fe^{2+} and O^{2-} , respectively.

B. Fe_3O_4 , Fe_2O_3 in nanoparticle form

Regarding the NPs of iron oxides, they offer unique properties, since they have high surface-to-volume ratio, a feature that renders them highly versatile and efficient in numerous applications [70-76]. Unlike their bulk counterparts, their magnetic properties are size and shape-dependent. In general, iron oxide NPs are superparamagnetic at room temperature, when their size is below 8-20 nm [78,91,93]; the energy barrier against magnetization reversal is comparable to thermal activation effects, resulting in their superparamagnetic behavior, which is generally characterized by negligible magnetic coercive field, H_c , and remanent magnetization, M_{rem} [91,92]. The critical size for which NPs become superparamagnetic is around 20 nm for Fe_3O_4 , 15 nm for $\gamma\text{-Fe}_2\text{O}_3$ and 8-20 nm for $\alpha\text{-Fe}_2\text{O}_3$ [93,78]. As their size increases, NPs gradually retain their bulk FM character.

For example, Li et al. [73] studied the correlation between particle size and magnetic properties of Fe_3O_4 NPs. Fig. 1.8 presents their results on the hysteresis loops of Fe_3O_4 NPs for different particle sizes. NPs with size ranging within 9.6-24.4 nm exhibit superparamagnetic character with nearly zero H_c and M_{rem} , while NPs with size in the range 31.9-287 nm display FM behavior, with M_{sat} increasing with NP size.

The shape of iron oxide NPs is an additional factor that affects their magnetic properties [94-97]. In a detailed study Kolhatkar et al. [94] highlight the relation between Fe_3O_4

nanospheres/nanocubes and their magnetic sensing ability; the comparative M_{sat} and H_c data for the respective NPs showed that that nanocubes exhibit enhanced magnetic properties. In addition Tadi et al. [97] provide a comparative review of H_c , M_{rem} and M_{sat} values for $\alpha\text{-Fe}_2\text{O}_3$ NPs of different shapes, evidencing noticeable morphology dependence which probably drives from the shape anisotropy.

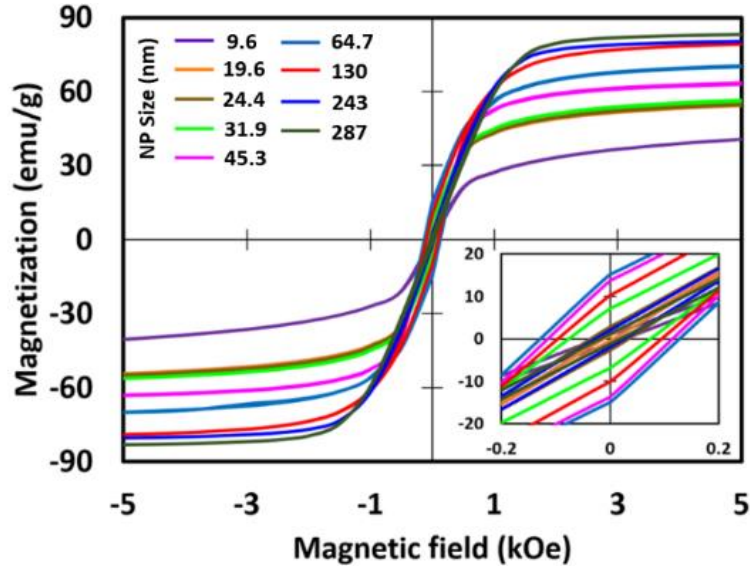


Fig. 1.8: Magnetization hysteresis loops, $M(H_{\text{ex}})$, of Fe_3O_4 NPs and particle size dependence, at room temperature [73].

It should be highlighted that Fe_3O_4 and Fe_2O_3 display fair magnetostriction. Regarding Fe_3O_4 , λ ranges within $20 \cdot 10^{-6}$ to $90 \cdot 10^{-6}$ for single crystals and within $30 \cdot 10^{-6}$ to $50 \cdot 10^{-6}$ for polycrystalline samples [98,99]. In addition, for single crystals of bulk $\alpha\text{-Fe}_2\text{O}_3$, the magnetostriction is lower, on the order of $10 \cdot 10^{-6}$ [100]. Regarding the case of Fe_3O_4 and Fe_2O_3 NPs, their magnetostriction is nearly unaltered compared to the bulk ones, except for the case of ultra-small Fe_3O_4 NPs (less than 9 nm), where a strong increase in magnetostriction has recently been observed [101,102].

1.3 Fundamentals of multiferroic materials

1.3.1 The direct and converse magnetoelectric effect

In general, ferroic is a rather conventional material that under specific conditions attains one kind of microscopic order parameter responsible for the appearance of macroscopically observed properties, e.g. electric, magnetic, elastic etc. On the contrary, a multiferroic (MF) material is of relatively exotic nature, since it combines two or more interacting order parameters that drive a cross-coupling of the respective macroscopic properties.

Among them, an ever-growing interest has been drawn in MF materials that combine ferroelectricity and ferromagnetism, along with a strong coupling between them, which gives rise to the so-called magnetoelectric (ME) effect [103,104]. Hence, the ME materials have the unique property of modifying their polarization/magnetization when subjected to an external magnetic/electric field, respectively.

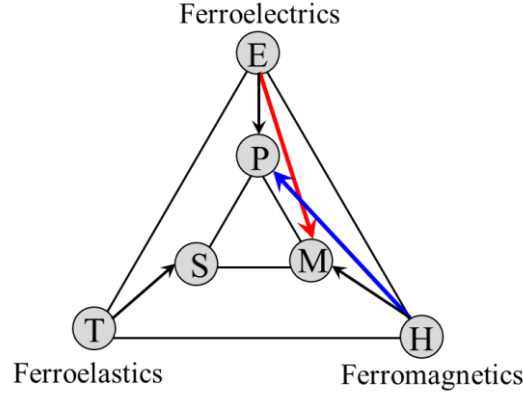


Fig. 1.9: Possible cross-couplings in multiferroics. The red and blue arrows denote the ME coupling between ferroelectrics and ferromagnetics.

Specifically, the *direct* ME effect describes the modification of P (or E) upon the application of H_{ex} (blue arrow in Fig. 1.9) as described by the following relations:

$$\Delta P = a \Delta H_{ex}, \text{ or } \Delta E = \alpha^{H \rightarrow E} \cdot \Delta H_{ex} \quad (1.17. a)$$

$$\text{with } a_{ij}^{H \rightarrow E} = \mu_0 \frac{dE_i}{dH_{ex,j}} \quad (1.17. b)$$

The *converse* ME effect, describes the modification of M upon the application of E_{ex} (red arrow in Fig. 1.9), as denoted by the relations below [105]:

$$\Delta M = \alpha^{E \rightarrow M} \cdot \Delta E_{ex} \quad (1.18. a)$$

$$\text{with } a_{ij}^{E \rightarrow M} = \mu_0 \frac{dM_i}{dE_{ex,j}} \quad (1.18. b)$$

The coefficients $\alpha^{H \rightarrow E}$ and $\alpha^{E \rightarrow M}$ ($\mu_0 = 4\pi \times 10^{-7}$ V s/A m) are the direct and converse ME coefficients, respectively.

1.3.2 Review in multiferroic materials

The term ‘*multiferroic*’ was first introduced by H. Schmid in 1994 [106]. Although the term is very recent, the existence of MF materials and ME coupling was predicted experimentally and theoretically by Röntgen (1888) [107] and by Curie (1894) [103], respectively. In turn, pioneering work on MF materials goes back to more than half a century [108-113], reaching its peak in 1973. Although the scientific interest declined for about two decades due to the inherent weakness in the performance of the already known MF compounds, a revival of ME effect was observed around 1990s; this is attributed to new degrees of freedom in designing MF compounds, new experimental techniques and novel concepts for understanding their behavior [114]. After this brief introduction, we will subsequently focus on the classification of MF ME materials in single phase and composites.

I. Single phase multiferroic magnetoelectric materials

In single phase MF ME materials the presence and the coupling of magnetic and electric order is the result of strong electron correlations. The simultaneous presence of ferroelectricity and magnetism is constrained not only by symmetry, but also by the physical requirements for ferroelectricity, such as dielectric behavior, and for magnetism, such as unpaired electrons [115-117]. These constraints imply that the number of MF ME materials in nature that inherently combine both ferroelectric and magnetic properties, is relatively small.

Depending on the physical mechanism of ferroelectricity, Khomskii classified the single phase ME materials in two groups, Type-I and Type-II.

Type-I single phase MF ME materials are those in which ferroelectricity and magnetism have different origins. While magnetic order derives from the exchange interactions between the unpaired spins, there are distinct mechanisms that can give rise to ferroelectricity; lone pair ferroelectricity, as in BiFeO_3 [118,119] and BiMnO_3 [120-122], charge ordering, as in TbMn_2O_5 [123] and geometric effects, as in YMnO_3 [124]. In particular, BiFeO_3 is the most widely investigated single phase ME in the recent years [125], since it has high Curie temperature. However, it is very weak ferromagnetic. In general, single phase MF MEs of Type-I show large polarization values and ferroelectricity appears at much higher T_c than magnetism. This difference in transition temperatures shows that ferroelectricity and magnetism involve different energy scales and mechanisms, leading to weak ME coupling.

Type-II single phase MF MEs correspond to materials in which ferroelectricity is induced by magnetism. This behavior can be observed in spiral magnets, such as TbMnO_3 [126] and $\text{Ni}_3\text{V}_2\text{O}_6$ [127] and in spin frustrated collinear systems, such as TbMn_2O_5 [128] and YMn_2O_5 [129]. This type of single phase MF MEs show small polarization values and ferroelectricity always appears at lower temperature than magnetic order. Accordingly, the low critical temperatures and/or weak ME coupling of the already known single phase MEs set certain limitations in their utilization.

II. Composite magnetoelectric materials

Alternatively to their single phase counterparts, MF ME composites constructed of distinct FE and FM building units, can be designed at will and exhibit better performance. Specifically, the coupling of their properties leads to large ME response even at room temperature, a fact that is rarely met in the single phase candidates [130,131]. For this reason, they find tremendous applications in functional devices such as information storage and magnetic field sensors [105,132-135].

The ME effect in these materials is known as a product tensor, first proposed by van Suchtelen in 1972 [136], that results from the cross interaction between the two phases in the composite. It can occur extrinsically via the following three interface mechanisms: (1) strain transfer [137-139] (2) exchange anisotropy [140], and (3) charge mediated coupling [141]. Among them, the first one is the most well established mechanism in MF ME composites. Specifically, according to the strain transfer mechanism, the ME effect is the result of the product of the PE effect, in the FE phase, and the magnetostrictive effect, in the magnetic phase:

$$\text{Direct ME effect} = \frac{\text{magnetic}}{\text{mechanical}} \times \frac{\text{mechanical}}{\text{electric}} \quad (1.19.a)$$

$$\text{Converse ME effect} = \frac{\text{electric}}{\text{mechanical}} \times \frac{\text{mechanical}}{\text{magnetic}} \quad (1.19.b)$$

This coupling is indirect in that mechanical strain (piezoelectric and magnetostrictive) mediates to achieve an electric response with the application of an H_{ex} (Eq. 1.19.a) or conversely, a magnetic response with the application of an E_{ex} (Eq. 1.19.b).

In order to achieve a noticeable strain-mediated ME coupling, it is important that there is a good elastic coupling between the FE and FM constituents. To this end, several architectures have been conceived; representative cases are shown in the Figs. 1.10(a)-(d). Namely:

1. *FM NPs embedded in a bulk PE matrix.* These structures, form particulate MF ME composites, where the interfacial strain is transmitted at the grain boundaries. They are usually composed of ferrite micro/nano particles embedded in a bulk PE material (Fig. 1.10(a)). Indicative compounds for the PE phase are the perovskite oxides PZT, PMN-PT and BaTiO₃ (BTO), while for the FM phase ferrites such as NiFe₂O₄ (NFO), CoFe₂O₄ (CFO), and NFO doped with Co, Cu, and/or Mn [142-145]. The ME coefficient for these composites ranges within 10-100 mV cm⁻¹Oe⁻¹, at maximum [144]. Their considerable advantage is the simple, versatile and low cost preparation, usually via the conventional solid state reaction. The usual problems are two; the formation of byproduct phases, due to the high sintering temperatures that could deteriorate the piezoelectricity/magnetostriction of the constituent phases, and also the fact that, by increasing the ferrite phase concentration above a critical value, makes the electric poling difficult due to its low resistivity.

2. *Laminate structure of PE and FM thick films/layers.* These structures form laminate composites (Fig. 1.10(b)), relying on the bonding between the plates of the composite for strain propagation, with ME coefficients around 60 V cm⁻¹Oe⁻¹, at maximum [146]. They are generally fabricated by cofiring thick layers (on the order of mm/μm) of FM and PE oxides at high temperature. The most common laminate ME composite is a simple bilayer structure, or a sandwich structure of a FM (or PE) layer sandwiched between two PE (or FM) layers, obtained by solid state reaction; for example, PZT, PMN-PT layers along with e.g NFO, CFO or (La,Ca)MnO₃ (LCMO) are some reported laminated structures [147-149]. Here, the leakage problem that is manifested in the case of (1) can be reduced, however, the high temperature cofiring of the two layers is still challenging due to the different shrinkage-thermal expansion mismatch and atomic interdiffusion during sintering.

3. *Epitaxial PE and FM vertical nanostructures.* With the epitaxial strain developing at the structurally coherent interfaces between the PE and FM phases, they exhibit ultra-high values of ME response, around 300 Vcm⁻¹Oe⁻¹ [150]. Representative nanostructures are BaTiO₃-CoFe₂O₄ [151] and BiFeO₃-CoFe₂O₄ [152]. Their fabrication is usually realized via self-assembly process; under the appropriate growth conditions, nanopillar arrays of the magnetic

components are formed in the FE matrix (Fig. 1.10(c)). Accordingly, due to the improved contact area between the two components, they display better elastic coupling that justifies their enhanced ME coefficient values. While they exhibit advantageous performance, their main disadvantage is the difficulty in the fabrication, especially for long range well-ordered structures.

4. *Epitaxial heterostructures consisting of FM films deposited on PE substrates or PE-FM bilayer and multilayers.* In these structures the ME coupling is weaker than in vertical nanostructures due to clamping effect, however their growth process is less demanding. We can categorize them in two subgroups of layered heterostructures: (i) FM thin films on bulk FE oxide substrates (Fig. 1.10(d)), and (ii) nanoscale heterostructures of FE and FM thin films. Different combinations of PE (e.g. BTO, PZT, PMN-PT) and FM (e.g. Fe, Co, CoFeB, $\text{La}_{1-x}\text{Sr}_x\text{MnO}_3$, Fe_3O_4) materials yield layered heterostructures of type (i) [153,154] and (ii) [155,156]. Regarding the preparation techniques, pulse laser deposition, molecular beam epitaxy, spin spray deposition and magnetron sputtering are widely employed for these structures.

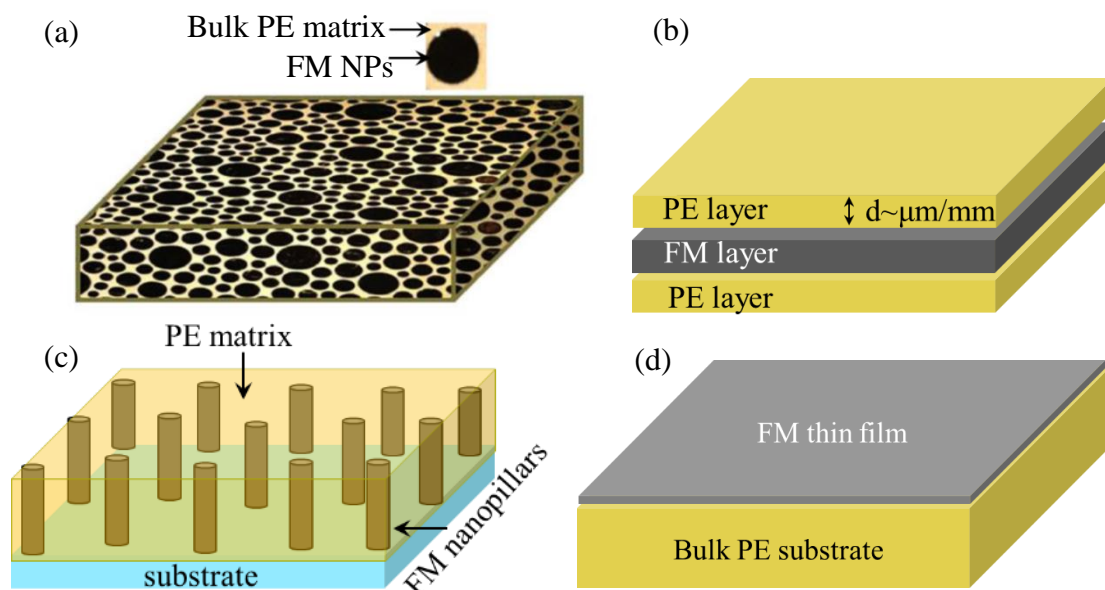


Fig. 1.10: (a)-(d) Schematic illustrations of representative composite magnetoelectrics' architectures: (a) Ferromagnetic, FM, nanoparticles, NPs, embedded in bulk piezoelectric, PE, matrix, (b) laminate structure of PE and FM thick films/layers, (c) Epitaxial PE and FM vertical nanostructures, and (d) Epitaxial heterostructures consisting of FM films deposited on PE substrates or PE-FM bilayer and multilayers

1.3.3 Review in the direct and converse magnetoelectric effect for bulk composite magnetoelectric materials

Here, we will briefly review the direct and converse ME effects in bulk ME composites, i.e. structures with type (1), (2) and (4.i) of the subchapter 1.3.2.II, since they are most related to

the subject of this Thesis. For the sake of simplicity, the ‘MF ME composites’ will be just called ‘ME composites’.

Among the two expressions of the ME effect, the converse one is the most widely investigated. Controlling magnetic properties by applying an electric field, rather than current, has become a considerable issue in the field of spintronics and ME composites. Regarding the composite structures with type (1), (2) (see subchapter 1.3.2.II) relevant studies have been performed. Park et al. [157] found decrease in M_{rem} with E_{ex} for the composite of $CoFe_2O_4$ micro-particles dispersed in a PZT matrix. In addition, Ma et al. [158] and Chen et al. [159] demonstrated electric-field controlled switching of magnetization of the magnetostrictive layers of FeBSiC/PZT and FeCoV/PMN-PT bilayer laminates, respectively. Noticeable tuning of the FM resonance frequencies has also been observed by applying a bias voltage; large shift at microwave frequencies has been demonstrated in bilayer laminates such as FeGaB/Pb(In_{1/2}Nb_{1/2})O₃-Pb(Mg_{1/3}Nb_{2/3})O₃-PbTiO₃ [160]. In addition, extended research on the converse ME effect has been realized for composite structures with type (4) (see 1.3.2.II), where FM thin films are either oxides or metals. Regarding FM oxide thin films on PE substrate, Eerenstein et al. [161] reported electrically induced giant, sharp and persistent magnetic changes at a single epitaxial interface in FM La_{0.67}Sr_{0.33}MnO₃ films on BTO substrates, driven from a strong ME coupling. Similar results were presented by Thiele et al. [162] for La_{0.70}Sr_{0.30}MnO₃ thin films on PMN-PT substrates.

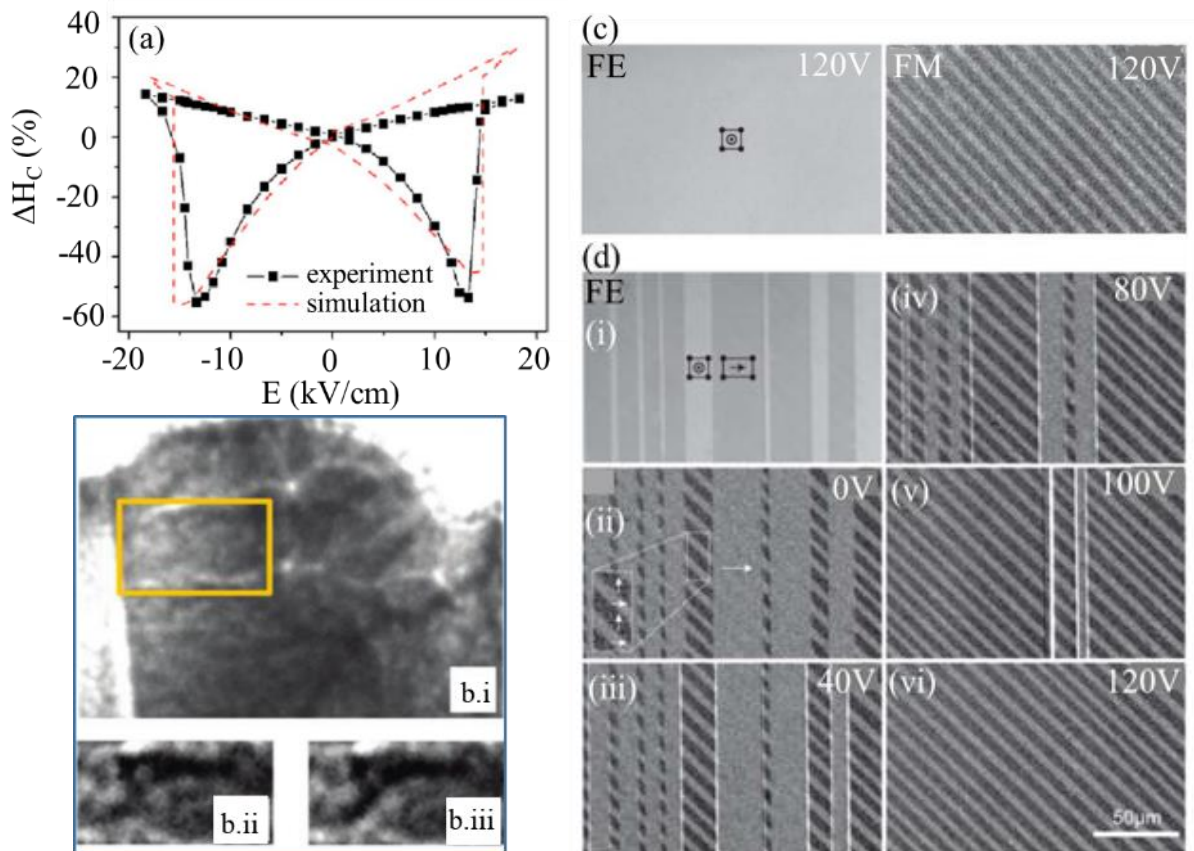


Fig. 1.11: Electric-field induced changes in (a) coercive field variation [163], (b.i)-(b.iii) Lorentz microscopy images of FM domains [164] and (c),(d) optical polarization microscopy images of FE and FM domains [165] (see text for details).

Regarding metallic thin films on PE substrate, Sahoo et al. [153] found electric field control of magnetic anisotropy and coercivity for Fe thin films deposited on BTO substrates. In addition Wang et al. [163] studied the Fe/BiScO₃-PbTiO₃ bilayer thin film and found dramatic change up to 60% in the magnetic coercive field upon the application of an electric field, as shown in Fig. 1.11(a). Interestingly, straightforward manifestations of the converse ME have been reported by employing microscopy techniques. Accordingly, Britlinger et al. [164] studied the thin film Fe_{0.7}Ga_{0.3}/BTO bilayer structure and reported direct observation of controlled switching of MDs using Lorentz microscopy upon E_{ex} application, as shown in Figs. 1.11(b.i)-(b.iii); the yellow rectangle in panel (b.i) is the area of interest, which is subsequently presented in panels (b.ii) and (b.iii) under the application of a low and a high electric field, respectively. In the same spirit, Lahtinen et al. [165] employed optical polarization microscopy and demonstrated electric-field control of local magnetic properties, such as writing and erasure of regular FM domain patterns and the motion of DWs in CoFe/BTO thin film bilayers. In Figs. 1.11(c) and 1.11(d) the evolution of FM domain structure is shown as function of out-of-plane bias voltage. First, as shown in Fig. 1.11(c), the BTO substrate is saturated by a bias voltage 120V, a fact that produces regular FM stripe pattern in CoFe. By reducing the voltage to zero (Fig. 1.11(d.i)) the FE substrate relaxes, obtaining alternating domain patterns which are also adapted by the FM film (Fig. 1.11(d.ii)); this evidences erasure of magnetic stripes, due to change in magnetic anisotropy. Subsequent increase of the voltage causes growth of the stripe domains, as gradually depicted in Figs. 1.11(d.iii)-(d.vi), until the regular magnetic stripe pattern is electrically rewritten.

The direct ME effect has been investigated to a lesser extent than the converse one, with most of the studies focusing on two main points: the direct ME coefficient $\alpha^{H \rightarrow E}$ and the modification of P with H_{ex}.

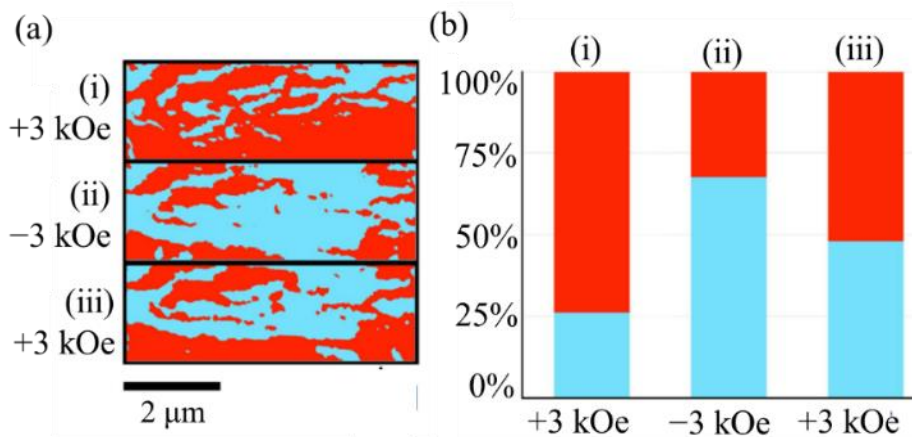


Fig. 1.12: (a) Phase images from piezoresponse force microscopy upon consecutive application of an external magnetic field, H_{ex} (i) +3 kOe, (ii) -3 kOe, and (iii) +3 kOe nominally; the positive H_{ex} favor the growth of polarization directions indicated by red contrast, while the negative H_{ex} favors the contraction. (b) Histograms with colors of the respective phases for each H_{ex} [166].

Regarding the first point, most of the studies have been conducted on composite structures with type (1) (see subchapter 1.3.2.II) [142-145]. Among them, Ryu et al. [144] reported the highest ME coefficient, $\alpha^{H \rightarrow E} = 115 \text{ mV cm}^{-1} \text{ Oe}^{-1}$ at $T = 1250 \text{ }^\circ\text{C}$, for the bulk particulate MF

80% (PZT)/20% (NiCo_{0.02}Cu_{0.02}Mn_{0.1}Fe_{1.8}O₄). Regarding the second point, Kumar et al. [139] examined the ME composite BiFeO₃-BaTiO₃ in which FM arises from a small fraction (~1 wt%) of BaFe₁₂O₁₉ that is formed during sintering. Interestingly, a very large increase (~34%) of the P_{sat} was observed under application of H_{ex}=10 kOe. In addition, corresponding studies performed by means of piezoresponse force microscopy demonstrate the modulation of FE domains, upon application of H_{ex} on the order of 2-9 kOe. Among them, Evans et al. [166] and Xie et al. [167] based on PZT as PE component, studied the changes in polarization and piezoresponse upon H_{ex}, for the cases of the ME composites PbZr_{0.53}Ti_{0.47}O₃-PbFe_{0.5}Ta_{0.5}O₃ single crystals and PbZrTiO-TbDyFe bilayer, respectively. These changes, were significant in magnitude, although partially reversible (Fig. 1.12) [166] or entirely irreversible [167].

1.4 Motivation of the Thesis

During the last decades, much attention has been paid on ME composite materials [142-147]. Relevant studies report that the FM and PE constituents of these composites can modulate their macroscopic physical properties under application of an external electric E_{ex} [157-163] and magnetic H_{ex} [139, 166] field, respectively. What is more, microscopy techniques (such as Lorentz, polarization, and piezoresponse force microscopy) are recently in the foreground for the investigation of ME composites under the simultaneous application of E_{ex} or H_{ex} [164, 165, 167]; these techniques aim to visualize in a straightforward way modulations in the microscopic physical characteristics of these composites under the presence of E_{ex} and H_{ex} (such as the modulation in the shape of their FM and FE domains, respectively).

Motivated by the aforementioned studies, this PhD Thesis aims to examine relevant ME composite structures regarding their response to E_{ex} and H_{ex}. Specifically, two different topologies will be investigated; firstly, FM thin film of Co (thickness of 30-50 nm) deposited on both sides of bulk PE single crystals of Pb(Mg_{1/3}Nb_{2/3})O_{3-x}PbTiO₃ (PMN-0.30PT) in a planar configuration FM/PE/FM, that is Co/PMN-0.30PT/Co and secondly, FM nanoparticles of Fe₃O₄ (diameter 50-100 nm) embedded into a bulk PE matrix of Pb(Zr_{0.52}Ti_{0.48})O₃ (PZT), that is PZT-xFe₃O₄, where x is the weight percentage concentration of Fe₃O₄.

Regarding the former topology, we stress that its PE part, PMN-0.30PT, exhibits ultra-high PE coefficients (d on the order of 2000 pm/V), while its FM part possesses high magnetization (m_{sat} on the order of 100 emu/g) and significant magnetostrictive behavior (λ on the order of 10⁻⁵). Hence, the aforementioned properties of the starting compounds, PMN-0.30PT and Co, are promising in that a noticeable ME coupling could be possibly developed between them. Plausibly, we expect that these properties can be easily retained, even after the preparation of the composite Co/PMN-0.30PT samples, by means of magnetron sputtering. Specifically, compared to the multiparametric preparation conditions of the PZT-xFe₃O₄ samples of the second topology (see below), the preparation conditions of Co/PMN-0.30PT ones are simpler. In addition, Co was chosen since from the experience in our lab we know that the magnetic domains hosted in the thin film rotate from in-plane to out-of-plane at a characteristic value of thickness. Thus, even the global magnetization of Co can probably be susceptible to modulation applied by a field of strain induced by the adjacent PMN-0.30PT single crystal.

Regarding the latter topology, we stress the following; in general, from a thorough review of the literature, we realized that ME composites of this topology have been investigated to less extent compared to ME composites of the planar topologies, as the one discussed above. This is usually attributed to the fact that they suffer from formation of byproducts, which in most cases have lost the desired properties of the starting constituents, having low PE coefficients, degraded magnetization, suppressed magnetostrictive behavior and low resistivity. In our case, PZT and Fe_3O_4 are two well-studied compounds to possess physical properties that, under specific experimental circumstances, could guarantee a noticeable ME coupling; the former possesses strong PE coefficients (d on the order of 260 pm/V), while the latter exhibits significant magnetization (m_{sat} on the order of 80 emu/g) and fair magnetostrictive behavior (λ on the order of 10^{-6}). However, since the composite samples of this topology, $\text{PZT-xFe}_3\text{O}_4$, will be prepared by solid state sintering, bringing out the desired ME coupling is not an easy task; a multiparametric landscape of preparation conditions (sintering temperature, sintering duration, weight percentage of constituents, pressure, atmosphere, etc.) should be investigated in a systematic way to reliably avoid the formation of most undesired byproducts. Since, to the best of our knowledge, $\text{PZT-xFe}_3\text{O}_4$ composites of this topology have not been investigated systematically, their study is surely worthy.

The piezoelectric/ferromagnetic hybrid nanostructures under discussion, namely the Co/PMN-0.30PT and PZT-xFe₃O₄, will be investigated thoroughly regarding the control of the FM and PE properties under application of the heteroconjugate, external applied fields, that is E_{ex} and H_{ex} , respectively, as discussed below.

Referring to the FM properties, we will focus on the study of the magnetic coercive field, H_c , saturation magnetization, m_{sat} , and the remanent magnetization, m_{rem} , under application of the heteroconjugate field that in this case is E_{ex} . Specifically, as a first step, we are interested in showing electric-field modulation of H_c , m_{sat} and m_{rem} , since these effects could fairly prove the existence of ME coupling between the FM and PE constituents of the composites. Furthermore, except for the electric-field modulation *per se*, as a second step, we are especially motivated to investigate m_{rem} , since it is a magnetic property directly related to technological applications (e.g. provides the magnetic memory element in information storage devices of magnetic nature); specifically, we aim to study the modulation of m_{rem} that can possibly be both reproducible and reliable under application of an E_{ex} . By the terms reproducible and reliable we mean the stability and reversibility of the modulation of m_{rem} , since these are two prerequisite key-characteristics for possible applications, such as handling of bit information by electric and/or magnetic fields. The corresponding data will be obtained by means of specialized magnetization measurements; we will employ a home-made sample rod so that, in addition to the standard external magnetic field, H_{ex} , an external electric field, $E_{\text{ex,z}}$ ($-10 \text{ kV/cm} \leq E_{\text{ex,z}} \leq +10 \text{ kV/cm}$), could also be applied. Thus, in this scheme, the sample magnetization can be measured under the simultaneous application of both H_{ex} and $E_{\text{ex,z}}$. The specialized magnetization measurements will be employed in a wide temperature range, from cryogenic to room-temperature conditions, i.e. $10 \text{ K} \leq T \leq 300 \text{ K}$. This range is selected in order to study the evolution of the underlying mechanisms that govern the possible ME coupling of the FM and FE order parameters of the two constituents. In addition, emphasis will be paid to room temperature measurements ($T=300 \text{ K}$), since these ME composites could pave the way for practical applications, such as low-power ME memory devices.

Referring to the PE properties, will we focus on the study of the in-plane (i.e. over the sample surface) PE coefficients, d_{zi} , under application of the heteroconjugate field that in this case is H_{ex} . Clearly, d_{zi} is a basic PE parameter, associated with performance (the strain developed per applied electric field), which is an important selection criterion for the utilization of a PE compound in a composite FM/PE material. In addition, as far as we know, d_{zi} has not been studied under application of an H_{ex} , until now. In general, in ME composites the magnetic-field control of FE properties is investigated to less extent compared to the electric-field control of FM ones, and only concerning the electric polarization and piezoresponce (see the last paragraph of subchapter 1.3.3, at the end of Introduction). In this context, we aim to resolve information on the impact of an H_{ex} on the in-plane PE strain of the Co/PMN-0.30PT and PZT- xFe_3O_4 composite samples, by means of a specialized OM-based PE technique. Accordingly, in addition to $E_{ex,z}$ ($-10 \text{ kV/cm} \leq E_{ex,z} \leq +10 \text{ kV/cm}$), we can simultaneously apply on demand a relatively low $H_{ex,z}=1 \text{ kOe}$ to the samples. In this scheme, we can visualize in a straightforward way the in-plane PE strain under application of both $H_{ex,z}$ and $E_{ex,z}$. The specialized OM-based PE measurements will be realized at room temperature ($T=300 \text{ K}$); a potentially pronounced modulation of the PE coefficients of the Co/PMN-0.30PT and PZT- xFe_3O_4 composite samples under H_{ex} could open the way for a new type of room temperature ME sensors.

References

- [1] J. Curie, and P. Curie, Bull. Soc. Min. de France, **3**, 90 (1880).
- [2] G. Lippman, Ann. de Chemie et de Physique **24**, 145, (1881).
- [3] P. Curie, and J. Curie, Comptes Rendus **93**, 1137 (1881).
- [4] T. Leisegang et al., Acta Crystallogr. Sect. A: Found. Adv. **70**, 362 (2004).
- [5] A. L. Kholkin, N. A. Pertsev, and A. V. Goltsev, "Piezoelectricity and Crystal Symmetry", Chapter 2
- [6] N. Soin, S. C. Anand, T. H. Shah, *Handbook of Technical Textiles, Energy Harvesting and storage textiles*, Elsevier (2016).
- [7] J. Fousek, and V. Janovec, J. Appl. Phys. **40**, 135 (1969).
- [8] D. Damjanovic, Rep. Prog. Phys. **61**, 1267 (1998).
- [9] G. H. Haertling, J. Am. Ceram. Soc, **82**, 4, 797-818 (1999).
- [10] D. Damjanovic, G. Bertotti, I. Mayergoyz, *Hysteresis in Piezoelectric and Ferroelectric Materials*, Science of Hysteresis, Volume III, 337-465, Elsevier (2005).
- [11] H. Kungl, T. Fett, S. Wagner and M. J. Hoffmann, J. Appl. Phys. **101**, 044101 (2007).
- [12] G. Viola et al., J. Adv. Dielectr. **3**, 1350007 (2013).
- [13] L. E. Cross, *Mater. Chem. Phys.* **43**, 108 (1996).
- [14] G. H. Haertling, *J. Am. Ceram. Soc.* **82**, 797 (1999).
- [15] B. Jaffe, W. R. Cook and H. Jaffe, *Piezoelectric Ceramics*, Academic Press, London, U.K., (1971).
- [16] M. E. Lines and A. M. Glass, *Principles and Applications of Ferroelectrics and Related Materials*, Claredon (1977).
- [17] B. Noheda *et al.*, Appl. Phys. Lett. **74**, 14 (1999).
- [18] R. Guo et al., Phys. Rev. Lett. **84**, 5423-5426 (2000).
- [19] N. Zhang et al., Nat. Commun. **5**, 5231 (2014).

- [20] F. Cordero, *Materials* **8**, 8195 (2015).
- [21] A. P. Singh, S. K. Mishra, R. Lal, and D. Pandey, *Ferroelectrics* **163**, 103 (1995).
- [22] L. Burianova, M. Sulc, and M. Prokopova, *J. Eur. Ceram. Soc.* **21**, 1387 (2001).
- [23] B. Noheda, *Curr. Opin. Solid State Mater. Sci.* **6**, 27 (2002).
- [24] S. K. Mishra, D. Pandey, A. P. Singh, *Appl. Phys. Lett.* **69**, 1707 (1996).
- [25] J. Yoo, Y. Kim, H. Cho, and Y.-H. Jeong, *Sensors and Actuators A: Physical.* **255** (2017).
- [26] Noliac specification sheet NCE55, CTS Inc.
- [27] M. H. Malakooti and H. A. Sodano, *Appl. Phys. Lett.* **102**, 061901 (2013).
- [28] Y. M. Jin, Y. Wang, A. G. Khachatryan, J. F. Li, and D. Viehland, *Phys. Rev. Lett.* **91**, 197601 (2003).
- [29] Y. U. Wang, *Phys. Rev. B* **76**, 024108 (2007).
- [30] L. J. Jones, M. Hoffman, J. E. Daniels, and A. J. Studer, *Appl. Phys. Lett.* **89**, 092901 (2006).
- [31] J. H. Park, B. K. Kim, K. H. Song, and S. J. Park, *Mater. Res. Bull.* **30**, 435 (1995).
- [32] G. Singh, V. S. Trivari, A. Kumar and V. K. Wadhavan, *J. Mater. Res.* **18**, 531 (2003).
- [33] G. A. Smolenskii, *J. Phys. Soc. Jpn. (Suppl.)* **28**, 26 (1970).
- [34] J.-H. Park, Y. Kim, and S. J. Park, *J. Korean Phys. Soc.* **32**, S967 (1998).
- [35] G. Burns and F. H. Dacol, *Phys. Rev. B* **28**, 2527 (1983).
- [36] S. Zhang, F. Li, *J. Appl. Phys.* **111**, 031301 (2012).
- [37] F. Cordero, F. Trequattrini, F. Craciun, and C. Galassi, *J. Phys. Condens. Matter* **23**, 415901 (2011).
- [38] S. W. Choi, T. R. ShROUT, S. J. Jang, and A. S. Bhalla, *Mater. Lett.* **8**, 253 (1989).
- [39] A. K. Singh, D. Pandey, O. Zaharko, *Phys. Rev. B* **74**, 024101 (2006).
- [40] A. A. Levin, A. I. Pommrich, T. Weissbach, D. C. Meyer, and O. B. Zeneli, *J. Appl. Phys.* **103**, 054102 (2008).
- [41] G. Xu, J. Wen, C. Stock, and P. M. Gehring, *Nat. Mater.* **7** (2008).
- [42] J. Wen, G. Xu, C. Stock, and P. M. Gehring, *Appl. Phys. Lett.* **93**, 082901 (2008).
- [43] M. E. Manley et al., *Sci. Adv.* **2** (2016).
- [44] D. Phelan et al., *PNAS* **111**, 1754 (2014).
- [45] E. W. Lee, *Sci. Progress* **41**, 58 (1933).
- [46] K. B. Hathaway and A. E. Clark, *MRS Bull.* **18**, 34 (1993).
- [47] B. A. Tavger and V. M. Zaitzev, *J. Exp. Theor. Phys. (USSR)* **3**, 430 (1956).
- [48] A. S. Borovik-Romanov, *Ferroelectrics* **162**, 153 (1994).
- [49] *Standard on magnetostrictive materials: Piezomagnetic nomenclature*, IEEE Trans. Sonics Ultrason. **20**, 67 (1973).
- [50] P. Weiss, *J. Phys. Theor. Appl.* **6**, 661 (1907).
- [51] B. D. Cullity and C. D. Graham, *Introduction to Magnetic Materials*, John Wiley & Sons Inc.-IEEE Press (2009).
- [52] R. O'Handley, *Modern Magnetic Materials: Principles and Applications*, John Wiley & Sons Inc. (2000).
- [53] S. Blundell, *Magnetism in Condensed Matter*, Oxford University Press (2001).
- [54] C. Kittel, *Introduction to Solid State Physics*, John Wiley & Sons Inc. (1971).
- [55] E.C. Stoner, *Rep. Prog. Phys.* **11**, 43 (1947).
- [56] E.P. Wohlfarth, *Rev. Mod. Phys.* **25**, 211 (1953).

- [57] D. E. Parkes et al., *Sci. Rep.* **3**, 2220 (2013).
- [58] H. Fujimori, S. Ohnuma, N. Kobayashi, and T. Masumoto, *J. Magn. Magn. Mater.* **304**, 32 (2006).
- [59] G. Wastlbauer and J. A. C. Bland, *Adv. Phys.* **54**, 137 (2005).
- [60] J. Osterwalder, *J. Electron Spectrosc. Relat. Phenom.* **117**, 71 (2001).
- [61] M. Hehn, S. Padovani, K. Ounadjela, and J. P. Bucher, *Phys. Rev. B.*, **54**, 5 (1996).
- [62] C. Kittel, *Phys. Rev.* **70**, 965 (1946).
- [63] D. J. Craik and P. V. Cooper, *Phys. Lett.* **41A**, 255 (1972).
- [64] R. Allenspach and M. Stampanoni, *Magnetic Surfaces, Thin Films, and Multilayers*, MRS Symposia Proceedings No. 231, Materials Research Society, Pittsburgh (1992).
- [65] E. V. Aristomenopoulou, PhD dissertation, *Tailoring the transport properties of a superconductor (sc) by means of ferromagnetic (fm) templates: focusing on planar fm/sc/fm nanostructures*, National Technical University of Athens (2016).
- [66] C. N. R. Rao, *Annu. Rev. Phys. Chem.* **40**, 291 (1989).
- [67] H. A. Kramers, *Physica* **1**, 182 (1934).
- [68] P. W. Anderson, *Phys. Rev.* **79**, 350 (1950).
- [69] C. Zener, *Phys. Rev.* **82**, 403 (1951).
- [70] H. Nemala et al., *J. Appl. Phys.* **116**, 034309 (2014).
- [71] K. L. Chen et al. *Sci. Rep.* **6**, 35477 (2016).
- [72] H. Maleki, A. Simchi, M. Imani, and B. F. O. Costa, *J. Magn. Magn. Mater.* **324**, 3997 (2012).
- [73] Q. Li et al., *Sci. Rep.* **7**, 9894 (2017).
- [74] M. Bibes and A. Barthelemy, *IEEE Trans. Electron. Devices* **54**, 1003 (2007).
- [75] S. Lee et al., *Nat. Mater.* **7**, 130 (2008).
- [76] T. P. Almeida et al., *Nat. Commun.* **5**, 5154 (2014).
- [77] X. Battle et al., *J. Appl. Phys.* **109**, 07B524 (2011).
- [78] Q. Li et al., *Sci. Rep.* **7**, 9894 (2017).
- [79] R. M. Cornell and U. Schwertmann, *The Iron Oxides; structure, properties, reactions occurrences and uses*, John Wiley & Sons Inc. (2003).
- [80] L. Neel, *Ann. Phys.*, **3**, 137 (1948).
- [81] E. J. W. Verwey and P. W. Haayman, *Physica* **8**, 979 (1941).
- [82] F. Mott, *Philos. Mag. B* **42**, 327 (1980).
- [83] Y. Yamada, *Philos. Mag. B* **42**, 377 (1980).
- [84] A. Yanase and N. Hamada, *J. Phys. Soc. Jpn.* **68**, 1607 (1999).
- [85] J. A. Cuenca et al., *J. Phys.: Condens. Matter* **28**, 106002 (2016).
- [86] U. S. Khan et al., *Mat. Sci. Poland* **33**, 278 (2015).
- [87] W. O'Reilly, *Rock and Mineral Magnetism*, Blackie (1984).
- [88] D. H. Tarling, F. Hrouda, *The Magnetic Anisotropy of Rocks*, Chapman & Hall (1993).
- [89] D. J. Dunlop, Ö. Özdemir, *Rock Magnetism: Fundamentals and Frontiers*, Cambridge University (1997).
- [90] I. V. Golosovsky et al., *Solid State Commun.* **141**, 178 (2007).
- [91] M. Aliahmand, and N. N. Moghaddam, *Mat. Sci. Poland* **31**, 264 (2013).
- [92] M. Knobel et al., *J. Nanosci. Nanotechnol.* **8**, 2836 (2008).
- [93] M. Chirita, and I. Grozescu, *Chem. Bull. Politehnica Univ.*, **54**, 68 (2009).

- [94] A. G. Kolhatkar et al., ACS Omega **2**, 1080 (2017).
- [95] P. Guardia, A. Labarta, and X. Batlle, J. Phys. Chem. C **115**, 390 (2011).
- [96] C. de Montferrant et al., Acta Biomater. **9**, 6150 (2013).
- [97] M. Tadic et al., J. Alloys Compd. **509**, 7639 (2011).
- [98] L. R. Bickford, J. Pappis, and J. L. Stull, Phys. Rev. **99**, 1210 (1955).
- [99] B. M. Moskowitz, J. Geophys. Res. **98**, 359 (1993).
- [100] H. M. A. Urquhart and J. E. Goldman, Phys. Rev. **101**, 1443 (1956).
- [101] G. Balaji, R. Aravinda Narayanan, A. Weber, F. Mohammad, and C. S. S. R. Kumar, Mater. Sci. Eng. B **177**, 14 (2012).
- [102] R. Gonçalez et al., J. Mater. Chem. C **4**, 45 (2016).
- [103] P. Curie, *J. Physique* **3**, 393 (1894).
- [104] A. J. Freeman, H. Schmid, *Magnetoelectric Interaction Phenomena in Crystals*, Proceedings of the MEIPIC-1 (1975).
- [105] J. Ma, J. Hu, Z. Li, and C.-W. Nan, Adv. Matter. **23**, 1062 (2011).
- [106] H. Schmid, Ferroelectrics **162**, 317 (1994).
- [107] W. C. Röntgen, Ann. Phys. **35**, 264 (1888).
- [108] D. N. Astrov, J. Exp. Theoret. Phys. (U.S.S.R) **38**, 948 (1960).
- [109] V. J. Folen, G. T. Rado, and E. W. Stader, Phys. Rev. Lett. **6**, 607 (1961).
- [110] G. T. Rado, and V. J. Folen, Phys. Rev. Lett. **7**, 310 (1961).
- [111] I. E. Dzyaloshinskii, Sov. Phys. JETP **10**, 628 (1959).
- [112] T. H. O'Dell, Phil. Mag. **7**, 82 (1962).
- [113] V. E. Wood, and A. E. Austin, Int. J. Magn. **5**, 303 (1973).
- [114] M. Fiebig, J. Phys. D: Appl. Phys. **38**, 123 (2005).
- [115] N. A. Hill, J. Phys. Chem. B **104**, 6694 (2000).
- [116] R. Ramesh and N. A. Spaldin, Nat. Mater. **6**, 21 (2007).
- [117] N. A. Spaldin, *Analogies and differences between ferroelectrics and ferromagnets*, Physics of ferroelectrics; Topics on applied physics **105**, 115, Springer (2007).
- [118] J. B. Neaton, C. Ederer, U. V. Waghmare, N. A. Spaldin, and K. M. Rabe, Phys. Rev. B **71**, 014113 (2005).
- [119] P. Ravindran, R. Vidya, A. Kjekshus, H. Fjellvåg, and O. Eriksson, Phys. Rev. B **74**, 224412 (2006).
- [120] N. A. Hill and K. R. Rabe, Phys. Rev. B **59**, 8759 (1999).
- [121] T. Atou, H. Chiba, K. Ohoyama, Y. Yamaguchi, and Y. Syono, J. Solid State Chem. **145**, 639 (1999).
- [122] S. Sanvito, and N. A. Hill, Chem. Matter. **13**, 2892 (2001).
- [123] J. Efremov, V. Dmutry, Van den Brink, and D. Khomskii. Nat. Mater., **3**, 853 (2004).
- [124] B. B. Van Aken, T. T. M. Palstra, A. Filippetti, and N. A. Spaldin, Nat. Mater. **3**, 164 (2004).
- [125] G. Catalan, and J. F. Scott, Adv. Mater. **21**, 2463 (2009).
- [126] T. Kimura, T. Goto, H. Shintani, K. Ishizaka, and Y. Tokura, Nature **426**, 55 (2003).
- [127] G. Lawes et al., Phys. Rev. Lett. **95**, 087205 (2005).
- [128] N. Hur et al., Nature **429**, 392 (2004).
- [129] L. C. Chapon, P. G. Radaelli, G. R. Blake, S. Park, and S. W. Cheong, Phys. Rev. Lett. **96**, 097601 (2006).

- [130] C. W. Nan, M. I. Bichurin, S. Dong, D. Viehland, and G. Srinivasan, *J. Appl. Phys.* **103**, 031101 (2008).
- [131] J. Ruy, S. Priya, K. Uchino, and H. E. Kim, *J. Electroceram.* **8**, 107 (2002).
- [132] Z. Xiao et al., *Sci. Rep.* **8**, 5207 (2018).
- [133] W. Eerenstein, N. D. Mathur, and J. F. Scott, *Nature* **442**, 759 (2006).
- [134] N. Ortega, A. Kumar, J. F. Scott, and R. S. Katiyar, *J. Phys.: Condens. Matter.* **27**, 504002 (2015).
- [135] J. F. Scott, *Nat. Mater.* **6**, 256 (2007).
- [136] J. van Suchtelen, *Phil. Res. Rep.*, **27**, 28 (1972).
- [137] Z. Wang, Y. Wang, W. Ge, J. Li, and D. Viehland, *Appl. Phys. Lett.* **103**, 132909 (2013).
- [138] G. Yu et al., *Appl. Phys. Lett.* **106**, 072402 (2015).
- [139] A. Kumar, B. Narayan, R. Pachat, and R. Ranjan, *Phys. Rev. B* **97**, 064103 (2018).
- [140] W. H. Chu et al., *Nat. Mater.* **7**, 478 (2008).
- [141] J. P. Velez, S. S. Jaswal, and E. Y. Tsybal, *Phil. Trans. R. Soc. A* **369**, 3069 (2011).
- [142] M. I. Bichurin, I. A. Kornev, V. M. Petrov, and I. Lisnevskaya, *Ferroelectrics* **204**, 289 (1997).
- [143] K. K. Patankaret al., *Mater. Chem. Phys.* **65**, 97 (2000).
- [144] J. Ryu, A. V. Carazo, K. Uchino, and H. E. Kim, *J. Electroceram.* **7**, 17 (2001).
- [145] K. K. Patankar, R. P. Nipankar, V. L. Mathe, R. P. Mahajan, and S. A. Patil, *Ceram. Int.* **27**, 853 (2001).
- [146] Y. M. Jia, H. S. Luo, X. Y. Zhao, and F. F. Wang, *Adv. Mater.* **20**, 4776 (2008).
- [147] G. Srinivasan et al., *Phys. Rev. B* **64**, 214408 (2001).
- [148] G. Srinivasan, E. T. Rasmussen, B. J. Levin, and R. Hayes, *Phys. Rev. B* **65**, 134402 (2002).
- [149] G. Srinivasan, R. Hayes, and M. I. Bichurin, *Solid State Commun.* **128**, 261 (2003).
- [150] J. Zhai, S. Dong, Z. Xing, J. Li, and D. Viehland, *Appl. Phys. Lett.* **89**, 083507 (2006).
- [151] H. Zheng et al., *Science* **303**, 661 (2004).
- [152] H. Zheng, *Adv. Mater.* **18**, 2747 (2006).
- [153] S. Sahoo et al., *Phys. Rev. B* **76**, 092108 (2007).
- [154] C. Cavaco, M. van Kampen, L. Lagae, and G. Borghs, *J. Mater. Res.* **22**, 2111 (2007)
- [155] L. Shu et al., *Appl. Phys. Lett.* **100**, 022405 (2012).
- [156] N. Lei et al., *Phys. Rev. B* **84**, 012404 (2011).
- [157] J. H. Park et al., *J. Magn. Magn. Mater.* **321**, 1971 (2009).
- [158] J. Ma, Y. H. Lin, and C. W. Nan, *J. Phys. D: Appl. Phys.* **43**, 012001 (2010).
- [159] Y. J. Chen, T. Fitchorov, C. Vittoria, and V. G. Harris, *Appl. Phys. Lett.* **97**, 052502 (2010).
- [160] Z. Hu et al., *Appl. Phys. Lett.* **106**, 022901 (2015).
- [161] W. Eerenstein, M. Wiora, J. L. Prieto, J. F. Scott, and N. D. Mathur, *Nat. Mater.* **6**, 348 (2007).
- [162] C. Thiele, K. Dorr, O. Bilani, J. Rodel, and L. Schultz, *Phys. Rev. B* **75**, 054408 (2007).
- [163] J. Wang, J. Hu, H. Wang, H. Jiang, and Z. Wu, *J. Appl. Phys.* **107**, 083901 (2010).
- [164] T. Brintlinger et al., *NanoLetters* **10**, 1219 (2010).
- [165] T. H. E. Lahtinen, K. J. A. Franke, and S. Van Dijken, *Sci. Rep.* **2**, 258 (2012).

- [166] D. M. Evans et al., *Nat. Commun.* **4**, 1534 (2013).
[167] S. H. Xie et al., *J. Appl. Phys.* **108**, 054108 (2010).

Chapter 2: Sample Preparation, characterization and research experimental techniques

This Chapter surveys the basic principles of the experimental techniques that were employed in this PhD Thesis. Depending on the scope of each technique, they are categorized as ‘sample preparation’, ‘characterization’ and ‘research’ experimental techniques, presented in the subchapters 2.1-2.3, respectively. To clarify the categorization between ‘characterization’ and ‘research’ experimental techniques we stress the following: the former ones were employed exclusively in standard mode of operation, for investigating the basic properties of the samples (such as crystallographic, electric, etc.), while the latter ones were used beyond their standard operation, ultimately utilizing most of their special capabilities to resolve crucial information for the consistent explanation of the experimental results. Particular emphasis is paid to the description of a prototype ‘research’ technique introduced by our group and further developed in the context of this Thesis. Detailed information is presented in the subchapter 2.3.1.

The following categories of samples were studied: (i) FM thin films of Co (thickness of 30-50 nm) deposited on both sides of bulk PE single crystals of $\text{Pb}(\text{Mg}_{1/3}\text{Nb}_{2/3})\text{O}_3\text{-xPbTiO}_3$ (PMN-0.30PT) in a planar configuration FM/PE/FM, that is Co/PMN-0.30PT/Co and (ii) FM NPs of Fe_3O_4 (diameter 50-100 nm) embedded into a bulk PE matrix of $\text{Pb}(\text{Zr}_{0.52}\text{Ti}_{0.48})\text{O}_3$ (PZT), that is PZT- xFe_3O_4 , where x is the weight percentage concentration of Fe_3O_4 . The respective discussion is presented in the subchapter 2.4.

2.1 Sample preparation experimental techniques

2.1.1. Magnetron sputtering

Magnetron sputtering is an effective and well-established physical vapor deposition (PVD) technique which has been widely used for thin film deposition. Among other PVD techniques, magnetron sputtering offers fair uniformity, and allows high deposition rate [1,2].

In Fig. 2.1(a), the basic principle of magnetron sputtering system is schematically presented. The basic sputtering process takes place in an evacuate chamber, where an inert gas (usually Argon, Ar) is inserted. The target/cathode is maintained in negative potential, while its aluminum shield/anode is grounded; as a result the Ar^+ ions accelerate towards the target, causing bombardment of its atoms. If the kinetic energy of the former is higher than the surface energy of the latter, then neutral atoms will be removed from the target and may condense on the substrate, as a thin film. In addition, secondary electrons are also emitted from the target, as a result of the ion bombardment; these electrons play an important role in maintaining the plasma, since they fill the outer shell of Ar^+ ions and neutralize them. Upon this process, the energy gained by Ar atoms is equally released as emitted photons.

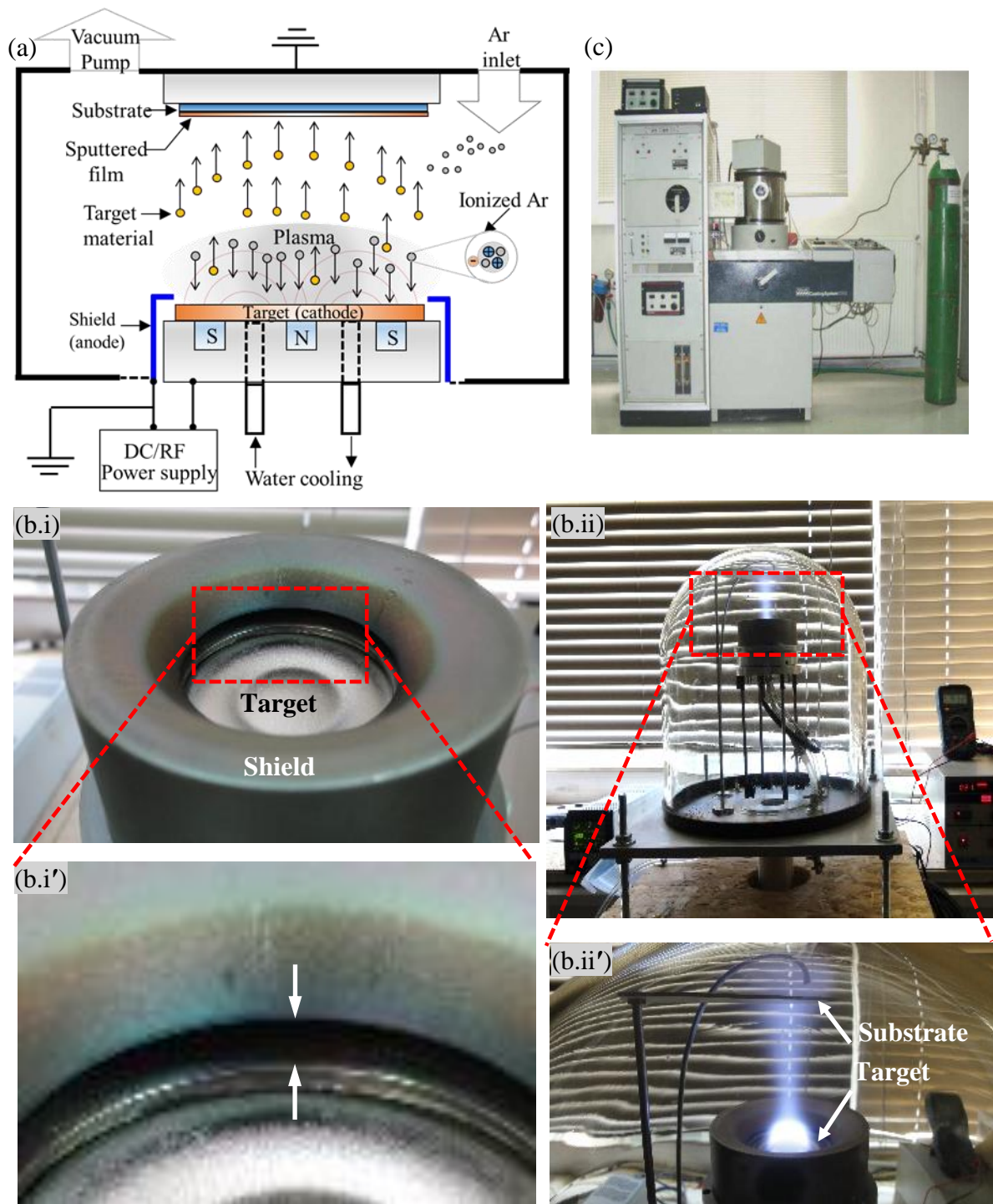


Fig. 2.1: (a) Schematic representation of the basic principle of magnetron sputtering deposition. (b.i)-(b.i'), (b.ii)-(b.ii') Photos of the magnetron sputtering chamber installed in the 'Laboratory of Multifunctional Materials, Structures and Devices' in the Department of Physics, National and Kapodistrian University of Athens. (b.i) The target material and its shield among which an AC/DC voltage is applied. (b.i') Magnification of (b.i) at the area denoted by the dashed rectangle; the narrow, adjustable space among the target and its shield is clearly shown by the arrows. (b.ii) Chamber during the sputtering process; (b.ii') magnification of (b.ii) at the area denoted by the dashed rectangle; the generated plasma, localized mostly near the target, can be clearly observed. Also, the vertical beam of plasma is clearly evident revealing the deposition of atoms originating from the target onto the substrate. (c) Photo of sputtering unit (Edward 306A, coating unit) employed for the preparation of Co thin films, installed at the Institute of Nanoscience and Nanotechnology of National Center for Scientific Research 'Demokritos'.

Though basic sputtering has been a successful technique, there are three main disadvantages: the low deposition rates, low ionization efficiencies in the plasma, and high substrate heating effects. These limitations can be overcome by magnetron sputtering. In particular, magnetrons make use of the fact that a magnetic field configured parallel to the target and normal to the electric field can constrain the secondary electrons to a helical trajectory in the vicinity of the target. In this way, the probability of an ion-atom collision increases. In addition, the overall ionization efficiency of the magnetron increases resulting to a highly dense plasma in the target region. In turn, this leads to higher bombardment of the target and thus higher deposition rates. To avoid the overheating of the permanent magnets and the potential loss of their permanent magnetization, there is a water cooling system, also shown in Fig. 2.1(a). Depending on the target material, the appropriate power supply is selected, that is DC for metallic targets, or RF for insulating targets.

Figs. 2.1(b.i)-(b.i') and 2.1(b.ii)-(b.ii') show photos of the magnetron sputtering that is installed in the 'Laboratory of Multifunctional Materials, Structures and Devices' in the Physics Department of the National and Kapodistrian University of Athens. It should be noted that these photos are shown for the sake of presentation, since the specific magnetron chamber is transparent and consequently the complete setup and procedure can be easily observed. Specifically, Fig. 2.1(b.i) shows the target material and its shield (both composing the magnetron gun) in perspective view. As mentioned above, an AC/DC voltage is applied between these two components in order to ionize the Ar gas. Fig. 2.1(b.i') shows a magnification of (b.i) in the area denoted by the dashed rectangle, in order to highlight the narrow space between the target and its shield, with the two arrows; this space is on the order of millimeters and it is adjustable so that a relatively high electric field can be generated by means of a low AC/DC voltage supply. In addition, Fig. 2.1(b.ii) shows in side view the complete chamber during the sputtering process and the respective plasma generation. Fig. 2.1(b.ii') is focused on the target area, (dashed rectangle in (b.ii)), where the plasma is predominantly localized. Also, the vertical beam of plasma is clearly evident revealing the deposition of atoms originating from the target onto the substrate.

The sputtering unit that was used for the preparation of Co/PMN-0.30PT/Co samples (Co thickness: 30-50 nm) during this PhD Thesis is an Edward 306A coating unit (Edwards, Sanborn, NY, USA), as shown in Fig. 2.1(c), equipped with a water-cooled turbo molecular pump (Oerlikon Leybold Vacuum GmbH, Germany) supported by a mechanical pump (Edwards High Vacuum Pump, BOC L.t.d., England). Two pressure gauges, i.e. a high and a low vacuum pressure gauge (Edwards Active Gauges, USA), are attached to the deposition chamber, in order to monitor the vacuum pressure inside the chamber. The former operates at the pressure regime between the atmospheric pressure (7.5×10^{-2} Torr) down to 10^{-5} Torr, while the latter operates in the pressure range below 10^{-5} Torr. Inside the sputtering chamber two magnetron guns are available, one biased with a DC power supply and the other biased with a RF power supply. Each magnetron gun contains 13 magnets of 5 kOe. The 12 magnets are placed anti-diametrically around the periphery of the target with the south pole facing up, while the last magnet is placed at the center of the target with the opposite pole (north pole) facing up. This configuration of the magnets restricts the magnetic field lines within the coverage area of the target. In the particular sputtering unit, the substrates are placed at a distance of 16 cm above the target.

2.1.2. Solid-state sintering

Solid state sintering is a widely applied technique for preparing bulk polycrystalline composites. The application of heat to a powder material below its melting point, causes bonding and densification of its particles. The driving force for sintering is the reduction of the surface energy of the system. A simple model of two spheres, each one corresponding to a particle of the powder material, can describe the sintering process on a microscopic scale [3]. Accordingly, when the two particles come into contact at high temperature (below the melting point) the driving force for matter transport is the difference in concentration between the source of matter (particle surface, volume or grain boundaries) and the sink for matter ('neck' region), as shown in Fig. 2.2(a) [4]. For the case of sintering of metal oxides, the matter transport consists in ion transport. The difference in ion concentrations originates from the difference in chemical potentials, that is the free energy per mol of ions. Accordingly, the difference in chemical potentials causes ion transport from the higher to the lower potential through diffusion, according to Fick's law:

$$J = -Bc \frac{d\mu}{dx} \quad (2.1)$$

where, J is the flux of the diffusing ions, B is the ions' mobility, c is the concentration per unit volume of ions, μ is the chemical potential and x is the direction of diffusion.

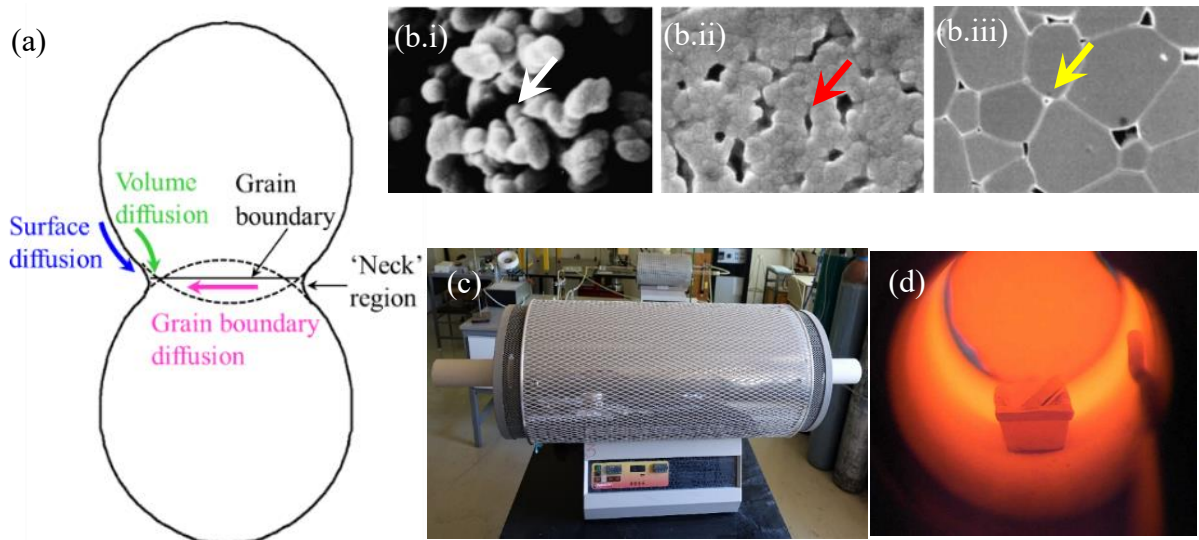


Fig. 2.2: (a) Modes of matter transport from the particle surface or grain boundary to the 'neck' region between two grains. (b.i)-(b.iii) Scanning Electron Microscopy images of the (b.i) initial, (b.ii) intermediate and (b.iii) final stages of sintering; the white, red and yellow arrows indicatively show (b.i) the small 'necks' connecting the particles, (b.ii) the continuous pore channels and (b.iii) the isolated pores [4]. (c) Photo of the tube furnace employed for the sintering process (Carbolite Co. Ltd, UK). (d) Representative photo of the inner of the furnace during the sintering process. The furnace is installed at the Institute of Nanoscience and Nanotechnology of National Center for Scientific Research 'Demokritos'.

The flux of the diffusing ions during solid state sintering occurs along different paths, as shown in Fig. 2.2(a); ions can be transported to the ‘neck’ region by surface, volume and grain boundary diffusion. Regarding the surface diffusion, ion transfer takes place from the convex surface region of the spheres, which are in higher μ , to the concave ‘neck’ regions, which are at lower μ . In addition, during volume and grain boundary diffusion, ion transport occurs from the particle volume and grain boundaries to the ‘neck’ region, respectively, through vacancies and interstitials that are present in the lattice [5,6]. A sintering run involves all these three mechanisms and takes place at three stages [5]. Figs. 2.2(b.i)-(b.iii) present representative Scanning Electron Microscopy (SEM) images of a metal oxide at the initial, intermediate and final sintering stage, respectively [4]; the white, red and yellow arrows show indicative characteristic features of each stage. Specifically, at the initial stage of sintering, ‘neck’ growth and densification take place, with the formation of small ‘necks’ connecting the particles, as shown by the white arrow in Fig. 2.2(b.i). Subsequently, as the ‘neck’ growth proceeds, a transition in the pore structure occurs to a system of tubular pores along the particle junctions, as shown by a red arrow in Fig. 2.2(b.ii). Once these tubular pores have shrunk to the point that they are unstable, they break up into isolated pores located at the grain junctions, as shown by the yellow arrow in Fig. 2.2(b.iii). This is the final stage of sintering and it is during this stage that the sintered material obtains its final microstructure (grain size, density), and also forms its desired properties [7].

Fig. 2.2(c) shows the tube furnace (Carbolite Co. Ltd, UK) that was used for the sintering of PZT- $x\text{Fe}_3\text{O}_4$ samples in this PhD thesis. The furnace is equipped with an alumina tube, in the center of which we placed the samples on an alumina crucible. In order to ensure homogeneous temperature in the furnace and safe laboratory conditions (due to Pb evaporation), the alumina tube’s ends were closed by aluminum caps that were connected with silicone tubes to lead any gases from the furnace to the open air. Fig. 2.2(d) shows a representative photo during the sintering process.

2.2 Characterization experimental techniques

2.2.1 X-Ray Diffraction

X-Ray Diffraction (XRD) is a useful technique for determining the crystallographic structure of a crystal. It corresponds to the elastic scattering of X-ray photons of an incident beam by atoms in a periodic lattice. In the ideal case, the arrangement of atoms in a crystal is periodic, lying at parallel planes with interplanar spacing d_{hkl} (where hkl the Miller indices used to uniquely identify the plane). As shown in Fig. 2.3(a) the constructive interference of the scattered monochromatic X-rays is determined by Bragg’s law:

$$N\lambda_{X\text{-rays}} = 2d_{hkl}\sin\theta \quad (2.2)$$

where N is an integer representing the order of reflection, $\lambda_{X\text{-rays}}$ is the wavelength of X-rays, d_{hkl} the interplanar spacing, and θ is the angle between the incident beam and the diffracted beam from lattice planes (hkl). By measuring the θ -angles under which the constructively

interfering beams leave the crystal, d_{hkl} can be determined for every single crystallographic phase. By varying the incident angle within a θ -range, diffraction peaks of various intensities are recorded, that is the diffraction pattern of the sample [8,9]. For unknown substances, the obtained diffraction data can be compared with standard line patterns available in the Powder Diffraction File (PDF) database, which is annually updated by the International Center for Diffraction Data.

The X-ray diffractometer (D500, Siemens) that was used during this PhD research (Fig. 2.3(b)) is equipped with a $\text{CuK}\alpha$ radiation source (wavelength $\lambda=1.54 \text{ \AA}$) and settled in a Bragg-Brentano geometry to employ θ - 2θ scans. The voltage and current conditions of the radiation source were 40 kV and 35 mA, respectively.

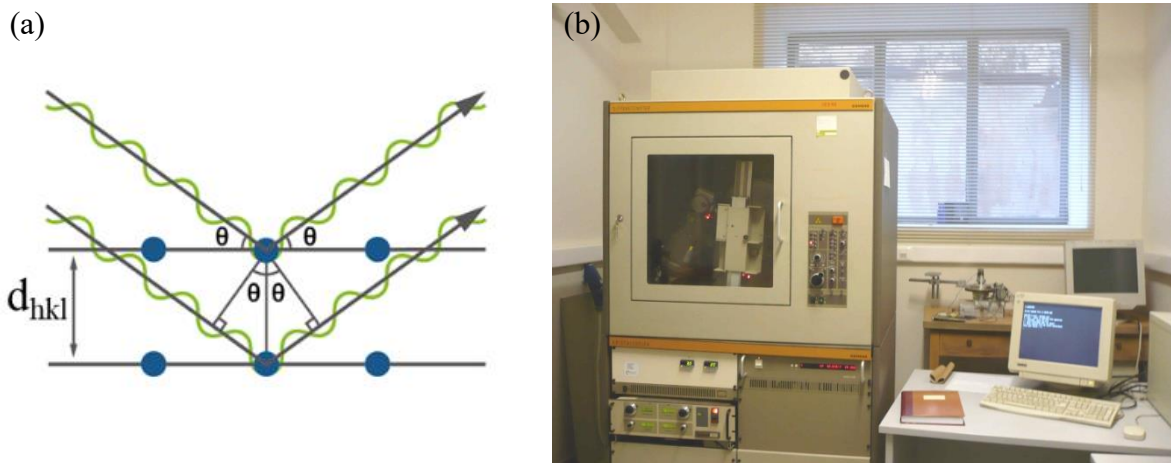


Fig. 2.3: (a) Schematic illustration of constructive interference of scattered monochromatic X-rays according to Bragg's law. (b) Photo of the X-ray diffractometer (D500, Siemens) installed at the Institute of Nanoscience and Nanotechnology of National Center for Scientific Research 'Demokritos'.

2.2.2 Current-voltage characteristics

The current-voltage (I-V) characteristics is a set of graphic curves referring to the voltage occurring across a sample of known dimensions upon varying the applied electric current. In this PhD thesis, I-V characteristics were taken in order to investigate the presence of leakage current, I_l , in the PZT- $x\text{Fe}_3\text{O}_4$ samples; since Fe_3O_4 is known to have a moderate conductivity at room temperature ($\sim 10^{-2}$ - $10^{-3} \Omega$), we want to investigate the maximum possible value of electric voltage that can be applied to the samples without losing their insulating properties. To this end, we used a DC-voltage supply (model IP-32, Healthkit Co., USA) to apply the voltage across each sample, while I_l was monitored with a digital multimeter (MY-67, V&A).

2.2.3 Local measurement of magnetic field by means of a Gaussmeter

A Gaussmeter is mostly employed for local magnetic field measurements (i.e. at a certain surface) using the Hall effect. The measurement relies on a probe sensor detecting the magnetic fields perpendicular to the sensor surface. The Gaussmeter sends a test current through the probe and a Hall voltage is generated that is proportional to the strength of the magnetic field.

In this Thesis, a commercially available handheld Gaussmeter (Model 410, Lake Shore Cryotronics Inc, Ohio, USA) was used for magnetic field measurements within the range 0.1 G-20 kG, with a resolution of 100 mG. With the Gaussmeter we mapped the magnetic field of a NdFeB permanent magnet hosted in a sample-carrying home-made aluminum platform (see Figs. 2.8(a)-(c)). Specifically, we recorded the magnetic field, H_{ex} , over the entire volume of the investigated sample and evaluated its homogeneity. To this end, the Gaussmeter with its probe was placed on a linear xyz stage with micrometer resolution, in order to record the H_{ex} along xy plane and along z axis (see Figs. 2.8(d) and 2.8(e), respectively).

2.2.4 Global polarization and strain measurements

Polarization and strain measurements are highly important for FE and PE characterization. Among a variety of techniques, the Sawyer-Tower (S-T) bridge and the Michelson laser interferometer are widely used for $P(E_{ex})$ and $S(E_{ex})$ measurements, respectively; these techniques are termed as ‘global’, since they record the response of the complete sample volume, providing average values.

Specifically, the S-T bridge [10], shown in Fig. 2.4(a), is a practical circuit for the characterization of FE materials, provided that they have low loss and high polarization [11]. As shown in Fig. 2.4(a), an AC-voltage is imposed on the surface of an electroded FE sample, placed on the horizontal plates of an oscilloscope; thus, the quantity plotted on the horizontal axis is proportional to the field across the crystal. A linear capacitor C_0 is connected in series with the FE sample and the voltage across C_0 is proportional to the polarization of the sample. In fact, the dielectric displacement (D) and the polarization (P) are connected by the relation:

$$D = \epsilon_0 E + P \quad (2.3)$$

where, D expresses the charge density collected by C_0 . Compared to the larger value of P , the contribution by $\epsilon_0 E$ can be omitted. Therefore, the obtained D is considered as P in practice. In modern equipment, P is collected through charge or current integration technique following with compensation by a variable resistor R (see schematic circuit in Fig. 2.4(a)) [12].

The Michelson laser interferometer is a well-established method for measuring distances with great accuracy, on the order of 1 pm. As schematically presented in Fig. 2.4(b), a laser beam splits at a beamsplitter (BS), where one part is reflected at the reference mirror and the other part at the measured PE sample. In order to reflect the incident light, the sample is usually coated with a reflective medium. The two beams recombine with each other at the BS and reach the detector, where they interfere either constructively or destructively; during constructive interference the two beams are in-phase and result in a bright fringe, while during destructive interference the beams are out-of-phase resulting in a dark fringe. The optical signal processing in the detector allows the interference of these two beams to be observed with the respective light intensity given by the relation:

$$I = I_m + I_r + 2I_m I_r [\cos(\frac{4\pi}{\lambda}(r_m - r_r))] \quad (2.4)$$

where I_m , I_r are the light intensities for the measured and reference beams, respectively, and $r_m - r_r$ is the optical path-length difference between the two beams. Under external voltage application the PE sample deforms, as shown in Fig. 2.4(b) with a dotted rectangle. Accordingly, the displacement, Δx , of the measurement arm causes change in the relative phase of the two beams. The detected intensity can be rewritten as [13]:

$$I(\Delta x) = \frac{1}{2}(I_{max} + I_{min}) + \frac{1}{2}(I_{max} - I_{min}) I_r \cos\left(\frac{4\pi\Delta x}{\lambda}\right) \quad (2.5)$$

where I_{max} and I_{min} are the maximum and minimum interference light intensities, which can be measured from the interference intensity curves. Hence, the displacement Δx can be deduced from the change in the detected light intensity, given by Eq. (2.5).

For this PhD Thesis, the polarization and strain data were obtained at room temperature using a TF Analyzer 2000 (AixACCT) ferroelectric analyzer connected with a high-voltage source (Trek Model 610E) and a laser interferometer (SP-S 120, SIOS); the complete experimental setup is shown in Fig. 2.4(c). The samples (Au-coated) were immersed in silicone oil during the measurements to prevent arcing. The waveform and frequency of the out-of-plane (along the samples' thickness) applied electric field, $E_{ex,z}$, are triangle and 10 Hz, respectively. We note that with the specific laser interferometer the out-of-plane strain, $S_{zz}(E_{ex,z})$ was measured.

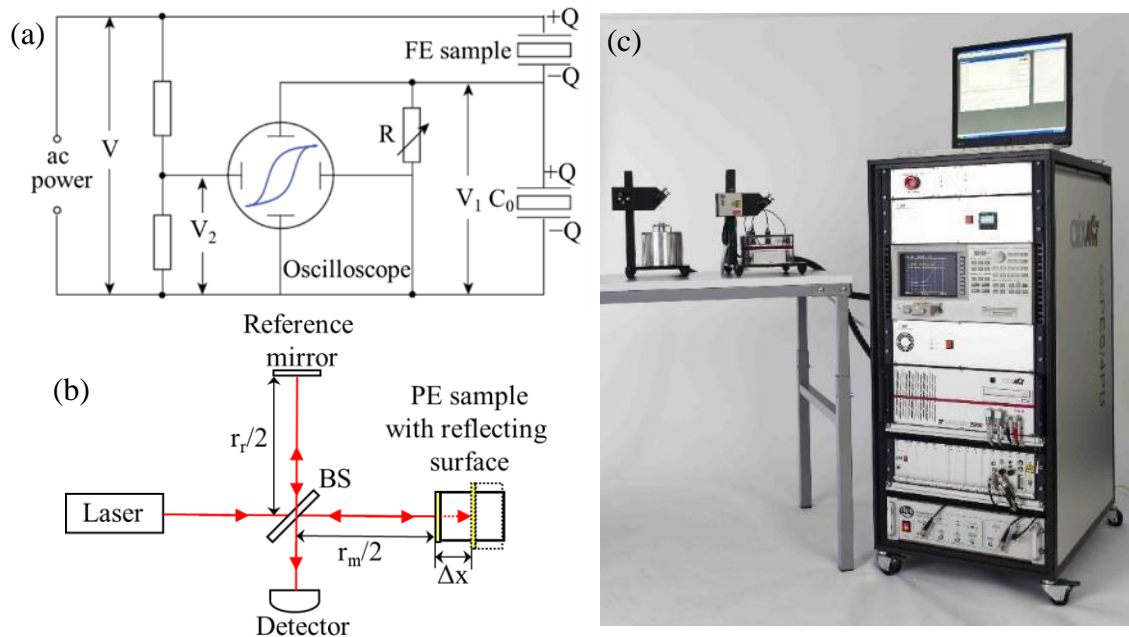


Fig. 2.4: (a) Schematic circuit of Sawyer-Tower bridge for measuring polarization under $E_{ex,z}$, $P(E_{ex,z})$. (b) Schematic illustration of a Michelson laser interferometer for measuring out-of-plane strain under $E_{ex,z}$, $S_{zz}(E_{ex,z})$. (c) Experimental setup for $P(E_{ex,z})$ and $S_{zz}(E_{ex,z})$ measurements (aixACCT Systems and SP-S 120, SIOS, GmbH, Germany) installed in the Australian Institute for Innovative Materials, University of Wollongong, Australia.

2.3 Research experimental techniques

2.3.1 Optical microscopy

Optical microscopy is a standard experimental technique that makes use of the visible light for the inspection of features on the surface of a sample when magnification is needed. Due to its simplicity and versatility, a conventional optical microscope (OM) was modified for the development of a prototype experimental technique for estimating directly the in-plane (i.e. over the sample surface) strain, for the majority of the PE materials employed today. By means of this technique, we have the opportunity to record the in-plane strain -and estimate the respective in-plane PE coefficients- *locally* over the sample surface, since we have integrated an in-plane slider with micrometer resolution on the translation stage of OM for thorough in-plane investigation of the sample. This is the reason that we include the OM in the subchapter ‘2.3 Research experimental techniques’. We note that a similar modification has been employed to a conventional atomic force microscope AFM [14]; however, it will not be discussed here, since the data presented in this Thesis refer exclusively to the OM-based technique. Below, we firstly survey the basic operation of an OM, and secondly we describe in detail the introduced modification mentioned above.

Basic operation of an OM: An OM makes use of the visible light of the electromagnetic spectrum (wavelength λ : 400-700 nm). Fig. 2.5(a) shows the OM that we employed, indicating its basic parts.

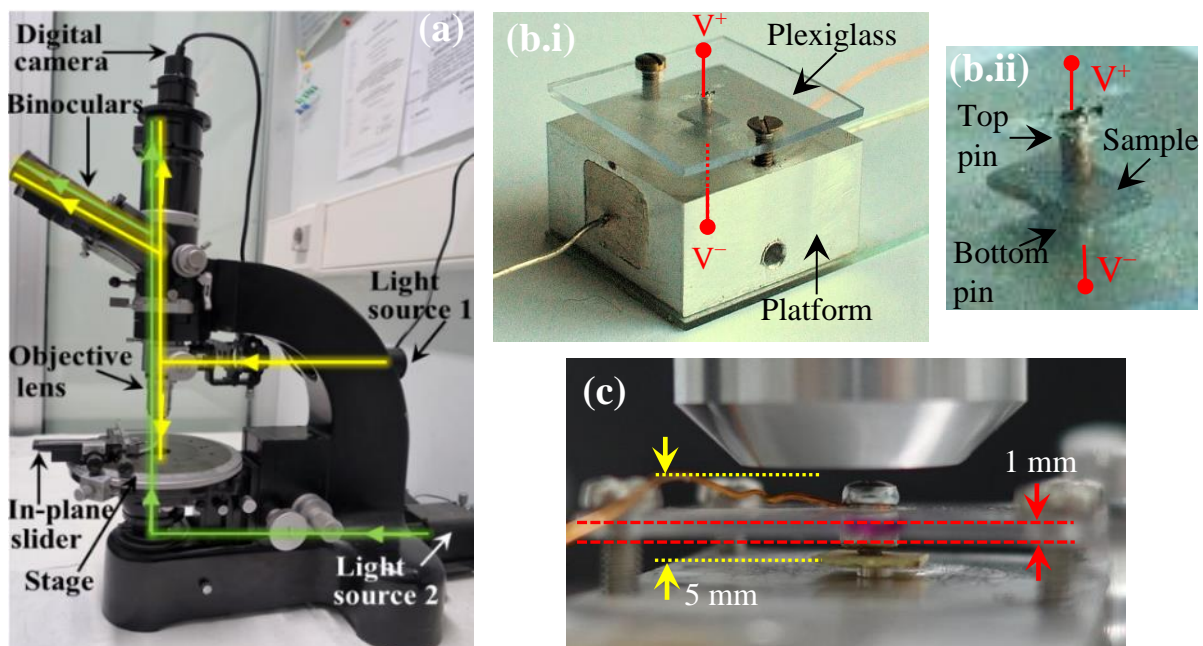


Fig. 2.5: (a) Photo of the Optical Microscope (OM) (Ortholux, Leitz, Wetzlar, Germany). The yellow and green arrows correspond to the optical paths of light in the reflective and transmittance operation modes, respectively. (b.i) Photo of the home-made sample-carrying platform. The plexiglass layer serves for supporting the top pin and for allowing OM observation. (b.ii) Detail of the sample area; The top and bottom pins serve for supporting coaxially the plate-shaped PZT sample at its center and for applying the external electric field, $E_{ex,z}$. (c) Photo of the sample-carrying platform adjusted to the OM (Lens: $\times 10$). The plexiglass layer is denoted by the red-colored dashed lines and arrows (thickness 1 mm); the distance between the upper sample surface and the front of the objective lens (airgap) is denoted by the yellow dotted lines and arrows (5 mm). This OM unit is installed at the Institute of Nanoscience and Nanotechnology of National Center for Scientific Research ‘Demokritos’.

The arrangement basically consists of the combination of two lenses, the objective and a pair of binoculars. The observation of the sample is realized either by reflected or by transmitted light; the corresponding optical paths are shown in Fig. 2.5(a) by yellow and green arrows, respectively. The most important parameters that characterize an OM is the magnification and the resolution. The total magnification of an OM results from the product of the objective and the binocular lenses' magnification. In the general case that digital cameras are integrated into an OM, replacing the binocular lenses, for the recording and storage of the observed images (as shown in Fig. 2.5(a)), the total magnification of the OM system is determined by the product of the objective lens and the camera's magnification.

The resolution of an OM, i.e. the minimum distance, d_{min} , of two points which can be still observed separately with OM, depends on the wavelength, λ , and on the numerical aperture (NA) of the objective lens, according to Rayleigh criterion [15]:

$$d_{min} = 0.61 \frac{\lambda}{NA} \quad (2.6.i)$$

From Eq. (2.6.i) it is obvious that the resolution improves (i.e. attains lower values) upon decreasing λ and increasing NA values. For a fixed light source (fixed λ), it is the NA that exclusively determines the resolution of OM; in turn, NA is described by the expression:

$$NA = n \cdot \sin\theta_{ap} \quad (2.6.ii)$$

where n is the refractive index of the medium between the sample surface and the objective lens, and θ_{ap} is the half of the aperture angle of the objective lens. When the light rays are propagated through air ($n_1=1$), NA has a standard value for each objective, indicated on its outer metallic jacket. Alternatively, when the light rays are propagated through a medium of higher refractive index ($n_2>1$), then, according to Eq. (2.6.ii), NA obtains a higher value, a fact that leads to an improved OM resolution (Eq. (2.6.i)). The improvement of resolution is attributed to two reasons; the first is schematically explained in Figs. 2.6(a.i) and 2.6(a.ii) for the cases of $n_1=1$ (i.e. air) and $n_2>1$ (e.g. cedar oil, $n_2=1.515$), respectively.

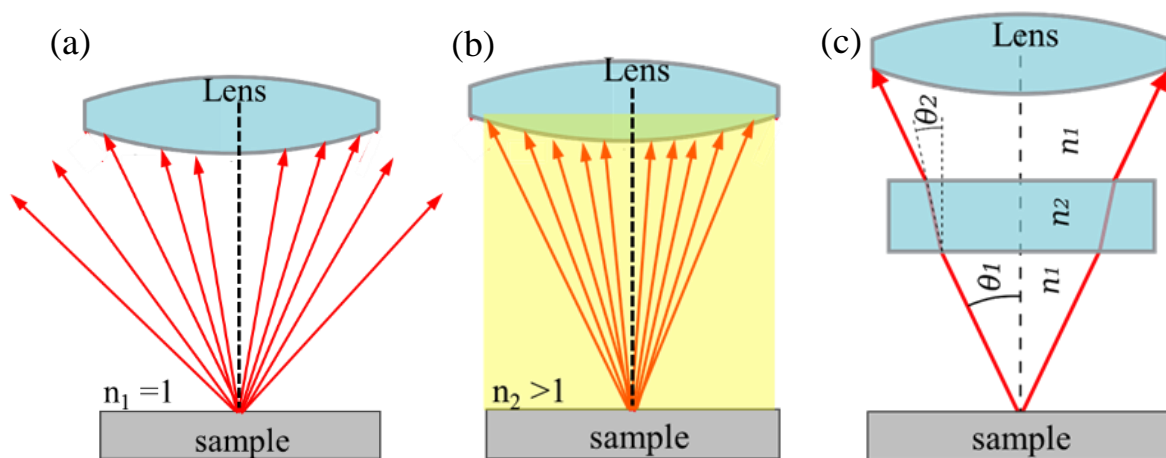


Fig. 2.6: (a), (b) Light rays reflected from the sample in (a) air ($n_1=1$) and (b) a medium with higher refractive index ($n_2>1$). In the case of the latter, the light rays converge more and they ultimately enter the objective lens. (c) Light rays reflected from the sample and propagate into mediums with different refractive index; this is the configuration regarding our experimental setup, where n_1 is the refractive index of air ($n_1=1$) and n_2 is the refractive index of plexiglass ($n_2=1.5$).

From Fig. 2.6(a.i) -corresponding to $n_1=1$ - we see that a significant amount of light rays that are reflected by the sample surface, do not converge toward the lens axis (dashed black vertical line) so that are not harvested by the objective lens. As a consequence these ‘lost’ rays are finally not integrated in the recorded image. On the other hand, from Fig. 2.6(a.ii) -corresponding to $n_2>1$ - we observe that the light rays converge towards the lens axis of the lens (dashed black vertical line); this fact results in greater light intensity entering into the lens and, thus, improved image contrast. Most important, the second reason is associated with an effective reduction of wavelength from its initial value λ (propagation in air), by a factor $1/n_2$, to a final value λ/n_2 (propagation in a medium of refractive index n_2). Having clarified the effect of a medium -other than air- on the resolution of OM, below, we will give some details about the NA (and the resultant resolution) that is at play in our case.

Specifically, for the observation of our samples with OM, we do not use the typical setup, i.e. sample/lens in air (Fig. 2.6(a)) or oil-immersed (Fig. 2.6(b)), but we rather use a modified setup, with a home-made sample carrying platform in which a plexiglass plate is utilized as shown in Fig. 2.5(b.i)-(c). Upon using this platform, the air gap between the sample surface and the lens, denoted by the yellow dotted lines and the respective arrows, is interrupted by the layer of plexiglass, denoted by the red dashed lines and the respective arrows. As a consequence, the light rays get refracted while propagating through plexiglass; this is shown schematically in Fig. 2.6(c). We estimated that the plexiglass occupies a percentage of 20% of the air gap (plexiglass thickness: 1mm, air gap: 5 mm). Hence, in our case, we can fairly assume an effective refractive index, n_{eff} , which can be roughly calculated by the relation $n_{\text{eff}}=80\%n_1+20\%n_2=1.1$, where $n_1=1$ (the refractive index of air) and $n_2=1.5$ (the refractive index of plexiglass). Accordingly, from Eq. (2.6.ii), we also have an effective numerical aperture, $NA_{\text{eff}}=0.275$. In turn, from Eq. (2.6.i), by assuming $\lambda=500$ nm, we estimated that the effective resolution of OM is $d_{\text{eff}}=1.1$ μm (taking into consideration the plexiglass layer) instead of $d=1.22$ μm (without considering the plexiglass layer). Hence, we deduce that with the use of plexiglass, the resolution improves by 10%.

At this point, it should be noted that the resolution of OM plays an important role in the image analysis of our data, that will be discussed in the subchapter 2.3.1.C, below. In general, we know that lenses with magnification as low as x10 are not designed for displaying significant resolution, as higher magnification ones do (e.g. x100). Nonetheless, the reason that we employed objective lens x10 to our study, and not an one of higher magnification (and resolution) is its convenient working distance. In general, the higher the objective lens’ magnification the shorter the working distance. Unfortunately, in our case we are forced to employ a lens of high working distance (that is of low magnification) because between the sample surface and the lens exist the plexiglass and the upper pin-electrode for application of the voltage.

Some additional specifications regarding our experimental setup are the followings: the OM that we used is an Ortholux (Leitz, Wetzlar, Germany) OM in the reflective mode by using a light emitting diode (LED) as the light source 1 (not shown in Fig. 2.5). The OM images were recorded with a digital microscope camera (Celestron, USA). The magnification in all the as-obtained (raw) OM images was x130 (objective lens: x10, camera: x13).

Local OM-based piezoelectric technique for recording the in-plane strain-electric field curve: Today, several competent methods are employed for measuring the strain that is induced to PE materials, such as laser interferometry, laser scanning vibrometers and PE force microscopy. These methods are well-established and provide reliable results of high accuracy. However, the instrumentation is generally quite expensive. To this end, a different approach based on OM was first introduced by our group for the measurement of PE strain under application of an external electric field, E_{ex} [14]. This method was further developed in the context of this Thesis so that simultaneous application of an external magnetic field, H_{ex} , is now also feasible (see below). This subchapter is divided in four sections: (A) Measurement protocol, image processing and data analysis, (B) Basic technical issues on the reliability of the technique and (C) Home-made platform for recording the PE deformations by OM under application of both electric (E_{ex}) and magnetic (H_{ex}) fields.

A. Measurement protocol, image processing and data analysis

The method is based on OM for the observation and recording of the in-plane deformations of a PE sample (along the sample surface, namely xy plane), caused by the application of an out-of-plane (along the sample thickness, namely z axis) external electric field, $E_{ex,z}$. Unlike other global techniques, such as laser interferometry, this technique is *local*, meaning that we can record the in-plane deformations selectively, at specific areas of the sample surface. To clarify this point, Fig. 2.7(a.i) presents schematically the surface of an investigated PE sample. The blue and red dashed lines denote the Cartesian symmetry axes x and y . We stress that, since for polycrystalline samples (without crystallographic texture and preferred orientation) the nature of deformation is isotropic and symmetric, the employed ‘ x ’ and ‘ y ’ axes are used to simply denote a coordinate system that serves as a guide-to-the-eye to illustrate the specific area of the sample in which the measurements were recorded. This is why in the following text we employ the terms ‘in-plane strain’ and ‘in-plane PE coefficients’, without distinguishing any specific axis. It is easy to understand that as we approach the symmetry center, O , of the sample the average deformation due to $E_{ex,z}$ application gets zero. Accordingly, in order to capture the deformation in its full range in our measurements we should choose the optical frame (OF) near the edge sides of the sample (Fig. 2.7(a.i); black dotted rectangles). Especially, if the OF is selected along a specific symmetry axis (SA) of the sample (namely ‘ x ’ or ‘ y ’), as shown in Fig. 2.7(a.i) with the blue and red dashed lines, the overall deformation should lie exclusively towards the direction of the SA [14]. This is clarified in Fig. (a.ii), where a representative OF along the x^+ axis is shown; the two normal components that correspond to expansion along y dimension are equal in magnitude and antiparallel, hence cancelling each other out (red dotted arrows), while the components that correspond to expansion along x dimension are equal in magnitude and parallel, so they add (blue dotted arrows).

Figs. 2.7(b.i) and 2.7(b.ii) schematically present a PE sample on the sample carrying platform in side view, under $E_{ex,z}=0$ and $E_{ex,z}\neq 0$, respectively. The top and bottom pins serve for both holding the sample coaxially at its center (O), so that it is left free to deform in all directions; furthermore they also serve for the application of $E_{ex,z}$ to the sample (see also Fig. 2.5(b.i), 2.5(b.ii) and 2.5(c), above). Now, let us say that the OFs are chosen along one of the in-plane SAs, namely ‘ x ’. Regarding $E_{ex,z}=0$, the sample is undeformed, with side length x , while concerning $E_{ex,z}\neq 0$, the sample is equally deformed by Δx on both respective sides.

Accordingly, the main concept of the technique is the direct comparison of the respective OM images, obtained prior to and after application of $E_{ex,z}$, enabling us to resolve in-plane deformations on the order of micrometers to hundreds of nanometers.

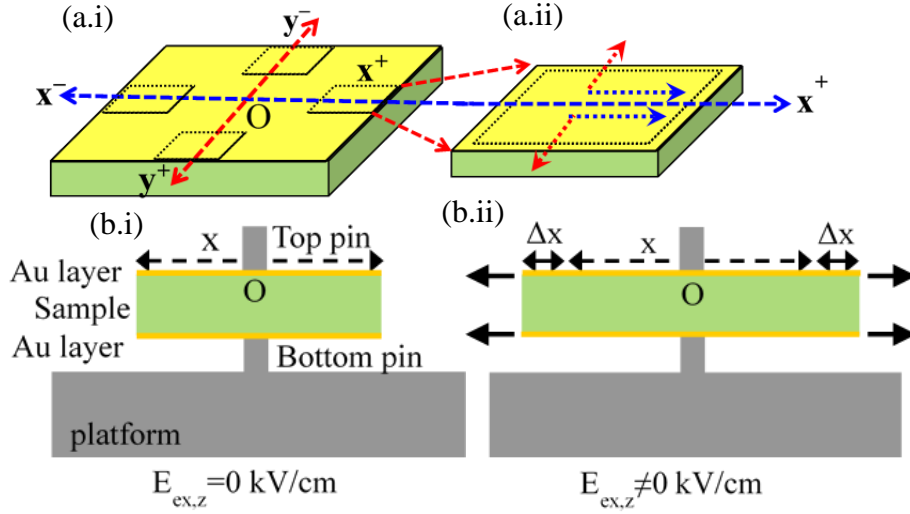


Fig. 2.7: (a.i), (a.ii) Schematic illustrations of a PE sample, in perspective view. (a.i) The blue and red dashed lines denote the in-plane symmetry axes (SAs) 'x' and 'y', respectively. The black dotted rectangles indicate the four different areas for observation with the optical microscope -optical frames (OFs)- lying along the SAs 'x' and 'y', near the edges of the sample. (a.ii) Detail of the sample edge; magnification of a representative OF shown in panel (a.i), along the SA 'x+'. The blue and red dotted arrows denote the direction of deformations along x and y dimensions, respectively. (b.i), (b.ii) Schematic illustration of a PE sample mounted on the sample-carrying platform, in side view; the sample is held coaxially by the top and bottom pins, at its center (O). (b.i) For $E_{ex,z}=0$ kV/cm, the sample is undeformed. (b.ii) For $E_{ex,z} \neq 0$ kV/cm, the sample is deformed equally well by the same amount Δx on both sides.

Both the experimental procedure and the subsequent processing of the data are discussed right below, step-by-step, while schematically presented in Fig. 2.8.

1st step: Prior to the application of the out-of-plane external electric field, $E_{ex,z}$, capture a raw photo of the area of interest along a symmetry axis with the desired magnification of the OM (Figs. 2.8(a') and 2.8(b)).

2nd step: Crop the subarea of interest from the raw photo (Fig. 2.8(c)). Measure one of its dimensions, that is L_1 (Fig. 2.8(d)).

3rd step: Enlarge the cropped photo of the subarea of interest at a desired new level, while keeping the same aspect ratio. Measure the same dimension as was done in the previous step, that is L_2 (Fig. 2.8(e)). The digital magnification level equals L_2/L_1 .

4th step: Define a characteristic point (CP) of the subarea of interest that should be easily identified during variation of $E_{ex,z}$.

5th step: For the i^{th} value of the out-of-plane externally applied electric field, $E_{ex,z,i}$, measure the respective shift, ΔL_i , experienced by the CP via a calibration lengthscale.

6th step: Calculate $2\Delta L_i/L$, where L is the respective length of the sample. This is the in-plane strain, $S_{z,i}$, for the specific i^{th} value of the out-of-plane electric field, $E_{ex,z,i}$.

7th step: Change $E_{ex,z,i}$ based on the desired sequence of values and apply the 5th and 6th steps.

8th step: Assemble all $(S_{z,i}-E_{ex,z,i})$ points. This is the desired ‘in-plane Strain’–‘out-of-plane Electric Field’ curve, $S_{z,i}(E_{ex,z})$.

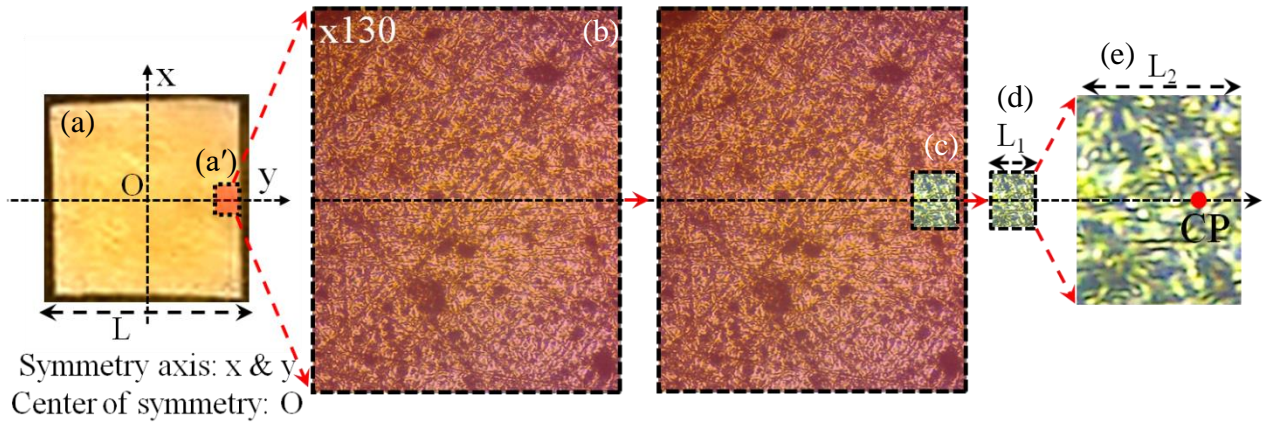


Fig. 2.8: (a) Top view of the investigated sample; (a') the captured area of interest along a SA is shown with the red-shaded rectangle. (b) The respective raw OM photo of the area of interest. (c)-(d) Subarea of interest, cropped from the raw photo, of dimension L_1 . (e) Enlarged cropped photo of the subarea of interest, at a desired digital magnification level, L_2/L_1 . A characteristic point is identified at the cropped and enlarged photo, denoted by the red dot.

The experimental procedure described above is now explained with more details for the representative realistic case of a PZT sample in Figs. 2.9(a.i)-2.9(a.iii) and 2.9(b.i)-2.9(b.iii). The inset (a.i') of Fig. 2.9(a.i) shows a photo of the investigated sample along with the illustrated SAs. The red circle locates the subarea of interest on which the investigation will be focused. The same area is also presented in Figs. 2.9(a.i)-2.9(a.ii) and 2.9(b.i)-2.9(b.ii). In general, we start the measurements from $E_{ex}=0$ kV/cm and subsequently we vary its value following a desired pre-calculated sequence that ranges within the maximum values that can be applied in our experimental set-up $-10 \text{ kV/cm} \leq E_{ex,z} \leq +10 \text{ kV/cm}$. Specifically, Figs. 2.9(a.i)-2.9(a.iii) and 2.9(b.i)-2.9(b.iii) present the corresponding OM images for two representative values, $E_{ex,z}=0$ kV/cm and $E_{ex,z}=+6$ kV/cm, respectively. For both sets of Figs. 2.9(a.i)-2.9(a.iii) and 2.9(b.i)-2.9(b.iii), the horizontal panels (i) correspond to the as-obtained (raw) images, while (ii) and (iii) correspond to subsequently processed images (i.e. cropped and enlarged). We recall that the sample's deformation can be determined by estimating the displacement of a CP on the sample surface. The CP should be easily identified so that is chosen on the basis of the surface texture and reflectivity. Specifically, since the subarea of interest is chosen along x^+ axis, the respective CP's displacement should lie along x^+ axis, as well. The dashed and dotted arrows in all Figs. represent the position of the CP in relation to the reference origin O; the dashed arrow corresponds to the initial position of the CP, x_i , ($E_{ex,z}=0$ kV/cm), while the dotted arrow to the final one, x_f , ($E_{ex,z}=+6$ kV/cm). Regarding the processed images, Figs. 2.9(a.ii), 2.9(b.ii) and 2.9(a.iii), 2.9(b.iii), they show the area of interest magnified, in two different magnification scales (x195 and x710, respectively), in order to highlight the CP's displacement. The latter ones show the subarea of interest in full image. Hence, the CP's displacement, $\Delta x = x_f - x_i$, is clearly distinguishable.

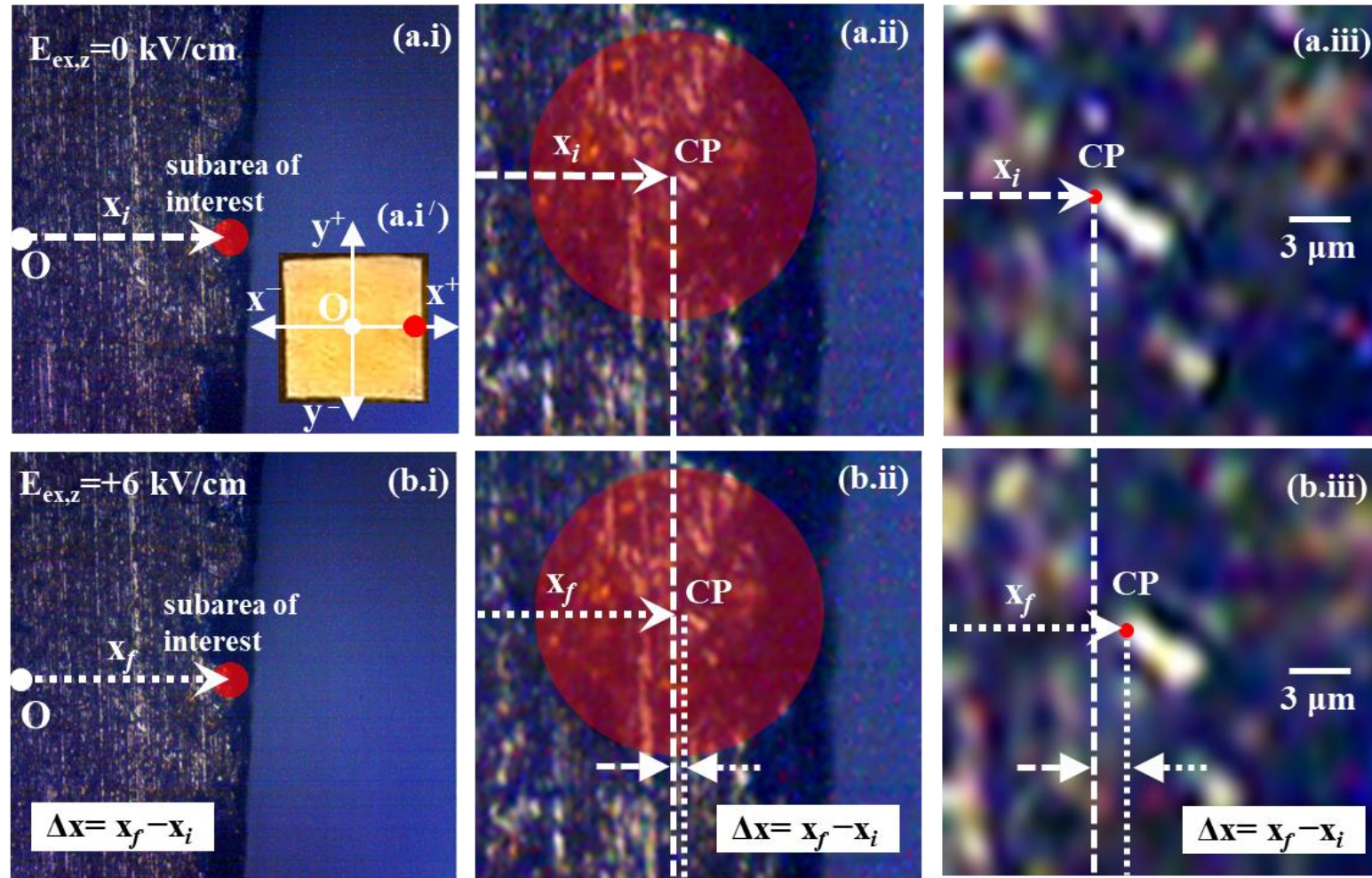


Fig. 2.9: (a.i)-(a.iii), (b.i)-(b.iii) OM images in top view of a characteristic point (CP) placed at the middle of the right edge of a square PZT plate, inset (a.i'), subjected to (a.i)-(a.iii) $E_{ex,z}=0$ kV/cm and (b.i)-(b.iii) $E_{ex,z}=+6$ kV/cm. (a.i), (b.i) Raw OM images with magnification $x130$. The subarea of interest, which includes a CP, is delimited by a red semi-transparent circle. The dashed and dotted arrows denote the length (x_i and x_f , respectively, where the lower index 'i' stands for initial while 'f' stands for final) between the center of the sample and a CP that should be shifted upon application of $E_{ex,z}$ from 0 kV/cm to +6 kV/cm (not discerned here due to increased/low length scale/magnification). The inset (a.i') of (a.i) shows the top view of the specific PZT plate investigated here with the red semi-transparent circle denoting the subarea of interest. (a.ii), (b.ii) Processed version of the raw OM images of (a.i),(b.i), where an additional digital magnification $x1.5$ has been applied (total magnification $x195$). The displacement, $\Delta x=x_f-x_i$, of the CP is shown by the vertical dashed and dotted lines and the respective horizontal arrows. (a.iii), (b.iii) Additionally processed version of the OM images of (a.ii),(b.ii), where an extra digital magnification $x3.65$ has been applied (total magnification $x710$). Now, the displacement of the CP is clearly distinguishable; the red dot signifies the end of x_i and x_f (dashed and dotted arrows, respectively). Scale bar represents $3 \mu\text{m}$.

The estimation of Δx ultimately enables us to calculate the respective in-plane strain-electric field curves, $S_{zi}(E_{ex,z})$, and subsequently the respective in-plane PE coefficients, d_{zi} (in the case of this example $i=x$). Accordingly, the estimated strain, $S_{zx}^+(E_{ex,z})$, is:

$$S_{zx}^+(E_{ex,z}) = \frac{x_f(E_{ex,z}) - x_i(E_{ex,z} = 0)}{x_i(E_{ex,z} = 0)} = \frac{\Delta x(E_{ex,z})}{x_i(E_{ex,z} = 0)} \quad (2.7)$$

For a symmetrical sample, without preferred orientation of deformation, the in-plane strain along x^+ axis, $S_{zx}^+(E_{ex,z})$, should be equal in magnitude with the in-plane strain along x^- axis, $S_{zx}^-(E_{ex,z})$. Hence, the total in-plane strain, $S_{zx}(E_{ex,z})$ of the sample along x^+x^- axis is estimated by the equation:

$$S_{zx}(E_{ex,z}) = 2 \cdot S_{zx}^+(E_{ex,z}) \quad (2.8)$$

The estimated $S_{zx}(E_{ex,z})$ curve for $E_{ex,z}$ ranging within $-10 \text{ kV/cm} \leq E_{ex,z} \leq +10 \text{ kV/cm}$, is shown in Fig. 2.10. Based on Eq. (1.6) in the subchapter 1.1.2, the respective d_{zx} is given by the expression below:

$$d_{zx} = \left(\frac{\partial S_{zx}}{\partial E_{ex,z}} \right) \quad (2.9)$$

It is worth mentioning that the PE coefficients' values highly depend on the electric field regime from which they are calculated (this issue is discussed in detail in the subchapter 3.2.1.V). Here, we apply Eq. (2.9) on the linear-like segments of the $S_{zi}(E_{ex,z})$ hysteresis curve, denoted by the thick red lines in Fig. 2.10. Accordingly, the mean absolute value of these in-plane PE coefficients is $\langle |d_{zx}| \rangle = 400 \text{ pm/V}$.

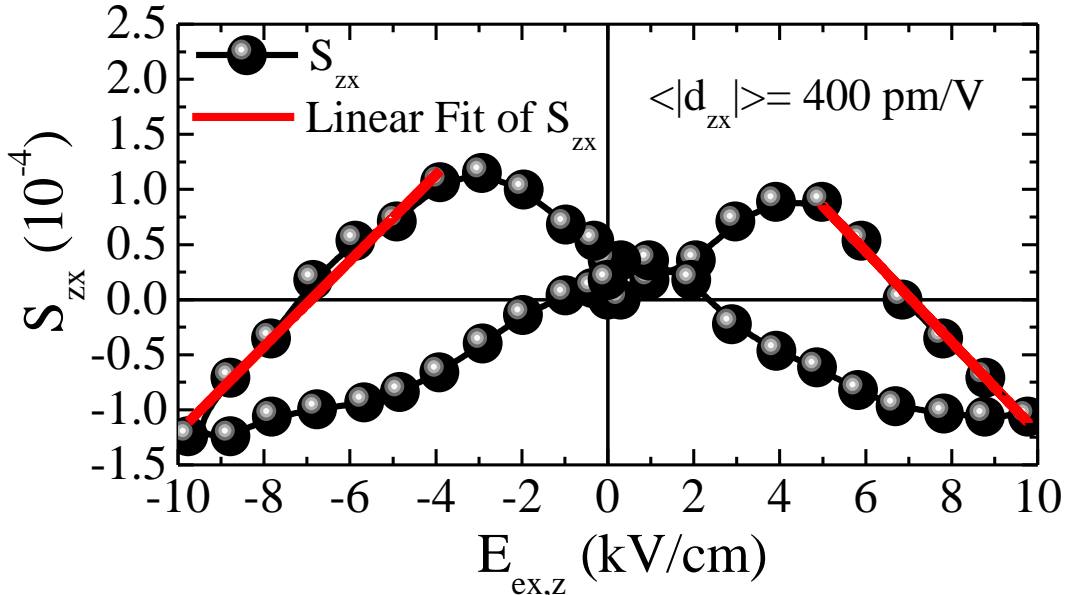


Fig. 2.10: A typical in-plane strain-electric field loop, $S_{zx}(E_{ex,z})$, for a PZT sample with $E_{ex,z}$ ranging within $-10 \text{ kV/cm} \leq E_{ex,z} \leq +10 \text{ kV/cm}$. The red thick lines denote the linear fitting from which the corresponding PE coefficients, d_{zx} , were calculated. The mean absolute value of these coefficients is $\langle |d_{zx}| \rangle = 400 \text{ pm/V}$.

B. Basic technical issues on the reliability of the technique

During the application of the aforementioned technique, two main technical issues emerge; the undesirable however inevitable in-plane mechanical shift of the stage and the appropriate length scale that should be used for the quantification of the in-plane measurements. Below we discuss both issues in detail.

Rejecting the in-plane mechanical shift of the stage

After the sample is placed on the platform, with the top and bottom pin holding it rigidly at its center of symmetry (Fig. 2.5(c)), the platform is mounted onto the stage of OM, as shown in Fig. 2.11(a). It should be highlighted that a specific protocol is followed right before starting the measurements, in order to reject the in-plane shifts caused by any possible drift between mechanical parts of the experimental setup.

Specifically, in any standard commercially available OM possible shifts due to undesired drift between its mechanical parts (e.g. optical stage and head), either over the xy plane (in-plane) or along the z axis (out-of-plane), are generally considered to be practically zero. In our case, another component, namely the sample-carrying platform, has been added onto the stage of the OM (Fig. 2.9(a)). This extra part is not rigidly fixed onto the stage; it is mounted to an in-plane slider by an adjustment clip. It is easy to understand that the sample-carrying platform is vulnerable to possible drift over the xy plane (in-plane), at least at a transient time period where mechanical relaxation exists. This could be a serious source of error, since in our case we want to record the in-plane deformation of the sample below the micrometer range. To eliminate such errors, we carefully monitored the in-plane shift along both the x and y axes to identify the end point of the transient state, after which any possible in-plane mechanical drift safely ceases, as shown in Figs. 2.11(b.i) and 2.11(b.ii), respectively. From these data we concluded that the transient state lasts for $t \approx 80$ min, at maximum. Accordingly, in all our experiments where the sample-carrying platform had to be removed and repositioned onto the stage of the OM (e.g. at the first measurement or when the NdFeB permanent magnet had to be used, see next subsection) we waited for almost 2 hours before starting our measurements.

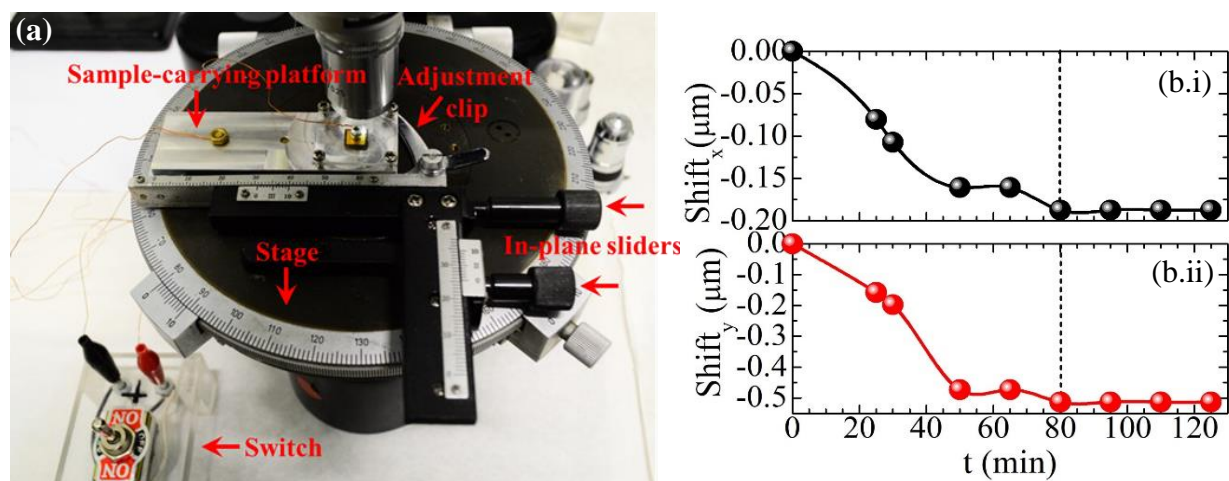


Fig. 2.11: (a) Perspective view of the OM stage upon recording the in-plane deformation of the sample, in order to calculate $S_{zx}(E_{ex,z})$ and $S_{zy}(E_{ex,z})$. The sample-carrying platform is mounted to a fixed in-plane slider by an adjustment clip. (b.i), (b.ii) Measurements of the in-plane shift along (b.i) x and (b.ii) y axes caused by any possible drift between mechanical parts of the experimental setup e.g. the sample-carrying platform and optical stage. After adequate time, $t \approx 80$ min, the in-plane shift along both x and y axes is practically zero.

In order to quantify the in-plane displacement of the CP, a standard length scale should be employed as already presented with the respective scale bar in Figs. 2.9(a.iii) and 2.9(b.iii). In general, the length scale can be obtained by means of a standard calibration sample. In this PhD Thesis we used the TGX1 and TGZ3 grating samples, shown below, Fig. 2.12. Specifically, OM and SEM images of the grating samples are shown in Figs. 2.12(a.i), 2.12(b.i) and in Figs. 2.12(a.ii), 2.12(b.ii), respectively; panels (a.i), (b.i) correspond to TGX1, while panels (a.ii), (b.ii) correspond to TGZ3. Also, Figs. 2.12(a.iii) and 2.12(b.iii) schematically show in perspective view the geometrical characteristics of the periodic structure of TGX1 and TGZ3 samples, respectively (the SEM and schematic images are taken from the company's catalogue). As mentioned above, the raw OM images of an investigated PE sample are processed to ultimately obtain a higher total digital magnification so that the CP's in-plane displacement is made visible/measurable. To quantify the in-plane measurements obtained in a sample under investigation, the exact same processing procedure should also be applied to a standard OM image of a calibration sample. From the latter standard OM image we can ultimately define the appropriate length scale that should be used for the in-plane measurements of the investigated sample as already shown with the respective scale bar in Figs. 2.9(a.iii) and 2.9(b.iii). More details on the estimation of the length scale can be found in Appendix A.

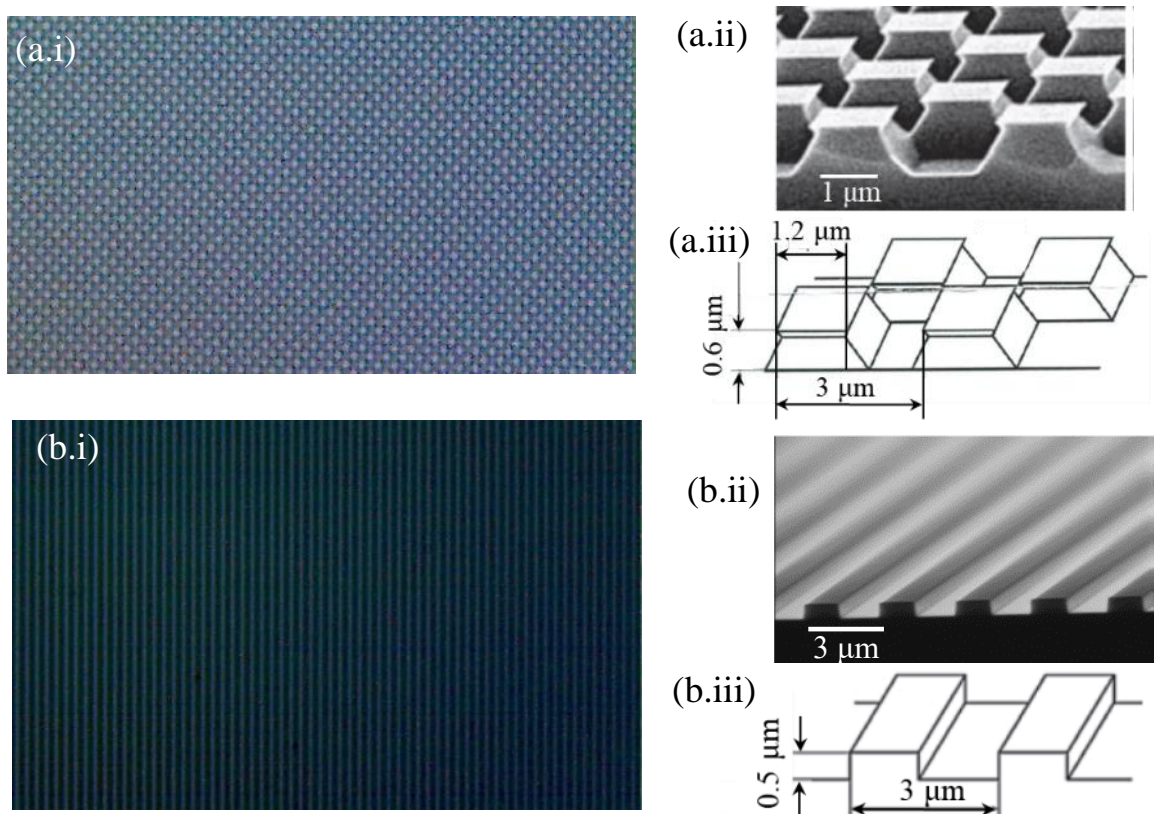


Fig. 2.12: (a.i)&(b.i) OM (magnification $\times 130$), (a.ii)&(b.ii) SEM and (a.iii)&(b.iii) schematic images of the standard calibration samples TGX1 and TGZ3 (NT-MDT Co, Moscow, Russia); panels (a.i)-(a.iii) correspond to the TGX1 and panels (b.i)-(b.iii) correspond to TGZ3.

C. Home-made platform for recording the PE deformations by OM under application of both an external electric and magnetic field

In order to use the technique described in section A, the sample is adjusted onto a home-made apparatus, that enables simultaneous application of both an external electric, $E_{ex,z}$, and magnetic, $H_{ex,z}$, field while we observe it with the OM. The first version of a similar aluminum home-made platform, however without the option of $H_{ex,z}$ application, was originally presented in our work in Ref. [7]. In the context of this Thesis, we made another version of the home-made platform which gives us the possibility to apply both a conjugate $E_{ex,z}$, as well as an heteroconjugate $H_{ex,z}$, at will (both fields are applied out-of-plane). The apparatus mainly consists of an aluminum platform especially designed to incorporate a permanent magnet at its bottom part. This permanent magnet enables the application of the desired magnetic field. The rest part of the platform and that of the experimental procedure are left the same. Thus, below we focus exclusively on the extra details of this platform. The entire construction and detailed data are shown in parts (A) and (B) of Fig. 2.13, respectively.

In part (A), Figs. 2.13(a)-(c), the respective home-made platform is shown, in side and bottom view, and it is explained in detail at its caption. As usual, the external electric field is applied using a DC-voltage supply (model IP-32, Healthkit Co, USA) and is delivered to the surfaces of the sample by employing a pair of pins that serve as electrodes. The external magnetic field is applied by a NdFeB permanent magnet (disc-shaped with diameter 20 mm and thickness 3 mm). The magnet is placed just below the sample, embedded inside the aluminum base, as shown in Figs. 2.13(a)-(c). By means of this experimental setup, the in-plane strain, $S_{zi}(E_{ex,z})$ (Fig. 2.10 above), can be recorded even under the presence of an $H_{ex,z}$. We note that all materials used in this construction are non-magnetic, else the magnetic field of the NdFeB permanent magnet would have lost its original form.

In part (B), Figs. 2.13(d)-(g), we show detailed data recorded by means of a Gaussmeter. This information is crucial since we aim to investigate the PE response upon the absence/presence of an external magnetic field, $H_{ex,z}$, so that its homogeneity should be fairly justified. In this context, accurate mapping of $H_{ex,z}$ was performed along both the z axis, as shown in Fig. 2.13(d), and along the xy plane (ρ coordinate), as shown in Figs. 2.13(e.i) and 2.13(e.ii). The sample is always placed at a distance $z_s=5$ mm from the magnet, with its center aligned with that of the latter. Specifically, referring to Fig. 2.13(d), we recorded $H_{ex,z}$ along z axis, at $\rho=0$ mm in the range $0 \text{ mm} \leq z \leq 10 \text{ mm}$. We deduced that the external magnetic field has the value $H_{ex,z}(z_s)=1$ kOe at $z_s=5$ mm, with small inhomogeneity, $\Delta H_{ex,z}=50$ Oe, occurring along the thickness of the sample (typical value: $t=0.5$ mm). This is indicated by the respective shaded area, referring to the thickness of the illustrated sample that is shown in perspective view. Referring to Figs. 2.13(e.i) and 2.13(e.ii), they present $H_{ex,z}$ along the ρ coordinate, at $z_s=5$ mm, in the range $0 \text{ mm} \leq \rho \leq 10 \text{ mm}$ (entire area of the permanent magnet) and $0 \text{ mm} \leq \rho \leq 5 \text{ mm}$ (delimited area of the permanent magnet), respectively. Regarding the former, we observe that $H_{ex,z}$ is generally symmetrical, while concerning the latter, small asymmetries can be inspected in the magnetic profile. Accordingly, to estimate the relative $H_{ex,z}$ inhomogeneity experienced by the sample, we considered a sample of typical in-plane dimensions $6 \times 6 \text{ mm}^2$ (grey rectangle). We observe that the inhomogeneity of the magnetic field over the sample surface is very small, on the order of $\Delta H_{ex,z}=30$ Oe at maximum. What is more, Figs. 2.13(f)

and 2.13(g) present two-dimensional and three-dimensional simulation plots, respectively, of $H_{ex,z}$ as a function of ρ , based on polynomial fitting of the experimental data of Fig. 2.13(e.i). Schematic illustrations of a representative sample are also shown in both Figs. 2.13(f) and 2.13(g) (in-plane dimensions $6 \times 6 \text{ mm}^2$). From Fig. 2.13(f), we observe that $H_{ex,z}$ exhibits fair homogeneity over almost the entire sample surface. Exclusively over a small portion of the sample, along its diagonals, we estimate that the inhomogeneity reaches the value $\Delta H_{ex,z}=40-50 \text{ Oe}$, at maximum. We note that the difference of $\Delta H_{ex,z}$ between the experimental (Fig. 2.13(e.ii)) and the simulation (Fig. 2.13(f)) plots is attributed to the fact that, in the case of the latter, the polynomial fitting causes a slight overestimation of the $H_{ex,z}$ value at ($\rho=0 \text{ mm}, z_s=5 \text{ mm}$). Fig. 2.13(g) shows aforementioned data in 3D plot, in perspective view for the sake of clarity. To conclude, Figs. 2.13(d)-(f) prove that the $H_{ex,z}$ produced by the permanent NdFeB magnet is plausibly homogeneous over the entire volume of the sample, since the estimated inhomogeneities, $\Delta H_{ex,z}=30-50 \text{ Oe}$ (both out-of-plane and in-plane) constitute a percentage of 3-5% of the maximum magnetic field value experienced by the sample at $z_s=5 \text{ mm}$, that is $H_{ex,z}=1000 \text{ Oe}$.

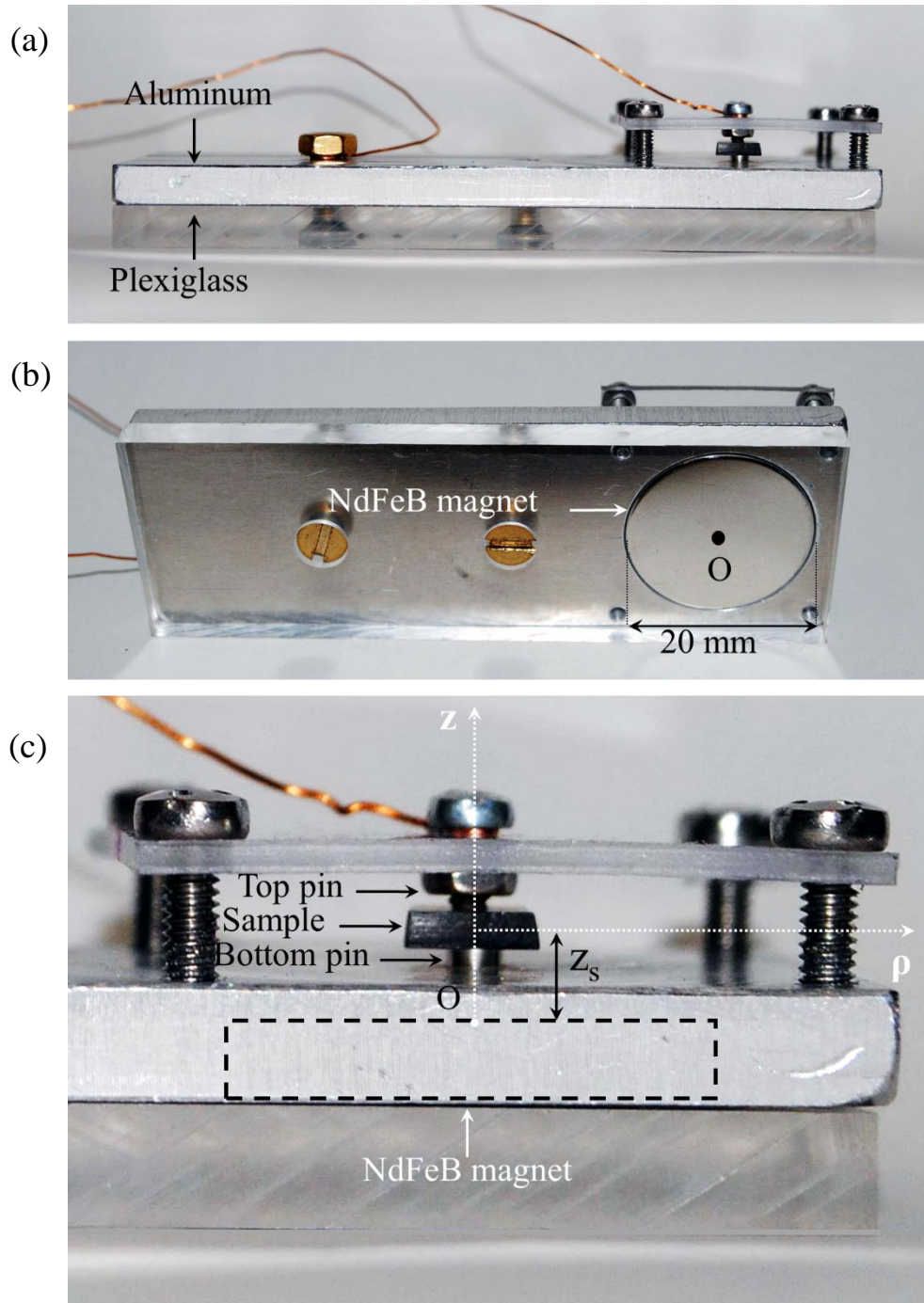


Fig. 2.13-Part (A): Home-made platform for the simultaneous application of the out-of-plane electric and magnetic fields, $E_{ex,z}$ and $H_{ex,z}$. (a) Side view and (b) perspective bottom view of the home-made platform constructed for the local observation of the sample, by means of an OM, under simultaneous application of an electric field, $E_{ex,z}$, produced by a DC-voltage supply and a constant magnetic field, $H_{ex,z}$ produced by a disc-shape NdFeB permanent magnet. $E_{ex,z}$ can be varied continuously within -10 kV/cm to $+10$ kV/cm during a set of measurements, while $H_{ex,z}$ is constant, 1 kOe, and exhibits azimuthal symmetry. (c) Detail of (a) in the sample area. The coaxial top and bottom pins hold the sample at its center so that the entire sample is left free to deform. The plexiglass plate, screwed firmly onto the aluminum part of the platform, serves as a basis of the top pin, while it allows us to observe the sample by OM, thanks to its transparency. The black dashed rectangle denotes the NdFeB magnet that is embedded in the aluminum platform, with its center, O , aligned with that of the sample. The coordinate axes z and ρ are shown with white dotted lines.

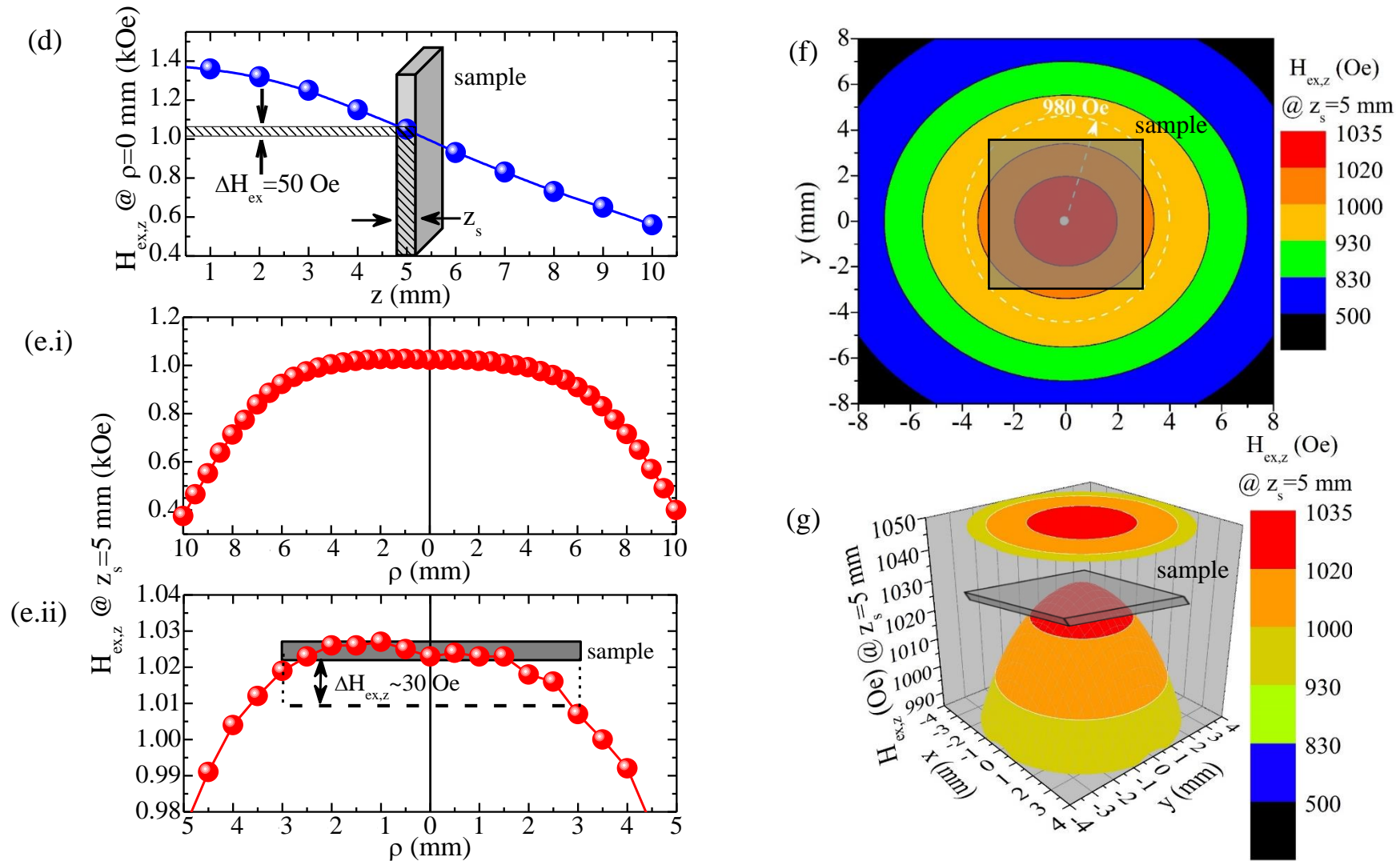


Fig. 2.13-Part (B): (d), (e) Experimental data of the $H_{ex,z}$ of the permanent NdFeB magnet along (d) the z axis and (e.i),(e.ii) the xy plane, that is along the ρ coordinate ($z_s=5$ mm). Specifically: (d) Variation of $H_{ex,z}$ with z within the range $0\text{ mm} \leq z \leq 10\text{ mm}$ at $\rho=0$ mm. At the sample area, $z_s=5$ mm, the magnetic field is $H_{ex,z}=1$ kOe, with a small inhomogeneity of $\Delta H_{ex,z}=50$ Oe along the sample's thickness (shaded area); the sample is schematically presented in perspective view. (e.i) Variation of $H_{ex,z}$ with ρ at $z_s=5$ mm, within the range $0\text{ mm} \leq \rho \leq 10\text{ mm}$. (e.ii) Data of panel (e.i) delimited within the range $0\text{ mm} \leq \rho \leq 5\text{ mm}$. A small asymmetry in the magnet's profile is revealed ($\Delta H_{ex,z}=30$ Oe at maximum) for a sample with typical in-plane dimensions $6 \times 6\text{ mm}^2$ (grey rectangle). (f),(g) Simulation plots referring to the variation of $H_{ex,z}$ with ρ at $z_s=5$ mm, based on polynomial fitting ($y=A_0+A_1x+A_2x^2+A_3x^3+A_4x^4$) that was performed to the experimental data of panel (e.i). Specifically: (f) Two-dimensional simulation plot of $H_{ex,z}$ with ρ ; a sample of typical in-plane dimensions $6 \times 6\text{ mm}^2$ is presented with a grey-shaded semi-transparent square; the white dashed circle denotes the $H_{ex,z}$ value at the corners of the sample. (g) Three-dimensional simulation plot of $H_{ex,z}$ with ρ in perspective view. The same typical sample of panel (f) is also illustrated here in perspective view.

2.3.2 Superconducting Quantum Interference Device

A superconducting quantum interference device (SQUID) is basically used as a standard technique to obtain information on the magnetic properties of samples upon variation of temperature and/or magnetic field. In this Thesis, we made a drastic modification of the sample probe, so that a heteroconjugate externally applied electric field, E_{ex} can be applied to the sample while simultaneously measuring its magnetization. This is why we include the SQUID in the subchapter '2.3 Research experimental techniques'. Below, we firstly survey the basic operation of a SQUID unit, and secondly we describe in detail the introduced modification mentioned above.

Basic operation of a SQUID unit: The SQUID is the most sensitive device available for magnetic measurements. The complete apparatus of a SQUID magnetometer is schematically shown in Fig. 2.14(a). The most basic parts of the magnetometer are, namely, the superconducting (SC) magnet, the SC detection coil system and the SQUID sensor. At first we will describe each one of these parts briefly, and subsequently, we will explain their function upon the measurement procedure, in detail.

Specifically, the SC magnet is fabricated from NbSn₃ SC wire, twisted in a solenoidal configuration, and it can produce a magnetic field, H , up to 5.5 T with accuracy on the order of 0.1 mT. Located at the center of the SC magnet, a coil system is used to detect the magnetic flux, Φ , originating from the sample's movement. The detection coil system is configured as a second order gradiometer. It consists of four single turn spirals, two outer and two inner ones. The outer spirals are twisted counterclockwise while the inner ones are clockwise. This configuration serves for the rejection of the first gradient of large magnetic fields produced by SC magnet, as well as for the elimination of external magnetic fields stemming from magnetic objects in the surrounding environment. The SC detection coil system is shown in Fig. 2.14(a), as a part of the SQUID magnetometer. Most important, the detection coils are connected to the input of the SQUID sensor, as shown in Fig. 2.14(b) in detail, so that changes in the magnetic flux, Φ , in the detection coils, are converted to voltage, V , with high accuracy, as shown in Fig. 2.14(c). These parts are immersed into liquid helium (He^4) bath in a vacuum shielded dewar. The presence of liquid He^4 ensures the proper function of all SC components (magnet, detection coil system and SQUID sensor) and also allows low temperature measurements by cooling the sample chamber. The latter is kept under vacuum and accommodates the metallic sample holder probe. By means of a temperature controller that is settled in the sample chamber, the sample's temperature can be adjusted within 1.8-400 K with accuracy on the order of 10 mK.

The magnetization measurements can start using a computer-controlled automatic system, with moving the sample along z axis (dotted line in Fig. 2.14) for a distance of 3 cm, which is sufficient so that the sample experiences a uniform magnetic field. During a single measurement, the total distance that the sample will cover (scan length) is divided in n -steps (the number of steps is determined by the user). In each one of the n -steps, the SC detection coils detect the magnetic flux as a function of z , thus recording $\Phi(z)$. In turn, this signal is inductively transferred to the SQUID sensor, as shown in Fig. 2.14 (b), where it is converted to voltage, $V(z)$ as presented in Fig. 2.14 (c). More specifically, the SQUID sensors are based on Josephson junctions [18,19] (SC/insulator/SC). There are two types of SQUID sensors, the DC-SQUID with two Josephson junctions connected in parallel and the RF-SQUID with a

single Josephson junction. Focusing on the latter, which is the one installed in the magnetometer of our laboratory, it consists of a SC ring and a weak Josephson junction (i.e. a thin insulating barrier). The voltage, V , that is induced is a periodic function of the applied magnetic flux with period $\Phi_0=2e/\hbar=2.07\times 10^{-15}$ Wb. Practically, the Josephson sensor gets ‘polarized’ by the application of current, I , of appropriate value, so that the sensor functions as a linear magnetic flux-to-voltage converter (Fig. 2.14(c)).

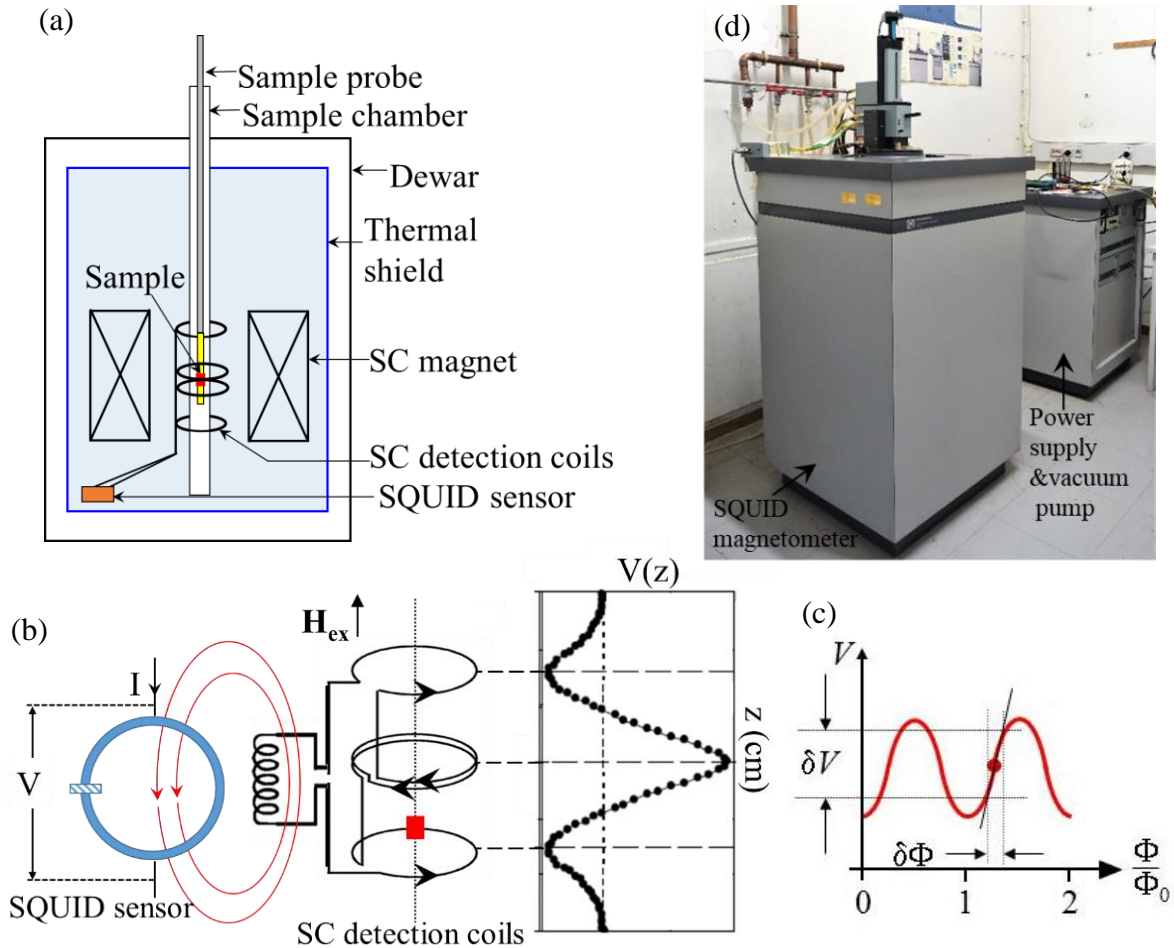


Fig. 2.14: (a) Schematic representation of the Superconducting Quantum Interference Device (SQUID) magnetometer with its basic parts. (b) Configuration of the SC detection coils coupled with the SQUID sensor. The respective output voltage as function of the sample’s position, $V(z)$, is also shown. (c) The output voltage at the SQUID sensor as a function of the magnetic flux. (d) SQUID magnetometer MPMS 5.5 T unit (Quantum Design, CA, USA). The present unit is installed at the Institute of Nanoscience and Nanotechnology of National Center for Scientific Research ‘Demokritos’.

Finally, the converted signal $V(z)$ should be fitted with the appropriate theoretical expression, so that we can estimate the magnetic moment of the sample, $m(z)$. This expression is given below:

$$V(z)=2\pi mR^2\{-1/[R^2+(L_1+z)^2]^{3/2} + 1/[R^2+(L_2+z)^2]^{3/2}+1/[R^2+(L_3-z)^2]^{3/2} -1/[R^2+(L_4-z)^2]^{3/2}\} \quad (2.10)$$

where L_i is the position of the i^{th} detection coil and z is the distance of the sample from the $z=0$ (i.e. the center of the SC magnet). Please note that the first and the last terms are negative due to their opposite twist compared to the intermediate ones. Fig. 2.15 schematically shows in detail the configuration of the detection coils and the sample. In our case, $R=0.97\text{-}1.01$ cm, $L_1=L_4=1.52$ cm $\kappa\alpha$ $L_2=L_3=0.05$ cm.

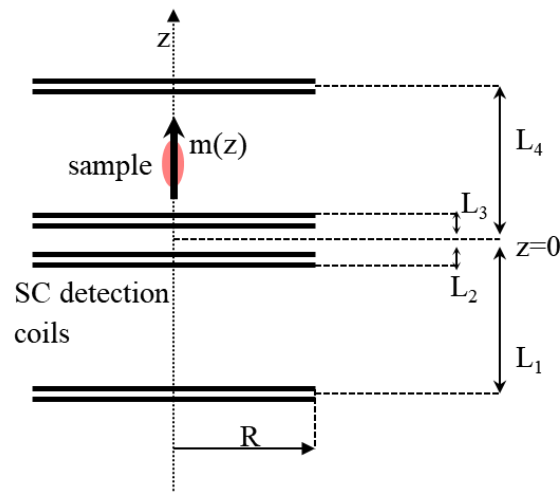


Fig. 2.15: Schematic representation of the detection coil system. The coils are placed symmetrically to $z=0$.

The SQUID magnetometer used in this PhD Thesis, shown in Fig. 2.12(c), is an MPMS 5.5 T unit (Quantum Design, San Diego, CA, USA), employed for typical magnetization measurements. In the next paragraph, a modification of the sample probe is described for the additional application of electric field to composite PE/FM samples, during magnetization measurements.

Modification of the sample probe for $E_{ex,z}$ application: Apart from the conventional measurements of magnetization under the application of a conjugate, externally applied magnetic field, H_{ex} , magnetization measurements were also employed under the simultaneous application a heteroconjugate electric field, $E_{ex,z}$, in this PhD Thesis. Specifically, magnetization measurements under $E_{ex,z}$ were employed for the PE/FM Co/PMN-0.30PT/Co and PZT-xFe₃O₄ composites, at $T=300$ K and $T=10$ K. To this end, a modified sample rod was constructed.

Beginning with the standard Quantum Design sample rod, it consists of a hollow cylinder with length $L=120$ cm, outer diameter 3 mm and wall thickness 0.25 mm. The rod is made from aluminum at its main part ($L_{Al}=100$ cm, with the upper part outside the sample chamber) -in order to reduce thermal losses from the sample chamber to the environment- and from copper at its lower part ($L_{Cu}=20$ cm) -in order to ensure good thermal conductivity between the sample chamber and the sample-.

Regarding the modification of the sample rod for $E_{ex,z}$ application, the two ends of the standard rod were cut (1 cm from each end), without affecting the required length for the centering process. Two copper wires (coated with insulating polyurethane paste) with $L=180$

cm and diameter 0.1 mm were twisted and inserted into the rod. With the wires overhanging, both ends of the rod were shielded with araldite. The length of the wires was chosen taking into consideration both the prerequisite distance for centering the sample and the possibility of partial replacement of the wires' ends after extensive use. The diameter of the copper wires was chosen, among others, for ensuring the temperature stability at cryogenic conditions; the copper wires were adequately thin to minimize heat transfer from the top part of the sample rod (being outside the cryostat, at room temperature) to the sample chamber. This detail is very important in order to maintain temperatures as low as 10 K. It is worth mentioning that the specific diameter value of the copper wires is crucial, since by using wires with larger diameter, e.g. 0.2 mm, the temperature could not be stabilized in the low temperature regime.

Figs. 2.16(a)-(g) show the modified sample rod (panels (a.i)-(a.iii)), and present in detail the procedure that we follow in order to apply external electric voltage to a sample attached to it (panels (b)-(g)). Specifically, Figs. 2.16(a.i) and 2.16(a.iii) show the upper and the lower part of the modified sample rod, respectively. Specifically, in Fig. 2.16(a.i) we see upper part of the rod together with the thin copper wires (diameter: 0.1 mm) that come out of it, for connection with the DC-voltage supply; the panel (a.ii) shows in magnification the black dashed rectangle of panel (a.i), corresponding to the thin copper wires. Fig. 2.16(a.iii) shows the lower part of the rod, with a piece of teflon attached to its end; onto the teflon, a straw that carries the sample, is adapted. For better comprehension of the procedure that we follow when using the modified sample rod for magnetic measurements we present Figs. 2.16(b)-(f). These Figs. show in magnification the detailed process in order to connect the electrodes for external electric voltage application to the sample, and subsequently to attach the sample onto the straw. Accordingly, in Fig. 2.16(b) we observe in perspective view the front copper wire that is mechanically and electrically connected to the sample with silver paste (we note that for both wires' ends we have previously removed their insulating coating). It should be noted that in the cases of the composite samples Co/PMN-0.30PT/Co and PZT-5%Fe₃O₄, the Co and Au metallic films (see subchapter 2.4) serve as electrodes for external electric voltage application, respectively. In Fig. 2.16(c) the sample is presented in side view with the copper wires connected to its lateral surfaces. The arrows denote the direction of the external electric field, $E_{ex,z}$, that is along the thickness of the sample (i.e. z-axis, or out-of-plane) and of the external magnetic field, H_{ex} , that is over the lateral surfaces of the sample (i.e. x-y plane, or in-plane). After the connection of the copper wires, the sample is inserted in the plastic straw and attached to it by sewing, as shown in Figs. 2.16(d) and 2.16(f), respectively. We note that the thread that we use has been measured in SQUID magnetometer and does not have magnetic properties. Finally, Fig. 2.16(f) presents the general top view of the lower part of the modified sample rod; at this point the rod is ready to be inserted in the sample chamber.

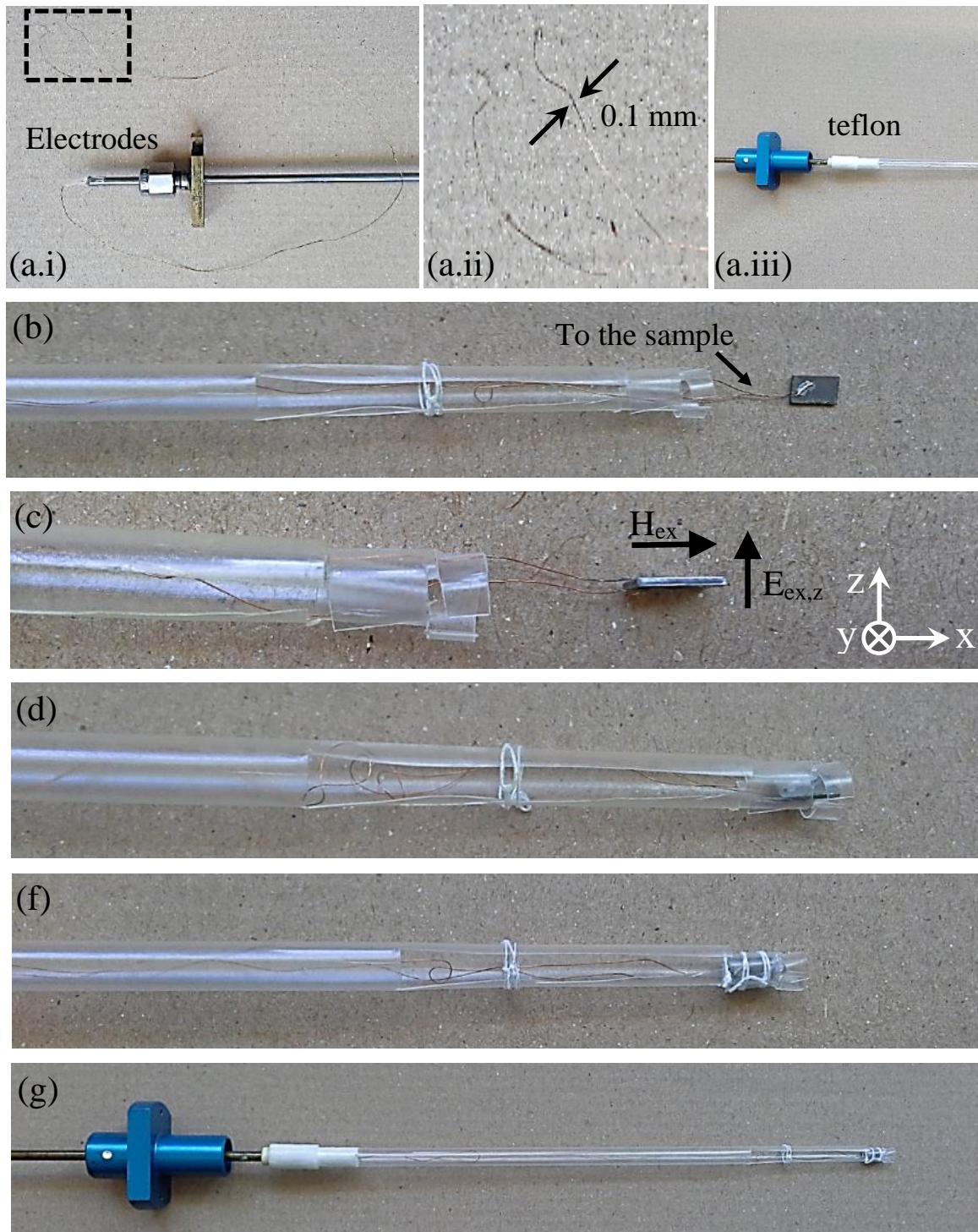


Fig. 2.16: (a)-(g) Photos of the modified sample-rod for magnetic with simultaneous E_{ex} application. (a.i) Upper part of the sample-rod; the copper wire electrodes for $E_{ex,z}$ application are shown in the dashed rectangle. (a.ii) the electrodes are shown in magnification. (a.iii) lower part of the rod; the sample-carrying straw is adapted to the lower part of the rod via a piece of teflon. (b)-(f) The lower part of the modified rod in magnification; the different panels show successively the process that we follow for applying E_{ex} to the sample and attaching it to the plastic straw (see text for details). (g) General top view regarding the lower part of the modified sample rod, ready to be inserted in the sample chamber of the SQUID magnetometer.

2.3.3 Scanning Electron Microscope

The Scanning Electron Microscope (SEM) is a powerful and standard microstructural characterization technique that utilizes a finely focused electron beam to reveal the detailed surface characteristics of a sample and provide information relating to its three-dimensional structure. Apart from the basic operation of SEM, in the context of this Thesis we also took advantage of its extra capabilities, namely Energy Dispersive X-Ray Spectroscopy (EDS), to perform elemental analysis and mapping. This is why we include the SEM in the subchapter '2.3 Research experimental techniques'. Below, we firstly survey the basic operation of a SEM unit, and secondly we describe in detail EDS analysis and mapping.

Basic operation of a SEM unit: The basic components of SEM, shown Fig. 2.17(a), are placed in the electron column that is kept under high vacuum (about 10^{-6} Torr) by a mechanical and a turbomolecular vacuum pumps. Specifically, electrons are generated in the electron gun by heating cathode filaments, and then they pass through the anode, which accelerates them to energies ranging within 0.1-30 keV. The electron beam is demagnified by electromagnetic (condenser) lenses, to form a much smaller diameter of the incident beam, and then focused on the sample surface by objective lenses. The beam that emerges from the final lenses enters the sample chamber, where it interacts with the sample to a depth (interaction volume) of approximately 1-5 μm , generating electrons and photons (Fig. 2.17(b)) some of which are used for the subsequent image formation. After the beam is focused, scan coils are used to move the beam to a series of discrete locations, line by line, until a rectangular 'raster' is generated on the sample [20]. Simultaneously, a similar raster is formed on the display monitor, while the scan coils are used to sweep the beam across the sample. The magnification of the image is set by the scan coils and results from the ratio of the dimensions of the raster on the sample and its respective dimensions on the display monitor. The spatial resolution of the SEM depends on the size of the electron spot, which in turn depends on both the wavelength of the electrons and the electron-optical system that produces the scanning beam, as well as on the interaction volume. Contemporary SEMs have high spatial resolution, ranging within 5-10 nm.

The principal signals used to form images in SEM are the secondary electrons (SE) and the backscattered electrons (BSE). These signals are capable of carrying information about the morphological topography and elemental topography of the sample, respectively. Specifically, SE are loosely bound outer shell electrons of the sample's atoms, which receive sufficient kinetic energy (on the order of eV) to be ejected from the atom and set into motion via inelastic scattering. The fact that they originate from depths just a few nanometers beneath the sample surface (~ 50 nm) renders them relatively accurate to produce the morphological topography of the sample, such as surface texture and roughness. It is worth noting that only the SE that reach the detector will be producing the image, while obstructed ones will produce dark contrast in the image. Regarding BSE, their kinetic energy is higher than this of SE (on the order of keV). Accordingly, they originate from depths around 500 nm beneath the sample surface (Fig. 2.17(b)) and undergo numerous elastic scattering events, until they deviate from the incident beam path at angles almost 180° , retaining most of their initial kinetic energy. Heavier elements (high atomic number, Z) will generate more BSE than light elements (low Z). Hence, a BSE image corresponds to elemental topography, since the contrast varies both due to topographic contrast and chemical contrast.

For non-conducting samples, an ultrathin coating of electrically conductive material is often required in order to obtain high quality images and to avoid electric charging during the scanning of the sample surface by the electron beam. In this case, grounding of the samples is also necessary, so that the conductive coating material acts as a channel and allow the charging electrons to be removed from the sample. Sputtering with Au is the most common practice, due to its high conductivity and its relatively small grain size that enables high-resolution imaging.

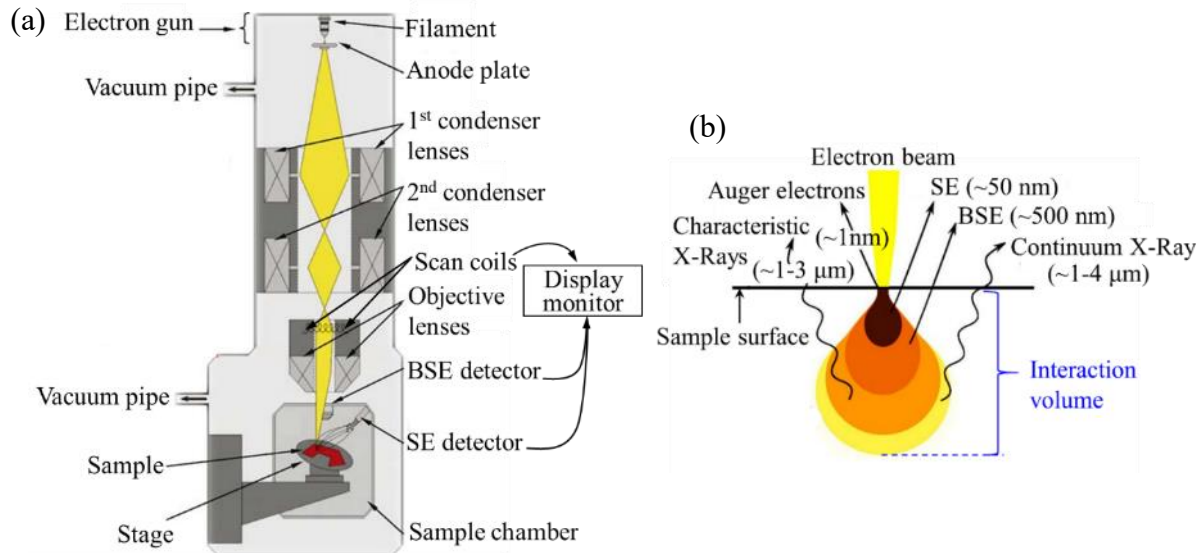


Fig. 2.17: (a) Schematic representation of the basic parts of the electron column of a Scanning Electron Microscope. (b) Schematic illustration of the signals emitted from different parts of the interaction volume.

Energy dispersive X-rays spectroscopy and elemental mapping: In general, the incident electron beam can generate X-ray photons in the beam–sample interaction volume beneath the sample surface (Fig. 2.17(b)). These X-ray photons, have characteristic energies corresponding to the constitutive elements of the sample. Specifically, the beam electrons can interact with the tightly bound electrons of the inner shells of the atom, and ejecting an electron from them. The ejected electron leaves the atom with a kinetic energy of a few eV to several keV and the atom is left as an ion in an excited, energetic state, as shown in Fig. 2.18(a.i). Within few picoseconds, the atom relaxes to its ground state through a limited set of allowed transitions of outer shell electron(s) filling the inner-shell vacancy, as shown in Figs. 2.18(a.ii) and 2.18(a.iii). The excess energy is released from the atom as characteristic X-ray photon (Fig. 2.18(a.iii)), as Auger electrons and/or as continuum X-ray radiation (bremsstrahlung, not shown in Fig. 2.15(a.iii)); among them, only the characteristic X-ray photons serve for EDS. An example of EDS spectrum is shown in Fig. 2.18(b.i) for a PZT-5%Fe₃O₄ sample (non-coated). It should be noted that except for the distinct peaks of characteristic X-rays, we can also observe a continuum background signal that is attributed to the bremsstrahlung radiation [20].

Complementary to EDS, elemental mapping is a very effective option of SEM. With elemental mapping useful information can be obtained through the combination of standard SEM imaging and EDS analysis. Specifically, for a certain investigated area of the sample surface, the local concentration of each distinct element can be surveyed. Each element can be

ascribed to a specific color of appropriate intensity so that the recorded information is easily accessible by the user.

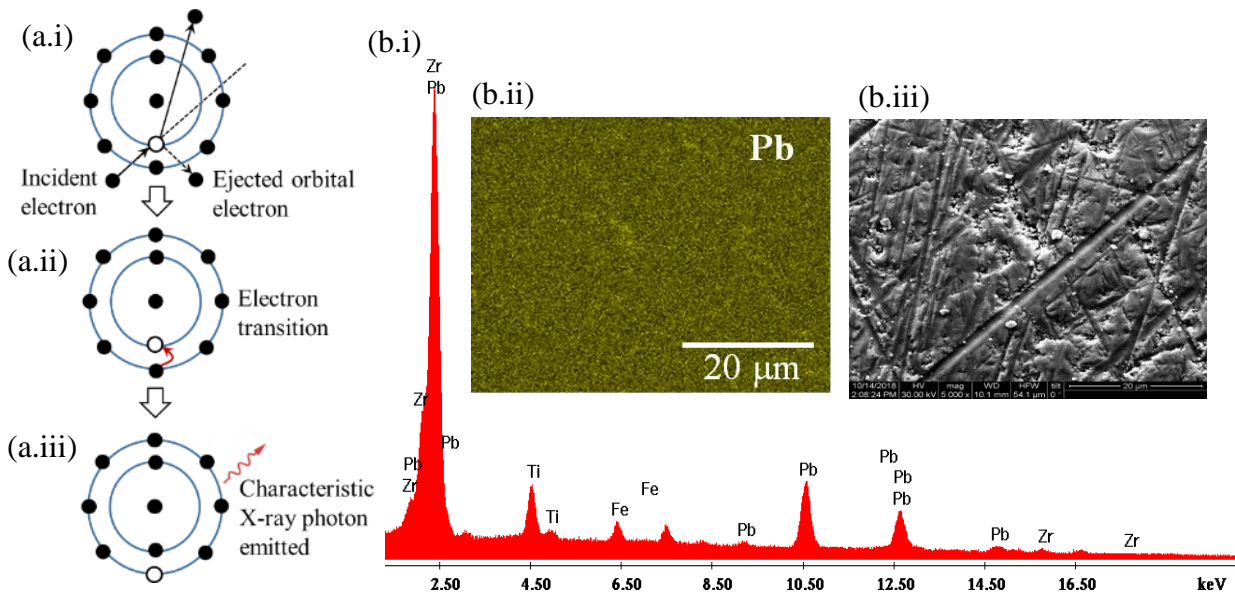


Fig. 2.18: (a.i)-(a.iii) EDS basic principle; generation of characteristic X-rays in a sample imaged by SEM. (a.i) Inner shell electron ionization in an atom (the incident electron is elastically scattered, while the unscattered direction of the incident electron is shown by the dotted line). (a.ii), (a.iii) Subsequent de-excitation by electron transition and X-ray photon emission, respectively. (b.i) EDS spectrum of a PZT-5%Fe₃O₄ sample (non-coated) and (b.ii) representative EDS elemental mapping images of Pb. (b.iii) SEI topography image that shows the respective investigated sample area from which EDS and elemental mapping were deduced.

Accordingly, the presence of color contrast can unveil inhomogeneities in the concentration of the elements over the investigated sample area. A representative example of elemental mapping is shown in Fig. 2.18(b.ii) for Pb. Fig. 2.18(b.iii) shows the SE imaging (SEI) topography image of the respective investigated sample area from which EDS and elemental mapping were deduced. Clearly, the information of Figs. 2.18(b.ii) and 2.18(b.iii) is entirely different.

For this PhD Thesis, SEM images were obtained by means of the Inspect Microscope (FEI, Hillsboro, OR, USA) shown in detail in Fig. 2.19. Specifically, in Figs. 2.19(a)-(c) the basic parts of the experimental unit are denoted by numbers. In Fig. 2.19(a): (1) electron column, (2) sample chamber, (3) vacuum pumps, (4) X-rays detector, (5) SE detector, (6) EDS spectrometer, cooled with liquid N₂, (7)-(8) monitors for sample imaging and EDS spectrometry, respectively. The inset (a.i) of Fig. 2.16(a) shows the Au sputtering unit (E5100, Quorum Technologies Ltd, Eats Sussex, UK) that was used for the coating of specific samples. Fig. 2.16(b) shows in perspective view the inside of the sample chamber, with the sample holder (9) mounted on the stage (10); the latter can move horizontally and vertically, tilt and rotate. The sample holder can hosts conventional pin stabs onto which the samples are placed and fixed with silver paste. As discussed above, depending the case, the samples can be non-coated or coated. For example, the insets (b.i) and (b.ii) of Fig. 2.19(b) show two PZT-5%Fe₃O₄ samples on conventional pin stabs, Au-coated and non-coated, respectively. The conical-like

metallic part (11) corresponds to the final lenses, which is the lower part of the electron column, just before the electron beam exits and interact with the sample surface. In addition, the SE detector (12) consists of a scintillator inside a Faraday cage, which is positively charged and attracts the SE. What is more, (13) corresponds to the camera that is used for monitoring the mechanical movements of the stage in real time. The red dotted rectangle area of Fig. 2.19(b) is presented in detail in Fig. 2.19(c). Since it is presented in bottom view, we can clearly observe the exit point of the electron beam (14), the BSE detector (15) and the X-rays detector (16).

Regarding sample preparation for SEM, when necessary, they were sputtered with a layer of Au (~100 nm) under medium vacuum (10^{-1} Torr). The electron gun of SEM works with W (tungsten) filament; during the measurements we employed typical values for the interfering parameters (i.e. acceleration voltage within 15-30 kV, working distance within 8-15 mm and spot size 3-8). Information on the topography for the evaluation of the microstructure was obtained with SEI, while elemental analysis to obtain both EDS spectroscopy information and compositional mapping images was recorded with BSE imaging. Au-coated samples were used for SEI, while both Au-coated and non-coated samples were used for BSE imaging to cross-check the results due to the overlapping of the M-spectral line of Au (2.123 keV) with the $L\alpha$ -spectral line of Zr (2.044 keV) and the M-spectral line of Pb (2.342 keV).

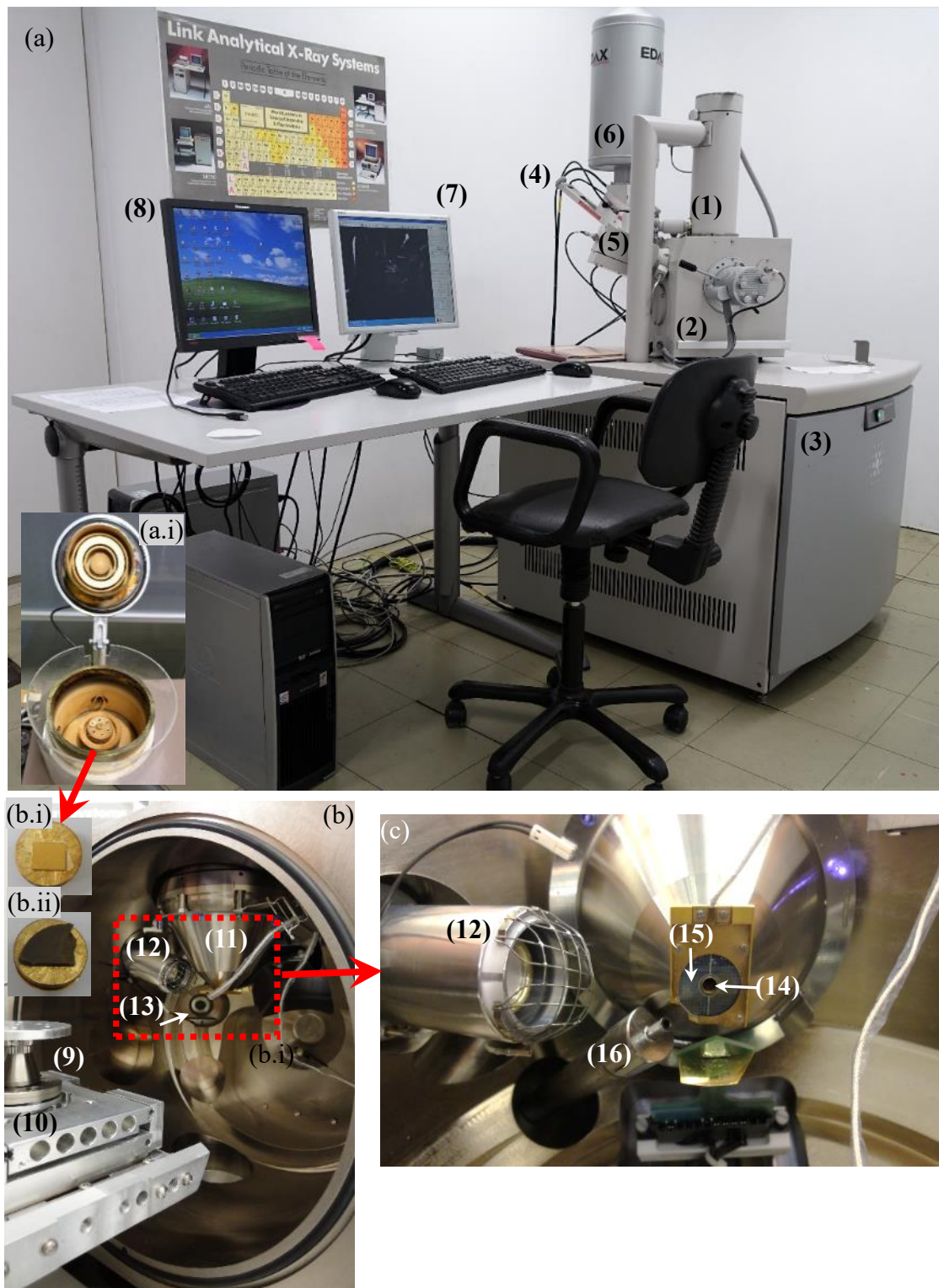


Fig. 2.19: (a) Photo of the SEM laboratory unit (FEI, Hillsboro, OR, USA) The inset (a.i) shows the sputtering unit (E5100, Quorum Technologies Ltd, Eats Sussex, UK). The specific unit is installed at the Institute of Nanoscience and Nanotechnology of National Center for Scientific Research 'Demokritos'. (b) Perspective view of the inside of sample chamber. The insets, (b.i) and (b.ii), show non-coated and Au-coated PZT-5%Fe₃O₄ samples, respectively, on pin stabs. (c) Bottom view of the dotted rectangle area of panel (b). The basic parts of the SEM unit are denoted by numbers in each panel (see text for details.)

2.4 Sample categories

2.4.1 Ferromagnetic Co thin films on PMN-xPT single crystals

A. PMN-xPT single crystals

The PMN-xPT single crystals with $x=0.30$ employed in this PhD Thesis were prepared by our colleague (and member of the Jury) Prof. S. J. Zhang. These crystals have been grown by a modified Bridgman method using powders of Pb_3O_4 , $MgNb_2O_6$, and TiO_2 (purity higher than 99.99%) as starting materials. Details on the preparation process can be found in Refs. [21-23]. After growth, the crystals were cut at rectangular shape with dimensions $5 \times 6 \times 0.5 \text{ mm}^3$, with large face perpendicular to [011] direction and side faces of (100) and (0-11). Thus, upon electric field application, the displacements along out-of-plane (that is thickness) and in-plane (that is surface) are based on the values of d_{31} , d_{32} , and d_{33} , being on the order of +800, +500, and -1200 pC/N (pm/V), respectively. The PMN-xPT single crystals that we used have a rhombohedral to tetragonal phase transition approximately at $T_{RT}= 368 \text{ K}$ and a Curie temperature approximately at $T_c= 408 \text{ K}$ [21-23]. The as-prepared PMN-0.30PT crystals exhibit a relatively rough surface landscape with a mean surface roughness in the range of 400-600 nm [24]. To ensure a relatively uniform coverage of the crystal surface with the Co thin film (see subchapter 2.4.1.B, below) we reduced the surface roughness through thorough polishing by using fine sandpaper (silicon-carbide P2500). Accordingly, the mean surface roughness was reduced below one hundred nanometers, exhibiting typical values in the range of 30-100 nm.

B. Co thin films

The Co outer layers were RF-sputtered (30 W) using the sputtering unit described in the subchapter 2.1.1.I. and shown in Fig. 2.1(b). The sputtering was realized at 3×10^{-3} Torr of Ar (99.999%) only when a base pressure in the range of 10^{-6} - 10^{-7} Torr was established upon adequate pumping. The high-quality FM Co outer layers act as electrodes for the application of the $E_{ex,z}$ to the PMN-0.30PT single crystal, so that the produced strain is eventually experienced by the Co thin films, as well. The thickness of Co layers fabricated was $d=30$ -50 nm; in this range, the Co layers are quite thick to ensure the uniform coverage of the surface of the polished PMN-xPT crystals (thus, enabling application of a uniform E_{ex}), though being thin enough to be entirely susceptible to the strain induced by the adjacent PMN-xPT crystal. In addition, it is known that in the range 30-50 nm, the orientation of magnetization of Co changes from in-plane to out-of-plane, and thus is susceptible to modulation. The Co/PMN-0.30PT/Co samples that were extensively investigated in this Thesis correspond to Co thickness $d=30 \text{ nm}$. Figs. 2.20(c.i) and 2.20(c.ii) show representative photos of bulk plain PMN-0.30PT and Co-sputtered PMN-0.30PT single crystals, respectively.

2.4.2. Fe₃O₄ nanoparticles embedded in a PZT matrix

In order to form the bulk hybrid compound PZT-xFe₃O₄ (x: the weight percentage concentration of Fe₃O₄), we used as starting materials PZT powder of PZT5H type, simply called PZT (NCE55, Noliac) and Fe₃O₄ (Sigma-Aldrich 98%, particle size: 50-100 nm). Specifically, Fe₃O₄ powder in concentration x=0%, 1%, 3%, 5%, 10%, 20%, 30% and 50% per weight, was grounded and mixed thoroughly with PZT powder into an agate mortar, in order to achieve homogeneous hybrid oxides. The mixed oxides were pressed into pellets at 35 MPa, with diameter 20 mm, placed on alumina crucibles and sintered at T_{sin}=1000 °C, for t=2h, in air. The heating (≈100 °C/h) and cooling (≈50 °C/h) rates of the furnace (Fig. 2.2(c)) were kept constant for all the samples prepared. In addition, pellets of plain PZT and Fe₃O₄ were also sintered under the same conditions, for reference. Figs. 2.17(b.i)-(b.vii) show representative photos of the sintered samples' powders, from which we can observe the evolution in their color upon increasing Fe₃O₄ concentration. Photos of the starting compounds (PZT and Fe₃O₄, before sintering) are also presented, for comparison. All powders have been attached to conventional microscope glasses with double face tape (this is the configuration that we use for XRD measurements).

Subsequently, the sintered pellets of PZT and PZT-5%Fe₃O₄ were cut into samples of different shapes and dimensions (see Table 2.1 below). In order to apply external electric field along the samples' thickness (let us say along z-axis), E_{ex,z}, as high as E_{ex,z}=±10 kV/cm, we reduced the thickness of the samples, t, from t=1 mm (as prepared) down to almost t=0.4 mm. To this end, the surfaces of the samples were polished using sandpaper, rinsed with ethanol and air dried. For E_{ex,z} application, Au films (~100 nm) were sputtered on both surfaces of the samples (E5100, Quorum Technologies Ltd, Eats Sussex, UK), which also serve as reflective surfaces for observation with OM. During sputtering, a macroscopic mask was employed to protect the lateral surfaces of the samples and avoid any short circuit while applying the E_{ex,z}. After sputtering, the samples were left unpoled. Figs. 2.20(c.i) and 2.20(c.ii) show representative photos of bulk plain PZT and Au-sputtered PZT samples, respectively.

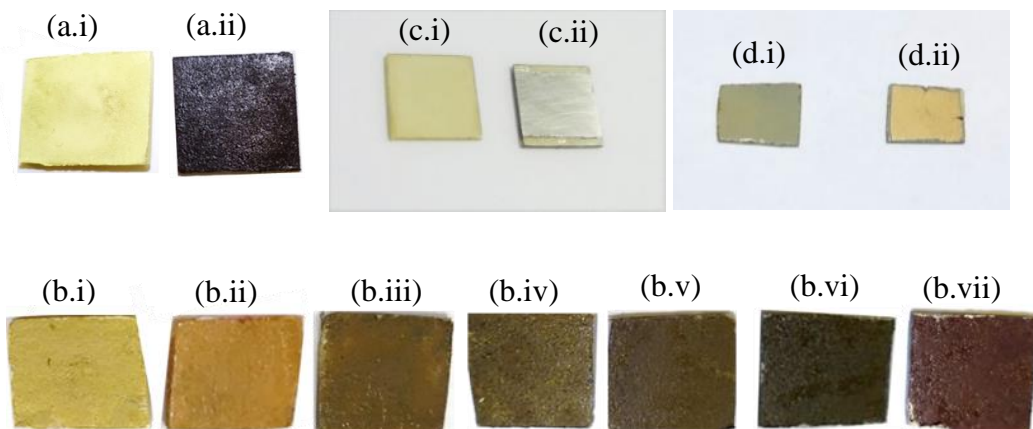


Fig. 2.20: Photos of powders corresponding to (a.i), (a.ii) the starting compounds: (a.i) PZT^{start} and (a.ii) Fe₃O₄^{start} and (b.i)-(b.vii) the sintered compounds PZT^{sin}, PZT-xFe₃O₄ and Fe₃O₄^{sin}: (b.i) PZT^{sin}, (b.ii) 5%, (b.iii) 10%, (b.iv) 20%, (b.v) 30%, (b.vi) 50%, and (b.vii) Fe₃O₄^{sin}. (c.i), (c.ii) and (d.i), (d.ii) Photos of the bulk: (c.i) plain PMN-0.30PT, (c.ii) Co-sputtered PMN-0.30PT single crystals and (d.i) plain PZT, (d.ii) Au-sputtered PZT samples.

2.4.3. Main sample series

During this PhD Thesis, twenty samples of Co/PMN-xPT/Co and seventy samples of PZT-xFe₃O₄ were prepared and preliminary studied. Based on the obtained results by means of the previously mentioned experimental techniques, the detailed investigation was focused on samples of the specific categories Co/PMN-0.30PT/Co, PZT and PZT-5%Fe₃O₄.

Table 2.1 summarizes the samples of the Co/PMN-0.30PT/Co, PZT and PZT-5%Fe₃O₄ sample categories (along with their respective dimensions) that were thoroughly examined by both the standard characterization and the specialized research techniques, presented above in this Chapter. Regarding the former, we refer to X-Ray Diffraction, magnetization measurements, current-voltage characteristics, global polarization/strain measurements and Secondary Electron Imaging, while regarding the latter, we refer to magnetization measurements under application of an external electric field, local strain measurements under application of an external magnetic field, Energy Dispersive X-Rays Spectroscopy and elemental mapping. The different sample series, S1-S5, correspond to different experiments/measurements (see chapter 3 for details); for the sake of simplicity, each sample is characterized by a sample code.

<i>Sample series</i>	<i>Sample Code</i>	<i>Samples</i>	<i>Dimensions (mm³)</i>
S1	S.1.1	Co/PMN-0.30PT/Co	5.0×6.0×0.5
	S.1.2	Co/PMN-0.30PT/Co	5.0×6.0×0.5
	S.1.3	Co/PMN-0.30PT/Co	5.0×6.0×0.5
S2	S.2.1	PZT	4.5×6.0×0.4
	S.2.2	PZT	4.5×4.5×0.4
	S.2.3	PZT	4.0×6.0×0.45
S3	S.3.1	PZT-5%Fe ₃ O ₄	4.0×4.0×0.4
	S.3.2	PZT-5%Fe ₃ O ₄	4.5×5.0×0.4
	S.3.3	PZT-5%Fe ₃ O ₄	3.0×6.0×0.4
	S.3.4	PZT-5%Fe ₃ O ₄	5.0×6.0×0.4
S4	S.4.1	PZT-5%Fe ₃ O ₄	Ø6×0.4 (disc, mm ²)
	S.4.2	PZT-5%Fe ₃ O ₄	7.0×7.0×0.4
	S.4.3	PZT-5%Fe ₃ O ₄	3.5×3.5×0.4
S5	S.5.1	PZT	6.0×6.0×0.4
	S.5.2	PZT-5%Fe ₃ O ₄	6.0×6.0×0.4

Table 2.1: Samples of the Co/PMN-0.30PT/Co, PZT and PZT-5%Fe₃O₄ samples series that were thoroughly studied in this PhD Thesis by all the techniques presented in this Chapter, together with their sample code and dimensions. The different sample series correspond to different experiments/measurements (see chapter 3 for details).

References

- [1] R. Prabu, S. Ramesh, M. Savitha, and M. Balachandar, ICSM Conference Proceedings, Coimbatore, India (2013).
- [2] P. J. Kelly and R. D. Arnell, Vacuum **56**, 159 (2000).

- [3] H. E. Exner, *Reviews on powder metallurgy and physical ceramics*, Volume 1, Freund Publishing House, Israel (1979).
- [4] J. E. Blendell, *Encyclopedia of Materials: Science and Technology*, Elsevier (2001).
- [5] R. M. German, *Sintering Theory and Practice*, John Wiley (1996).
- [6] W. D. Kingery, H. K. Bowen, and D. R. Uhlmann, *Introduction to Ceramics*, John Wiley (1976).
- [7] M. Zeibekis, G. Vertsioti, and D. Stamopoulos, *J. Phys.D: Appl. Phys.* **49**, 105304 (2016).
- [8] W.L. Bragg, *Proceedings of the Cambridge Philosophical Society* **17**, 43 (1913).
- [9] C. Kittel, *Introduction to Solid State Physics*, 7th Ed., John Wiley, New York (1996).
- [10] C. B. Sawyer and C. H. Tower, *Phys. Rev.* **35**, 269 (1930).
- [11] A. M. Glazer, P. Grooves, and D. T. Smith, *J. Phys. E: Sci. Instrum.* **17**, 95 (1984).
- [12] L. Jin, F. Li, and S. Zhang, *J. Am. Ceram. Soc.* **97**, 1 (2014).
- [13] Q. M. Zhang, W. Y. Pan, and L. E. Cross, *J. Appl. Phys.* **63**, 2492 (1988).
- [14] D. Stamopoulos, and S. J. Zhang, *J. Alloys Compd.* **612**, 34 (2014).
- [15] T. Pfeifer, R. Freudenberg, G. Dussler, D. Brocher, *Measurement* **30**, 1 (2001).
- [16] E. G. van Putten et al., *Phys. Rev. Lett.* **106**, 193905 (2011).
- [17] G. Vertsioti, S. J. Zhang, and D. Stamopoulos, *Sci. Rep.* **9**, 2178 (2019).
- [18] B. D. Josephson, *Phys. Lett.* **1**, 7 (1962).
- [19] A. Barone and G. Paterno, *Physics and applications of the Josephson effect*, Wiley (1982).
- [20] J. Goldstein, D. Newbury, D. Joy, C. Lyman, P. Echlin, E. Lifshin, L. Sawyer and J. Michael, *Scanning electron microscopy and x-ray microanalysis*, 3rd Ed., Springer (2003).
- [21] S. Zhang and F. Li, *J. Appl. Phys.* **111**, 031301 (2012).
- [22] F. Li, S. Zhang, Z. Xu, X. Wei, J. Luo, and T. R. Shrout, *J. Appl. Phys.* **108**, 034106 (2010).
- [23] X. B. Li and H. S. Luo, *J. Am. Ceram. Soc.* **93**, 2915 (2010).
- [24] D. Stamopoulos, M. Zeibekis and S. J. Zhang, *J. Appl. Phys.* **114**, 134309 (2013).

Chapter 3: Experimental results and discussion

This chapter summarizes representative experimental results obtained in the context of this PhD Thesis, along with the relative discussion for their interpretation. The results are categorized in the subchapters 3.1 and 3.2, according to the topology of the investigated samples; in the subchapter 3.1, we present results for FM thin films of Co deposited on both sides of bulk PE single crystals of PMN-0.30PT, that is Co/PMN-0.30PT/Co, while in the subchapter 3.2 we communicate the main experimental results of this PhD Thesis, which refer to FM NPs of Fe_3O_4 (diameter 50-100 nm) embedded into a bulk PZT matrix, that is PZT- $x\text{Fe}_3\text{O}_4$, where x is the weight percentage concentration of Fe_3O_4 . Notably, in the subchapters 3.2.1-3.2.3 we present the results coming from a series of experiments that focus on the magnetic/piezoelectric properties of the composites under the influence of the heteroconjugate, externally applied electric/magnetic fields.

3.1 Ferromagnetic Co thin films on PMN-0.30PT single crystal substrates

In the last decades, composite multiferroic, MF, materials with planar topology, composed by FM films deposited onto a PE substrate have attracted great interest due to their potential applications in functional devices [1-4]. Interestingly, many candidate applications of planar FM/PE MF composites are actually based on the manipulation of the remanent magnetization, m_{rem} , by an external electric field, E_{ex} . In the context of this PhD Thesis relevant hybrid structures were studied, composed by the PE PMN-0.30PT, and the FM Co (thickness: 30-50 nm). The PMN-0.30PT constituent is in single crystal form, while Co comes in thin film form, altogether composing a FM/PE/FM hybrid structure. The preparation of PMN-0.30PT single crystals and Co thin films have been discussed in the subchapters 2.1.1 and 2.4.1.A, respectively. In this study the external electric field is applied along the thickness of the sample (i.e. out-of-plane, let us say along z -axis), denoted by $E_{\text{ex},z}$, while the external magnetic field is applied along the sample surface (i.e. in-plane), simply denoted by H_{ex} .

In this layered composite, the Co outer layers are employed as electrodes to apply $E_{\text{ex},z}$ to the PMN-0.30PT crystal. Specifically, the stress induced by PMN-0.30PT shall be ultimately delivered to the Co outer layers and alter their magnetic properties. We recall here that PMN-0.30PT was chosen, since near this composition its PE response gets maximum. In addition, the thickness of Co outer layers was chosen between 30-50 nm taking into account that: (i) the layers should be thin enough (until few tens of nanometers) so that the induced strain can be ultimately delivered to them throughout their entire thickness and (ii) for layer thickness in the range 30-50 nm the magnetization of Co switches from in-plane to out-of-plane, and thus it is more vulnerable to be modulated. Our study corresponds to samples with Co thickness 30 nm.

Specifically, in the subchapter 3.1.1, we present data of crystallographic data for the Co/PMN-0.30PT/Co composite. Also, FE/PE and magnetization data are shown for the PMN-0.30PT single crystal. In the subchapter 3.1.2 two special protocols are described, referring to magnetization measurements of the Co/PMN-0.30PT/Co composite under application of $E_{\text{ex},z}$. Accordingly, the subchapter 3.1.3 is divided in two parts, presenting data of: (i) isothermal magnetization, $m(H_{\text{ex}})$, at $T=10$ K and $T=300$ K, and (ii) isofield magnetization at $H_{\text{ex}}=0$, that

is remanent magnetization, $m_{\text{rem}}(T)$, of the Co outer layers under the influence of different $E_{\text{ex},z}$. Most important, we focus on the evolution of $m_{\text{rem}}(T)$ in the entire temperature range $10 \text{ K} \leq T \leq 300 \text{ K}$. Finally, we interpret this temperature-dependent behavior, based on the underlying physical mechanisms that control the Co/PMN-0.30PT/Co composite.

3.1.1 Characteristic physical properties

I. Crystallographic data

Fig. 3.1 shows typical XRD data of a representative Co/PMN-0.30PT/Co composite, at room temperature. The assignment of the peaks corresponds to the PMN-0.30PT single crystal; from these data we can see that the single crystals are along the [110] direction. We note that the peaks corresponding to Co thin film is too weak to be detected in the presence of the stronger peaks due to the bulk PMN-0.30PT single crystal. In addition, some of the expected peaks of Co (e.g. in the range $40^\circ \leq 2\theta \leq 50^\circ$) are probably superimposed with those of the bulk PMN-0.30PT phase, a fact that renders the detection of the former even more difficult.

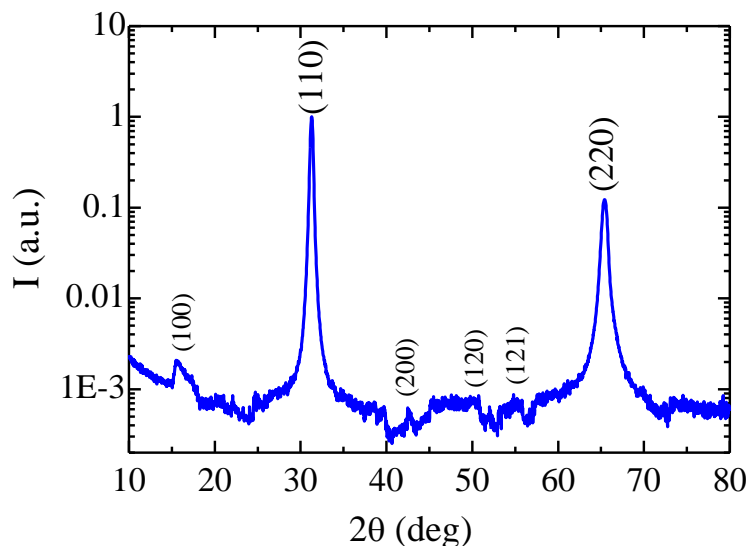


Fig. 3.1: XRD data of a representative Co/PMN-0.30PT/Co composite sample. The assignment of the peaks corresponds to the PMN-0.30PT single crystal; the peaks of Co thin films (30 nm) are too weak to be detected, and probably superimposed with these of PMN-0.30PT.

II. Polarization and out-of-plane strain data

Figs. 3.2(a) and 3.2(b) present representative polarization, $P(E_{\text{ex},z})$ and the out-of-plane strain, $S_{zz}(E_{\text{ex},z})$ data upon varying $E_{\text{ex},z}$ within $-10 \text{ kV/cm} \leq E_{\text{ex},z} \leq 10 \text{ kV/cm}$. The $P(E_{\text{ex},z})$ data exhibit the typical hysteretic behavior of FE materials. The loop is rather tetragonal, with coercive field $E_c^{\pm} = \pm 2.6 \text{ kV/cm}$. In general, the tetragonal loops and the relatively small coercive field values are common in single crystals, since their domains can be switched completely with respect to an external electric field. Accordingly, they possess lower E_c compared to polycrystalline

materials; regarding the latter, the polarization can be switched up to 83% at maximum, due to the random distribution of their grains [5,6].

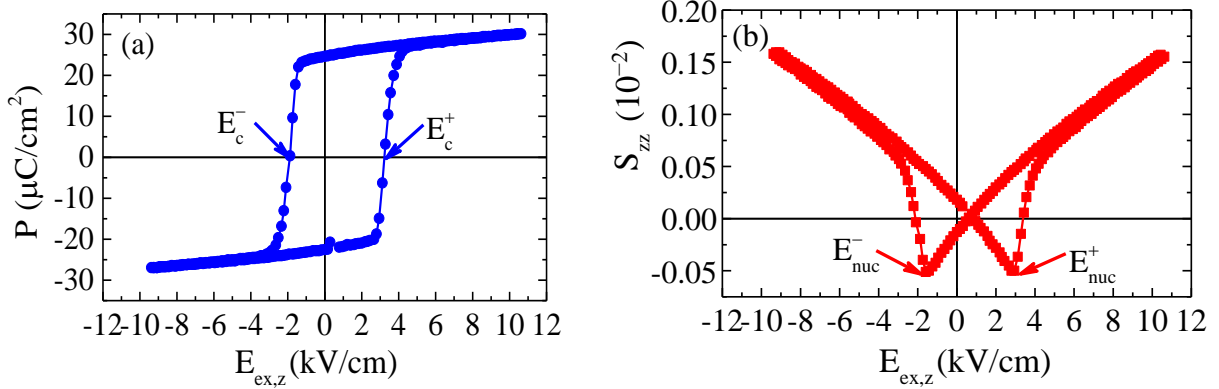


Fig. 3.2: (a) Polarization, $P(E_{ex,z})$ and out-of-plane strain, $S_{zz}(E_{ex,z})$ of a PMN-0.30PT single crystal under $E_{ex,z}$ in the range $-10 \text{ kV}/\text{cm} \leq E_{ex,z} \leq +10 \text{ kV}/\text{cm}$. In panels (a) and (b), the characteristic coercive, E_c , and nucleation, E_{nuc} , fields are indicated by arrows.

Regarding the out-of-plane strain data, the $S_{zz}(E_{ex,z})$ curve shows the typical ‘butterfly’ behavior. As already discussed in the subchapter 1.1.3, the minima of $S(E_{ex,z})$ correspond to the nucleation fields, $E_{nuc}^{\pm} = \pm 2.5 \text{ kV}/\text{cm}$, that occur at electric fields slightly smaller than E_c^{\pm} .

III. Magnetization data

In the following subchapter 3.1.2 we employ magnetic measurements for the hybrid Co/PMN-0.30PT/Co in order to investigate the effect of $E_{ex,z}$ on the magnetization of Co. Hence, it is of high importance to study primarily the magnetic behavior of PMN-0.30PT in the same temperature range. Accordingly, we recorded its magnetization upon varying temperature from 10 K to 300 K, at $H_{ex}=10 \text{ Oe}$, as shown in Fig. 3.3.

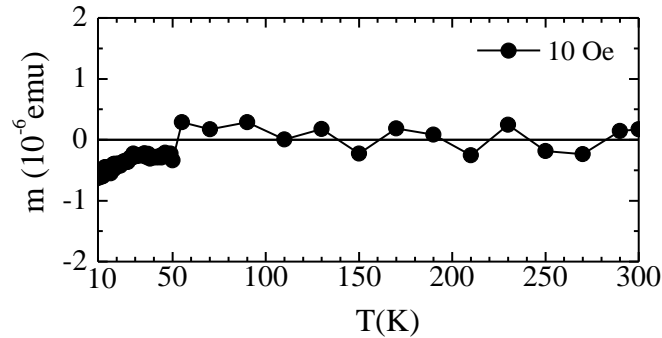


Fig. 3.3: Magnetization of a PMN-0.30PT single crystal upon varying temperature from 10 K to 300 K at $H_{ex}=10 \text{ Oe}$.

From these data it is obvious that the magnetization of the PMN-0.30PT crystal is rather low (on the order of 10^{-6} emu) in the entire temperature range. As it will be subsequently shown below, in subchapter 3.1.2, the magnetization of the hybrid Co/PMN-0.30PT/Co is on the order of 10^{-3} emu , even at $H_{ex}=0 \text{ Oe}$. Thus, we can plausibly assume that the measured magnetic

signal for the Co/PMN-0.30PT/Co composite sample is attributed exclusively to the Co thin films.

3.1.2 Magnetization measurements protocol under $E_{ex,z}$

For the purpose of this study, magnetization measurements were obtained by means of SQUID magnetometer and are divided in two categories: isothermal, $m(H_{ex})$, and isofield, $m(T)$ measurements. The protocols that were followed for each category are described right below.

Measurement Protocol (I): We studied in detail two representative cases; the first focuses on potential applications, thus referring to room temperature conditions, $T=300$ K, while the second refers to entirely cryogenic conditions, $T=10$ K. The measurement protocol for obtaining the isothermal $m(H_{ex})$ loops at $T=300$ K was as following: while temperature is maintained at $T=300$ K at zero external magnetic field, H_{ex} , we applied the external electric field, $E_{ex,z}$, and then H_{ex} is gradually varied from positive to negative saturation while recording the $m(H_{ex})$ loop. The measurement protocol for obtaining the isothermal $m(H_{ex})$ loops at $T=10$ K was as following: beginning from $T=300$ K with $H_{ex}=0$, we applied $E_{ex,z}$, and cool the sample to the desired temperature (electric-field cooling process). Then H_{ex} is gradually varied from positive to negative saturation while recording the $m(H_{ex})$ loop.

Measurement Protocol (II): The measurement protocol for obtaining the isofield ($H_{ex}=0$) remanent state as a function of temperature, $m_{rem}(T)$, was as following: while recording $m(H_{ex})$ at $T=300$ K, we increase H_{ex} until positive saturation is reached and then we decrease it down to $H_{ex}=0$ Oe. This is the remanent FM state, m_{rem} (at $T=300$ K). Fig. 3.4 shows a representative case of how m_{rem} was prepared at $T=300$ K. Then, we apply the desired $E_{ex,z}$ and decrease the temperature from $T=300$ K down to $T=10$ K while recording $m_{rem}(T)$.

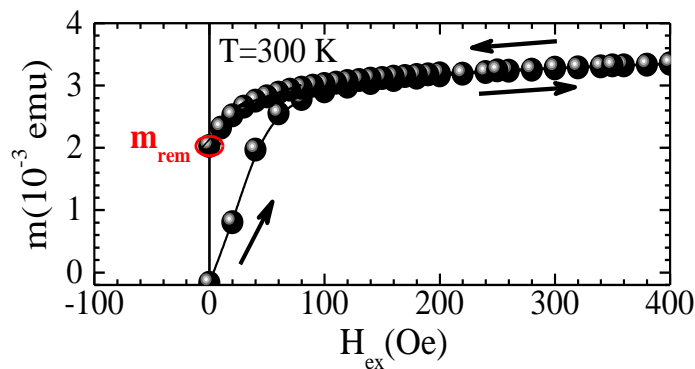


Fig. 3.4: Settling of the remanent FM state, m_{rem} for a Co/PMN-0.30PT/Co composite; m_{rem} is prepared by increasing the external magnetic field, H_{ex} until positive saturation and subsequently by decreasing it down to zero. After the settling of m_{rem} at $T=300$ K, external electric field, $E_{ex,z}$, can be applied by will.

3.1.3 Magnetization data under $E_{ex,z}$ application

I. $m(H_{ex})$ measurements at $T=10$ K and $T=300$ K under $E_{ex,z}$ application

Figs. 3.5(a) and 3.5(c) show representative $m(H_{ex})$ loops obtained at $T=10$ K and $T=300$ K, respectively, for a Co/PMN-0.30PT/Co composite upon varying H_{ex} from -1 kOe to $+1$ kOe

and under the application of various $E_{ex,z}$ values. Fig. 3.5(b) shows the modulation of the coercive field, referring to the descending and the ascending branch of $m(H_{ex})$, H_c^- and H_c^+ , respectively, upon $E_{ex,z}$ application at $T=10$ K. The data were obtained according to the Measurement Protocol (I) (see subchapter 3.1.1, above). We note that, in order to highlight the features of these loops, we focus on the low magnetic field regime in Figs. 3.5(a) and 3.5(c), in which H_{ex} ranges within $-130 \text{ Oe} \leq H_{ex} \leq +80 \text{ Oe}$, and $-40 \text{ Oe} \leq H_{ex} \leq +40 \text{ Oe}$, respectively.

In Fig. 3.5(a) $m(H_{ex})$ loops at $T=10$ K are shown. We observe clear modulation of the magnetic coercive field, H_c , with $E_{ex,z}$ that displays both qualitative and quantitative characteristics. Regarding the former, we notice modulation of H_c both on the descending (ΔH_c^-) and on the ascending (ΔH_c^+) branch, although ΔH_c^- is significantly higher. This is attributed to phenomena of thermomagnetic history, which means that if we had followed another protocol, as for example beginning from the negative magnetic saturation, then we would observe the inverse image (H_c^+ would be mostly modulated under $E_{ex,z}$ application). In addition the modulation of H_c^- is not monotonic, as also observed in other relative studies [7,8]. Most important, regarding the quantitative characteristics of H_c modulation at $T=10$ K, Fig. 3.5(b) presents H_c^\pm as a function of $E_{ex,z}$. As discussed right above, H_c^+ exhibits a rather small percentage variation which can be estimated by the relation $[(H_c^{\min} - H_c^{\max})/H_c^{\max}] \times 100\%$ on the order of 22%, at maximum. On the other hand, we can see that H_c^- shows a noticeable percentage modulation on the order of 47%, at maximum, between $E_{ex,z}=+2.5$ kV/cm and $E_{ex,z}=0$ kV/cm. Regarding $m(H_{ex})$ at $T=300$ K, shown in Fig. 3.5(c), we notice that H_c practically remains unresponsive to $E_{ex,z}$.

Concerning the underlying mechanisms that motivate and/or promote the modulation of H_c upon $E_{ex,z}$ application at $T=10$ K, we suggest the following: (a) the pinning of the existing magnetic domain walls, MDWs, which can be effectively enhanced either by the surface/interface roughness or by the ‘bulk’ static disorder that are introduced due to the developed strain [9-12] and (b) the modulation of MDWs population that inevitably should accompany the modulation of the MD size; the latter is caused by the deformation of the FM film thickness, d , which in turn is motivated by the induced strain (the MD size w is proportional to the square root of d , that is $w \sim d^{1/2}$) [13,14]. Concerning the fact that H_c remains unresponsive to $E_{ex,z}$ at $T=300$ K, we believe that the thermal energy, $k_B T$, progressively counterbalances the pinning energy of MDWs as T increases and finally, at $T=300$ K, ultimately dominates.

The aforementioned modulation of H_c under $E_{ex,z}$ application at $T=10$ K, shown in Figs. 3.5(a) and 3.5(b), is of considerable importance for the concept of next generation ME devices. In fact, even at cryogenic conditions, the important work of Gajek et al. [15] showed that the single phase MF epitaxial $\text{La}_{0.1}\text{Bi}_{0.9}\text{MnO}_3$ can operate as a four-state memory unit controllable by an $E_{ex,z}$. In our case, we proved that the application of a relatively low electric field can significantly alter the coercive field of the Co/PMN-0.30PT/Co composite at $T=10$ K. In general, the modulation of magnetization by an electric field can be a promising tool for electric-writing in magnetic recording media based on ME materials; ideally, the reversal of the magnetization between two distinct positive and negative saturation states by an electric field. In order to make an estimation of the modulation of magnetization in quantitative terms, Figs. 3.6(a) and 3.6(b) show the previously presented experimental curves and the respective ideal schematic ones, on a comparative basis. Regarding the former, we present the

experimental $m(H_{ex})$ data for which the maximum modulation of H_c^- was observed (i.e. $|\Delta H_c^-| = (|H_c^-(0 \text{ kV/cm}) - H_c^-(+2.5 \text{ kV/cm})| / H_c^-(+2.5 \text{ kV/cm}) \times 100\% = 47\%$), that is between $E_{ex,z} = +2.5 \text{ kV/cm}$ (red colored symbols) and $E_{ex,z} = 0 \text{ kV/cm}$ (blue colored symbols). The inset of Fig. 3.6(a) shows the difference in the magnetization of the two curves, $\Delta m(H_{ex})$, between the respective descending branches; we observe that $\Delta m(H_{ex})$ exhibits minimum for $H_{ex} = -70 \text{ Oe}$, signifying the H_{ex} value where the maximum modulation of magnetization occurs. Accordingly, in Fig. 3.6(a), the magnetization $m_A(-70 \text{ Oe})$ for $E_{ex,z} = +2.5 \text{ kV/cm}$ can be represented by point A and the magnetization $m_{A'}(-70 \text{ Oe})$ for $E_{ex,z} = 0 \text{ kV/cm}$ by point A'; the respective modulation of magnetization, $\Delta m_{AA'}$, is indicated with a green arrow, with its absolute value $|\Delta m_{AA'}(-70 \text{ Oe})| = 1.9 \text{ emu}$. The dotted green line serves as a guide-to-the-eye. The percentage of the modulation $\Delta m_{AA'}(-70 \text{ Oe})$ over the total remanent magnetization, $m_{rem}^{tot}(0)$ (segment BB') is: $(|\Delta m_{AA'}(-70 \text{ Oe})|^{exp} / m_{rem}^{tot}(0)^{exp}) \times 100\% = 35\%$ (the upper indice 'exp' stands for experimental). This percentage modulation indicates that 35% of the magnetic dipoles have switched, from positive to negative magnetization values.

Regarding the ideal case, we represented our experimental data with two schematic $m(H_{ex})$ curves of orthogonal profile, referring to $E_{ex,z} = +2.5 \text{ kV/cm}$ (red colored curve) and $E_{ex,z} = 0$ (blue colored curve). For the sake of comparison, we consider the same saturation magnetization value with the respective experimental ones. Also, we take $H_{ex} = -70 \text{ Oe}$ as the magnetic field where the maximum modulation of magnetization occurs between $E_{ex,z} = +2.5 \text{ kV/cm}$ and $E_{ex,z} = 0 \text{ kV/cm}$ (green dotted line). Accordingly, we can represent the modulation of magnetization from point C ($E_{ex,z} = +2.5 \text{ kV/cm}$) to C' ($E_{ex,z} = 0 \text{ kV/cm}$) with a green arrow. Obviously, in this ideal case, the percentage of the modulation $\Delta m_{CC'}(-70 \text{ Oe})$ over the total remanent magnetization of the square loop, $|m_{rem}^{tot}(0)|^{sch}$ (segment DD'), is $(|\Delta m_{CC'}(-70 \text{ Oe})|^{sch} / m_{rem}^{tot}(0)^{sch}) \times 100\% = 100\%$. Hence, from the comparison of the Figs. 3.6(a) and 3.6(b), we observe that in our case, a considerable amount of magnetic dipoles have been switched under the variation of electric field from $E_{ex,z} = +2.5 \text{ kV/cm}$ to $E_{ex,z} = 0 \text{ kV/cm}$.

Returning back to the realistic samples investigated in this thesis, the Co/PMN-0.30PT/Co can be considered as a ME composite with two different magnetization states that can be utilized as bits for the storage of digital information; the "0" refers to the state with negative magnetization, while the "1" refers to the state of positive magnetization, as shown in Fig. 3.6(a) (from A to A'). Accordingly, these two distinct magnetization states can be recorded by a reading head to survey the information stored in these bits. Relevant results have been reported by Liu et al. [16] showing electric-field control of coercive field, which resulted in magnetization switching in the FeMn/Ni₈₀Fe₂₀/FeGaB/PZN-PT multiferroic composite. In the same spirit, Li et al. [8] presented a magnetic memory cell composed of Fe_{0.93}Ge_{0.07} film grown on a fully poled FE BiScO₃-PbTiO₃ substrate, in which electric field induces two distinct coercive field states as writing bits. Accordingly, the aforementioned results reveal that planar ME structures have great potential in electric-field writing of novel memory devices. In this context, reading heads based on the ME effect in laminated MF composites have also been developed [17] alternatively to the conventional ones based on magnetoresistance effects.

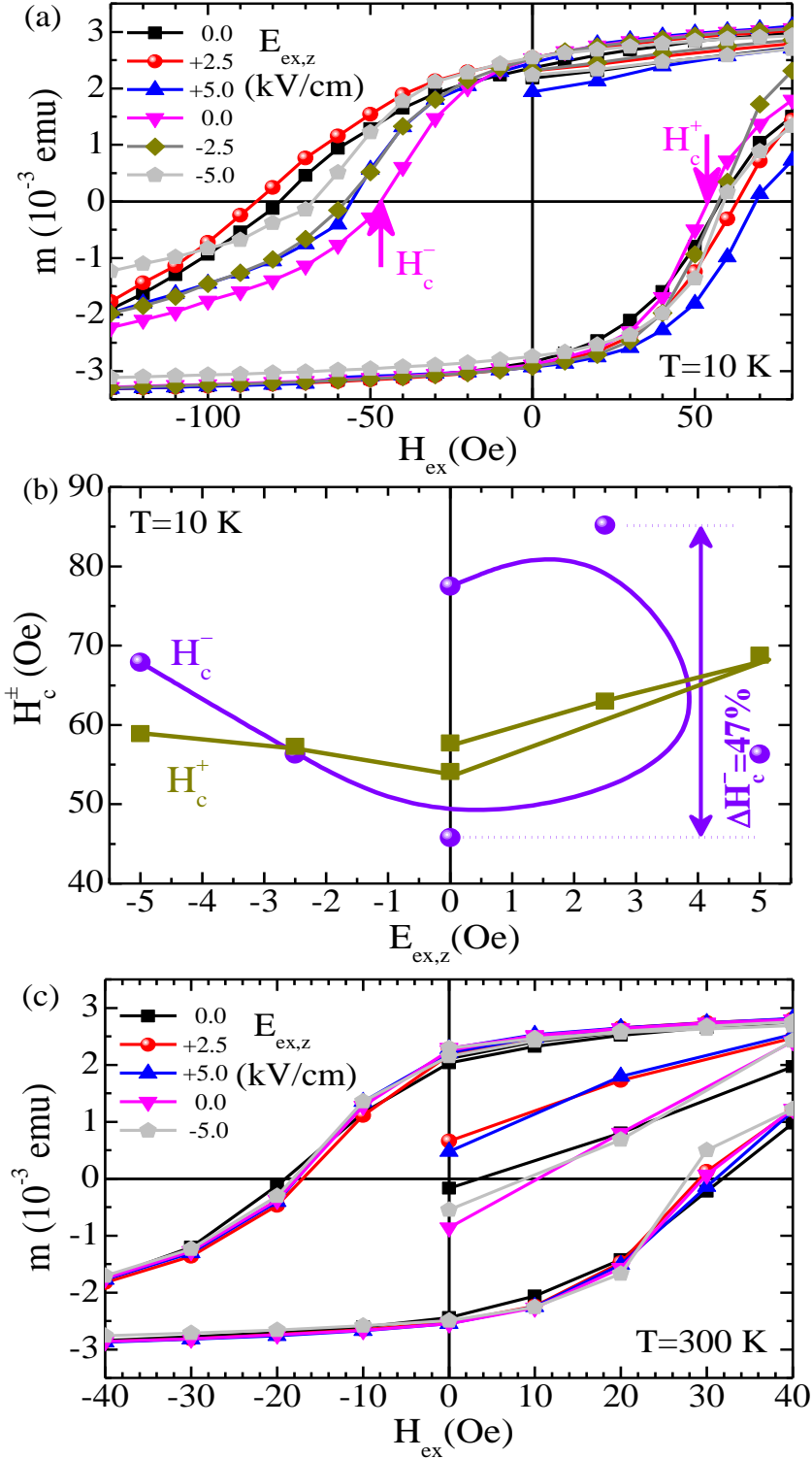


Fig. 3.5: Isothermal $m(H_{ex})$ loops for a Co/PMN-0.30PT/Co composite upon application of various $E_{ex,z}$ values at (a) $T=10$ K and (b) the respective modulation of the magnetization of the descending branch, upon variation of $E_{ex,z}$. (c) $m(H_{ex})$ loops at $T=300$ K. In both cases ($T=10$ K and $T=300$ K) the loops are focused in the low H_{ex} field regime.

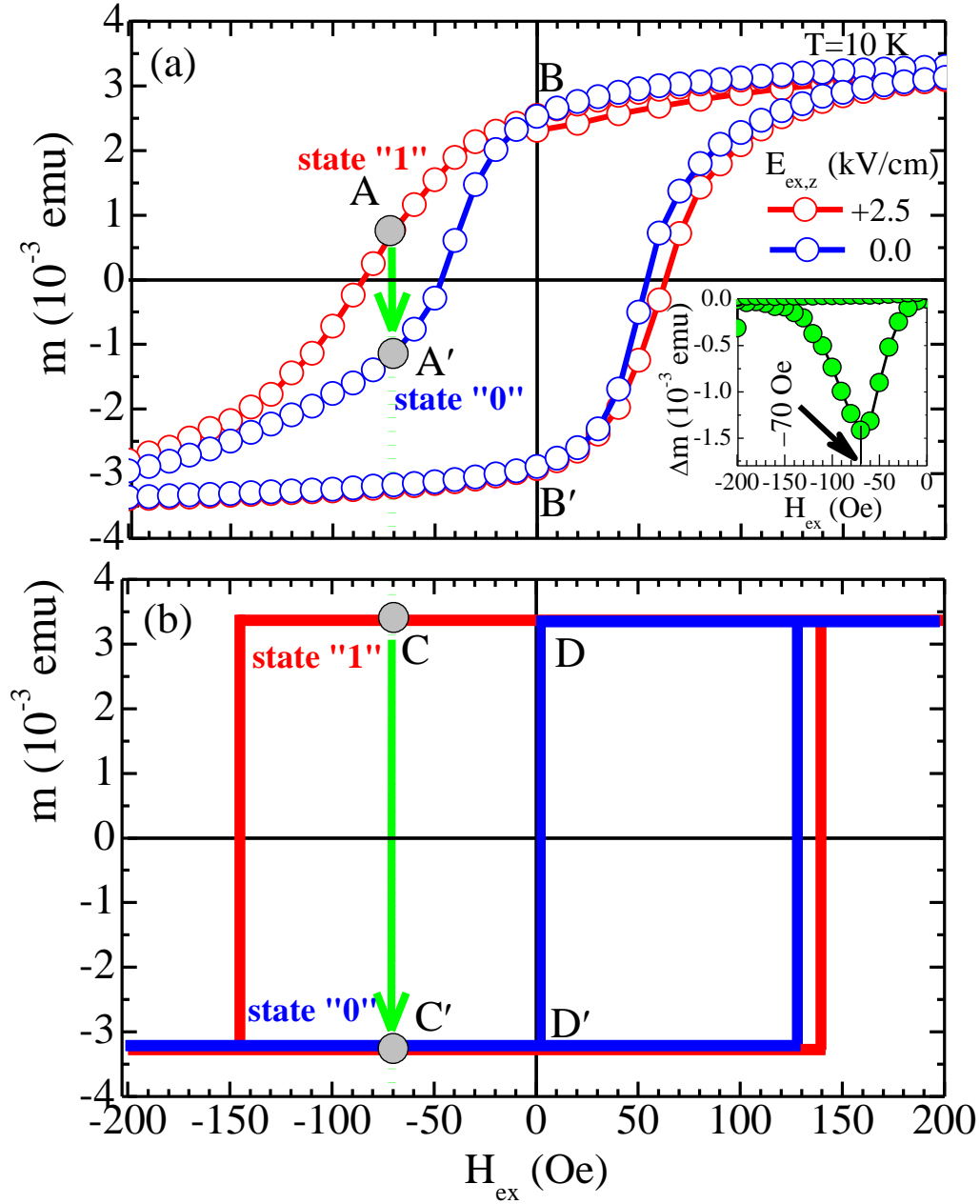


Fig. 3.6: (a) Isothermal $m(H_{ex})$ curves for a Co/PMN-0.30PT/Co composite upon application of $E_{ex,z} = +2.5$ kV/cm (red colored symbols) and $E_{ex,z} = 0$ kV/cm (blue colored symbols) at $T = 10$ K; the inset shows the difference in magnetization, $\Delta m(H_{ex})$, between the negative branches with minimum at $H_{ex} = -70$ Oe. The points A and A' correspond to $m_A(-70 \text{ Oe})$ for $E_{ex,z} = +2.5$ kV/cm and to $m_{A'}(-70 \text{ Oe})$ for $E_{ex,z} = 0$ kV/cm, respectively; the green arrow denotes the switching of magnetization between A and A'. Points B and B' correspond to the positive and negative remanent magnetization of the curves. (b) Schematic counterparts of the $m(H_{ex})$ curves of panel (a). The solid red and blue schematic curves correspond to $E_{ex,z} = +2.5$ kV/cm and $E_{ex,z} = 0$, respectively, showing the extreme cases of the highest and the lowest H_c . The points C and C' correspond to $m_C(-70 \text{ Oe})$ for $E_{ex,z} = +2.5$ kV/cm and to $m_{C'}(-70 \text{ Oe})$ for $E_{ex,z} = 0$ kV/cm, respectively; the green arrow denotes the switching of magnetization between C and C'. Points D and D' correspond to the positive and negative remanent magnetization of the tetragonal loop (the dashed lines in both panels serve as guide-to-the-eye).

II. $m_{\text{rem}}(T)$ measurements under $E_{\text{ex},z}$ application

Here, we focus our study on the investigation of the stability of the remanent magnetization, m_{rem} , referring to the FM Co outer layers upon $E_{\text{ex},z}$ application to the Co/PMN-0.30PT/Co composite. Regarding the experimental process, at first, the remanent magnetic state was prepared according to Measurement Protocol (II) (see subchapter 3.1.1, above). Subsequently, m_{rem} was measured upon varying the temperature in the whole range from $T=300$ K down to $T=10$ K, at a specific value of $E_{\text{ex},z}$. The process was repeatedly executed for different $E_{\text{ex},z}$ values.

Figs. 3.7(a)-(c) show typical results for $E_{\text{ex},z}=0$ kV/cm, $E_{\text{ex},z}=\pm 2.5$ kV/cm and $E_{\text{ex},z}=\pm 5.0$ kV/cm, respectively. From these data, we can clearly observe abrupt changes of the recorded $m_{\text{rem}}(T)$, in the form of distinct suppression events, or else $m_{\text{rem}}(T)$ degradation; we term these events magnetic instabilities (MIs). In fact, MIs of different origin are also met in other areas of magnetism, such as Barkhausen effect [18-22] and superconductivity, such as flux-lines avalanche effect [23-28]. Regarding the former [18], MIs mainly occur during reversal of the magnetization and are related to a sequence of distinct jumps, sometimes accompanied by crackling noise, due to the interaction between MDs and MDWs with quench and thermal disorder. The quench disorder refers to structural disorder, either of point (e.g. atomic vacancies) or correlated (e.g. dislocations) nature, while the thermal disorder refers to the thermal energy. The competition between quench and thermal disorder can lead to nucleation/reversal of MDs and depinning of MDWs that are subsequently free to move [19-22]. Notably, the Barkhausen effect has great significance regarding technological applications, since it is detrimental to the stability of magnetic data storage devices. In addition, the flux-lines avalanche effect [23] is associated with the interplay of three energy scales, the interaction energy between flux lines, the pinning energy of flux lines with quench disorder, and the thermal disorder [26-29]. More specifically, upon the entrance of flux lines in a superconductor they self-assemble in a critical state so that the current reaches a critical value, just before movement of flux lines occurs [30,31]. An avalanche event is observed when thermal activation promotes overcritical conditions and causes abrupt movement of bundles of flux lines that ultimately appear in the form of magnetization jumps [26-28]. In our case, the observed MIs are exclusively motivated by $E_{\text{ex},z}$, as we show in Figs. 3.7(a)-(c); in this context, we introduce the term electric-field induced MIs (EMIs).

Specifically, the sequence of the measurements was realized upon varying electric field as following: $E_{\text{ex},z}=0$ kV/cm (1st) \rightarrow $+2.5$ kV/cm \rightarrow $+5$ kV/cm \rightarrow 0 kV/cm (2nd) \rightarrow -2.5 kV/cm \rightarrow -5 kV/cm. From Fig. 3.7(a) it is clear that, for $E_{\text{ex},z}=0$ kV/cm, EMIs do not exist, since $m_{\text{rem}}(T)$ increases gradually and smoothly upon decreasing temperature from $T=300$ K to $T=10$ K. On the other hand, from Figs. 3.7(b) and 3.7(c) it is evident that for $E_{\text{ex},z}\neq 0$ kV/cm, EMIs appear and they are enhanced with increasing $E_{\text{ex},z}$. The enhancement is demonstrated by two facts: first, upon increasing $|E_{\text{ex},z}|$ the temperature range where EMIs occur gets wider, and second the overall degradation of $m_{\text{rem}}(T)$ increases.

In quantitative terms, the degradation of m_{rem} for $E_{\text{ex},z}=+2.5$ kV/cm (Fig. 3.7(b)) is expressed as an intense EMI at $T=200$ K, that causes a percentage degradation on the order of 2.5%. In addition, for $E_{\text{ex},z}=+5.0$ kV/cm (Fig. 3.7(c)), m_{rem} degradation is manifested as the cumulative action of many EMIs in the temperature range 170 K $< T < 300$ K, which produces a much higher

percentage degradation, on the order of 16.4%. Regarding the EMIs for the respective negative $E_{ex,z}$ values ($E_{ex,z}=-2.5$ kV/cm and $E_{ex,z}=-5.0$ kV/cm), we observe that they are smaller in magnitude, but, notably, their cessation occurs at the same temperature with their counterpart curve for positive $E_{ex,z}$. At $T=170$ K, we can see that the EMIs corresponding to the maximum applied $E_{ex,z}=\pm 5$ kV/cm ultimately cease; for this reason, we define this characteristic temperature as $T_{ces}=170$ K.

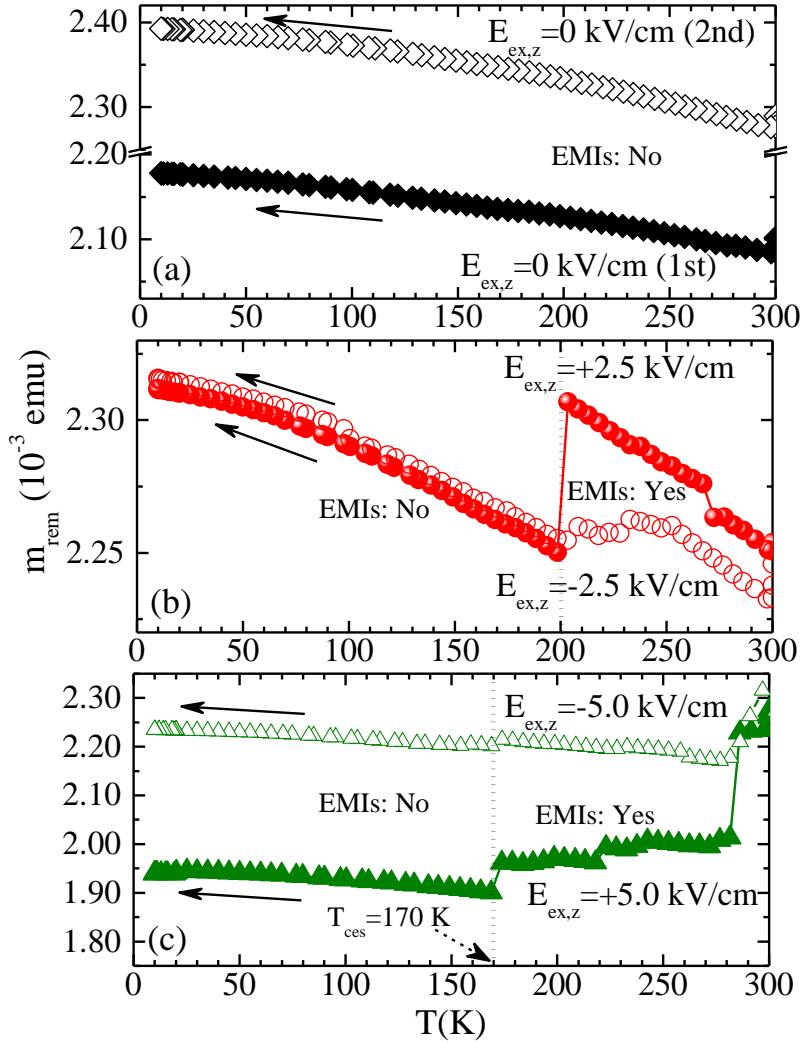


Fig. 3.7: Isofield ($H_{ex}=0$) measurements referring to the evolution of the remanent ferromagnetic state, $m_{rem}(T)$, of a Co/PMN-0.30PT/Co composite upon variation of temperature from $T=300$ K to $T=10$ K for (a) $E_{ex,z}=0$ kV/cm, (b) $E_{ex,z}=\pm 2.5$ kV/cm and (c) $E_{ex,z}=\pm 5.0$ kV/cm. The sequence of measurements was $E_{ex,z}=0$ kV/cm (1st) \rightarrow +2.5 kV/cm \rightarrow +5 kV/cm \rightarrow 0 kV/cm (2nd) \rightarrow -2.5 kV/cm \rightarrow -5 kV/cm. In panels (b) and (c) electric-field induced magnetic instabilities (EMIs) are observed in the high temperature regime that is delimited by the vertical dotted lines. The EMIs are ultimately ceased below temperature $T_{ces}=170$ K.

The occurrence of EMIs only at the high temperature regime signifies that they are thermally activated. This fact evidences that there is an interplay between the thermal activation and pinning processes. Although, as clearly deduced from a direct comparison between Figs.

3.7(a)-(c), the thermal energy alone, is not capable to surpass the barriers that delimit metastable states of m_{rem} and thus to motivate MIs in the absence of $E_{\text{ex,z}}$.

Except for the magnetic properties of the Co/PMN-0.30PT/Co composite, it is determinant that we also consider its PE properties in the same temperature range. Recent studies [32-34] have investigated the properties of PMN-xPT crystals in the whole temperature range from room temperature down to cryogenic conditions. Accordingly, they report that all of the important PE characteristics, such as the relative dielectric constant K , elastic compliance coefficient s_{ij} , PE coefficients d_{ij} , exhibit a bimodal behaviour between the high and low temperature regimes with an inflection regime, $T_{\text{inf}} \approx 170$ K [34], as for example shown in Fig. 3.8 below, for the PE coefficient d_{31} of a PMN-0.33PT crystal (reproduced from [34]). We observe that, as temperature decreases from $T=300$ K, the PE coefficient $d_{31}(T)$ exhibits power-law-like decrease in the two temperature regimes (high and low), with a plateau at $T_{\text{inf}} \approx 170$ K.

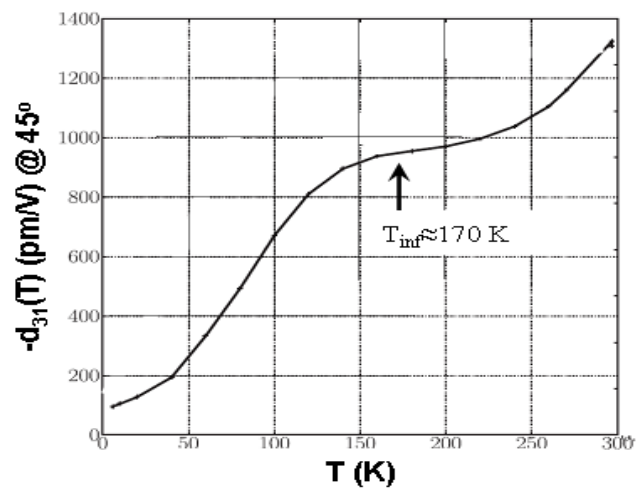


Fig. 3.8: Temperature evolution of the transverse strain coefficient d_{31} for a PMN-xPT crystal with $x=0.33$ (reproduced from [34]).

By comparing the $m_{\text{rem}}(T)$ data of Figs. 3.7(a)-(c), referring to a Co/PMN-0.30PT/Co composite, with the $d_{31}(T)$ curve of Fig. 3.8 of the literature [34], referring to a PMN-0.33PT crystal (i.e. composition very similar with the PE single crystal that we employed), we deduce that $T_{\text{ces}} \approx T_{\text{inf}}$. Hence, we can plausibly assume that there is correlation of the underlying mechanisms that cause the cessation of EMIs, Figs. 3.7(a)-(c), and the decrease of d_{31} (Fig. 3.8), as temperature decreases below T_{ces} and T_{inf} , respectively. Regarding the decrease of d_{31} and the formation of a plateau below T_{inf} (Fig. 3.8), it was attributed to the establishment of intense collective pinning of FE domain walls by structural disorder (i.e. point defects) that hampers their motion [32-35]. In this spirit, we can fairly assume that in the Co/PMN-xPT/Co composite, there is a coupling between the FE domains of the PMN-0.30PT crystal and the FM domains of the Co outer layers so that the latter are forced to follow the dynamics of the former. Accordingly, the instabilities of FM domains (that is EMIs) are observed in the high temperature regime since they are motivated by the reconfiguration of FE domains (due to the relatively easy motion of walls). In turn, the EMIs cease below T_{ces} since FE domain walls are

relatively quenched below T_{inf} , once collective pinning by structural disorder dominates over thermal activation.

These results concerning the stability of the remanent state, are of great importance for candidate applications of planar PE/FM MF composites. In general, the manipulation of the remanent FM state by an external electric field has been widely reported [38-40], since it is a parameter that can be effectively modulated. To clarify this practice, we stress the following; in the subchapter 3.2.1.I, it was discussed that we can establish two distinct H_c states, i.e. the bit states “0” and “1”, by modulating E_{ex} . Similarly, these bit states can be physically represented by an m_{rem} state oriented along two predetermined opposite directions, out-of-plane or in-plane. Accordingly, the reversal of m_{rem} by using E_{ex} is a bit write in ME memory devices; this practice minimizes energy consumption and prohibits thermal runaway. Hence, the study of vulnerability of m_{rem} to degradation close to room temperature is crucial; as observed in our case, the appearance of EMIs is a factor that could hamper the utilization of the respective MF composite in applications [41].

The experimental data presented in the subchapters 3.1.2.I and 3.1.2.II clearly reveal the existence of ME coupling between the FM and the FE constituents of the Co/PMN-0.30PT/Co composite. Regarding the underlying mechanism of this coupling, we suggest that it is the strain transfer, as reported in many ME composites with planar structures [36,37]; the contact of the piezoelectric PMN-0.30PT single crystals with the magnetostrictive Co thin films gives rise to ME coupling, due to the converse PE and direct magnetostrictive effects, respectively.

The reproducibility of the results presented in the subchapters 3.1.2 and 3.1.3, above, was confirmed by employing three different Co/PMN-0.30/PT/Co composite samples (see samples ‘S.1.1’-‘S.1.3’ in Table 2.1, at the end of chapter 2).

3.2 Fe₃O₄ nanoparticles embedded in a PZT matrix

Bulk composites based on PE and FM oxides are hybrid systems with simple and low cost fabrication, in which the ME coupling usually takes place via strain at the interfaces of the respective phases [42,43]. The PE $\text{Pb}(\text{Zr}_x\text{Ti}_{1-x})\text{O}_3$ is a well-studied oxide compound family that is commonly used in ME composites thanks to its noticeable properties, especially in the composition with $x=0.52$, $\text{Pb}(\text{Zr}_{0.52}\text{Ti}_{0.48})\text{O}_3$ (PZT). For this reason, many studies concerning ME composites have been conducted using bulk PZT as FE constituent, combined with a variety of ferro/ferri-magnetic alloys or oxides [44-48] for potential applications in various fields including the data storage applications [49]. Among other FM oxides, magnetite, Fe_3O_4 , is one of the most studied thanks to its easy preparation, high magnetization and fair magnetostriction. To our knowledge, there have not been reports on bulk composite ME system of Fe_3O_4 NPs embedded in a PZT matrix, particularly concerning its behavior under external fields (electric or magnetic). Accordingly, we were motivated to study this composite system; in the subchapter 3.2.1 we survey its characteristic physical properties (electric, crystallographic, magnetic, ferroelectric and microstructural/compositional) while, in the subchapters 3.2.2 and 3.2.3, we investigate the control of its FM/PE properties under the application of $E_{\text{ex}}/H_{\text{ex}}$, respectively. In general, all measurements were performed at room temperature, and refer to sintered samples (sintering conditions: $T=1000$ °C, for $t=2$ h in air);

in case non-sintered samples (i.e. starting materials) were utilized, it will be clarified in the respective part of the text. Also, in this study, the external electric field is always applied along the thickness of the sample (i.e. out-of-plane, let us say z-axis), denoted by $E_{ex,z}$. Regarding the external magnetic field, when applied out-of-plane, it is denoted by $H_{ex,z}$, while when applied along the sample surface (i.e. in-plane), it is simply denoted by H_{ex} .

3.2.1 Characteristic physical properties

I. Electrical resistance and current-voltage characteristics

Electrical resistance, R , and electric current-voltage, I-V (or else electric field) characteristics were preliminary employed to the complete series of PZT- x Fe₃O₄ samples ($x=0-50\%$ w/w), in order to choose the appropriate insulating sample for the subsequent, main study of the Thesis, since the measurements are performed under the application of an $E_{ex,z}$ (see subchapters 3.2.2 and 3.2.3). Accordingly, the most basic criterion is that the sample should remain strongly insulating for a reasonable range of electric field values.

Fig. 3.9(a) presents the R of the PZT- x Fe₃O₄ samples at room temperature, as a function of the weight percentage concentration of Fe₃O₄ (x). We observe that generally, R values range within $10^5-10^9 \Omega$ and decrease with increasing x ; this is expected since, at room temperature, PZT exhibits high resistivity ($\sim 10^{10}-10^{12}$ Ohmcm), while Fe₃O₄ exhibits moderate resistivity ($\sim 10^{-2}-10^{-3}$ Ohm cm) [50,51]. The addition of Fe₃O₄ NPs can be clearly observed in the color of the PZT- x Fe₃O₄ composites, as representatively shown in Fig. 3.9(a) for $x=5\%$, 20% and 50%. The former mostly maintains the color of PZT, since the Fe₃O₄ concentration is low ($x=5\%$), while the latter ($x=50\%$) has a darker color, close that of Fe₃O₄ starting powder (see also Fig. 2.18 of the subchapter 2.4.2). The behavior of $R(x)$ is non-monotonic, exhibiting a drastic decrease for $x=20\%$, while for x up to 50%, $R(x)$ attains a more conventional monotonic behavior. As a consequence, for composites with Fe₃O₄ concentration $x>10\%$, the leakage current is noticeable and causes drastic limitation to the applied $E_{ex,z}$ range. This can also be observed in Fig. 3.9(b), where the leakage current, I_l , is shown for the respective Fe₃O₄ concentrations as function of $E_{ex,z}$. From this Fig. we can clearly observe that the samples with $x=1\%$, 3%, 5% and $x=10\%$ remain insulating. On the other hand, the samples with $x=20\%$ and $x=50\%$ exhibit noticeable I_l for comparatively much lower values of $E_{ex,z}$, while the sample with $x=30\%$ has an intermediate I_l , which still does not allow $E_{ex,z}$ application.

Regarding the drastic decrease of $R(x)$ at $x=20\%$ we attribute it to a phase separation-like behavior. Specifically, for this specific value, $x=20\%$, the iron oxide NPs are not uniformly distributed in the PZT matrix, Accordingly, the phase separated composite with nominal global content of $x=20\%$ hosts areas with a significant distribution of the true local content in iron oxide NPs. Inevitably, this is accompanied by a distribution in the value of the local electrical resistance. Since the *electric* current prefers to flow through pathways of higher iron oxide local content (that exhibit significantly lower local R), the global R of the sample with $x=20\%$ should decrease as well.

Therefore, according to the results of Figs. 3.9(a) and 3.9(b), the samples with $x=1\%$, 3%, 5% and 10% are candidates for further investigation, since they are characterized by high

electrical resistance, $R > 200 \text{ M}\Omega$, low leakage current and thus, remain insulating under $E_{ex,z}$ application up to $E_{ex,z} = \pm 10 \text{ kV/cm}$. Hence, it is necessary to inspect the magnetic properties of the samples with $x=1\%$, 3% , 5% and 10% in order to select the most appropriate Fe_3O_4 concentration for further investigation.

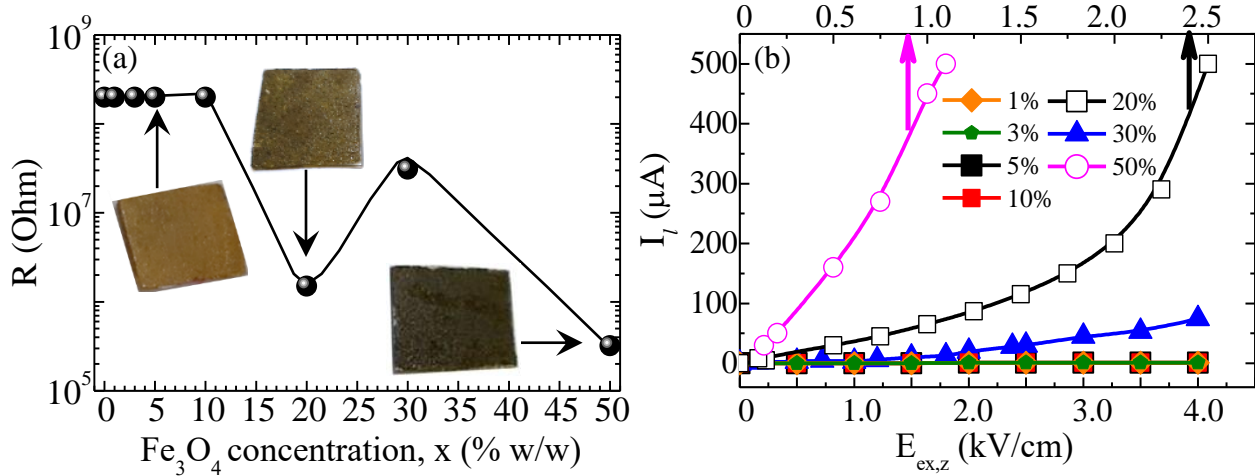


Fig. 3.9: (a) Electrical resistance, R , as a function of Fe_3O_4 concentration, x (% w/w) for a series of bulk composite $\text{PZT-xFe}_3\text{O}_4$ samples with $x=1\%$, 3% , 5% , 10% , 20% , 30% , 50% . (b) Electric leakage current, I_l , under the application of an out-of-plane electric field, $E_{ex,z}$, for $\text{PZT-xFe}_3\text{O}_4$ samples, with $x=1\%$, 3% , 5% , 10% , 20% , 30% , 50% . The bottom/top horizontal axes correspond to the data of $x=5\%$, 10% , 30% / $x=20\%$, 50% samples.

II. Magnetization data

We recorded the magnetization as a function of the magnetic field, $m(H_{ex})$, under variation of H_{ex} within -5 kOe and $+5 \text{ kOe}$ for the samples with $x=1\%$, 3% , 5% and 10% , as shown in Fig. 3.10(a). Here, it should be noted that what we directly measure from the SQUID magnetometer is the magnetic moment (in emu). Nevertheless, in a less strict sense, we will refer to the measured magnetic moment as ‘magnetization’, since all samples studied here have the same volume. In addition, the data in Figs. 3.10(a) are calibrated per unit mass (emu/g).

As expected, the samples with the lowest Fe_3O_4 concentration, $x=1\%$ and $x=3\%$, display the lowest magnetization values at $H_{ex}=5 \text{ kOe}$, that is $m(5 \text{ kOe})=9 \text{ emu/g}$ and 17 emu/g , respectively. In turn, the samples with $x=5\%$ and $x=10\%$ exhibit the highest and very similar values, $m(5 \text{ kOe})=24 \text{ emu/g}$ and 27 emu/g at $H_{ex}=5 \text{ kOe}$, respectively. Accordingly, among the samples with $x=5\%$ and $x=10\%$, we chose to employ the former for further investigation under $E_{ex,z}$. The reason is twofold; first, we aim to study samples that are highly insulating (the lowest the Fe_3O_4 concentration, the most insulating the sample is), and second, we want to avoid any possible phase segregation caused by the Fe_3O_4 NPs (as in the case of $x=20\%$), ensuring the best homogeneity in the distribution of NPs in the PE matrix.

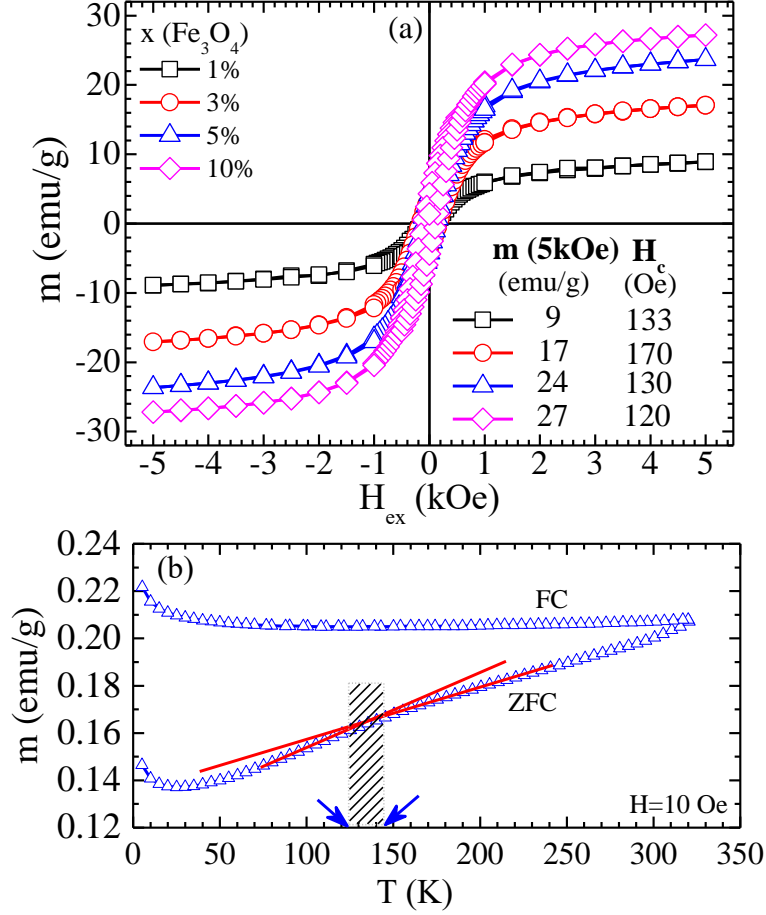


Fig. 3.10: (a) Isothermal $m(H_{ex})$ loops for the PZT- $x\text{Fe}_3\text{O}_4$ samples with $x=1\%$, 3% , 5% and 10% . The respective saturation magnetization, m_{sat} , at $H_{ex}=5$ kOe and the coercive field, H_c , values are also shown in the figure. (b) Isofield $m(T)$ curve for the PZT- 5% sample, at $H_{ex}=10$ Oe. A broad ‘knee’ is denoted by the intersection of the two red solid lines within the temperature range $T=125$ K- 145 K, delimited by the grey patterned rectangle; this feature could be associated with the Verwey transition of Fe_3O_4 nanoparticles.

For reasons of completeness, we also examined the isofield $m(T)$ curve for the PZT- $5\%\text{Fe}_3\text{O}_4$ sample at $H_{ex}=10$ Oe, in the temperature range from 5 K to 320 K, as shown in Fig. 3.10(b). We observe that the zero-field cooling (ZFC) branch is characterized by smoothly increasing magnetization, with a rather broad ‘knee’ around $T=130$ K, denoted by the dotted blue line at the intersection of the two red solid lines; we assume that this feature is associated with the characteristic Verwey transition of the Fe_3O_4 NPs. In the field-cooling (FC) branch the magnetization remains almost constant with a slight increase only below $T=50$ K.

Accordingly, the experimental results from this point onwards are focused on the PZT- $5\%\text{Fe}_3\text{O}_4$ composite and its parent constituents, namely PZT and Fe_3O_4 . Therefore, in the Fig. 3.11 below we present $m(H_{ex})$ data for the sintered Fe_3O_4 NPs, PZT, and the final PZT- $5\%\text{Fe}_3\text{O}_4$ composites. Also, for reasons of comparison, we show the $m(H_{ex})$ data for the non-sintered Fe_3O_4 NPs (starting material: star. mat.). This combined presentation aims to help us obtain information about the magnetic properties of the final PZT- $5\%\text{Fe}_3\text{O}_4$ composite.

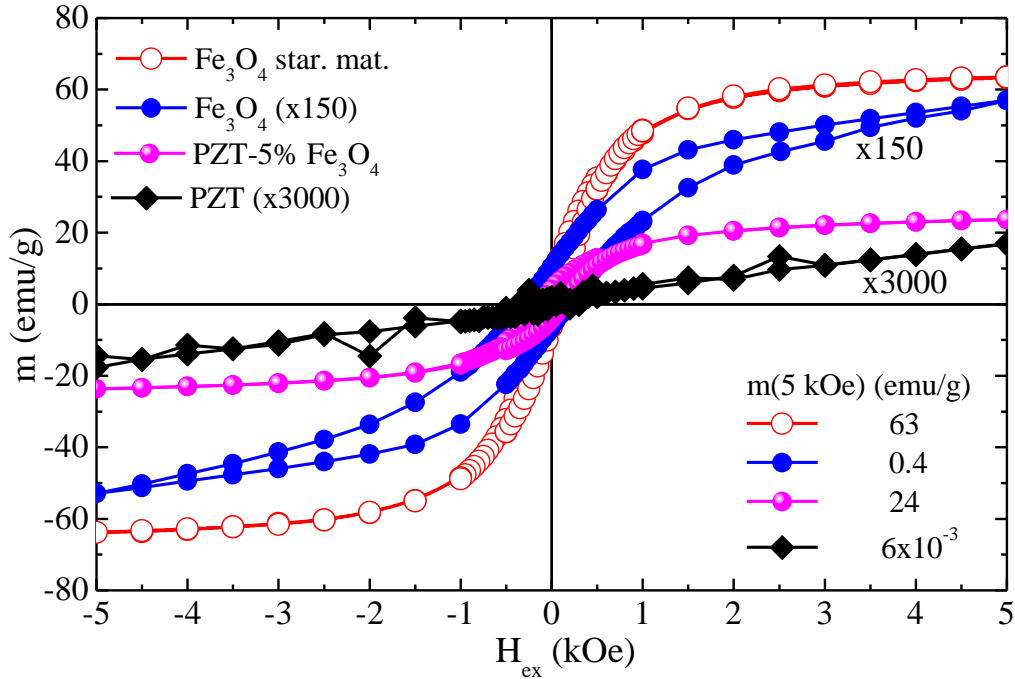


Fig. 3.11: Magnetization curves, $m(H_{ex})$, for the non-sintered (starting material) Fe_3O_4 nanoparticles, NPs, and for the sintered Fe_3O_4 NPs, PZT, and PZT-5% Fe_3O_4 samples upon variation of an external magnetic field H_{ex} in the range $-5 \text{ kOe} \leq H_{ex} \leq +5 \text{ kOe}$. We note that the data of sintered Fe_3O_4 NPs and PZT is multiplied by a factor of 150 and 3000, respectively, for the sake of presentation. The magnetization values that were obtained at the maximum H_{ex} , $m(5 \text{ kOe})$, are also presented for each sample: 63 emu/g for non-sintered Fe_3O_4 NPs, 0.4 emu/g for sintered Fe_3O_4 NPs, 6×10^{-3} emu/g for sintered PZT, and 24 emu/g for the sintered PZT-5% Fe_3O_4 .

Thus, the magnetization values obtained for the maximum magnetic field, $H_{ex}=5 \text{ kOe}$, are $m(5 \text{ kOe})=0.4 \text{ emu/g}$, $6 \times 10^{-3} \text{ emu/g}$, 24 emu/g, and 63 emu/g, respectively. Accordingly, we notice that the non-sintered Fe_3O_4 NPs have high magnetization value, 63 emu/g, in accordance with respective values of the literature. Regarding the sintered Fe_3O_4 NPs in free form (not embedded in a PZT matrix), we observe that they exhibit extremely lower magnetization value, 0.4 emu/g at $H_{ex}=5 \text{ kOe}$. This magnetization value is characteristic of hematite ($\alpha\text{-Fe}_2\text{O}_3$) [52] and it is attributed to the complete oxidation of Fe_3O_4 to $\alpha\text{-Fe}_2\text{O}_3$. This is also reflected to the color of the respective powders of Fe_3O_4 before and after sintering, shown in Figs. 2.17(a.ii) (black colored powder) and 2.17(b.vii) (reddish-brown colored powder), respectively, in the subchapter 2.4.2. Referring to sintered PZT, it exhibits negligible magnetization, $6 \times 10^{-3} \text{ emu/g}$, as expected. Hence, from the aforementioned data we deduce that, for the sintered PZT-5% Fe_3O_4 composite, the obtained magnetization value at $H_{ex}=5 \text{ kOe}$, 24 emu/g, originates from Fe_3O_4 NPs that have not oxidized to $\alpha\text{-Fe}_2\text{O}_3$; we stress that a percentage of the respective NPs is protected by the surrounding PZT matrix. Specifically, taken into account the magnetization values $m(5 \text{ kOe})$, we can estimate that 38% of the NPs remain in the Fe_3O_4 form after sintering.

III. Crystallographic data

In Figs. 3.12(a)-(c) XRD spectra are shown for the PZT, Fe_3O_4 and the PZT-5% Fe_3O_4 composites, in the 2θ range 20° - 90° . This combined presentation aims to help us obtain information about the crystallographic structure of the final PZT-5% Fe_3O_4 composite.

Specifically, these data reveal that the crystallographic phases that coexist in the PZT-5% Fe_3O_4 composite are referring to PZT, Fe_3O_4 and α - Fe_2O_3 (hematite). Similarly to SQUID data, the XRD data in Fig. 3.12 show the inevitable formation of α - Fe_2O_3 , since Fe_3O_4 is partially oxidized to α - Fe_2O_3 when sintered in air. Interestingly, we observe that no further byproducts have been formed. Regarding the peak splitting observed in the vicinity of $2\theta=45^\circ$, 50.5° , 56° , 65.5° and 74° , it is attributed to the coexistence of the tetragonal and rhombohedral PZT phases; schematic illustrations of the respective phases are shown in panels (d.i) and (d.ii). As evidenced by the combined XRD data, this feature is motivated and/or promoted by the existence of $\text{Fe}_3\text{O}_4/\alpha$ - Fe_2O_3 NPs. Notably, it has been reported that for stoichiometry inside the MPB (i.e. $\text{Pb}(\text{Zr}_{0.52}\text{Ti}_{0.48})\text{O}_3$) the crystallographic structure is vulnerable to transformations induced by a wide range of external parameters (e.g. pressure, strain, temperature) [21,22,53]. Accordingly, the introduction of $\text{Fe}_3\text{O}_4/\alpha$ - Fe_2O_3 NPs in the PZT matrix can probably advance the partial transformation of the latter into the tetragonal phase; this can be ascribed to mechanical strain generated by the mismatch of the respective lattice constants. These results are in nice qualitative agreement with the SQUID results presented above (Fig. 3.11) and they reveal that the former PZT-5% Fe_3O_4 system evolves to a PZT-5%($\text{Fe}_3\text{O}_4/\alpha$ - Fe_2O_3) composite; in the rest of the Thesis the compounds will be simply denoted PZT-5% Fe_3O_4 for the sake of clarity.

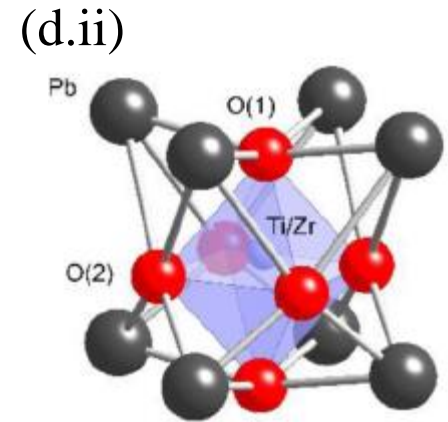
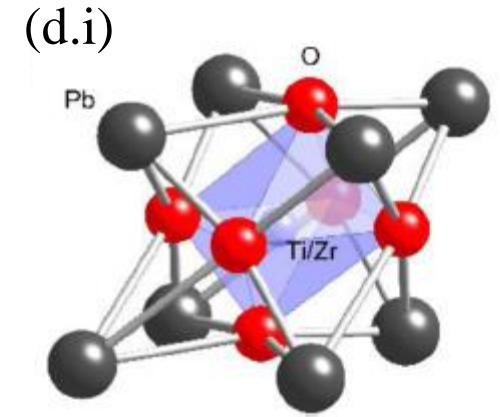
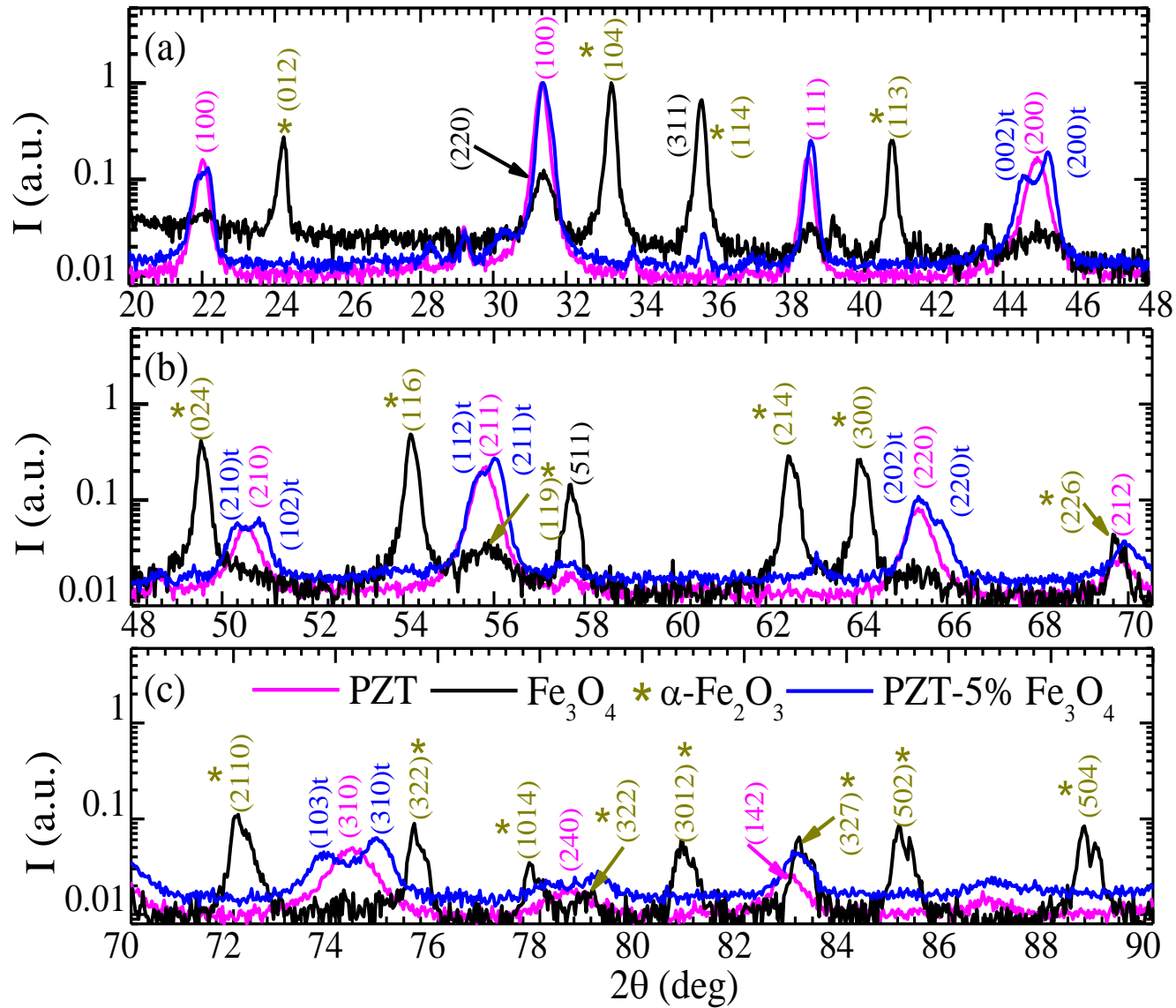


Fig. 3.12: X-ray diffraction, XRD, data of PZT, Fe_3O_4 and PZT-5% Fe_3O_4 , in the 2θ range (a) 20° - 48° and (b) 48° - 70° (c) 70° - 90° . The new peaks that arise indicate the formation of hematite, $\alpha\text{-Fe}_2\text{O}_3$, driven from the oxidation of the magnetite, Fe_3O_4 , NPs. The broadened/splitted peaks that are assigned at $2\theta=45^\circ$, 50.5° , 56° , 65.5° and 74° evidences that PZT accommodates both the rhombohedral and the tetragonal phases. (d.i), (d.ii) Schematic illustrations of (d.i) rhombohedral and (d.ii) tetragonal phases of PZT [54].

IV. Polarization and out-of-plane strain data

Fig. 3.13 presents the polarization, $P(E_{ex,z})$ and out-of-plane strain, $S_{zz}(E_{ex,z})$ data in Figs. 3.13(a.i), 3.13(b.i) and Figs. 3.13(a.ii), 3.13(b.ii), respectively, as obtained by global techniques that were employed by our collaborator and member of the Jury, Prof. S. J. Zhang. The data in panels (a.i), (a.ii) correspond to a plain PZT sample, while the data in panels (b.i) and (b.ii) correspond to a composite PZT-5%Fe₃O₄ sample (see samples ‘S.5.1’ and ‘S.5.2’, respectively, in Table 2.1, at the end of chapter 2). We note that all the panels are on the same scale horizontally and vertically so that the respective data can be directly compared.

Specifically, for PZT, $P(E_{ex,z})$ is shown in Fig. 3.13(a.i) upon varying $E_{ex,z}$ within $-15 \text{ kV/cm} \leq E_{ex,z} \leq +15 \text{ kV/cm}$ and $-20 \text{ kV/cm} \leq E_{ex,z} \leq +20 \text{ kV/cm}$. Clearly, $P(E_{ex,z})$ exhibits the typical hysteresis loop of FE materials, with coercive field $E_c = \pm 6 \text{ kV/cm}$. It should be noted that generally E_c depends on the $E_{ex,z}$ applied. The corresponding $S_{zz}(E_{ex,z})$ curves are shown in Fig. 3.13(b.i), exhibiting the typical hysteretic ‘butterfly’ behavior, with $E_{nuc} = \pm 5.5 \text{ kV/cm}$. We observe that in the case of PZT $E_{nuc} \approx E_c$.

For PZT-5%Fe₃O₄, $P(E_{ex,z})$ is shown in Fig. 3.13(b.i) upon varying $E_{ex,z}$ within $-15 \text{ kV/cm} \leq E_{ex,z} \leq +15 \text{ kV/cm}$ and $-20 \text{ kV/cm} \leq E_{ex,z} \leq +20 \text{ kV/cm}$. We observe that the respective curves also show hysteretic behavior. Compared to PZT, they are broader, with lower saturation polarization and they are more slanted. Accordingly, the respective coercive field $E_c = \pm 8-10 \text{ kV/cm}$, is higher compared to PZT. Regarding the corresponding $S_{zz}(E_{ex,z})$ curves, shown in Fig. 3.13(b.ii), we observe that they also exhibit butterfly behavior; compared to the ones of PZT -which are symmetric- these curves display some asymmetry between their positive and negative branches.

Based on the aforementioned results, the comparison of $P(E_{ex,z})$ and $S_{zz}(E_{ex,z})$ curves of the plain PZT and the composite PZT-5%Fe₃O₄ reveals the following: the introduction of the FM Fe₃O₄ NPs in the PE PZT matrix causes the former to act as structural disorder that pins the FE domain walls of the latter efficiently, a phenomenon motivated and/or promoted by the similar sizes of the FE domains of PZT and the FM NPs of Fe₃O₄ (50-100 nm) [55-57].

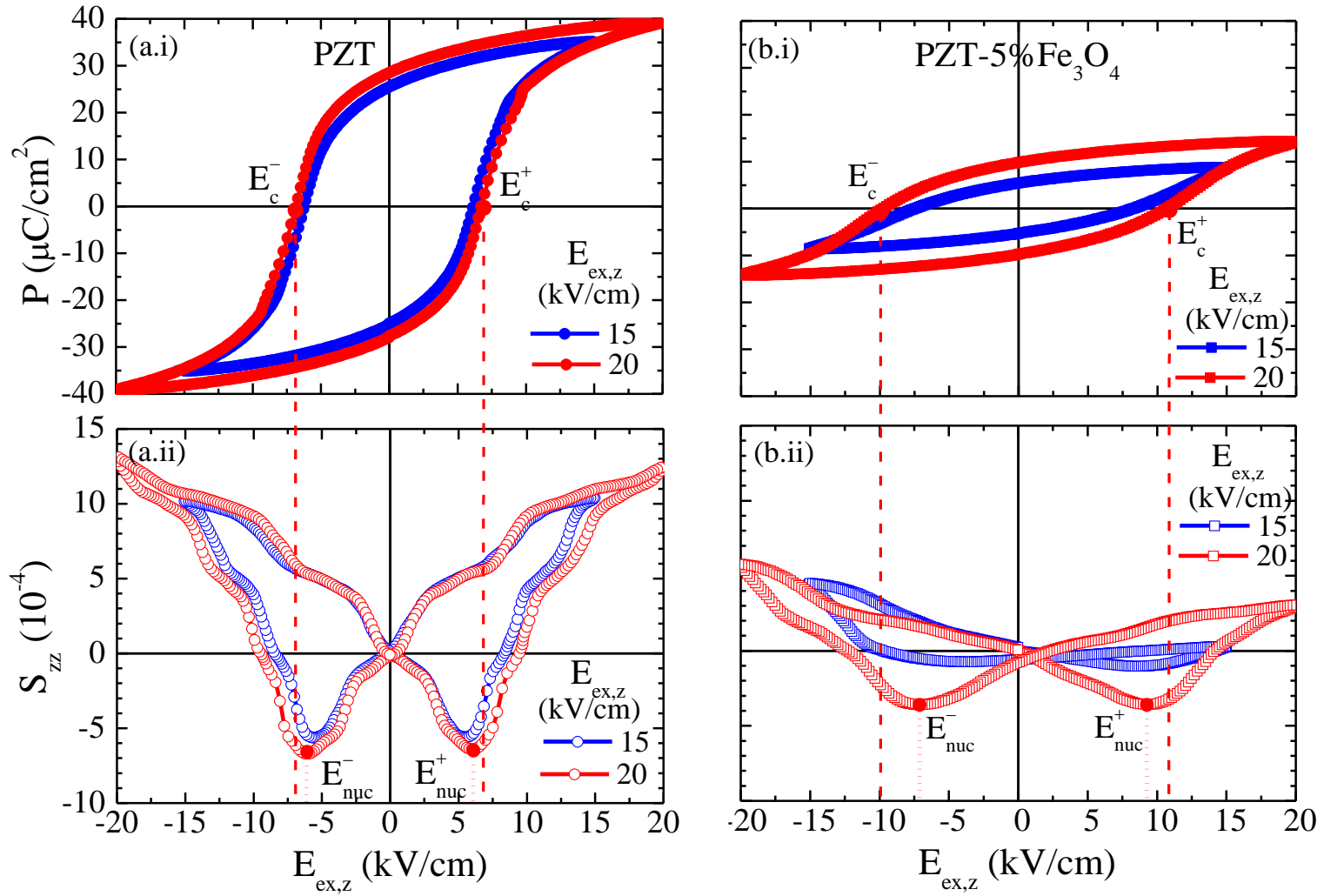


Fig. 3.13: (a.i), (b.i) and (a.ii), (b.ii) Electric polarization, $P(E_{\text{ex},z})$, and out-of-plane strain, $S_{zz}(E_{\text{ex},z})$, data upon variation of $E_{\text{ex},z}$ in the range $-15 \text{ kV/cm} \leq E_{\text{ex},z} \leq +15 \text{ kV/cm}$ (blue colored symbols) and $-20 \text{ kV/cm} \leq E_{\text{ex},z} \leq 20 \text{ kV/cm}$ (red colored symbols); (a.i), (a.ii) refer to plain PZT and (b.i), (b.ii) refer to composite PZT-5% Fe_3O_4 . Note that all panels are on the same scale, horizontally and vertically.

V. In-plane strain data

Except for the out-of-plane strain curves that were recorded by means of a global technique (Figs. 3.13(a.ii) and 3.13(b.ii)), in this Thesis we mainly recorded in-plane strain loops, $S_{zi}(E_{ex,z})$, $i=x,y$, of the plain PZT and the composite PZT-5%Fe₃O₄, via the local OM-based PE technique described in the subchapter 3.3.1. In Figs. 3.14(a.i) and 3.14(a.ii), we show representative data for a PZT sample (see sample ‘S.2.2’ of Table 2.1, in the end of chapter 2). We note that we chose a corner of the respective sample as the area of interest for recording the $S_{zi}(E_{ex,z})$ curves. This is the reason that we observe strain in both x and y axes (the sample is deformed isotropically, since it is polycrystalline and unpoled). Below, we will focus on the $S_{zi}(E_{ex,z})$ curves corresponding to the plain PZT along with the respective in-plane PE coefficients, d_{zi} , and nucleation fields, E_{nuc}^{\pm} ; $S_{zi}(E_{ex,z})$ data corresponding to the composite PZT-5%Fe₃O₄ will be presented thoroughly in the subchapters 3.2.2 and 3.2.3, below.

The $S_{zx}(E_{ex,z})$ and $S_{zy}(E_{ex,z})$ loops shown in Figs. 3.14(a.i) and 3.14(b.i), exhibit the typical butterfly hysteretic behavior; we recall that these data correspond to a PZT sample sintered at $T_{sin}=1000$ °C (for $t=2$ h in air). Before presenting the estimated d_{zi} and E_{nuc}^{\pm} values for $T_{sin}=1000$ °C, let us bring to the reader’s attention that, in general, the PE strain, and the accompanying d_{zi} and E_{nuc}^{\pm}/E_c^{\pm} values, are strongly affected by the sintering temperature of PZT (when keeping constant sintering duration and atmosphere). Specifically, in a relevant study of our group [53] we recorded the $S_{zi}(E_{ex,z})$ for PZT samples sintered at different T_{sin} , ranging within 1100 °C $\leq T_{sin} \leq 1250$ °C. The $S_{zx}(E_{ex,z})$ and $S_{zy}(E_{ex,z})$ curves corresponding to a PZT sample sintered at $T_{sin}=1180$ °C (for $t=2$ h in air) are shown in Figs. 3.14(a.ii) and 3.14(b.ii), respectively. A direct comparison between Figs. 3.14(a.i), 3.14(b.i) (PZT sintered at $T_{sin}=1000$ °C) and 3.14(a.ii), 3.14(b.ii) (PZT sintered at $T_{sin}=1180$ °C) reveals higher strain values in the case of the latter. Figs. 3.14(c.i) and 3.14(c.ii) summarize the absolute $|d_{zi}|$ and $|E_{nuc,i}|$ values that were deduced by the $S_{zi}(E_{ex,z})$ data for PZT samples sintered at $T_{sin}=1000$ °C- 1250 °C, as a function of T_{sin} . Regarding the estimation of d_{zi} and E_{nuc} it would be useful to clarify some points, right below.

Estimation of d_{zi} ($i=x,y$)

The in-plane PE coefficients, d_{zi} , can be estimated by the Eq. (1.6) of subchapter 1.1.2, which in our case can be rewritten as shown by the relation below:

$$d_{zi} = \left(\frac{\partial S_{zi}}{\partial E_{ex,z}} \right) \quad (3.1)$$

At this point, we should notice a point that is often neglected in the literature; according to Eq. (3.1), it is clearly understood that the PE coefficients correspond to the slope of a particular linear part of the $S_{zi}(E_{ex,z})$ curve. Hence, we can obtain high d_{zi} values, estimated from the parts of the $S_{zi}(E_{ex,z})$ curve with the maximum slope, low d_{zi} values, estimated from parts of the $S_{zi}(E_{ex,z})$ curve of minimum slope, or even intermediate d_{zi} values, resulting from the mean value obtained from extended parts of the $S_{zi}(E_{ex,z})$ curves that exhibit mixed behavior. For example, in Fig. 3.14(a.i), the d_{zx} value that was estimated from the decreasing branch of the $S_{zx}(E_{ex,z})$ curve (thick black line and arrow) is significantly higher from the one estimated from

the increasing branch (thin magenta line and arrow); the respective values read 414 pm/V and 211 pm/V. Thus, in order to avoid possible misinterpretations, we clearly state from which specific part of the $S_{zi}(E_{ex,z})$ curve we estimate the respective piezoelectric coefficients, d_{zi} . Accordingly, we stress that the d_{zi} values illustrated in Fig. 3.14(c.i) were estimated from the decreasing branches of the $S_{zi}(E_{ex,z})$ curves (denoted by thick black line and arrow), as shown in Fig. 3.14(a.i).

Estimation of $E_{nuc,i}$ ($i=x,y$)

The nucleation fields, $E_{nuc,i}$, were estimated from the peaks of the $S_{zi}(E_{ex,z})$ curves, denoted by the black dotted arrows in Fig. 3.4(a.i); the $|E_{nuc,i}^{\pm}|$ values for each curve were calculated by the relation $|E_{nuc,i}| = (|E_{nuc,i}^{-}| + |E_{nuc,i}^{+}|) / 2$.

Accordingly, Figs. 3.14(c.i) and 3.14(c.ii) evidence that $|d_{zi}|$ show a non-monotonic behavior with an unexpectedly high maximum value $|d_{zi}| \sim 1100$ pm/V at $T_{sin} = 1180$ °C. These features are accompanied by a progressive increase of the nucleation field, reaching maximum value $|E_{nuc,i}| \sim 4.5-5.0$ kV/cm at $T_{sin} = 1250$ °C. Regarding the results for the PZT sample sintered at $T_{sin} = 1000$ °C (i.e. the T_{sin} that we mainly employed for the preparing the samples in this Thesis) we observe that they are in line with the rest of the data, exhibiting $|d_{zi}|$ and $|E_{nuc,i}|$ values that lie on the baseline, with $|d_{zx}| \approx |d_{zy}| \approx 400$ pm/V. For the nucleation field, we observe that $E_{nuc,x} \approx E_{nuc,y} = 4$ kV/cm.

Clearly, based on the data shown in Fig. 3.14(c.i), we conclude that it would be very advantageous to sinter our PZT- x Fe₃O₄ composites at the optimum temperature $T_{sin} = 1180$ °C, so that the PZT matrix obtains the maximum PE response. Nevertheless, the optimum sintering temperature for the PZT, that is advantageous for its PE properties, is detrimental for the FM properties of the Fe₃O₄ NPs. In fact, from the magnetization and XRD data of PZT-5%Fe₃O₄ we show that, even at $T_{sin} = 1000$ °C, a significant percentage of Fe₃O₄ NPs gets oxidized upon sintering in air (38% Fe₃O₄/62% α -Fe₂O₃). Hence, at an elevated temperature, as high as $T_{sin} = 1180$ °C, we expect that almost 100% of Fe₃O₄ NPs would transform into α -Fe₂O₃, a fact that would deteriorate the magnetic properties of the composite, leading to lower magnetization and magnetostriction. A possible solution to this phenomenon, i.e. to sinter PZT- x Fe₃O₄ at higher T_{sin} without extensive Fe₃O₄ oxidation, would be to sinter the samples under an inert atmosphere.

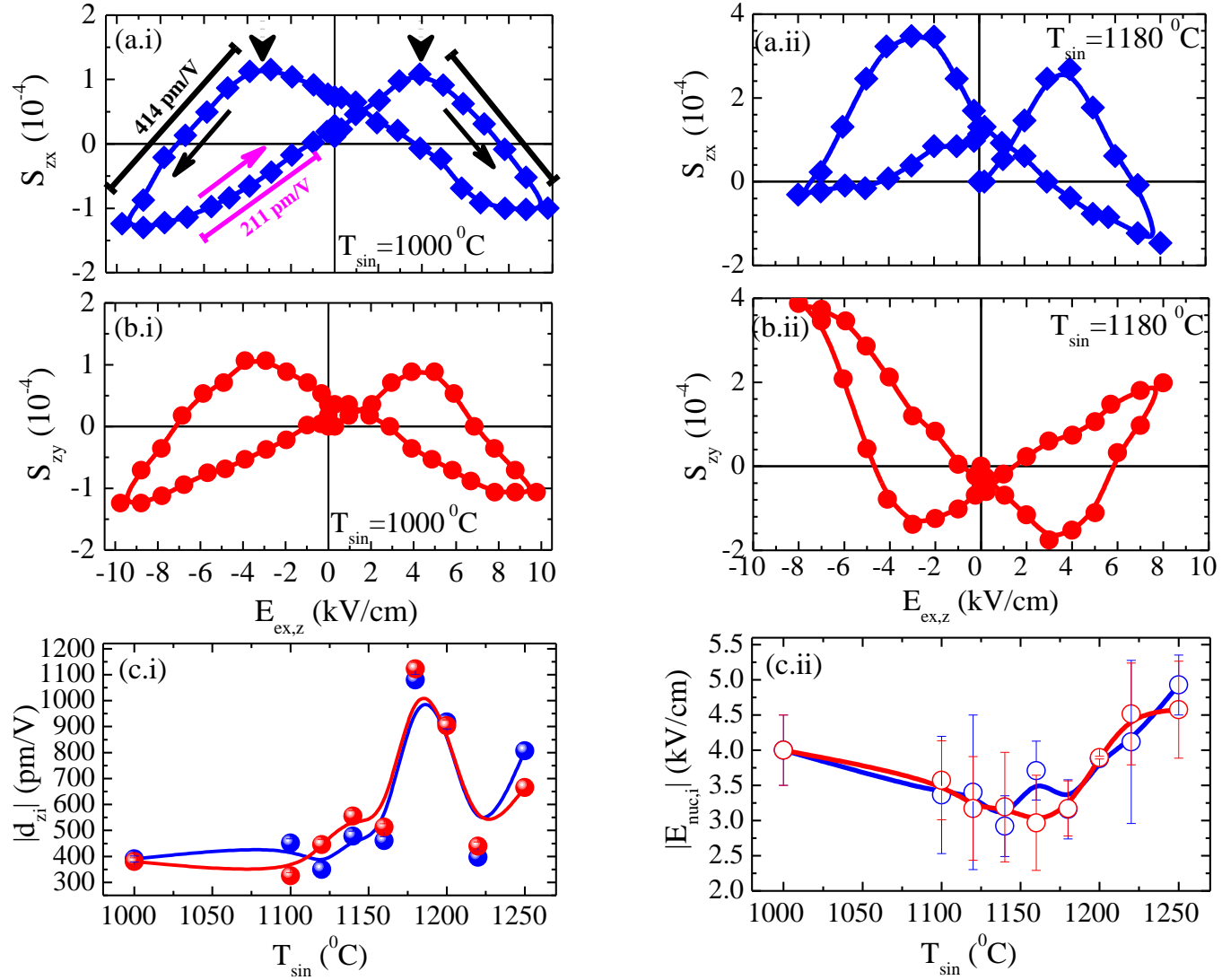


Fig. 3.14: (a.i), (b.i) and (a.ii), (b.ii) present the in-plane strain curves, $S_{zi}(E_{ex,z})$ ($i=x,y$), for two PZT samples sintered at (a.i), (b.i) $T_{sin}=1000^\circ\text{C}$ (dimensions: $4.5 \times 4.5 \times 0.4 \text{ mm}^3$) and (a.ii), (b.ii) $T_{sin}=1180^\circ\text{C}$ (dimensions: $5.0 \times 5.0 \times 0.5 \text{ mm}^3$). The thick black lines and the dotted arrows in panel (a.i) indicate the parts of the loops from which the in-plane PE coefficients, d_{zi} , and the nucleation fields, $E_{nuc,i}$ were estimated. (c.i), $|d_{zi}|$ and (c.ii) $|E_{nuc,i}|$ deduced by the in-plane $S_{zi}(E_{ex,z})$ curves of PZT samples as a function of T_{sin} ($1000^\circ\text{C} \leq T_{sin} \leq 1250^\circ\text{C}$). Please note that in the left panels (a.i), (b.i) the scale of the vertical axis is almost half compared to the one of the respective right panels (a.ii), (b.ii).

Table 3.1 summarizes the absolute values of $|E_{nuc,i}|$ and $|d_{zi}|$ for the PZT and PZT-5%Fe₃O₄ samples that were investigated under $E_{ex,z}$ in this Thesis (see also Table 2.1, in end of chapter 2). Please notice that, in the case that the investigated area was chosen close to a sample's corner, the $|E_{nuc,x}|/|E_{nuc,y}|$ and $|d_{zx}|/|d_{zy}|$ have non-zero value; on the other hand, in the case that the investigated area lies along one of the symmetry axis, let us say y-axis, exclusively $|E_{nuc,y}|$ and $|d_{zy}|$ have non-zero value. Furthermore, the average values $\langle |E_{nuc,i}| \rangle$ and $\langle |d_{zi}| \rangle$ are also shown in Table 3.1. Regarding the average absolute value of the nucleation field, we can see that $\langle |E_{nuc,i}| \rangle = 4$ kV/cm for PZT and $\langle |E_{nuc,i}| \rangle = 6$ kV/cm for PZT-5%Fe₃O₄; as discussed above this is attributed to the pinning of FE domains of the PZT matrix by Fe₃O₄ NPs. Regarding the average absolute value of the in-plane PE coefficients, we found that $\langle |d_{zi}| \rangle = 380$ -390 pm/V for both PZT and PZT-5%Fe₃O₄ compounds. Hence, we conclude that the PE properties are practically unaltered by the addition of Fe₃O₄ NPs.

<i>Samples</i>	<i>Sample code</i>	$ E_{nuc,x} / E_{nuc,y} $ (kV/cm)	$ d_{zx} / d_{zy} $ (pm/V)	$\langle E_{nuc,x} \rangle / \langle E_{nuc,y} \rangle$ (kV/cm)	$\langle d_{zx} \rangle / \langle d_{zy} \rangle$ (pm/V)
PZT	S.2.1	3.85/4	376/400	4/4	390/380
PZT	S.2.2	4/4	387/400		
PZT	S.2.3	4/4	407/340		
PZT-5%Fe ₃ O ₄	S.3.1	6/6	350/425	-/6	-/380
PZT-5%Fe ₃ O ₄	S.3.2	5.5/6	370/383		
PZT-5%Fe ₃ O ₄	S.4.1	-/6	-/375		
PZT-5%Fe ₃ O ₄	S.4.2	-/6	-/385		
PZT-5%Fe ₃ O ₄	S.4.3	-/5.5	-/350		

Table 3.1: Absolute values of the nucleation field, $|E_{nuc,i}|$, and the in-plane PE coefficients, $|d_{zi}|$, ($i=x,y$) estimated for samples of the samples series PZT and PZT-5%Fe₃O₄ by the OM-based PE techniques (see subchapter 2.3.1), along with their mean absolute values $\langle |E_{nuc,i}| \rangle$, $\langle |d_{zi}| \rangle$ (see text for details).

VI. Microstructure data

The microstructure of the PZT-5%Fe₃O₄ composite was studied with SEM. Specifically, Figs. 3.15(a.i)-(c.i) and 3.15(a.ii)-(c.ii) present secondary electron imaging (SEI) topography images corresponding to two PZT-5%Fe₃O₄ samples, in their as-prepared (non-polished) and polished Au-coated form, respectively, with magnification x5000 ((a.i), (b.i)), x10000 ((a.ii), (b.ii)), x50000 ((a.iii), (b.iii)). We recall that the polishing and Au coating were performed in order to reduce the thickness of the sample, t , (via polishing), aiming to apply the maximum possible $E_{ex,z}$ with a relatively low voltage (via Au coating). The thickness of the samples was $t=1$ mm, before polishing, and $t=0.4$ mm, after polishing; thus the thickness reduction was on the order of 60%. Accordingly, we stress that the topography image of the as-prepared sample (Fig. 3.15(a)) corresponds to its surface, while the image of polished Au coated sample (Fig. 3.15(b)) corresponds to its bulk (i.e. sample volume).

In this context, the sample surface exhibits a relatively porous microstructure, as shown in Figs. 3.15(a.i) and 3.15(b.i) with magnification x5000 and x10000, respectively. Specifically, for the image with the highest magnification value, x50000, shown in Fig. 3.15(c.i), we can observe fairly well the grains of the unpolished PZT-5%Fe₃O₄. The thin yellow dashed lines denote the most discernable grain-boundaries. The solid blue arrows denote the size of two representative grains, corresponding to the smaller (0.8 μ m) and the largest (2 μ m) ones found in the image, respectively. It should be mentioned that the image quality in panels (a.i)-(c.i) is very satisfying taking into account that the respective sample surface is non-conductive (without Au sputtering).

Regarding the bulk of the sample, we observe that it is fairly compact with minimal porosity, as shown in Figs. 3.15(a.ii)-(c.ii), with magnification x5000, x10000 and x50000, respectively (the scratches observed in the latter image were caused by polishing). Comparing the images with the highest magnification, x50000, for the polished Au-sputtered sample (Fig. 3.15(c.ii)) and for the non-polished one (Fig. 3.15(c.i)), we can see that in the case of the former, the grains cannot be discerned, due to their larger size, a result that manifests fair densification.

The difference in the porosity level between the surface and the bulk of the PZT-5%Fe₃O₄ sample is attributed to the evaporation of PbO that is known to take place during the sintering of PZT at high temperatures [58]; obviously PbO evaporation gets maximum close to the sample surface, leading to higher porosity.

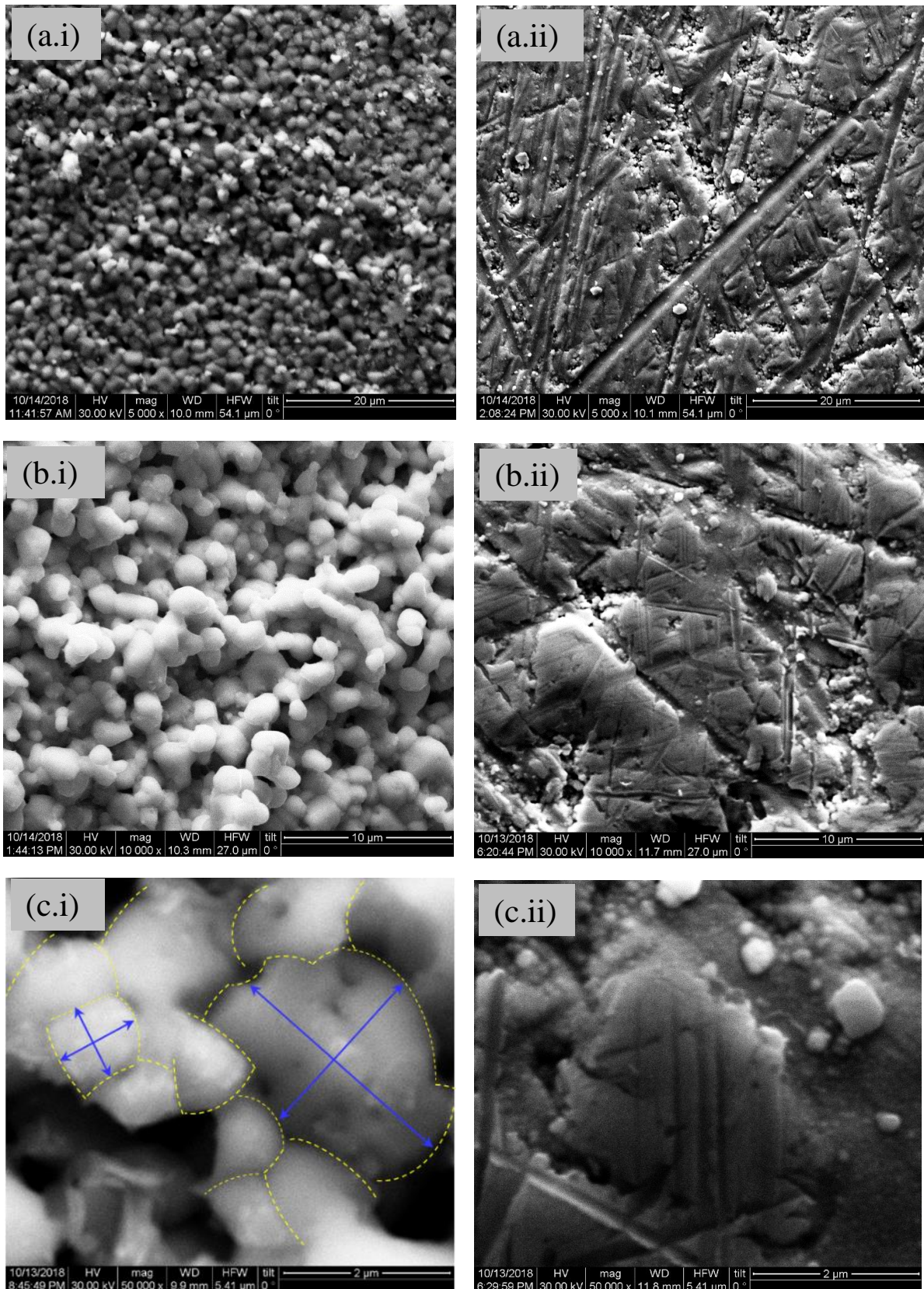


Fig. 3.15: Secondary electron imaging, SEI, topography images with magnification (a.i),(a.ii) $\times 5000$, (b.i),(b.ii) $\times 10000$, (c.i),(c.ii) $\times 50000$ for two PZT-5%Fe₃O₄ sintered samples in their non-polished ((a.i)-(c.i)) and polished Au-coated ((a.ii)-(c.ii)) form. In panel (c.i) the grain boundaries are indicated with thin yellow dashed lines; the blue solid arrows indicatively show the size of two grains, relatively small and large ones. In panel (c.ii) the fair densification is manifested by the large grain size.

VII. Elemental analysis and homogeneity investigation

Except for the standard SEI topography images presented in the previous subchapter, we also performed EDS elemental analysis and mapping. This detailed study aimed to investigate the constituent elements and their homogeneity in a PZT-5%Fe₃O₄ sample, in its as-prepared (non-polished) and in its polished Au-coated form.

Specifically, for the as-prepared PZT-5%Fe₃O₄ sample, the elemental analysis and mapping are presented in Figs. 3.16(a) and 3.16(b)-(e), respectively. The SEI topography image of the corresponding sample is shown in Fig. 3.16(f), referring to the as-prepared sample surface. As expected, the BSE-based EDS analysis confirmed the presence of Pb, Zr, Ti, and Fe in the composite and their relative peak intensities are consistent with their respective compositions in the sample.

Figs. 3.16(b)-(e) show the elemental distribution maps in the form of color-dotted images, referring to the constituent elements Pb, Zr, Ti, and Fe. We recall that, what we can deduce from these type of images is the presence of possible inhomogeneities in composition, which can be manifested by variations in the color intensity. Accordingly, Figs. 3.16(b)-(e) reveal that all elements are well distributed, with some small inhomogeneity features, which are fairly expected for two reasons; first, the stoichiometry of the Pb(Zr_xTi_{1-x})O₃ compound that we employed, that is $x=0.48$, lies within the MPB region, where there is intrinsic crystallographic phase coexistence of the tetragonal and rhombohedral phases, schematically shown in panels (h.i) and (h.ii). This is clearly shown in the respective phase diagram that we present here again, in the inset Fig. 3.16(g) (for extensive description of the phase diagram, see subchapter 1.1.4.I). Moreover, in our case, there is an additional partial transformation into the tetragonal phase due to the presence of iron oxide NPs (Fe₃O₄/Fe₂O₃) in the PZT matrix, as evidenced by the XRD data in the subchapter 3.2.1.II. Second, the PZT stoichiometry might be somehow altered over the surface of the as-prepared sample, since, in this area, PbO loss gets maximum during sintering [58]

In the same spirit, elemental analysis and mapping were also performed for the polished Au-coated PZT-5%Fe₃O₄ sample, presented in Figs. 3.17(a) and 3.17(b)-(f), respectively. The SEI topography image of the corresponding sample is shown in Fig. 3.17(g), referring to the bulk of the sample. The BSE-based EDS spectrum is similar to the one shown in Fig. 3.16(a), with the additional Au peaks. We note that in this case, the Pb, Zr, Ti, and Fe peaks are not as well discernable as in Fig. 3.16(a), due to the occurrence of the high intensity Au peaks in the spectrum.

Regarding the elemental mapping, shown in Figs. 3.17(b)-(f), we observe that the constituent elements Pb, Zr, Ti and Fe are fairly distributed in the bulk of the sample, with some inhomogeneity features, which are fewer than the ones observed for the as-prepared sample (Figs. 3.16(b)-(e)).

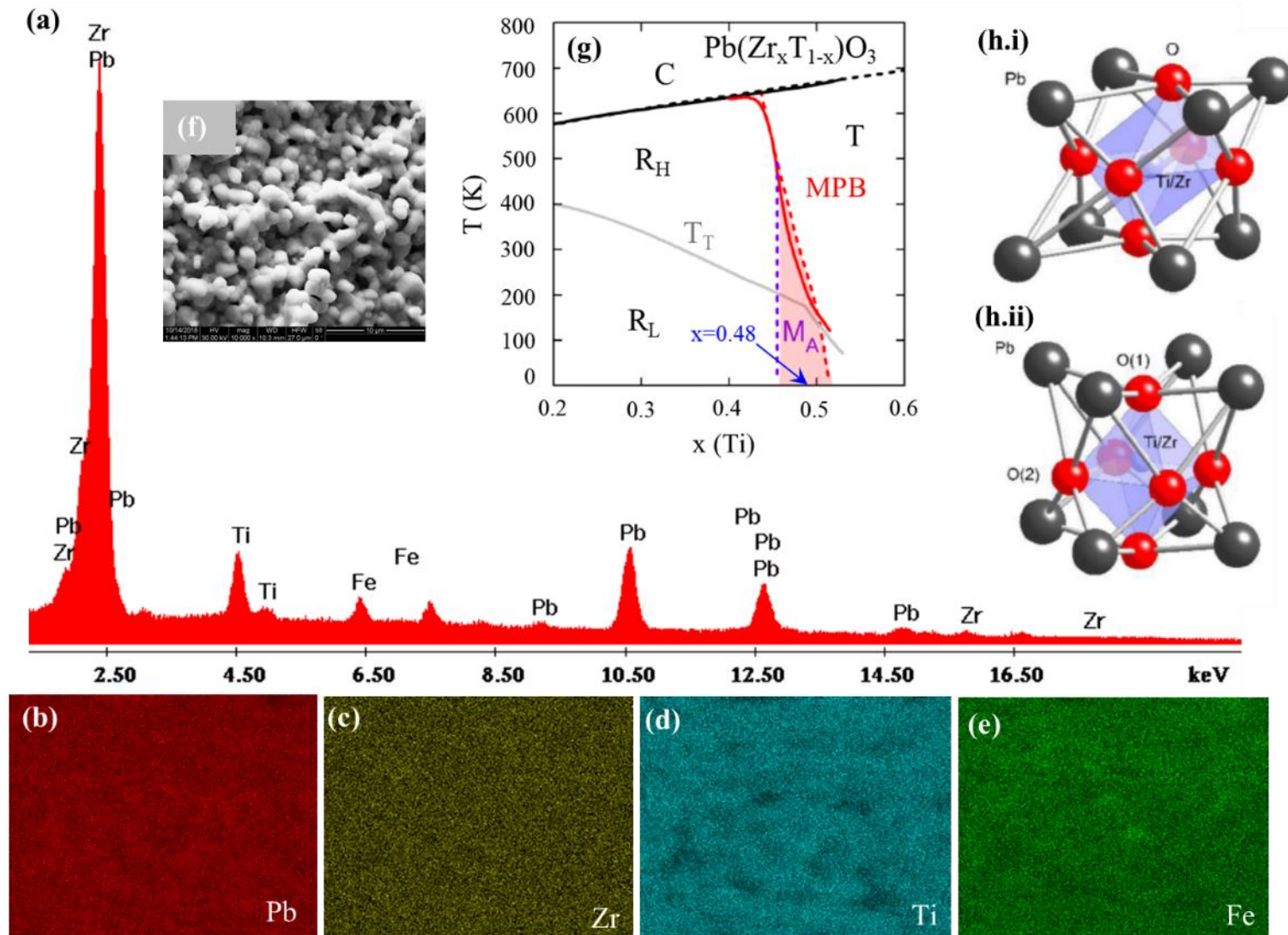


Fig. 3.16: (a) BSE-based EDS spectrum for elemental analysis and (b)-(e) BSE-based EDS compositional mapping referring to (b) Pb, (c) Zr, (d) Ti, and (e) Fe, for an as-prepared (sintered, without polishing) PZT-5%Fe₃O₄ composite. (f) SEI topography image from a representative area of the corresponding sample (magnification $\times 10000$). (g) Phase diagram of $Pb(Zr_xTi_{1-x})O_3$; the composition that we employed is $x=0.48$, shown denoted by an arrow. (h.i), (h.ii) Schematic illustrations of (h.i) rhombohedral and (h.ii) tetragonal phases of PZT [54].

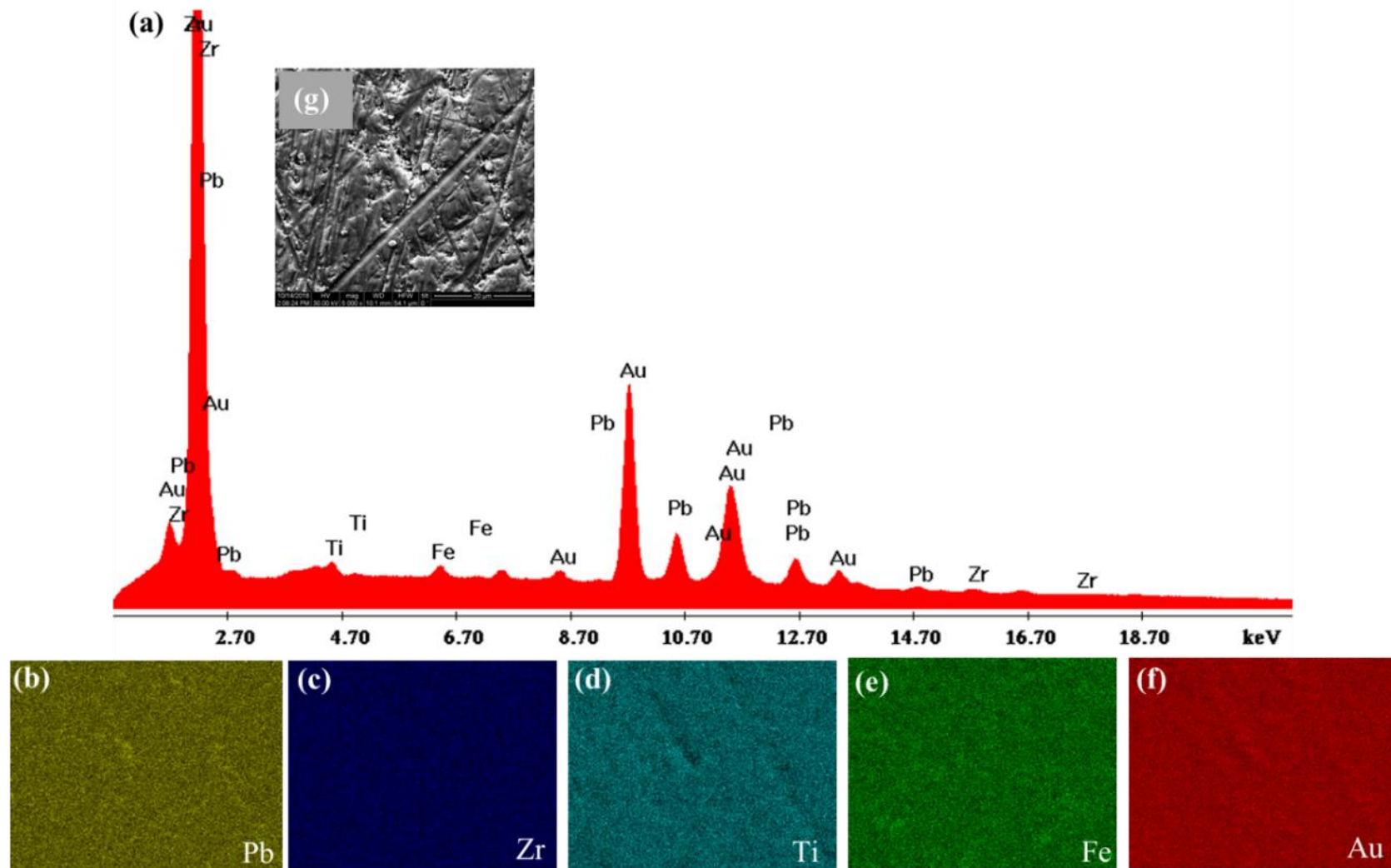


Fig. 3.17: (a) BSE-based EDS spectrum for elemental analysis and (b)-(f) BSE-based EDS compositional mapping referring to (b) Pb, (c) Zr, (d) Ti, (e) Fe and (f) Au, for a sintered polished Au-coated PZT-5%Fe₃O₄ composite. (g) SEI topography image from a representative area of the corresponding sample (magnification x5000).

3.2.2 Electric-field control of the magnetic properties for a PZT-5%Fe₃O₄ composite

Here, we study the effect of an external, out-of-plane electric field, $E_{ex,z}$, on the magnetic properties, especially on the remanent magnetization, m_{rem} , of a PZT-5%Fe₃O₄ composite. Specifically, we investigate the relaxation of m_{rem} for different values of $E_{ex,z}$, that is $m_{rem}(t, E_{ex,z})$. First, we describe the measurement protocol that we followed to settle m_{rem} under $E_{ex,z}$, and subsequently we present the relaxation measurements in order to obtain the $m_{rem}(t, E_{ex,z})$ data. Appropriate fitting of $m_{rem}(t, E_{ex,z})$ data was performed in order to investigate the effect of $E_{ex,z}$ on the fitting parameters. In addition, we surveyed the in-plane strain, $S_{zi}(E_{ex,z})$ ($i=x,y$), and the polarization $P(E_{ex,z})$ under $E_{ex,z}$ application, $P(E_{ex,z})$, for the specific composite. This study aims to investigate the effect of different $E_{ex,z}$ on the magnetic properties of PZT-5%Fe₃O₄ by revealing the interconnection between its FM and PE constituents.

I. Magnetization measurement protocol under $E_{ex,z}$

The magnetization measurement protocol is divided in two parts; the ‘*settlement of m_{rem}* ’ which refers to $m(H_{ex})$ measurements ($T=300$ K) and the ‘*relaxation of m_{rem}* ’ which refers to $m_{rem}(t, E_{ex})$ measurements ($H_{ex}=0$ Oe, $T=300$ K).

Settling of m_{rem} : The protocol that was employed in order to settle m_{rem} in the absence/presence of $E_{ex,z}$ is the following: regarding m_{rem} at $E_{ex}=0$ kV/cm, we start from $H_{ex}=0$ Oe and $E_{ex}=0$ kV/cm, subsequently we set the external magnetic field to $H_{ex}=10$ kOe and then we reduce it to zero. Regarding m_{rem} under the presence of different $E_{ex,z}$ values in the entire range -9 kV/cm $\leq E_{ex} \leq +9$ kV/cm, the same protocol, was followed. Fig. 3.18(a) indicatively shows the variation of magnetization with H_{ex} for the settlement of m_{rem} , under $E_{ex,z}=0$ kV/cm and $E_{ex,z}=+9$ kV/cm. This is schematically represented in the insets of Fig. 3.18(a), (a.i) and (a.ii), for a PZT-5%Fe₃O₄ sample. In this context, the respective data correspond to two cases; in the first one, m_{rem} is settled without any mechanical deformation of the PZT-5%Fe₃O₄ sample, while in the second one, m_{rem} is settled under the application of mechanical deformation. In Fig. 3.18(b), $m(H_{ex})$ is shown exclusively for $H_{ex}=0$ Oe, in order to resolve the two different states of m_{rem} obtained under $E_{ex,z}=0$ kV/cm and $E_{ex,z}=+9$ kV/cm. We notice that the application of an $E_{ex,z}=+9$ kV/cm causes a significant shift of m_{rem} by $\Delta m_{rem}=m_{rem}(E_{ex}=+9$ kV/cm) $-m_{rem}(E_{ex}=0$ kV/cm) $=+3.6 \times 10^{-5}$, a value that can be clearly detected by the SQUID magnetometer.

Relaxation of m_{rem} : After settling m_{rem} as described right above, its evolution with time, $m_{rem}(t)$, is presented in Fig. 3.18(c) in the duration window $t:0-20$ min, for $E_{ex,z}=0$ kV/cm and $E_{ex,z}=+9$ kV/cm. We observe that m_{rem} exhibits a non-linear relaxation. Following the same protocol $m_{rem}(t)$ were obtained for various values of $E_{ex,z}$, ranging within -9 kV/cm $\leq E_{ex,z} \leq +9$ kV/cm, as shown in Figs. 3.20(a)-(c), with the open symbols. Specifically, the sequence of measurements was realized by varying the applied external electric field as following: $E_{ex,z}=+6$ kV/cm $\rightarrow +3$ kV/cm $\rightarrow 0$ kV/cm $\rightarrow -3$ kV/cm $\rightarrow -6$ kV/cm $\rightarrow -9$ kV/cm $\rightarrow +9$ kV/cm. As mentioned above, in Fig. 3.18(c), all $m_{rem}(t)$ curves display non-linear relaxation.

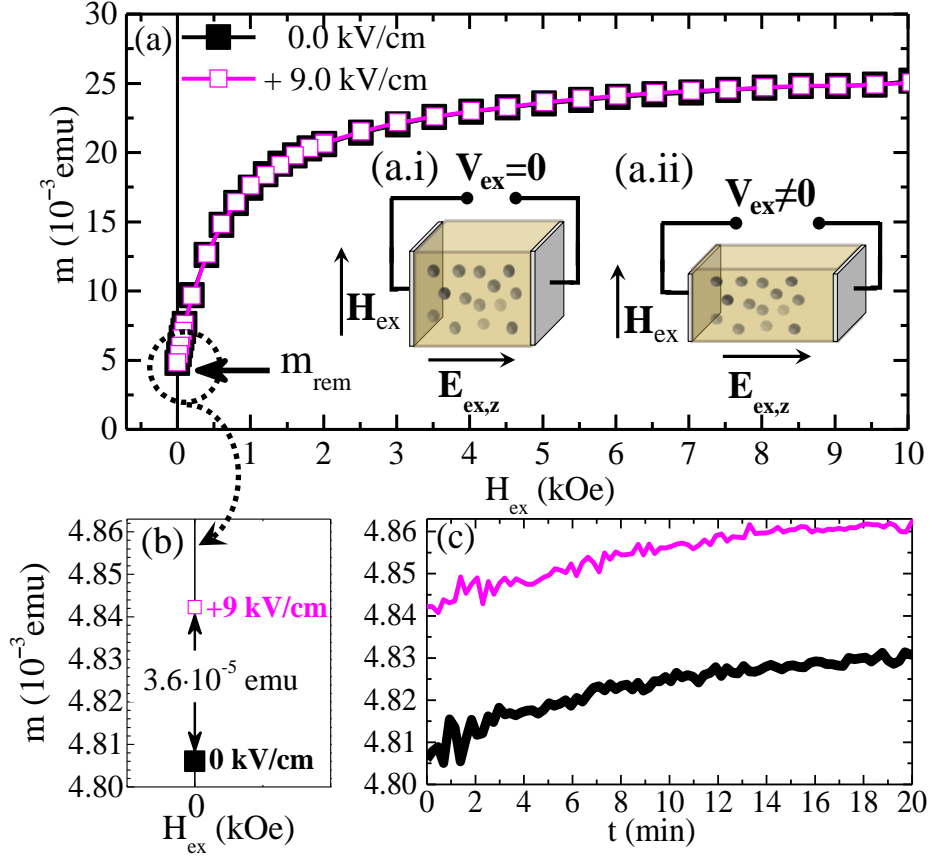


Fig. 3.18: (a) Settling of remanent magnetic state, m_{rem} , upon application of $E_{ex,z} = 0$ kV/cm and +9 kV/cm, for a PZT-5% Fe_3O_4 sample. The insets (a.i) and (a.ii) schematically present the H_{ex} and $E_{ex,z}$ configuration, for the two indicative cases where $E_{ex,z} = 0$ kV/cm and $E_{ex,z} \neq 0$ kV/cm. (b) The low H_{ex} regime in magnification. The values of m_{rem} for $E_{ex} = 0$ kV/cm and $E_{ex} = +9$ kV/cm exhibit a distinct difference on the order of 3.6×10^{-5} emu. (c) Relaxation of the remanent magnetization, $m_{rem}(t)$ for $E_{ex} = 0$ kV/cm (black thick curve), +9 kV/cm (magenta thin curve).

II. Fitting of $m_{rem}(t)$ data

Figs. 3.19(a)-(c) present the experimental data (open symbols), which have been well fitted (dotted lines) by means of the exponential expression that is shown right below.

$$m_{rem}(t) = Ae^{-\frac{t}{T_1}} + y_o \quad (Eq. 3.2)$$

The values A , T_1 and y_o , that were extracted from the exponential fittings, along with the $m_{rem}(0) = A + y_o$, are shown in Figs. 3.20(a)-3.20(d) as a function of $E_{ex,z}$. Particularly, exponential fitting was performed in four different time windows: $\Delta t = 0-20$ min, 1-20 min, 2-20 min and 5-20 min (below we will explain the strategy of this choice). Accordingly, the respective values A , T_1 and y_o and $m_{rem}(0) = A + y_o$ were estimated for each one of these time windows.

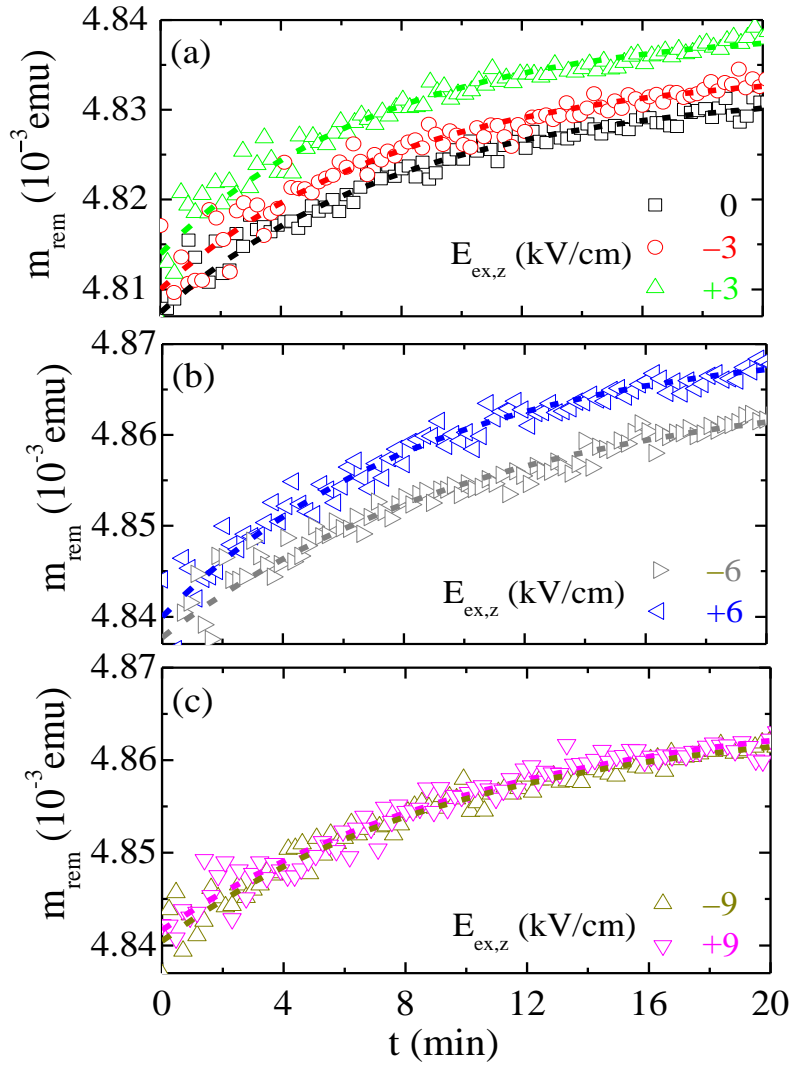


Fig. 3.19: (a), (b), (c) Evolution of m_{rem} over time, recorded for $t=20$ min for different electric fields, $E_{\text{ex},z}$. (a) $E_{\text{ex},z}=0$ kV/cm, ± 3 kV/cm, (b) $E_{\text{ex},z}^{\pm}=\pm 6$ kV/cm and (c) $E_{\text{ex},z}^{\pm}=\pm 9$ kV/cm. The experimental data of $m_{\text{rem}}(t)$ are shown with open data points and evidence an exponential behavior. Fitting of these data with the relation of Eq. (3.2) is shown with dotted lines. Please, notice that the vertical scale is the same in all three panels. The measurements sequence was $E_{\text{ex},z}=+6 \rightarrow +3 \rightarrow 0 \rightarrow -3 \rightarrow -6 \rightarrow -9 \rightarrow +9$ (kV/cm).

The values of m_{rem} for $t=0$ (that is the initial m_{rem} values), $m_{\text{rem}}(0)=A+y_0$, are shown in Fig. 3.20(c) upon varying $E_{\text{ex},z}$. It can be observed that, for $E_{\text{ex},z}=0$ kV/cm, ± 3 kV/cm, the values of $m_{\text{rem}}(0)$ are similar, with $m_{\text{rem}}(0)=4.810 \times 10^{-3}$ emu. At $E_{\text{ex},z}^{\pm}=\pm 6$ kV/cm, there is a step-like increase of $m_{\text{rem}}(0)$ that remains constant up to $E_{\text{ex},z}^{\pm}=\pm 9$ kV/cm. Moreover, since all $m_{\text{rem}}(0)$ curves almost coincide, it can be deduced that these data are independent of the time window selected. According to the exponential fitting expression described by Eq. (3.2), T_1 is related with the ‘relaxation constant’ of m_{rem} . As it can be noticed from Fig. 3.20(d), T_1 is almost unresponsive to $E_{\text{ex},z}$, since the respective data lie on a baseline with approximately $T_1=10$ min. Interestingly, for the specific electric fields, T_1 is independent of the time range of fitting. On the contrary, we observe that in the vicinity of $E_{\text{ex},z}=-6$ kV/cm the T_1 value shifts from the baseline to much higher values, for all time windows; this fact is indicative of slower relaxation

of m_{rem} . Accordingly, since this data clearly prove that T_1 is a function of $E_{\text{ex},z}$, we can term it ‘relaxation function’, $\text{RF}(E_{\text{ex},z})=T_1(E_{\text{ex},z})$.

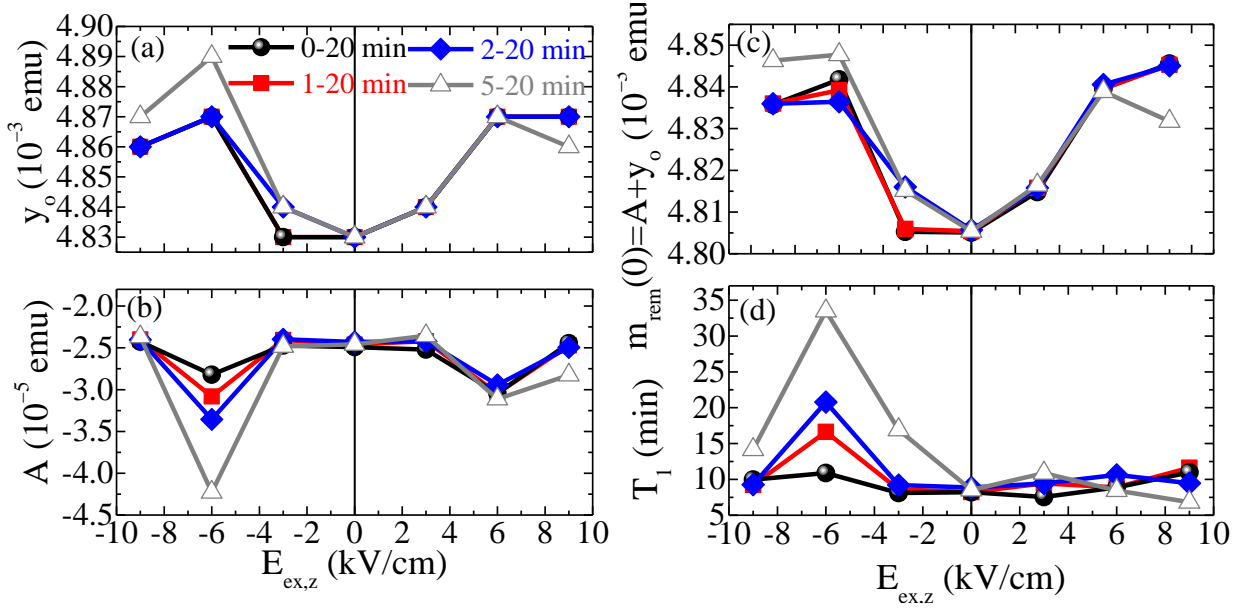


Fig. 3.20: Parameter values obtained from exponential fitting (a) y_0 , (b) A , (c) $m_{\text{rem}}(0)=A+y_0$ and (d) T_1 with varying E_{ex} . The different symbols-colors of the data correspond to fitting for four different time windows: 0-20 min (black spheres), 1-20 min (red squares), 2-20 min (blue rhombi) and 5-20 min (gray open triangles). The sequence of the measurements was $E_{\text{ex},z}=+6 \rightarrow +3 \rightarrow 0 \rightarrow -3 \rightarrow -6 \rightarrow -9 \rightarrow +9$ (kV/cm).

At this point, we will explain the strategy of employing different time windows in the fitting procedure of the raw data of Figs. 3.19(a)-(c); though this issue is of technical origin it reveals significant information on the underlying physics. It is a fact that SQUID magnetometers exhibit a relatively high noise level in the measured signal right after any change in the externally applied magnetic field, H_{ex} ; the higher the variation of H_{ex} , the higher the noise level [59] Hence, when small magnetization signals are to be measured, a waiting time (up to a few minutes) usually precedes the actual measurement [59]. Thus, in our case, we change H_{ex} only once, that is when we go from the saturation magnetic state with $H_{\text{ex}}=10$ kOe to the remanent magnetic state, m_{rem} , with $H_{\text{ex}}=0$. Taking into consideration that the variation in H_{ex} is relatively high, 10 kOe, the first data points of the measured magnetization during relaxation are relatively ‘noisy’. This is clearly evidenced in the raw data presented in Fig. 3.18(c) and Figs. 3.19(a)-(c), since we observe that the data points for $t < 3-4$ min are more ‘noisy’ when compared to those recorded for $t > 3-4$ min. The aforementioned issue of technical nature could certainly affect the parameters obtained through the fitting of the experimental data by means of relation $m_{\text{rem}}(t)=Ae^{-t/T_1}+y_0$ (Eq. 3.2). Accordingly, in order to study this point, we performed the four distinct sets of fitting of the raw data, Figs. 3.19(a)-(c). For each set of fitting, the time window was progressively shortened (first: 0-20 min, second: 1-20 min, third: 2-20 min and fourth: 5-20 min).

The parameters that were obtained by the fitting are shown comparatively in Figs. 3.20(a)-(d). Regarding the parameters y_0 and $m_{\text{rem}}(0)$, we observe that they exhibit a rather robust behavior in all four fitting procedures. Although, regarding the parameters A and T_1 , we can see that they are clearly affected by the time interval used during the fitting. Specifically, in the

case of the parameter A, a ‘dip’ is clearly evident, while in the case of the parameter T_1 , a ‘peak’ develops at the exact same value of external electric field, $E_{ex,z} = -6$ kV/cm. Notably, these features are most observed for the case where the ‘noisy’ data points of the initial time interval are ignored, else the features somehow weaken. Most important, a remarkable characteristic that is unveiled from the technical issue discussed above is that the parameters A and T_1 are strongly affected from the time window used for the fitting only in the vicinity of $E_{ex,z} = -6$ kV/cm; in any other case, $E_{ex,z}$ does not affect A and T_1 , irrespectively of the choice of the time window.

III. In-plane strain and polarization data

Aiming to investigate the nature of the aforementioned features, detailed measurements were performed in order to study the piezoelectric and ferroelectric properties of the composite PZT-5%Fe₃O₄ system. To this end, we investigated the in-plane strain and the polarization as shown in Figs. 3.21(a) and 3.21(b), respectively.

More specifically, the in-plane strain data, $S_{zi}(E_{ex,z})$ ($i=x,y$), were obtained using the OM-based technique described in the subsection 2.3.1 for the PZT-5%Fe₃O₄ composite. Since the employed technique is *local*, we can record the piezoelectric strain in any area of choice over the sample surface; here the investigated area was selected in the left corner of the sample. The corresponding in-plane $S_{zx}(E_{ex,z})$ and $S_{zy}(E_{ex,z})$ hysteresis butterfly-like curves were recorded under $E_{ex,z}$ within -10 kV/cm $\leq E_{ex,z} \leq +10$ kV/cm, as shown in Figs. 3.21(a) and 3.21(b), respectively. We observe that these curves exhibit their maxima into the grey shaded areas, around $E_{peak}^{\pm} = \pm 6$ kV/cm. The parts indicated in red lines-symbols correspond to the sequence of $E_{ex,z}$ values applied while performing the $m_{rem}(t)$ measurements, shown in Figs. 3.21(a)-(c).

The electric polarization of the PZT-5%Fe₃O₄ composite is presented in Fig. 3.21(c) as a function of $E_{ex,z}$, $P(E_{ex,z})$. In the same plot, the respective derivative of polarization, $dP(E_{ex,z})/dE_{ex,z}$, is shown under $E_{ex,z}$ within -15 kV/cm $\leq E_{ex,z} \leq +15$ kV/cm. Interestingly, from the $dP(E_{ex,z})/dE_{ex,z}$ data we can estimate the nucleation field; the intersection of the two red lines in Fig. 3.21(c) denote the point where the slope of $dP(E_{ex,z})/dE_{ex,z}$ exhibits a slight change, just before its maximum at E_c^{\pm} . Accordingly, we conclude that the nucleation fields occur around $E_{nuc}^{\pm} = \pm 6$ kV/cm. Obviously, the data presented in the Figs. 3.21(a)-(c) show that the peaks observed for the in-plane strain coincide with the nucleation of FE domains, i.e. $E_{peak}^{\pm} = E_{nuc}^{\pm} = \pm 6$ kV/cm.

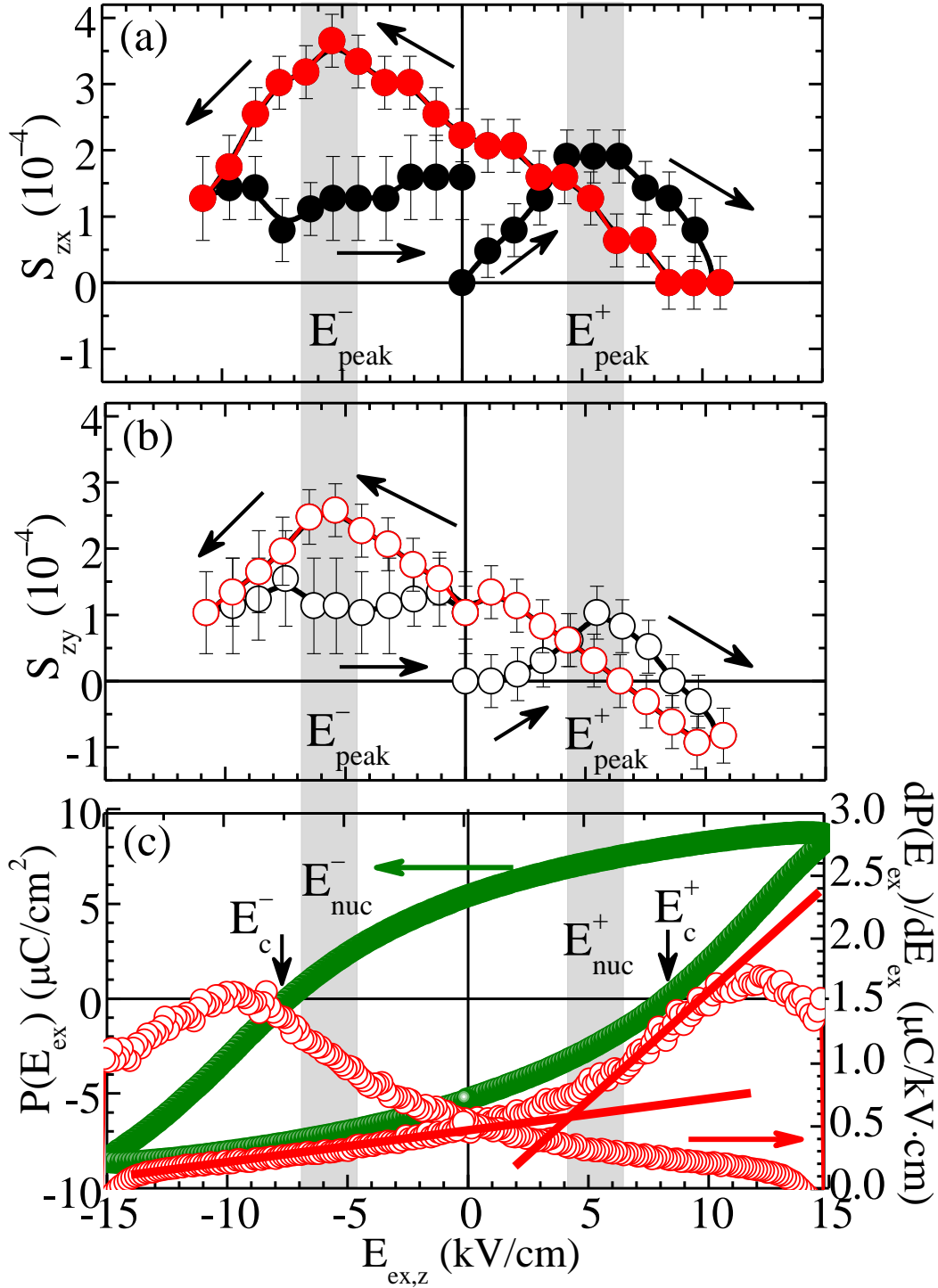


Fig. 3.21: (a), (b) In-plane strain along the symmetry axis (a) x (S_{zx}) and (b) y (S_{zy}) under electric field, $E_{ex,z}$ application. The gray-shaded areas highlight the $S(E_{ex})$ maxima that occur around $E_{peak}^\pm = \pm 6$ kV/cm. The specific parts of the $S_{zx}(E_{ex,z})$ and $S_{zy}(E_{ex,z})$ curves denote in red solid and open circles, respectively trace the sequence of $E_{ex,z}$ applied during the $m_{rem}(t)$ measurements. (c) Polarization under $E_{ex,z}$ application, $P(E_{ex})$ (green solid spheres) and the respective derivative of polarization, $dP(E_{ex})/dE_{ex}$ (red open circles); here, the grey shaded areas denote the smoothly changing slope of $dP(E_{ex})/dE_{ex}$. The intersection point of the red thick lines occurs around the nucleation field, $E_{nuc}^\pm = \pm 6$ kV/cm, just before the coercive field, $E_c^\pm = \pm 7.5$ kV/cm is reached.

IV. Comparison of the magnetization, in-plane strain and polarization data

By comparing the data presented above, namely magnetization (Figs. 3.20(a)-(d)), piezoelectric (Figs. 3.21(a)-3.21(b)) and polarization (Fig. 3.21(c)), an interconnection is clearly revealed, that is the development of a ME coupling between the FM and PE ingredients of the PZT-5%Fe₃O₄ composite. More specifically, the fitting parameter y_0 exhibits local maxima (Fig. 3.20(a)) while A exhibits local minima (Fig. 3.20(b)) at $E_{ex,z}^{\pm}=\pm 6$ kV/cm. Consequently, the net $m_{rem}(0)=A+y_0$ increases up to $E_{ex,z}^{\pm}=\pm 6$ kV/cm and saturates for higher values of $E_{ex,z}$ (Fig. 3.20(c)). Moreover, the relaxation function $RF(E_{ex,z})=T_1(E_{ex,z})$ exhibits a maximum at $E_{ex,z}^{-}=-6$ kV/cm, which is a proof of slower relaxation of m_{rem} at this electric field value. Taking all these results into consideration, it is clear that the extrema points of the fitting parameters related to the relaxation of m_{rem} occur at $E_{ex,z}^{\pm}=\pm 6$ kV/cm, an electric field that coincides with $E_{peak}^{\pm}=E_{nuc}^{\pm}=\pm 6$ kV/cm. We recall that at E_{nuc}^{\pm} the FE domains appear and start to move/rotate, ultimately motivating zeroing of electric polarization at the coercive field, E_c^{\pm} . What it more, since electric polarization is metastable and thus susceptible to relaxation in the interval of electric fields from E_{nuc}^{\pm} to E_c^{\pm} , we can plausibly conclude that in our case the relaxation of the remanent magnetic state is affected by the relaxation of the electric polarization due to the ME coupling.

To quantify the strain-mediated coupling between the respective PE PZT matrix and FM Fe₃O₄ NPs constituents, we estimated the in-plane converse ME coefficient, $\alpha_{in-plane,z}^{E \rightarrow M}$, from the data of Fig. 3.20(c), that is the variation of $m_{rem}(0)$ as a function of $E_{ex,z}$. We recall that in general, the converse ME coupling coefficient is given by the relation $\alpha_{ij}^{E \rightarrow M}=\mu_0 dM_{ij}(E_i)/dE_i$, with $\mu_0=4\pi \times 10^{-7}$ Vs/Am (Eq. (1.16(b))). Specifically, in our case, for the sintered sample PZT-5% Fe₃O₄ studied, we can estimate only the in-plane converse ME coefficient, irrespectively of the x and y axes, which cannot be distinguished, since the sample exhibits isotropic in-plane behavior. We recall that the external electric field, $E_{ex,z}$, is applied out-of-plane (along thickness of the sample, denoted as the z-axis) while the magnetization of the sample, $M(E_{ex})$, is measured along an arbitrarily chosen in-plane direction (along sample surface, denoted as the xy-plane).

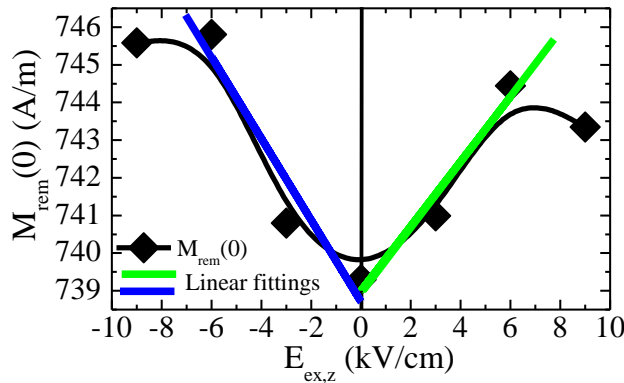


Fig. 3.22. Volume magnetization, that is $m_{rem}(0)$ per unit volume, of the PZT-5%Fe₃O₄ sample, upon variation of $E_{ex,z}$ within ± 10 kV/cm (the data of Fig. 3.14(c) where used). The green and blue thick lines represent the linear fitting performed in the positive and negative segments of $M_{rem}(0)$ curve, respectively, in order to estimate the corresponding in-plane converse ME coefficients, $\alpha_{in-plane,z}^{E \rightarrow M}$.

In formal terms, the magnetization $M(E_{ex})$ is calculated from the experimental data of Fig. 3.20(c) that actually correspond to the magnetic moment, $m(E_{ex,z})$, based on the relation $M_{rem}(0)=m_{rem}(0)/V_{sample}$, where V_{sample} is the sample volume (we assume that the magnetization of the sample is uniform). The calculated $M_{rem}(E_{ex,z})$ is shown above, in the Fig. 3.22. According to Eq. 1.16(b), the in-plane converse ME coefficient $\alpha_{in-plane,z}^{E \rightarrow M}$ can be estimated from the slope of the data around $E_{ex,z}=0$, through a simple linear fitting. Accordingly, since the data of Fig. 3.20(c) coincide for all time windows, we performed linear fitting to the ones that refer to the time window 5-20 min (magenta colored symbols), shown with the green and blue thick lines for $E_{ex,z}$ in the positive and negative direction. Hence, the respective in-plane converse ME coefficients are $\alpha_{in-plane,z}^{E \rightarrow M}=1.1 \times 10^{-11}$ s/m and 1.4×10^{-11} s/m. These values are in very good agreement with the relevant values of the literature, corresponding to planar ME heterostructures such as MgO-based ones [60], and bulk structures such as $Bi_{1-x}Ca_xFeO_3$ [61] and $CoFe_2O_4$ -BaTiO₃ [62].

The reproducibility of the results presented in the subchapter 3.2.2, right above, was confirmed by employing four different PZT-5%Fe₃O₄ samples; two samples for the magnetization measurements and two samples for the in-plane strain measurements (see the samples ‘S.3.1’, ‘S.3.2’ and ‘S.3.3’, ‘S.3.4’, respectively, in Table 2.1, at the end of chapter 2).

3.2.3 Magnetic-field control of the piezoelectric properties for a PZT-5%Fe₃O₄ composite

Complementary to the study of the previous subchapter, here we investigate the effect of a constant magnetic field on the PE properties of a PZT-5%Fe₃O₄ composite. Specifically, we present the recorded in-plane strain under the presence/absence of an external magnetic field, applied out-of-plane, $H_{ex,z}$, along with the respective calculated in-plane PE coefficients. Moreover, we compare these results with the respective ferroelectric ones, and especially the derivative of ferroelectric polarization, $dP(E_{ex,z})/dE_{ex,z}$; this comparison reveals the motivation for the interaction between FM and PE constituents that leads to the modulation of PE coefficients by the $H_{ex,z}$.

I. Piezoelectric data for PZT-5%Fe₃O₄ samples in the absence/presence of an $H_{ex,z}$

The constitutive in-plane strain-electric field curves, $S(E_{ex,z})$, of two PZT-5%Fe₃O₄ samples were estimated experimentally by using the OM-based technique already described in detail in the subchapter 2.3.1.A for an out-of-plane $E_{ex,z}$ up to 10 kV/cm. For this study, we made a modification in the home-made aluminum platform presented in the subchapter 2.3.1.B, so that a constant, also out-of-plane magnetic field, $H_{ex,z}$, is applied at will, by a NdFeB permanent magnet. By means of this experimental setup, the in-plane strain curves, $S_{zx}(E_{ex,z})$ and $S_{zy}(E_{ex,z})$, were recorded under the absence/presence of an $H_{ex,z}$. It should be noted that a specific protocol was followed for recording the in-plane strain curves, discussed at the subchapter 2.3.1.C.

The in-plane PE coefficients obtained upon application and removal of a constant $H_{ex,z}$ are shown in Fig. 3.23 for a square-shaped sample, (a.i)-(d.i), and for a disc-shaped sample, (a.ii)-(d.ii). The insets of the panels (a.i) and (a.ii) present photos of the specific samples together with an arbitrarily chosen coordinate system; the latter is used to assist us to define the

symmetry axes x (SA_x) and y (SA_y). For both samples, the investigated area was chosen at the edge of the sample, along SA_y , as shown with a white dot.

Regarding the experimental process, six consecutive $S(E_{ex,z})$ loops were recorded assigned by a loop index; first, without the application of $H_{ex,z}$ (loop index: 1 and 2), next, under the presence of $H_{ex,z}=1$ kOe (loop index: 3 and 4) and finally, when removing $H_{ex,z}$ (loop index: 5 and 6). In the Figs. 3.23(a.i) and 3.23(a.ii) the mean absolute value of the in-plane PE coefficient in the y -direction, $\langle |d_{zy}| \rangle$, is presented for the complete sequence of measurements. We note that the other in-plane PE coefficient in the x -direction, d_{zx} , is not shown, since it is obviously zero [53].

More specifically, Figs. 3.23(a.i) and 3.23(a.ii) present detailed data on $\langle |d_{zy}| \rangle$ before the application (loop index: 1 and 2), upon application (loop index: 3 and 4) and after removal (loop index: 5 and 6) of a constant $H_{ex,z}=1$ kOe. As already shown from the magnetization data shown in Figs 3.11, the specific magnetic field value ($H_{ex,z}=1$ kOe) is adequate to bring the soft FM NPs of PZT-5% Fe_3O_4 at 75% of its saturation magnetization. The piezoelectric coefficient value $\langle |d_{zy}| \rangle$, for each loop, is calculated from taking the mean of the absolute values of the slopes $|dS_{zy}/dE_{ex,z}|$ corresponding to the linear parts of the respective $S_{zy}(E_{ex,z})$ curve. In Figs. 3.23(b.i)-(d.i) and Figs. 3.23(b.ii)-(d.ii) representative data sets of $S_{zy}(E_{ex,z})$ are shown for the square-shaped and disc-shaped sample, respectively, referring to loop index: 2 (without $H_{ex,z}$, (b.i) and (b.ii)), loop index: 4 (with $H_{ex,z}$, (c.i) and (c.ii)) and loop index: 6 (without $H_{ex,z}$, (d.i) and (d.ii)). It should be noted that, as expected according to the basics principles of this method [53], the respective $S_{zx}(E_{ex,z})$ loops are practically horizontal lines, since the investigated area lies exclusively onto SA_y .

According to the in-plane $S_{zy}(E_{ex,z})$ presented in Figs. 3.23(b.i)-(d.i)/(b.ii)-(d.ii) we deduce that with the first turn of $H_{ex,z}$ application, the $S_{zy}(E_{ex,z})$ curves become narrower (Figs. 3.23(b.i)/(b.ii) vs Figs. 3.23(c.i)/(c.ii)). Interestingly, upon subsequent removal of $H_{ex,z}$ the $S_{zy}(E_{ex,z})$ curves retrieve their original form, almost completely; obviously, the in-plane PE coefficients follow this behavior. Hence, what we observe from these measurements is a drastic decrease of the in-plane PE coefficients on the order of 50-60%, which is retrieved when $H_{ex,z}$ is removed, as clearly shown in Figs. 3.23(a.i) and 3.23(a.ii).

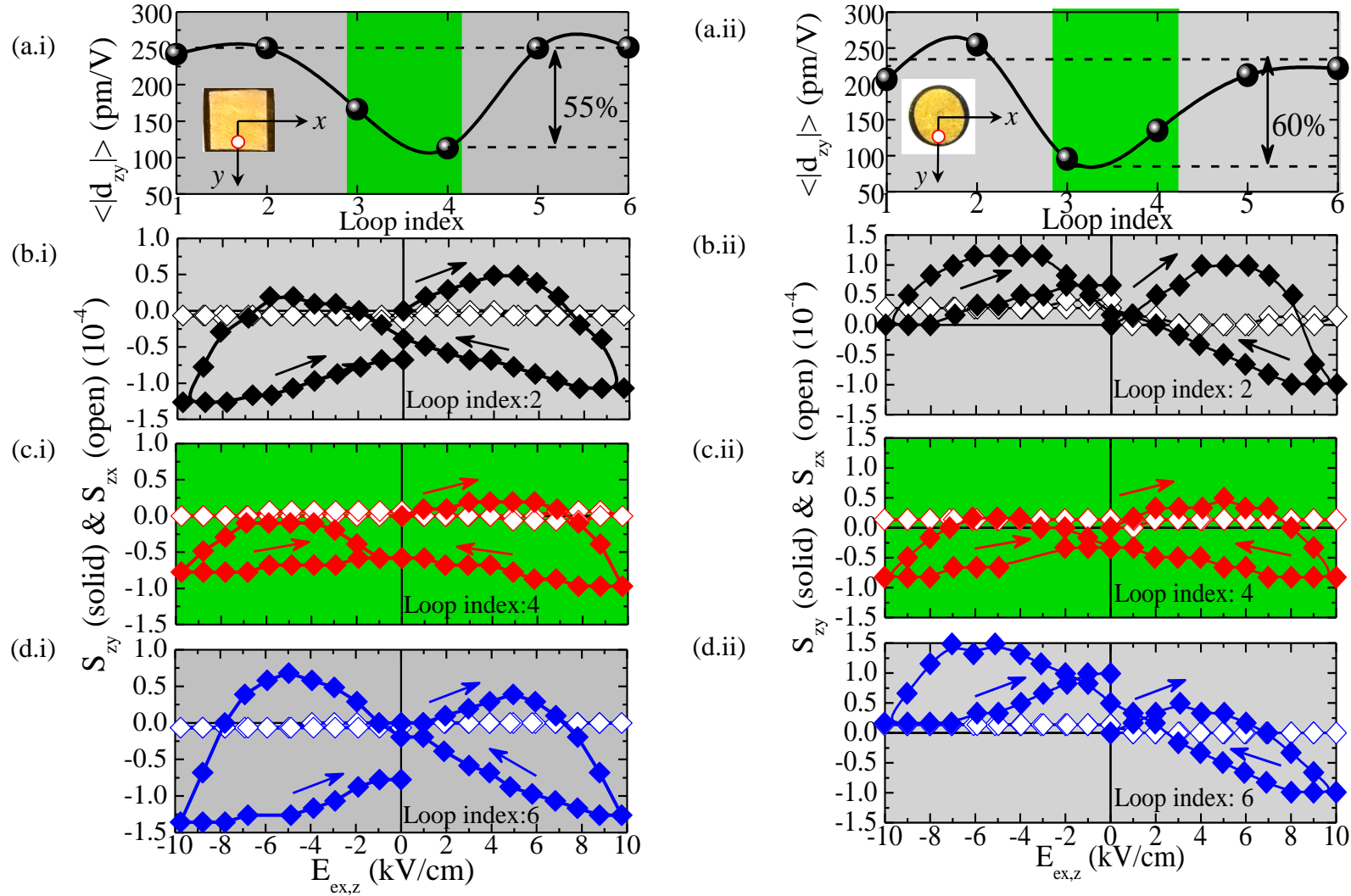


Figure 3.23. (a.i)-(d.i) & (a.ii)-(d.ii) PE data corresponding to (a.i)-(d.i) square-shaped (sample side: 7 mm) and (a.ii)-(d.ii) disc-shaped (diameter 6 mm), PZT-5%Fe₃O₄ samples. The inset photos show the respective samples, along with the arbitrarily chosen x and y Cartesian coordinate system. The investigated area is denoted with a dot placed on SA_y for both samples. (a.i) & (a.ii) Mean absolute values of PE coefficients for loop index 1-6 (see text for details regarding their calculation), under the subsequent application and removal of $H_{ex,z}=1$ kOe; specifically, in the absence of $H_{ex,z}$ (Loop index: 1 & 2), under application of $H_{ex,z}$ (Loop index: 3 & 4) and after the removal of $H_{ex,z}$ (Loop index: 5 & 6). (b.i)-(d.i)/(b.ii)-(d.ii) representative $S_{zy}(E_{ex,z})$ and $S_{zx}(E_{ex,z})$ loops (solid and open rhombi, respectively) for the square/disc-shaped sample upon application and removal of $H_{ex,z}=1$ kOe; (b.i)/(b.ii) in the absence of $H_{ex,z}$ (Loop index: 2), (c.i)/(c.ii) under application of $H_{ex,z}$ (Loop index: 4) and (d.i)/(d.ii) after the removal of $H_{ex,z}$ (Loop index: 6). The arrows trace the sequence of $E_{ex,z}$ application. Please, notice that the vertical scale is the same in each group of three panels, (b.i)-(d.i) and (b.ii)-(d.ii), for reasons of comparison.

II. Polarization and leakage current data for both PZT and PZT-5%Fe₃O₄ samples

Figs. 3.24(a)-(c) present comparatively the electric polarization, $P(E_{ex,z})$, its derivative, $dP/dE_{ex,z}$, and the leakage current, I , respectively, upon varying $E_{ex,z}$ in the range $-20 \text{ kV/cm} \leq E_{ex,z} \leq +20 \text{ kV/cm}$, for both PZT and PZT-5%Fe₃O₄ samples.

According to Fig. 3.24(a) it becomes clear that the FM Fe₃O₄ NPs render PZT ferroelectrically harder, since the coercive field, E_c , of the latter increases from 6.7 kV/cm (for plain PZT) to 10.7 kV/cm (for PZT-5%Fe₃O₄). The coercive fields of PZT and PZT-5%Fe₃O₄ are denoted with red and blue thick open circles, respectively, corresponding to the coercive fields E_c^\pm . As already mentioned, the increase of $|E_c^\pm|$ is attributed to the pinning of the FE domains of PZT by the FM Fe₃O₄ NPs. This effect can be probably promoted by the similar size (50-100 nm) of the FE domains of PZT and the Fe₃O₄ NPs. What is more, the nucleation fields, E_{nuc}^\pm , where the ferroelectric domains appear and begin to move/rotate, just before polarization reversal at E_c^\pm , are also indicated with the black open rectangles on $P(E_{ex,z})$ curves. The latter have been designated by the change of slope of the $P(E_{ex,z})$ segments within $E_{ex,z}^\pm=0$ and $E_{ex,z}^\pm=E_c^\pm$; interestingly, we observe that within this $E_{ex,z}$ range both $P(E_{ex,z})$ curves almost coincide until their concurrent splitting at E_{nuc}^\pm . Hence, though E_c^\pm increase with the addition of Fe₃O₄ NPs due to structural disorder, E_{nuc}^\pm remain practically unaltered, approximately at $E_{nuc}^\pm = \pm 6 \text{ kV/cm}$. The red/blue and grey-shaded areas in all panels serve as guides-to-the-eye, aiming to highlight the connection of the features presented in the panels (b) and (c) with the characteristic fields E_c^\pm and E_{nuc}^\pm respectively.

Accordingly, regarding the derivative of polarization, $dP/dE_{ex,z}$, presented in Fig. 3.24(b) for PZT and PZT-5%Fe₃O₄, we can see that the peaks exhibited for both curves are associated with the respective E_c^\pm , as denoted by the blue and red shaded-areas. Also, the gray-shaded areas trace the $P(E_{ex,z})$ segments that correspond to E_{nuc}^\pm around 6 kV/cm. From the $dP/dE_{ex,z}$ data, it becomes clear that the nucleation process occurs more abruptly for PZT (where $E_c^\pm \approx E_{nuc}^\pm$) and more gradually for PZT-5%Fe₃O₄ (where $|E_c^\pm| > |E_{nuc}^\pm|$).

Fig. 3.24(c) presents the leakage current, I , upon variation of $E_{ex,z}$ for PZT and PZT-5%Fe₃O₄. In accordance with the $P(E_{ex,z})$ and $dP/dE_{ex,z}$ data presented in Figs. 3.24(a) and 3.24(b), respectively, I also displays peaks in both curves, signifying that the maximum current density occurs at E_c^\pm . Also, these peaks change polarity depending on the applied $E_{ex,z}$ and are clearly associated with the domain switching that occurs at E_c^\pm . The gray-shaded areas corresponding to E_{nuc}^\pm are also shown.

The reproducibility of the results presented in the subchapter 3.2.3, right above, was confirmed by employing three different PZT-5%Fe₃O₄ samples for the in-plane strain measurements (see the samples ‘S.4.1’-‘S.4.3’ in Table 2.1, at the end of chapter 2).

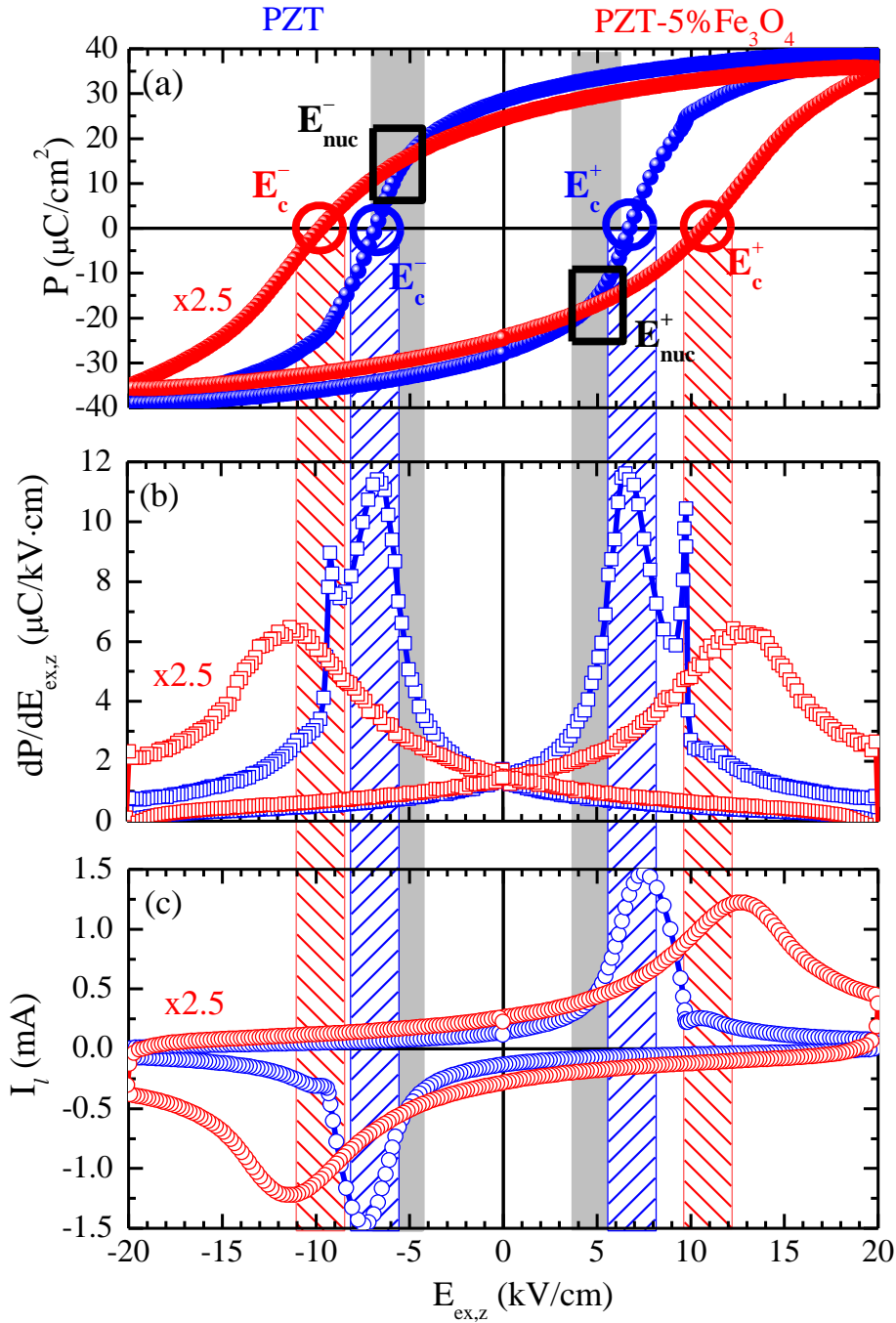


Fig. 3.24: (a)-(c) Electric polarization, $P(E_{ex,z})$, derivative of polarization, $dP/dE_{ex,z}$, and leakage current, $I_l(E_{ex,z})$, respectively, upon $E_{ex,z}$ ranging within $-20 \text{ kV/cm} \leq E_{ex,z} \leq +20 \text{ kV/cm}$, for both PZT (blue colored symbols) and PZT-5% Fe_3O_4 (red colored symbols) samples. In panel (a), the coercive (E_c^\pm) and nucleation (E_{nuc}^\pm) fields are denoted with blue/red circles and black rectangles, respectively. Accordingly, in all panels, the parts of the curves denoted by the blue/red-shaded areas correspond to E_c^\pm while the ones denoted by the gray shaded areas, correspond to E_{nuc}^\pm . In particular, in panels (b) and (c), the peaks of $dP(E_{ex,z})/dE_{ex,z}$ and $I_l(E_{ex,z})$ (indicated by the arrows) correspond to E_c^\pm , while the smoothly changing parts of the curves (highlighted by the gray-shaded areas) correspond to E_{nuc}^\pm . All the data referring to PZT-5% Fe_3O_4 samples (red colored symbols) are multiplied by a factor of 2.5 for the sake of presentation.

III. Comparison of in-plane strain and polarization data

The comparison of the data presented above, namely the in-plane strain, $S_{zy}(E_{ex,z})$ and electric polarization, $P(E_{ex,z})$, clearly demonstrates that the peaks observed in the $S_{zy}(E_{ex,z})$ curves of Figs. 3.23(b.i)-(d.i)/(b.ii)-(d.ii) correspond to the nucleation fields, E_{nuc}^{\pm} . Accordingly, we deduce that the nucleation process (formation/movement/rotation of FE domains which leads to strain maximization) gets suppressed when $H_{ex,z}$ is applied, while it recovers upon $H_{ex,z}$ removal. Notably, these results clearly evidence that the FM Fe_3O_4 NPs do not simply serve as *static structural disorder*, but also introduce *reconfigurable magnetic disorder* that modifies the in-plane strain-electric field curves and the accompanying PE coefficients when an external magnetic field is applied at will. This certainly demonstrates the existence the ME coupling between the two constituents that was also discussed in the study of the previous subchapter 3.2.2.

The results of this study referring to magnetic-field control of the PE coefficients d_{zi} ($i=x,y$), meet three significant characteristics; first, the modulation of the in-plane PE coefficients is impressive in magnitude, 60%, for the two samples examined. Second, the modulation is almost completely reversible, while third, these features are feasible at room temperature upon using a relatively low magnetic field, $H_{ex,z}=1$ kOe. At this point, it is worth to recall the discussion in the subchapter ‘1.3.3 Review in the direct and converse magnetoelectric effect for bulk composite multiferroics’, focusing on the direct ME effect that is the subject of this subchapter. Accordingly, recent relevant studies reviewed in there, report variations of similar magnitude in other relevant parameters upon H_{ex} application such as the polarization and piezoresponse but not in the variation of the PE coefficients, presented here. For example, D. M. Evans et al. report an average change of 60% in the polarization of $PbZr_{0.53}Ti_{0.47}O_3$ - $PbFe_{0.5}Ta_{0.5}O_3$ single crystals for a relatively high H_{ex} variation of 6 kOe, between the +3 kOe and -3 kOe states. However, as already reported by the authors, this variation, although noticeable in magnitude, it is partially reversible upon reversing once again H_{ex} back to +3 kOe, with the polarization attaining a 40% higher value in comparison to that of the original state. Moreover, S. H. Xie et al. demonstrated a percentage variation on the order of 40% in the piezoresponse of a $PbZrTiO$ - $TbDyFe$ bilayer upon application of +2 kOe. In this case, the authors report a further increase of the piezoresponse upon reversing the magnetic field to -2 kOe, a clear proof that in this case the overall process is entirely irreversible.

3.2.4 Underlying mechanism of the ME coupling in the PZT-5% Fe_3O_4 composite

The experimental results that were previously discussed in the subchapters 3.2.2 and 3.2.3 show that the modulation of the FM/PE properties of a PZT-5% Fe_3O_4 composite by an $E_{ex,z}/H_{ex,z}$ is attributed to the ME interactions between its PE and FM constituents. In general, the ME coupling is known to occur via three different mechanisms; charge modulation, exchange interaction modulation and strain transfer [63]. The first two mechanisms are active at a short range, by a FE/FM interface. Thus, we believe that for the case of the PZT-5% Fe_3O_4 composite the strain transfer mechanism is at play, since it is active at length scales on the order of 100-200 nm [64,65]. In fact, many studies in MF composites, often refer to strain transfer between

PE/FM interfaces [66-68]. For example, Yu et al. [66] reported strain-induced modulation of perpendicular magnetic anisotropy in $(1-x)\text{Pb}(\text{Mg}_{1/3}\text{Nb}_{2/3})\text{O}_3\text{-PbTiO}_3$ substrate/Ta/CoFeB/MgO/Ta structures. The in-plane biaxial strain produced by electric-field application to the $(1-x)\text{Pb}(\text{Mg}_{1/3}\text{Nb}_{2/3})\text{O}_3\text{-PbTiO}_3$ substrate is transferred to the CoFeB layer by tuning its perpendicular magnetic anisotropy. Additionally, Wang et al. [67] reported strain-mediated magnetic anisotropy variation upon electric field application for CoFe_2O_4 thin films on $(1-x)\text{Pb}(\text{Mg}_{1/3}\text{Nb}_{2/3})\text{O}_3\text{-PbTiO}_3$ single crystals, with $x=28\%$, 29.5% and 30% ; the rhombohedral to orthorhombic structural transition of $(1-x)\text{Pb}(\text{Mg}_{1/3}\text{Nb}_{2/3})\text{O}_3\text{-PbTiO}_3$ induced a large strain to the CoFe_2O_4 thin films. What is more, recently Kumar et al. [68], based on the strain transfer mechanism, interpreted the results obtained in a relevant multiferroic $\text{BiFeO}_3\text{-BaTiO}_3$ alloy system in which FM arises from a small fraction (~ 1 wt%) of $\text{BaFe}_{12}\text{O}_{19}$ that is formed during sintering. A noticeable increase of the saturation polarization ($\sim 34\%$) was observed upon applying a magnetic field on the order of 10 kOe; this finding was attributed this finding to the transfer of magnetostrictive strain from the FM $\text{BaFe}_{12}\text{O}_{19}$ grains to the adjacent FE ones.

In an analogous manner, the strain transfer for PZT-5% Fe_3O_4 composite occurs thanks to the remarkable PE behavior of PZT and the magnetostrictive nature of Fe_3O_4 (and Fe_2O_3) NPs. Specifically, as we discussed in the subchapter 1.2.4.II.B, the magnetostriction constant, λ , of bulk Fe_3O_4 ranges within 20×10^{-6} to 90×10^{-6} for single crystals and 30×10^{-6} to 50×10^{-6} for polycrystalline samples, whereas λ is around 10×10^{-6} for bulk Fe_2O_3 . Regarding Fe_3O_4 and Fe_2O_3 NPs, the magnetostrictive constants remain almost the same with the bulk ones, except for ultrasmall NPs with size on the order of 5 nm. Interestingly, the magnetostriction constant values of Fe_3O_4 and Fe_2O_3 are almost comparable to the PE coefficient ones of PZT (10^{-4}). Hence, we can plausibly assume that the elastic interactions is a key characteristic that motivates/promotes an efficient interface strain transfer between the iron oxide NPs (especially the Fe_3O_4 ones) and the surrounding PZT matrix.

In this context, regarding the electric-field control of magnetic properties (see subchapter 3.2.2) we believe that the strain generated from the PZT matrix, due to the converse PE effect, is transferred across the interfaces to the Fe_3O_4 NPs, affecting their remanent magnetization, via the converse magnetostrictive effect. In turn, regarding the magnetic-field control of PE properties (see subchapter 3.2.3), we suggest that the strain originating from the magnetostrictive iron oxides, due to the direct magnetostrictive effect, can be transported to the PZT matrix, altering its PE strain. Notably, the fact that the experimental procedure was almost reversible upon the removal of the magnetic field (i.e. the PE coefficients were almost restored) indicates that the underlying cause was a linear magnetostrictive effect [69], [70].

References

- [1] Z. Xiao et al., *Sci. Rep.* **8**, 5207 (2018).
- [2] W. Eerenstein, N. D. Mathur, and J. F. Scott, *Nature* **442**, 759 (2006).
- [3] N. Ortega, A. Kumar, J. F. Scott, and R. S. Katiyar, *J. Phys.: Condens. Matter.* **27**, 504002 (2015).
- [4] J. F. Scott, *Nat. Mater.* **6**, 256 (2007).
- [5] M. Hehn, S. Padovani, K. Ounadjela, and J. P. Bucher, *Phys. Rev. B* **54**, 3428 (1996).

- [6] L. Jin, F. Li, and S. Zhang, *J. Am. Ceram. Soc.* **97**, 1 (2014).
- [7] J. Wang et al., *J. Nanomater.* **2010**, 142750 (2010).
- [8] Z. Li, J. Wang, Y. Lin, C. W. Nan, *Appl. Phys. Lett.* **96**, 162505 (2010).
- [9] E. Arzt, *Acta Mater.* **46**, 5611 (1998).
- [10] Y. P. Zhao et al., *J. Appl. Phys.* **89**, 1325 (2001).
- [11] M. Li, G. C. Wang, and H. G. Min, *J. Appl. Phys.* **83**, 5313 (1998).
- [12] M. Li, Y. P. Zhao, G. C. Wang, and H. G. Min, *J. Appl. Phys.* **83**, 6287 (1998).
- [13] J. Brandenburg, R. Huhne, L. Schultz, and V. Neu, *Phys. Rev. B* **79**, 054429 (2009).
- [14] S. P. Li, A. Samad, W. S. Lew, Y. B. Xu, and J. A. C. Bland, *Phys. Rev. B* **61**, 6871 (2000).
- [15] M. Gajek et al., *Nat. Mater.* **6**, 296 (2007).
- [16] M. Liu, J. Lou, S. Li, and N. X. Sun, *Adv. Funct. Mater.* **21**, 2593 (2011).
- [17] M. Vopsaroiu, J. Blackburn, M. G. Cain, *J. Phys D: Appl. Phys.* **40**, 5027 (2007).
- [18] H. Barkhausen, *Z. Phys.* **20**, 401 (1919).
- [19] A. Benassi and S. Zapperi, *Phys. Rev. B* **84**, 214441 (2011).
- [20] G. Durin and S. Zapperi 2006 *The Science of Hysteresis* vol II ed G. Bertotti and I. D. Mayergoyz (New York: Academic) 181.
- [21] S. Zapperi, P. Cizeau, G. Durin, and H. E. Stanley, *Phys. Rev. B* **58**, 6353 (1998).
- [22] D.-H. Kim, S.-B. Choe, and S.-C. Shin, *Phys. Rev. Lett.* **90**, 087203 (2003).
- [23] R. G. Mints and A. L. Rakhmanov, *Rev. Mod. Phys.* **53**, 551 (1981).
- [24] P. Esquinazi, et al., *Phys. Rev. B* **60**, 12454 (1999).
- [25] P. S. Swartz and C. P. Bean, *J. Appl. Phys.* **39**, 4991 (1968).
- [26] R. G. Mints and E. H. Brandt, *Phys. Rev. B* **54**, 12421 (1996).
- [27] D. Stamopoulos, A. Speliotis, and D. Niarchos, *Supercond. Sci. Technol.* **17**, 1261 (2004).
- [28] D. Stamopoulos and D. Niarchos, *Physica C* **417**, 69 (2004).
- [29] P. Esquinazi, et al., *Phys. Rev. B* **60**, 12454 (1999).
- [30] C. P. Bean, *Rev. Mod. Phys.* **36**, 31 (1964).
- [31] A. M. Campbell and J. E. Evetts, *Adv. Phys.* **21**, 199 (1972).
- [32] F. Wang, S. W. Or, X. Zhao, and H. Luo, *J. Phys. D: Appl. Phys.* **42**, 182001 (2009).
- [33] F. Wang, W. Shi, S. W. Or, X. Zhao, and H. Luo, *Mater. Chem. Phys.* **125**, 718 (2011).
- [34] F. Martin, H. J. M. ter Brake, L. Lebrun, S. J. Zhang, and T. Shrout, *J. Appl. Phys.* **111**, 104108 (2012).
- [35] Y. N. Huang et al., *Phys. Rev. B* **55**, 16159 (1997).
- [36] C. Thiele, K. Dörr, O. Bilani, J. Rödel, and L. Schultz, *Phys. Rev. B* **75**, 054408 (2007).
- [37] N. Lei et al., *Nat. Commun.* **4**, 1378 (2013).
- [38] X. Tang et al., *Sci. Rep.* **8**, 1628 (2018).
- [39] F. Wang, C. Zhou, D. Gesang, C. Jiang, *Nanoscale Res. Lett.* **12**, 104 (2017).
- [40] T. Wu et al., *Appl. Phys. Lett.* **98**, 012504 (2011).
- [41] D. Stamopoulos, M. Zeibekis, G. Vertsioti, and S. J. Zhang, *J. Appl. Phys.* **116**, 084304 (2014).
- [42] M. Etier et al., *Ferroelectrics* **448**, 77 (2013).
- [43] M. Naveed-Ul-Haq et al., *Sci. Rep.* **6**, 32164 (2016).
- [44] D. Dipti, J. K. Juneja, S. Singh, K. K. Raina, and C. Prakash, *Ceram. Int.* **41**, 6108 (2015).

- [45] J. H. Park, M. G. Kim, S.-J. Ahn, S. Ryu, and H. M. Jang, *J. Magn. Magn. Mater.* **321**, 1971 (2009).
- [46] S. Narendra Babu, S. V. Suryanarayana, and T. Bhimasankaram, *J. Alloys Compd.* **473**, 418 (2009).
- [47] K. Singh and D. Kaur, *J. Phys. D: Appl. Phys.* **50**, 145002 (2017).
- [48] G. Srinivasan, E.T. Rasmussen, and R. Hayes, *Phys. Rev. B* **67**, 014418 (2003).
- [49] M. Bibes and A. Barthelemy, *Nat. Mater.* **7**, 425 (2008).
- [50] M. Takahashi, *Jap. J. Appl. Phys.* **10**, 5 (1971).
- [51] N. M. Botrous El Badramany, E. F. Mina, H. D. Merchant, S. Arafa, R. P. Poplawsky, *J. Am. Ceram. Soc.* **62**, 3 (1979).
- [52] Cornell, R. M. & Schwertmann, U. *The Iron oxides: Structure, Properties, Reactions, Occurrences and Uses*, WILEY-VCH Verlag GmbH & Co (2003).
- [53] M. Zeibekis, G. Vertsioti, and D. Stamopoulos, *J. Phys.D: Appl. Phys.* **49**, 105304 (2016).
- [54] A. Henriques et al., *AIP Adv.* **4**, 117125 (2014).
- [55] W. Cao, W. and C. A. Randall, *J. Phys. Chem. Solids* **57**, 1499 (1996).
- [56] A. Gruverman, A. et al., *Appl. Phys. Lett.* **71**, 24 (1997).
- [57] S. K. Mishra and D. Pandey, *J. Phys.: Condens. Matter* **7**, 9287 (1995).
- [58] M. Safar, T. W. Button, and M. Zabcik, Proceedings of the 2017 Joint IEEE International Symposium on the Applications of Ferroelectric (ISAF)/International Workshop on Acoustic Transduction Materials and Devices (IWATMD)/Piezoresponse Force Microscopy, Atlanta, GA, USA, (2017).
- [59] Quantum Design MPMS Application Note 1014-822 (2001).
- [60] J.-M. Hu, C.-J. Duan, C.-W. Nan, and L.-Q. Chen, *npj Comput. Mater.* **3**, 18 (2007).
- [61] S. Chen et al., *J. Alloys Compd.* **506**, 537 (2010).
- [62] V. V. Shvartsman, F. Alawneh, P. Borisov, D. Kozodaev, and D. C. Lupascu, *Smart Mater. Struct.* **20**, 075006 (2011).
- [63] S. van Dijken, S., *Handbook of Spintronics Vol. 1* (eds Xu, Y. et al.) Ch. 10, 365, Springer, Netherlands (2015).
- [64] W. Cao and C. A. Randall, *J. Phys. Chem. Solids* **57**, 1499 (1996).
- [65] A. Gruverman et al., *Appl. Phys. Lett.* **71**, 24 (1997).
- [66] G. Yu et al. *Appl. Phys. Lett.* **106**, 072402 (2015)
- [67] Z. Wang, Y. Wang, W. Ge, J. Li, and D. Viehland, *Appl. Phys. Lett.* **103**, 132909 (2013).
- [68] A. Kumar, B. Narayan, R. Pachat, and R. Ranjan, *Phys. Rev. B* **97**, 064103 (2018).
- [69] G. Vertsioti, M. Pissas, S. J. Zhang, D. Stamopoulos, *J. Appl. Phys.* **126**, 044104 (2019).
- [70] G. Vertsioti, S. J. Zhang, and D. Stamopoulos, *Sci. Rep.* **9**, 2178 (2019).

Chapter 4: Applicability and limitations of the OM-based local experimental technique for the estimation of the in-plane strain-electric field curves and piezoelectric coefficients

In this chapter we inspect more profoundly the experimental technique that was previously presented in the subchapter ‘2.3.1 Optical Microscopy-Generic local experimental technique for recording the in-plane strain-electric field curve by means of optical microscopy’. Specifically, we evaluate its accuracy; to this end, in the subchapter 4.1 we present an empirical model that we introduced, referring to the relative error in strain, $\delta S/S$, estimated from Eq. 2.7 of the subchapter 2.3.1, under variation of the relevant parameters met in experimental practice (such as resolution of the optical microscope, nominal strain value of the material for a specific electric field regime and size of the sample) for reference materials employed in current technological applications (such as $\text{BiFeO}_3\text{-BaTiO}_3$, $\text{Pb}(\text{Zr,Ti})\text{O}_3$ and $\text{Pb}(\text{Mg,Nb})\text{O}_3\text{-PbTiO}_3$). In the subchapter 4.2 we present simulations based on this empirical model, in order to quantify the accuracy of the technique, taking into account realistic parameter values. For better comprehension, we suggest to the general reader to address the subchapter 2.3.1 and Appendix A.

4.1. Empirical model

As already discussed in the subchapter 2.3.1.A, we have defined as x_i the initial position of the CP in a strain-free sample, as x_f the final position of the CP under $E_{\text{ex,z}}$ application (see Figs. 2.8(a.i)-2.8(a.iii) and 2.8(b.i)-2.8(b.iii)), and as $\Delta x = x_f - x_i$ the respective displacement. The estimated PE strain, i.e. the relative length change of the sample’s dimensions, is:

$$S = \frac{x_f - x_i}{x_i} = \frac{\Delta x}{x_i} \quad (4.1)$$

with S depending on the endogenous PE properties of the material. Obviously, in the case of materials with larger PE response (i.e. larger S), the respective displacements Δx become more distinguishable; as a result, Δx measurement can be performed more accurately, by means of the technique described in the subchapter 3.3.1. Accordingly, the error stemming from Δx reading should be proportionate to Δx :

$$\delta \Delta x = C_1 \cdot \Delta x \quad (4.2)$$

with C_1 a numerical factor. Specifically, C_1 should be a function of Δx , that is $C_1(\Delta x)$, and satisfy the boundary conditions:

$$\begin{aligned} \lim_{\Delta x \rightarrow \infty} C_1(\Delta x) &= 0 \quad (4.3.i) \\ \lim_{\Delta x \rightarrow R_{\text{OM}}} C_1(\Delta x) &= 1 \quad (4.3.ii) \end{aligned}$$

where R_{OM} is the resolution corresponding to a processed OM image (see Appendix A).

The first boundary condition value is obvious. Regarding the second, we consider that $\delta S = \Delta x$ when $\Delta x \rightarrow R_{OM}$, since the case that the error is higher than the parameter that we measure (i.e. $\delta S > \Delta x$) has no physical meaning.

More specifically, as mentioned above for $\Delta x \leq R_{OM}$, $C_1(\Delta x) = 1$. On the other hand, for $\Delta x \geq R_{OM}$, $C_1(\Delta x)$ should follow the commonly used exponential distribution. The respective expressions are shown below:

$$\begin{aligned} C_1(\Delta x) &= 1, \text{ for } \Delta x \leq R_{OM} \quad (4.4.i) \\ C_1(\Delta x) &= e^{-(\Delta x - R_{OM})}, \text{ for } \Delta x \geq R_{OM} \quad (4.4.ii) \end{aligned}$$

From equations (4.1) and (4.2), the error in the estimated strain is given by the relation:

$$\delta S = \frac{\delta \Delta x}{x_i} = C_1 \cdot \frac{\Delta x}{x_i} \quad (4.5)$$

Also, from equations (4.4.ii) and (4.5) the error in the estimated strain, δS , can be written as:

$$\delta S = \frac{R_{OM}}{x_i} e^{-(\Delta x - R_{OM})} \quad (4.6)$$

Accordingly, the boundary conditions shown below should be satisfied:

$$\begin{aligned} \lim_{\Delta x \rightarrow \infty} \delta S &= 0 \quad (4.7.i) \\ \lim_{\Delta x \rightarrow R_{OM}} \delta S &= \frac{R_{OM}}{x_i} \quad (4.7.ii) \end{aligned}$$

Hence, from equations (4.1) and (4.6), the relative error in the strain estimated by the technique described in the subchapter 2.3.1 is expressed as:

$$\frac{\delta S}{S} = \frac{R_{OM}}{S \cdot x_i} e^{-(S \cdot x_i - R_{OM})} \quad (4.8)$$

Equation (4.8) describes an empirical model that was employed for the simulations presented in the next subchapter 4.3 (Figs. 4.2-4.4). The introduced parameters are R_{OM} , x_i , and S ; the range of their input values was selected taking into consideration technical characteristics of our experimental technique (referring to R_{OM} and x_i) and endogenous properties of commonly used PE materials (referring to S).

4.2. Simulations data

In the context of the OM-based PE technique that we employ, we have deduced that the resolution corresponding to a processed OM image, R_{OM} , is $R_{OM} = 0.20 \mu\text{m}$ (for details, see Appendix A). However, since this is a generic technique that can be used for various optical microscopes with different resolving power (better or worse than ours) in the following simulations we will use a broader range of R_{OM} , within $0.10\text{-}0.50 \mu\text{m}$.

Regarding x_i , we considered realistic sample size values within the length scale $2 \cdot 10^3 \mu\text{m}$ and $10 \cdot 10^3 \mu\text{m}$. As it is explained in detail in Ref. [1], the initial distance of the CP from the symmetry center, x_i , (see also Fig. 2.8 of subchapter 2.3.1.A for details) is practically the half of the total sample length, along the respective symmetry axis. Thus, we introduce x_i values ranging between $1 \cdot 10^3 \mu\text{m}$ and $5 \cdot 10^3 \mu\text{m}$. For simplicity reasons, we will refer to x_i as sample size for the rest of this chapter.

Additionally, we introduced S , an endogenous property of each material which is the nominal value of strain under a specific electric field regime, clearly determining the displacement of the CP. We examined three indicative materials, $\text{BiFeO}_3\text{-BaTiO}_3$ (BTO-BFO), PZT and PMN-PT, corresponding to low, intermediate and high PE strain, respectively; we introduced S values ranging between $1 \cdot 10^{-4}$ and $5 \cdot 10^{-3}$ [2-4]. The latter are representative strain values for these materials corresponding to electric field on the order of 10 kV/cm , which is the maximum $E_{\text{ex,z}}$ applied to our samples.

The 3D plot shown in figure 2 is a representative simulation of $\delta S/S$, for constant $x_i = 5 \cdot 10^3 \mu\text{m}$, and variable S and R_{OM} , ranging within $1 \cdot 10^{-4} \leq S \leq 5 \cdot 10^{-3}$ and $0.1 \mu\text{m} \leq R_{\text{OM}} \leq 0.5 \mu\text{m}$, respectively. As expected, $\delta S/S$ decreases with increasing S -i.e. as the displacements of a CP get enhanced- and with decreasing R_{OM} -i.e. as the resolution improves.

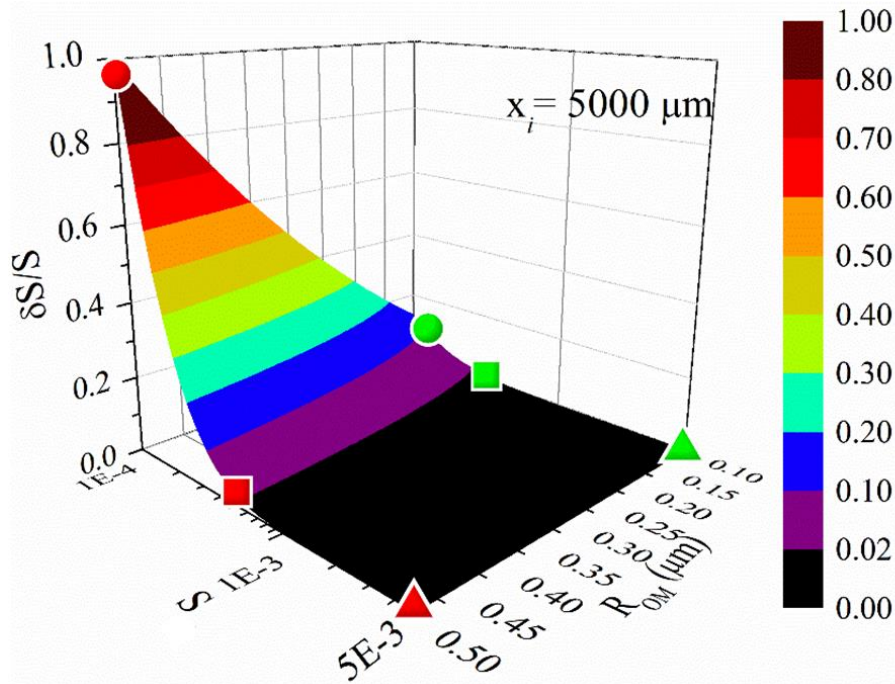


Fig. 4.1: Simulation of relative error in the estimated strain, $\delta S/S$, according to Eq. (4.8) with parameters the length in a strain-free sample, x_i , the resolution of the OM, R_{OM} , (in linear scale) and the strain, S (in logarithmic scale). The simulation has been realized by varying the pair of values (S, R_{OM}) , within the range $1 \cdot 10^{-4} \leq S \leq 5 \cdot 10^{-3}$ and $0.10 \mu\text{m} \leq R_{\text{OM}} \leq 0.50 \mu\text{m}$, under constant $x_i = 5 \cdot 10^3 \mu\text{m}$. The circles, squares and triangles address S values representative to BTO-BFO ($S_{\text{en}} = 1 \cdot 10^{-4}$), PZT ($S = 5 \cdot 10^{-4}$) and PMN-PT ($S = 5 \cdot 10^{-3}$), respectively, for $R_{\text{OM}} = 0.50 \mu\text{m}$ (red symbols) and $R_{\text{OM}} = 0.10 \mu\text{m}$ (green symbols).

The circles, squares and triangles in Fig. 4.1 correspond to the representative cases of materials BTO-BFO ($S = 1 \cdot 10^{-4}$), PZT ($S = 5 \cdot 10^{-4}$) and PMN-PT ($S = 5 \cdot 10^{-3}$), respectively. For each one,

we spotted the respective $\delta S/S$ value corresponding to $R_{OM}=0.10 \mu\text{m}$ (green colored-shapes) and $R_{OM}=0.50 \mu\text{m}$ (red colored-shapes). Accordingly, for the optimum resolution value, $R_{OM}=0.10 \mu\text{m}$, $\delta S/S$ is 0.13 (13%) for BTO-BFO, 0.005% (0.5%) for PZT and practically negligible for PMN-PT. For the worst case resolution value, $R_{OM}=0.50 \mu\text{m}$, $\delta S/S$ strongly increases up to 1 (100%) for BTO-BFO, it attains the low value of 0.03 (3%) for PZT while for the advantageous material PMN-PT, it remains practically negligible. Regarding the materials with the higher PE performance, PZT and PMN-PT, the relative error in the estimated strain is less than $\delta S/S=5\%$ over the whole R_{OM} range. This fact indicates that their PE deformations can be accurately estimated using our technique. On the contrary, for materials with lower PE performance, like BTO-BFO, the relative error increases drastically with R_{OM} . Consequently, in the rest of the chapter we present simulations for materials with $S \geq 5 \times 10^{-4}$, which are in fact those mainly employed in technological applications [5-7]. In this context, three sets of detailed simulations will be presented below in Figs. 4.2-4.4, based on the empirical model described by Eq. (4.8). The parameters R_{OM} , x_i and S , range within $0.10 \mu\text{m} \leq R_{OM} \leq 0.50 \mu\text{m}$, $1 \times 10^3 \mu\text{m} \leq x_i \leq 1 \times 10^3 \mu\text{m}$ and $5 \times 10^{-4} \leq S \leq 5 \times 10^{-3}$, respectively. In each Fig., two of the parameters vary simultaneously, while the third one remains constant.

Figs. 4.2(a) and 4.2(b) show $\delta S/S$ upon varying x_i and R_{OM} , while S is kept constant, taking the values $S=5 \times 10^{-4}$ and $S=5 \times 10^{-3}$, respectively. In both Figs. we observe that $\delta S/S$ decreases with increasing x_i and with decreasing R_{OM} . Specifically, in Fig. 4.2(a) we observe that in the case of $S=5 \times 10^{-4}$ (representative of PZT), $\delta S/S$ remains below the tolerable value of 0.10 (10%) in the whole R_{OM} range only when the sample size does not exceed the threshold value $x_i \geq 2.5 \times 10^3 \mu\text{m}$. On the contrary, in figure 4.2(b) we see that in the case of a relatively higher $S=5 \times 10^{-3}$ (representative of PMN-PT), $\delta S/S$ is practically negligible in the whole range of both x_i and R_{OM} .

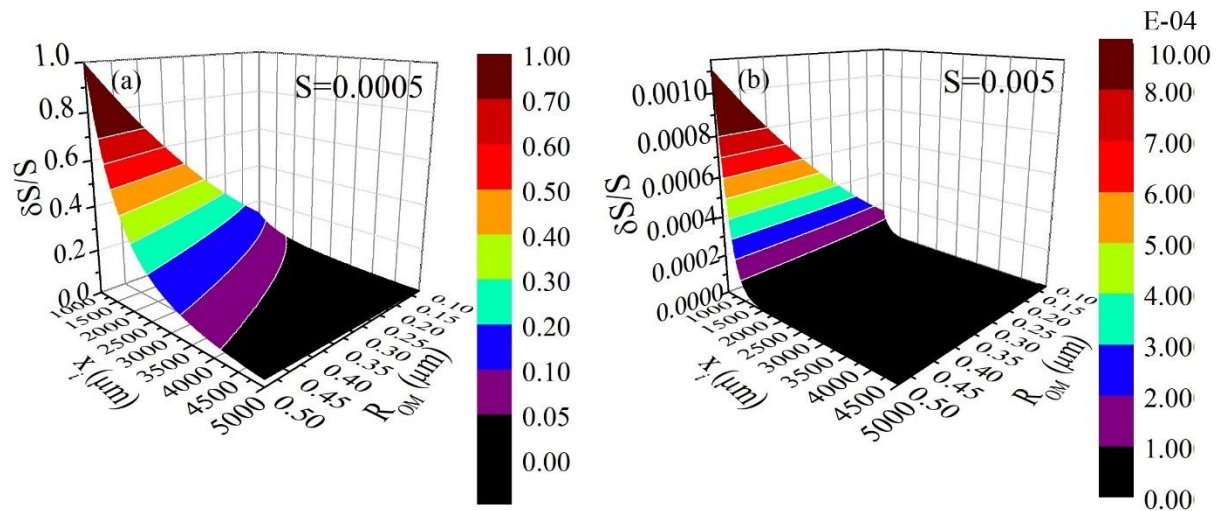


Fig. 4.2: Simulations of relative error in the estimated strain, $\delta S/S$, according to Eq. (4.8), realized by varying the pair of parameters (x_i, R_{OM}) , within the range $1000 \mu\text{m} \leq x_i \leq 5000 \mu\text{m}$ and $0.10 \mu\text{m} \leq R_{OM} \leq 0.50 \mu\text{m}$, under constant (a) $S=5 \times 10^{-4}$ (representative of a PZT sample) and (b) $S=5 \times 10^{-3}$ (representative of a PMN-PT sample). Please notice that the color scale in this panel is on the order of 10^{-4} .

Figs. 4.3(a) and 4.3(b) present $\delta S/S$ upon varying S and x_i , while R_{OM} is kept constant with $R_{OM}=0.10 \mu\text{m}$ and $R_{OM}=0.50 \mu\text{m}$, respectively; these simulations aim to examine the effect R_{OM} on $\delta S/S$. Both Figs. 4.3(a) and 4.3(b) show that $\delta S/S$ decreases with increasing S and x_i . For the optimum resolution value, $R_{OM}=0.10 \mu\text{m}$ (Fig. 4.3(a)), we observe that $\delta S/S \leq 0.10$ (10%) for the majority of (S, x_i) values (exclusively the two higher and narrow color zones correspond to $\delta S/S$ up to 14%). For the worst case resolution value, $R_{OM}=0.50 \mu\text{m}$ (Fig. 4.3(b)), $\delta S/S \leq 0.10$ (10%) exclusively over the black-colored zone, with upper boundary delimited by the values $S=5 \times 10^{-4}$, $x_i=3 \times 10^3 \mu\text{m}$ and $S=1 \times 10^{-3}$, $x_i=1 \times 10^3 \mu\text{m}$.

Finally, the effect of sample size on $\delta S/S$ is examined in Figs. 4.4(a) and 4.4(b); these Figs. present $\delta S/S$ upon variation of S and R_{OM} , for constant sample size $x_i=1 \times 10^3 \mu\text{m}$ and $x_i=5 \times 10^3 \mu\text{m}$, respectively. In consistency with the data shown in Figs. 4.2 and 4.3, $\delta S/S$ decreases with increasing S and with decreasing R_{OM} .

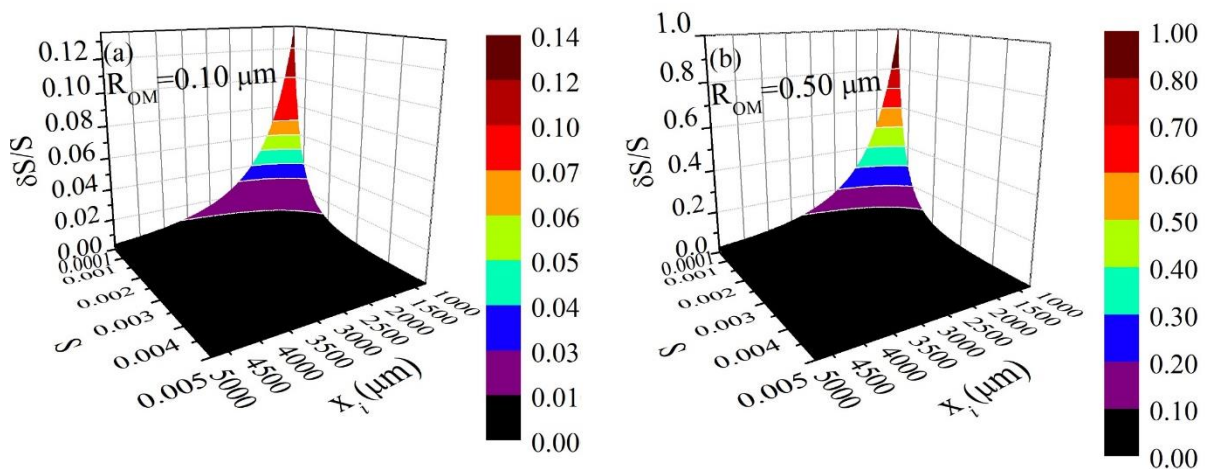


Fig. 4.3: Simulations of relative error in the estimated strain, $\delta S/S$, according to Eq. (4.8), realized by varying the pair of parameters (S, x_i) , within the range $5 \times 10^{-4} \leq S \leq 5 \times 10^{-3}$ and $1 \times 10^3 \mu\text{m} \leq x_i \leq 5 \times 10^3 \mu\text{m}$, under constant (a) $R_{OM}=0.10 \mu\text{m}$ (the best case resolution) and (b) $R_{OM}=0.50 \mu\text{m}$ (the worst case resolution).

Specifically, Fig. 4.4(a) shows that for sample size $x_i=1 \times 10^3 \mu\text{m}$, the tolerable values of $\delta S/S$ (i.e. $\delta S/S \leq 0.10$ or 10%) lie exclusively over the black color zone, with upper boundary line delimited by the values $S=6 \times 10^{-4}$, $R_{OM}=0.10 \mu\text{m}$ and $S=2 \times 10^{-3}$, $R_{OM}=0.50 \mu\text{m}$. On the contrary, Fig. 4.4(b) shows that for larger sample size, $x_i=5 \times 10^3 \mu\text{m}$, $\delta S/S$ is considerably lower, $\delta S/S \leq 0.03$ (3%), over the whole range of (S, R_{OM}) values. Please notice that $\delta S/S$ obtains its maximum, that is $\delta S/S=0.03$ (3%), for $S=5 \times 10^{-4}$, $R_{OM}=0.50 \mu\text{m}$, which is in agreement with the results of Fig. 4.1 (red square symbol). The decrease of the $\delta S/S$ upon increasing the sample size is totally expected and can be easily understood taking into consideration the Eq. (4.1), shown above. Specifically, since the strain of the PE material should remain constant (as an intrinsic property), the deformation Δx should be smaller for a smaller sample size and larger for a larger sample size, x_i .

This is a fact that we have also observed experimentally, in the context of the study presented in the subchapter 3.2.3. Here, we will combine these experimental data with simulations based on the empirical model presented above. For reasons of comparison, in Figs. 4.5(a.i)-(d.i) and 4.5(a.ii)-(d.ii), we show the $S_{zi}(E_{ex,z})$ curves and the respective in-plane PE coefficients, d_{zi} ($i=x,y$), upon application and removal of a permanent magnetic field $H_{ex,z}=1\text{kOe}$, to two PZT-5% Fe_3O_4 samples; a larger one with dimensions $7\times 7\text{ mm}^2$ (i.e. $x_i=3.5\times 10^3\text{ }\mu\text{m}$) and a smaller one with dimensions $3.5\times 3.5\text{ mm}^2$ (i.e. $x_i=1.75\times 10^3\text{ }\mu\text{m}$), respectively.

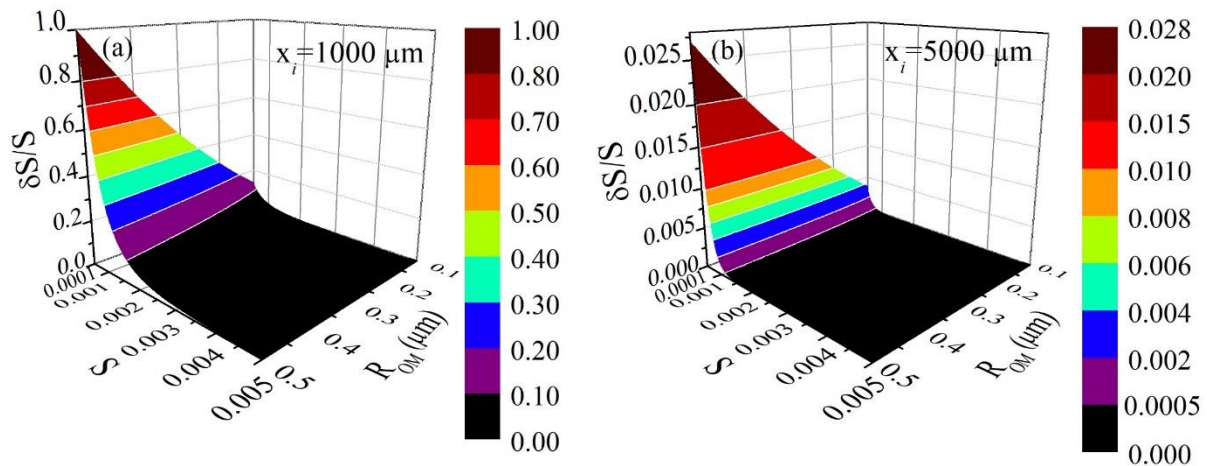


Fig. 4.4: Simulations of relative error in the estimated strain, $\delta S/S$, according to Eq. (4.8), realized by varying the pair of parameters (S, R_{OM}) , within the range $5\times 10^{-4}\leq S\leq 5\times 10^{-3}$ and $0.10\text{ }\mu\text{m}\leq R_{OM}\leq 0.50\text{ }\mu\text{m}$, under constant (a) $x_i=1\times 10^3\text{ }\mu\text{m}$ (total sample length: $2\times 10^3\text{ }\mu\text{m}$) and (b) $x_i=5\times 10^3\text{ }\mu\text{m}$ (total sample length: $10\times 10^3\text{ }\mu\text{m}$).

From Figs. 4.5(a.i), we observe that the modulation of the in-plane PE coefficients ($((d_{zi}(H_{ex,z}=0)-d_{zi}(H_{ex,z}\neq 0))/d_{zi}(H_{ex,z}=0))\times 100\%$) for the case of $x_i=3.5\times 10^3\text{ }\mu\text{m}$ is on the order of 55%. On the other hand, from Fig. 4.5 (a.ii) we observe that for the smaller PZT-5% Fe_3O_4 sample, with $x_i=1.75\times 10^3\text{ }\mu\text{m}$, the respective modulation is lower, on the order of 35%. This fact could be attributed to the underestimation of the PE deformations, Δx , in the case of the smaller sample. Clearly, the smaller the Δx , the less discernable it gets, since at some point Δx would be comparable in magnitude with (or even smaller than) the digital resolution of our unit, $R_{OM}=0.20\text{ }\mu\text{m}$, that is after processing of the raw OM images (see Appendix A).

In order to have a sense of the relative error coming in the estimated strain, $\delta S/S$, for the case of the large and small square PZT-5% Fe_3O_4 samples shown above, we performed simulations, as shown in Figs. 4.6(a) and 4.6(b), respectively, based on Eq. (4.8). Together with the data corresponding to PZT-5% Fe_3O_4 samples sintered at $T_{\text{sin}}=1000\text{ }^\circ\text{C}$ (represented with open symbols) [8], we also present simulations corresponding to PZT-5% Fe_3O_4 samples with the same dimensions, though sintered at $T_{\text{sin}}=1180\text{ }^\circ\text{C}$ (represented with solid symbols). We recall that $T_{\text{sin}}=1180\text{ }^\circ\text{C}$ is the temperature at which we observe the maximum PE strain values of PZT (up to $S_{\text{max}}=4\times 10^{-4}$) [1]. Also, at this point, we should note that the presence of Fe_3O_4 NPs does not affect the strain of the samples when no external magnetic field is applied. Hence, the maximum strain values for the composite PZT-5% Fe_3O_4 are practically the same with plain PZT.

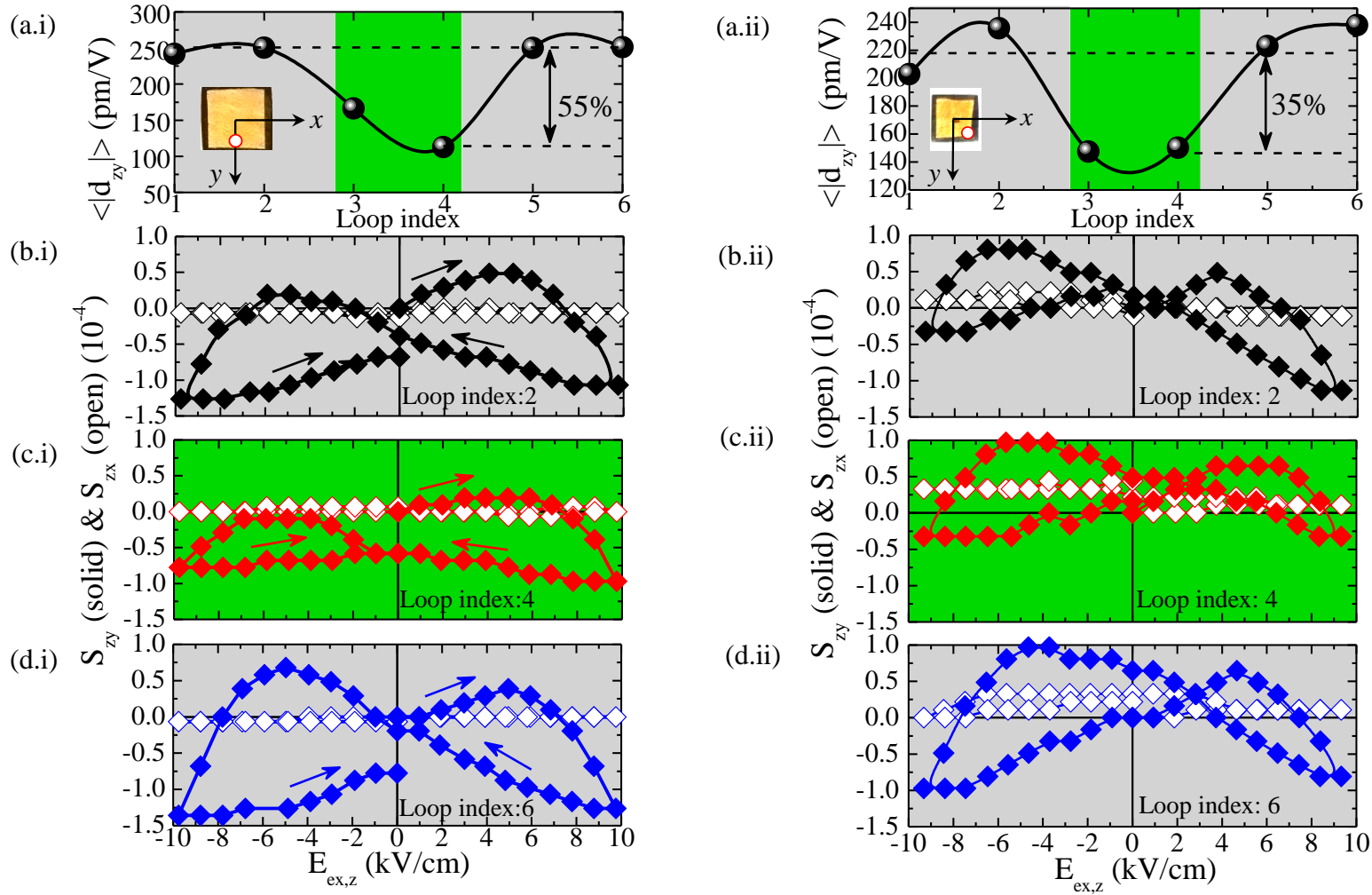


Fig. 4.5: (a.i)-(d.i) & (a.ii)-(d.ii) PE data corresponding to a (a.i)-(d.i) large square-shaped (sample side: 7mm) and a (a.ii)-(d.ii) small square-shaped (sample side 3.5 mm), PZT-5%Fe₃O₄ samples. The inset photos show the respective samples, along with the arbitrarily chosen x and y Cartesian coordinate system. The investigated area is denoted with a dot placed on SA_y for both samples. (a.i) & (a.ii) Mean absolute values of PE coefficients for loop index 1-6 (see text for details regarding their calculation), under the subsequent application and removal of $H_{ex,z}=1$ kOe; specifically, in the absence of $H_{ex,z}$ (Loop index: 1 & 2), under application of $H_{ex,z}$ (Loop index: 3 & 4) and after the removal of $H_{ex,z}$ (Loop index: 5 & 6). (b.i)-(d.i)/(b.ii)-(d.ii) representative $S_{zy}(E_{ex,z})$ and $S_{zx}(E_{ex,z})$ loops (solid and open rhombi, respectively) for the square/disc-shaped sample upon application and removal of $H_{ex,z}=1$ kOe; (b.i)/(b.ii) in the absence of $H_{ex,z}$ (Loop index: 2), (c.i)/(c.ii) under application of $H_{ex,z}$ (Loop index 4) and (d.i)/(d.ii) after the removal of $H_{ex,z}$ (Loop index: 6). The arrows trace the sequence of $E_{ex,z}$ application. Please, notice that the vertical scale is the same in each group of three panels, (b.i)-(d.i) and (b.ii)-(d.ii), for reasons of comparison.

In this context, we considered as input parameters the corresponding S , R_{OM} and x_i values. Specifically the variable parameters S and R_{OM} were selected according to the following factors: (i) the maximum strain of the PZT-5%Fe₃O₄ samples sintered at $T_{sin}=1000$ °C and $T_{sin}=1180$ °C and (ii) the resolution corresponding to processed OM images. Regarding the maximum strain values, S_{max} , for PZT-5%Fe₃O₄ samples sintered at $T_{sin}=1000$ °C and $T_{sin}=1180$ °C, these are $S_{max}=1.5 \times 10^{-4}$ and $S_{max}=4 \times 10^{-4}$, respectively; therefore, S varies within the range $1.5 \times 10^{-4} \leq S \leq 4 \times 10^{-4}$. Also, regarding the resolution of a processed image, R_{OM} , we already know that it is $R_{OM}=0.20$ μm , at best (see Appendix A). Hence, we choose R_{OM} to typically range within $0.20 \mu\text{m} \leq R_{OM} \leq 0.40 \mu\text{m}$. The size of the samples was kept constant, $x_i=3.5 \times 10^3$ μm (total sample length: 7×10^3 μm) and $x_i=1.75 \times 10^3$ μm (total sample length: 3.5×10^3 μm), referring to the insets of Figs. 4.5 (a.i) and 4.5(a.ii), respectively.

Firstly, we discuss the results of the large PZT-5%Fe₃O₄ samples ($x_i=3.5 \times 10^3$ μm). Regarding the samples of lower strain ($S=1.5 \times 10^{-4}$) -sintered at $T=1000$ °C- we see that the relative error in the estimated strain, $\delta S/S$, is on the order of 27%, 35% and 45%, as represented in Fig. 4.6(a) with a black, red and magenta open symbol, for the respective cases with $R_{OM}=0.20$ μm , 0.25 μm and 0.30 μm . Regarding the samples of higher strain ($S=4 \times 10^{-4}$) -sintered at $T=1180$ °C- we observe that $\delta S/S$ decreases drastically, on the order of 4%, 6% and 10% for samples, as represented in Fig. 4.6(a) with a black, red and magenta solid symbol, for the respective cases with $R_{OM}=0.20$ μm , 0.25 μm and 0.30 μm .

Secondly, we discuss the results on the small PZT-5%Fe₃O₄ samples ($x_i=1.75 \times 10^3$ μm). Regarding the samples of lower strain ($S=1.5 \times 10^{-4}$) -sintered at $T=1000$ °C- we observe that $\delta S/S$ is on the order of 70%, 90% and 100%, as represented in Fig. 4.6(b) with a black, red and magenta open symbol, for the respective cases with $R_{OM}=0.20$ μm , 0.25 μm and 0.30 μm . Regarding the samples of higher strain ($S=4 \times 10^{-4}$) -sintered at $T=1180$ °C- we observe that $\delta S/S$ decreases dramatically, on the order of 18%, 22% and 30%, as shown in Fig. 4.6(b) with a black, red and magenta solid symbol, for the respective cases with $R_{OM}=0.20$ μm , 0.25 μm and 0.30 μm .

From these extensive simulations, we focus on the data corresponding to $R_{OM}=0.20$ μm , the optimum resolution value that possibly is at play in our case (see Appendix A). Accordingly, we deduce that, for the larger samples ($x_i=3.5 \times 10^3$ μm), $\delta S/S$ either remains tolerable (27% for $S=1.5 \times 10^{-4}$) or very small (4% for $S=4 \times 10^{-4}$). Hence, regarding these samples, the OM-based technique can give fairly reliable results. In turn, for the smaller samples ($x_i=1.75 \times 10^3$ μm), $\delta S/S$ is very high (70% for $S=1.5 \times 10^{-4}$) or fairly small (18% for $S=4 \times 10^{-4}$). Thus, regarding the smaller samples, only the ones with adequately high strain can be examined with the OM-based technique, so that we can obtain trustworthy results.

Most important, it should be highlighted that the aforementioned $\delta S/S$ values estimated by this model, corresponding to $x_i=3.5 \times 10^3$ μm (total sample side 7×10^3 μm), are in very good agreement with the experimentally calculated ones (see Fig. B.1 in Appendix B) corresponding to samples with $x_i > 2.5$ μm (total sample side 5×10^3 μm). This fact clearly proves the consistency of our empirical model. Obviously, the high $\delta S/S$ values estimated by the model for $x_i=1.75 \times 10^3$ μm (total sample side 3.5×10^3 μm), indicate that we should avoid the investigation of samples that have similar dimensions (or smaller) by means of our local OM-based PE technique.

As a concluding remark, the multiparametric landscape of distinct factors, such as sample size, resolution of the OM unit, strain magnitude of the sample, should be finely preevaluated for the reliable utilization of this local OM-based technique on the recording of the $S(E_{ex,z}, H_{ex,z})$ curves and the subsequent estimation of the piezoelectric coefficients.

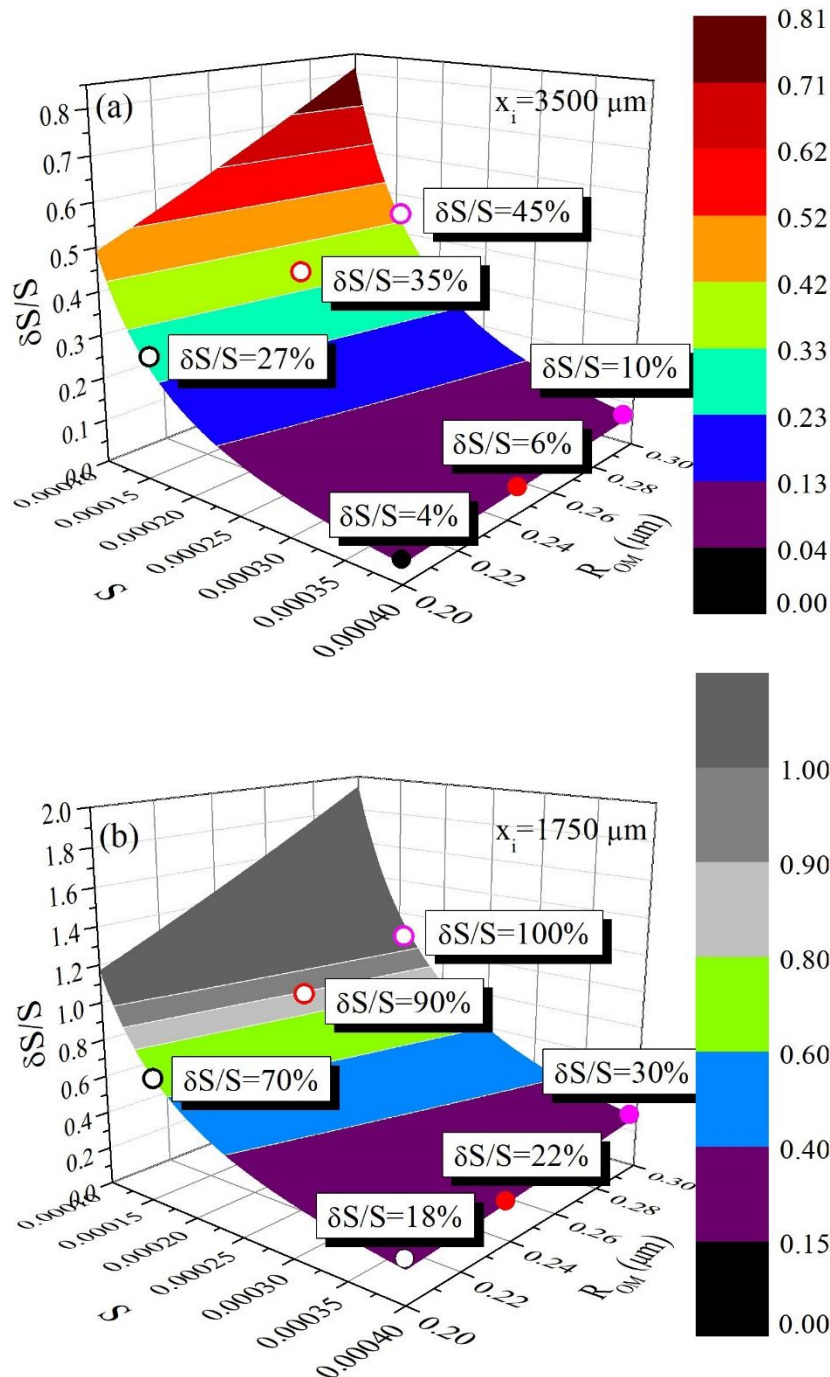


Fig. 4.6: Simulations of the relative error in the estimated strain, $\delta S/S$, according to Eq. (4.8), upon varying the parameters S , R_{OM} within the range $1 \times 10^{-4} \leq S \leq 4 \times 10^{-4}$ and $0.20 \mu\text{m} \leq R_{OM} \leq 0.30 \mu\text{m}$, under constant (a) $x_i = 3.5 \times 10^3 \mu\text{m}$ (total sample length: $7 \times 10^3 \mu\text{m}$) and (b) $x_i = 1.75 \times 10^3 \mu\text{m}$ (total sample length: $3.5 \times 10^3 \mu\text{m}$). The black, red and magenta-colored symbols correspond to $R_{OM} = 0.20 \mu\text{m}$, $0.25 \mu\text{m}$ and $0.30 \mu\text{m}$. The open and solid symbols correspond to $S_{en} = 1.5 \times 10^{-4}$ and 4×10^{-4} , respectively.

To summarize, according to the output results of the simulations presented in Figs. 4.2-4.4, the consistency of our empirical model is proven, validating the reliability and accuracy of our experimental technique. In addition, we stress that simulations based on this model can be an important and time-saving tool for the experimental practice; within an appropriately chosen range of S_{en} , R_{OM} and x_i values, the simulations can give the optimum match of these parameters in order to minimize the $\delta S/S$ error. In particular, the sample size is a parameter that we can ultimately control, by appropriately fabricating our samples (polycrystalline or single crystals). A general conclusion on the local OM-based technique used in this Thesis for the estimation of in-plane PE coefficients is as following: its reliability and accuracy (proven in this chapter) along with its ease and versatility in use (documented in subchapter 2.3.1) make it suitable for standard PE characterization among a wide range of materials used in current technological applications.

References

- [1] M. Zeibekis, G. Vertsioti, and D. Stamopoulos, *J. Phys.D: Appl. Phys.* **49**, 105304 (2016).
- [2] S. Kim, G. P. Khanal, H. W. Nam, I. Fujii, S. Ueno, C. Moriyoshi, Y. Kuroiwa and S. Wada, *J. Appl. Phys.* **122**, 164105 (2017).
- [3] M. H. Malakooti and H. A. Sodano, *Appl. Phys. Lett.* **102**, 061901 (2013).
- [4] A. Levin, A. I. Pommrich, T. Weissbach, D. C. Meyer and O. B. Zeneli O B, *J. Appl. Phys.* **103**, 054102 (2008).
- [5] S. Zhang and F. Li, *J. Appl. Phys.* **111**, 031301 (2012).
- [6] S. Zhang et al. *J. Cryst. Growth* **318**, 846 (2011).
- [7] Y. Zhang, J. Roscow, M. Xie and C. Bowen *J. Eur. Ceram. Soc.* **38**, 4203 (2018).
- [8] G. Vertsioti, S. J. Zhang and D. Stamopoulos, *Sci. Rep.* **9**, 2178 (2019).

Chapter 5: Conclusions and perspectives

Conclusions

In the frame of this PhD thesis we studied composite materials, with ferromagnetic (FM) and piezoelectric (PE) constituents, with respect to their response under application of the heteroconjugate externally applied electric (E_{ex}) and/or magnetic (H_{ex}) fields. On the purely experimental part of the present PhD Thesis, two general topologies were investigated, FM thin films of Co (thickness 30-50 nm) on both sides of bulk PE single crystals of $Pb(Mg_{1/3}Nb_{2/3})O_3-xPbTiO_3$ (PMN-0.30PT) in a planar configuration FM/PE/FM, that is Co/PMN-0.30PT/Co and FM nanoparticles (NPs) of Fe_3O_4 (diameter 50-100 nm) embedded into a bulk PE matrix of $Pb(Zr_{0.52}Ti_{0.48})O_3$ (PZT). Parts (A) and (B) summarize the conclusions of the former and latter topology, respectively. On the simulation part of the present PhD Thesis, a thorough comparison between an empirical model and experimental data was applied. Part (C) presents the main conclusions of these simulations.

(A) Main conclusions on Co/PMN-0.30PT/Co composites

(A.1) Characterization of Co(30 nm)/PMN-0.30PT/Co(30 nm)

Among all the Co/PMN-0.30PT/Co composites with Co thickness ranging within 30-50 nm, we focused on the ones with thickness 30 nm. Regarding these samples, at first, we examined their distinct PE and FM building units separately, paying special attention to the properties of the PE substrate, that is PMN-0.30PT. We stress that the specific material lies well inside the morphotropic phase boundary (MPB), where the highest PE response occurs.

The crystallographic structure of the latter showed that the single crystal is cut along [110] direction. In addition its FE characterization revealed that the PMN-0.30PT has a low coercive field, E_c , and rather tetragonal electric polarization loop, $P(E_{ex,z})$, as expected for single crystals.

The PE characterization showed the typical ‘butterfly’ loop, $S(E_{ex,z})$, with high strain values, which is characteristic of PMN-xPT crystals with $x \approx 0.30$.

What is more, the magnetic characterization of PMN-0.30PT by means superconducting quantum interference device (SQUID), evidenced that its magnetization is rather low (on the order of 10^{-6}). Thus, regarding the composite Co/PMN-0.30PT/Co, we conclude that the measured magnetization corresponds exclusively to the Co thin films.

Finally, the crystallographic structure of the composite shows that it is of high quality, with distinct peaks that correspond to both PMN-0.30PT and Co.

(A.2) Electric-field control of magnetic properties for the Co(30 nm)/PMN-0.30PT/Co(30 nm) composite

For the purpose of this study we employed magnetization measurements while varying the externally applied magnetic field in-plane, $m(H_{ex})$ for $T=10$ K, $T=300$ K, and while varying temperature, $m(T)$, for $H_{ex}=0$ (i.e. the remanent magnetization $m_{rem}(T)$), with simultaneous application of external electric field out-of-plane, $E_{ex,z}$, following specific measurement protocols. From these data we reported modulation of the magnetic coercive field, H_c , and of

the remanent magnetic state, m_{rem} , which are discussed below in (A.2.I) and (A.2.II), respectively.

(A.2.I) Electric-field modulation of H_c

We recorded several $m(H_{\text{ex}})$ loops at $T=10$ K and at $T=300$ K, each one with the simultaneous application of an $E_{\text{ex},z}$, ranging within $-5 \text{ kV/cm} \leq E_{\text{ex},z} \leq +5 \text{ kV/cm}$.

Regarding $m(H_{\text{ex}})$ recorded at $T=10$ K, we observed clear modulation of H_c for all $E_{\text{ex},z}$ applied, with a notable percentage variation of H_c on the order of 47%, at maximum (between $+2.5 \text{ kV/cm}$ and 0 kV/cm). We attributed the modulation of H_c to two mechanisms; first the pinning of the existing magnetic domain walls, MDWs, which can be effectively enhanced either by the surface/interface roughness or by the ‘bulk’ static disorder that are introduced due to the developed strain and second, the modulation of MDWs population that inevitably should accompany the modulation of the MD size. The latter is caused by the deformation of the FM film thickness, which in turn is motivated by the induced strain (the MD size w is proportional to the square root of the film thickness, d , that is $w \sim d^{1/2}$).

Regarding $m(H_{\text{ex}})$ recorded at $T=300$ K, H_c does not display modulation with $E_{\text{ex},z}$. We ascribe this fact to the thermal energy, $k_{\beta}T$, that progressively counterbalances the pinning energy of MDWs as T increases and finally, at $T=300$ K, ultimately dominates.

(A.2.II) Electric-field modulation of m_{rem}

For this study we recorded $m_{\text{rem}}(T)$ in the temperature range $T=10$ K-300 K under application of an external electric field out-of-plane, ranging within $-5 \text{ kV/cm} \leq E_{\text{ex},z} \leq +5 \text{ kV/cm}$. We observed that for $E_{\text{ex},z} \neq 0$ m_{rem} exhibits degradation in the form of distinct suppression events that we term electric field-induced MIs (EMIs), since they are exclusively motivated by $E_{\text{ex},z}$.

We observed that the overall degradation of m_{rem} increases with $E_{\text{ex},z}$ and ceases below a characteristic temperature $T_{\text{ces}}=170$ K. From this fact, we deduce that EMIs are thermally activated; although, we found that the thermal energy alone is not sufficient to motivate the metastable states of m_{rem} and promote the EMIs. This was proven from measuring $m_{\text{rem}}(T)$ data with $E_{\text{ex},z}=0$ which did not show any EMI, evidencing that the EMIs, except for thermally activated, they are also strain mediated.

From $m_{\text{rem}}(T)$ data with $E_{\text{ex},z} \neq 0$ it is clear that there is an interplay between thermal activation energy, which promotes the EMIs, and pinning of MDWs, which hampers them. Interestingly, published PE data referring to PMN-0.33PT evidenced an inflection point for the PE coefficients at $T_{\text{inf}} \approx 170$ K. Comparing this result with our magnetic data for the composite Co/PMN-0.30PT/Co, we conclude that the degradation of the m_{rem} is motivated by the strain induced to the PMN-0.30PT substrate by $E_{\text{ex},z}$.

Summarizing our study on Co/PMN-PT/Co, we demonstrated that this planar structure can be used as a solid basis for the development of PE/FM-based devices, for instance referring to electric-field-controlled magnetic storage. Also, it highlights the limitations in the temperature regime, which is indispensable for the reliable operation of this structure.

(B) Main conclusions on PZT-5%Fe₃O₄ composite

(B.1) Characterization of PZT-xFe₃O₄

After thorough electric and magnetic characterization of PZT-xFe₃O₄ samples with different Fe₃O₄ concentration (x=0%, 1%, 3%, 5%, 10%, 20%, 30%, 50%) we deduced that the most appropriate sample for further investigation under the application of an external electric field out-of-plane, $E_{ex,z}$, is the PZT-5%Fe₃O₄, since it exhibits negligible leakage current ($I < 1 \mu A$) within the electric field regime that we can apply with our equipment ($E_{ex,z} = \pm 10$ kV/cm), and also adequately high magnetization (24 emu/g). To this end several samples with the specific concentration $x=5\%$ were fabricated and were characterized in detail.

Specifically, we obtained magnetization data by means of SQUID corresponding to PZT-5%Fe₃O₄ and its sintered parent compounds PZT, Fe₃O₄ as well as to the non-sintered parent Fe₃O₄ (all in bulk form) for reasons of comparison. From these data we deduced the followings; first, since the magnetization of PZT is very low ($6 \cdot 10^{-3}$ emu/g) we can fairly assume that exclusively the Fe₃O₄ NPs contribute to the magnetization measured for the PZT-5%Fe₃O₄ composite. Second, the non-sintered parent Fe₃O₄ exhibits relatively high magnetization (63 emu/g), characteristic of the soft FM magnetite, while after sintering at ambient atmosphere Fe₃O₄ exhibits low magnetization (0.4 emu/g), denoting that it has entirely transformed to α -Fe₂O₃. Third, by comparing the magnetization value obtained for the PZT-5%Fe₃O₄ composite with the ones obtained for the non-sintered and the sintered parent Fe₃O₄, we deduced that a percentage of 38% of the NPs remains in the Fe₃O₄ form after sintering, while the rest is oxidized to α -Fe₃O₄ (for the sake of simplicity the composite is still referred as PZT-5%Fe₃O₄, even after sintering). This result indicates that the PE matrix can partially prevent the oxidation of the Fe₃O₄ NPs to α -Fe₃O₄.

The crystallographic data obtained by XRD confirm the coexistence of α -Fe₂O₃ in the composite PZT-5%Fe₃O₄, without showing any byproduct formation during sintering. In addition, these data manifest that the introduction of Fe₃O₄/ α -Fe₂O₃ NPs in the PZT matrix advances the partial transformation of the latter into the tetragonal phase. In fact, the stoichiometry of the parent PZT compound was at the MPB, where phase coexistence (rhombohedral and tetragonal) is known to occur. Therefore, regarding the PZT-5%Fe₃O₄ composite, the partial phase transformation from a mixture of rhombohedral and tetragonal phases to the tetragonal one, can be ascribed to the mechanical strain generated by the mismatch of the respective lattice constants.

Furthermore, thorough microstructural study of the PZT-5%Fe₃O₄ composite by means of scanning electron microscopy revealed that its bulk is fairly compact with minimal porosity, while its surface is relatively porous due to the associated maximization of PbO loss that occurs near it, during sintering. Elemental analysis information by means of energy dispersive X-rays spectroscopy from the entire surface of the PZT-5%Fe₃O₄ samples proved the existence of the Pb, Zr, Ti, and Fe elements. Their distribution was checked via elemental mapping analysis, indicating fair homogeneity for all the constituent elements; some inhomogeneity features observed are attributed to the aforementioned inherent phase coexistence in PZT; this is associated with local variations in the stoichiometry of the PZT matrix, which affects the distribution of Pb, Zr, Ti and also Fe, since the Fe₃O₄ NPs are embedded in the PZT matrix in the PZT-5%Fe₃O₄ composite.

Ferroelectric and piezoelectric characterization was employed using standard ‘global’ techniques, which refer to the entire volume of the PZT and PZT-5%Fe₃O₄ samples. These data confirmed that polarization and out-of-plane strain (i.e. the strain along the thickness of the sample) exhibit the typical hysteretic behavior upon varying E_{ex,z}. The introduction of the FM Fe₃O₄ NPs in the PZT renders the latter one harder, increasing its electric coercive field. This is attributed to the fact that the Fe₃O₄ NPs act as structural disorder that pin the FE domain walls of the PZT efficiently. This phenomenon could be probably motivated and/or promoted by the similar sizes of the FE domains of PZT and the FM Fe₃O₄ NPs (50-100 nm). Finally, a complementary ‘local’ piezoelectric technique, introduced by our group, was used in order to study the in-plane strain, or else the strain over specific areas over the sample surface. Some important points regarding the characterization of PZT and PZT-5%Fe₃O₄ samples with this technique are the followings; first, the values of in-plane PE coefficient, d_{zi}, (i=x,y with xy plane denoting the sample surface) do not vary with the addition of Fe₃O₄ NPs. Second, the <|d_{zi}> value corresponding to an entire S(E_{ex}) loop are in agreement with ones given in the literature (~260 pm/V). The nucleation field, E_{nuc}, (i.e. the electric field at which the FE domains appear and start to move/rotate towards the reversal of polarization) estimated from S(E_{ex,z}) upon varying E_{ex,z} from -10 kV/cm to +10 kV/cm is E_{nuc}[±]=4 kV/cm for PZT and E_{nuc}[±]=6 kV/cm for PZT-5%Fe₃O₄.

(B.2) Electric/magnetic field control of the magnetic/piezoelectric properties for the PZT-5%Fe₃O₄ composite

This study aimed to the investigation of the magnetic/piezoelectric properties of the PZT-5%Fe₃O₄ under E_{ex,z}/H_{ex,z}, respectively. We found electric-field control of m_{rem} and magnetic-field control of the piezoelectric coefficients, d_{zi}, that are discussed in B.2.i and B.2.ii, below. Also, in B.2.iii, we summarize the main conclusions regarding the underlying mechanism that dominates and motivates these phenomena.

(B.2.i) Electric-field control of m_{rem}

After settling the remanent magnetic state, m_{rem}, of PZT-5%Fe₃O₄ under E_{ex,z} application, ranging within -9 kV/cm ≤ E_{ex,z} ≤ +9 kV/cm, we recorded the m_{rem}(t) curves for a time window t:0-20 min; m_{rem}(t) data were well fitted by the exponential expression $m_{rem}(t) = Ae^{-\frac{t}{T_1}} + y_0$. What is more, the fitting was performed in four different time windows: Δt=0-20 min, 1-20 min, 2-20 min and 5-20 min, in order to eliminate the high noise level that comes in the measurement of the initial experimental points after the change of the external magnetic field. We found that m_{rem}(0), that is the initial m_{rem} value: (i) exhibited maxima for E_{ex,z}=±6 kV/cm and (ii) its value was practically independent of the time window selected for the fitting. Most important T₁, that is related to the relaxation constant, showed maxima exclusively in the vicinity of E_{ex,z}=-6 kV/cm, while in any other case, E_{ex,z} does not affect T₁. This proves that the relaxation is suppressed around this characteristic E_{ex,z} value; this feature becomes evident as the time window of fitting shortens. Since T₁ displays strong dependence on the E_{ex,z}, we term it ‘relaxation function’, RF(E_{ex,z})=T₁(E_{ex,z}); the maximization of RF(E_{ex,z}) manifests slower relaxation of the m_{rem} near E_{ex,z}=-6 kV/cm. From electric polarization, P(E_{ex,z}), and in-plane strain, S(E_{ex,z}), data obtained for PZT-5%Fe₃O₄, we found

that the nucleation fields are $E_{\text{nuc}}^{\pm} = \pm 6$ kV/cm. In fact, we know that electric polarization is metastable and thus susceptible to relaxation for electric fields in the interval between the nucleation, E_{nuc}^{\pm} , and coercive, E_c^{\pm} , fields. By combining the aforementioned data, we can plausibly conclude that in our case the relaxation of the remanent magnetic state is affected by the relaxation of the electric polarization due to a magnetoelectric (ME) coupling between the FM and PE constituents. The in-plane converse ME coefficients that we estimated by the magnetic data, $\alpha_{\text{in-plane},z}^{\text{E} \rightarrow \text{M}} = 1.1 \times 10^{-11}$ s/m and 1.4×10^{-11} s/m, are in very good agreement with values reported in the literature for relevant systems.

(B.2.ii) Magnetic-field control of d_{zi} ($i=x, y$)

For this study we used the local piezoelectric technique developed by our group, using a sample-carrying platform in order to host a permanent magnet that can be removed at will. Using a Gaussmeter, we found that in the vicinity of the PZT-5%Fe₃O₄ samples, the external magnetic field, $H_{\text{ex},z}$ that in this case is applied out-of-plane, is fairly homogeneous and its value is sufficient to bring the FM Fe₃O₄ NPs close to saturation. Accordingly, we recorded the in-plane strain during consecutive cycles referring to initial absence, upon application and ultimate removal of $H_{\text{ex},z}$. From these data we estimated the respective in-plane PE coefficients, d_{zi} . We note that in our case $i=y$, although due to the isotropic character of the PZT-5%Fe₃O₄ samples, x and y are not distinct in-plane axes and thus arbitrarily chosen; accordingly, here we simply use the subscript “ i ”. We deduced that the application of the external magnetic field, $H_{\text{ex},z}$, caused dramatic decrease of d_{zi} on the order of 50-60%. Most important, this modulation is almost reversible when removing $H_{\text{ex},z}$.

From combined data referring to both electric polarization, $P(E_{\text{ex},z})$, and leakage current, $I(E_{\text{ex},z})$, coming from an experimental technique probing the entire volume of the PZT-5%Fe₃O₄ samples, we found that the nucleation field is $E_{\text{nuc}} = \pm 6$ kV/cm. This global information is very important, since the direct comparison with the local, OM based $S(E_{\text{ex},z})$ data revealed the consistent identification of E_{nuc} ; marked by the global polarization data through the deviation from the linear behavior of the respective derivative, $dP(E_{\text{ex},z})/dE_{\text{ex},z}$, and by the local OM based ones by the recorded peaks in the $S(E_{\text{ex},z})$ curves.

By combining all data, we conclude that the nucleation process (appearance/movement/rotation of FE domains) gets suppressed when $H_{\text{ex},z}$ is applied, while it recovers upon $H_{\text{ex},z}$ removal. Notably, our results manifest that there is a ME coupling between the FM and the PE constituents of the PZT-5%Fe₃O₄ samples; the FM Fe₃O₄ NPs do not simply serve as static structural disorder, but also introduce reconfigurable magnetic disorder that modifies the in-plane strain-electric field curves and the accompanying PE coefficients when an external magnetic field is applied at will.

(B.2.iii) Underlying mechanism of the ME coupling in PZT-5%Fe₃O₄

For the case of PZT-5%Fe₃O₄ composite, we attribute the ME coupling to the strain transfer mechanism, since it is active at length scales on the order of 100-200 nm, which is comparable to the sizes of FE PZT domains and FM Fe₃O₄ NPs (50-100 nm). Specifically, the strain transfer occurs due to the PE and magnetostrictive nature of PZT and Fe₃O₄/Fe₂O₃ NPs, respectively. Since the magnetostriction of Fe₃O₄/Fe₂O₃ is almost comparable to the PE strain of PZT (10^{-4}), we can plausibly assume that the elastic interactions is a key characteristic that

motivates/promotes an efficient interface strain transfer between the iron oxide NPs and the surrounding PZT matrix.

In this context, regarding the electric-field control of magnetic properties we believe that the strain generated from the PZT matrix, due to the converse PE effect, is transferred across the interfaces to the Fe₃O₄ NPs, affecting their remanent magnetization, via the converse magnetostrictive effect. In turn, regarding the magnetic-field control of PE properties we suggest that the strain originating from the magnetostrictive iron oxides, due to the direct magnetostrictive effect, can be transported to the PZT matrix, altering its PE strain.

Summarizing our study on the PZT-5%Fe₃O₄ composite, we stress that it manifests a multifunctional character with noticeable performance under the application of both electric and magnetic fields, thus fairly termed ME. The low cost and facile production together with the room temperature feasibility that it displays can set the grounds for future applications based on relevant bulk PE/FM structures. For instance, such ME composites could constitute a cornerstone for devices in which the PE response should be magnetic field controlled at will.

(C) Main conclusions on the applicability and limitations of the OM-based local experimental technique for the estimation of the in-plane strain-electric field curves and piezoelectric coefficients

We performed 3D simulations based on an empirical model, aiming to evaluate the applicability and limitations of the generic experimental technique based on optical microscopy that was extensively used in this PhD Thesis. The parameters employed for the simulations (resolution of the optical microscope, strain of the material, and size of the sample) were varied systematically within a realistic range of values met in experimental practice and technological applications. The simulations showed in a consistent way that the relative error in the estimated strain decreases with increasing the sample size and the strain of the material, and with improving the resolution of the optical microscope. Specifically, we focused on materials employed in practical applications such as PZT and PMN-PT, exhibiting strain within 5×10^{-4} - 5×10^{-3} , with typical sample size within 1×10^3 - 5×10^3 μm , and also on resolution on the order of 0.10-0.50 μm . Accordingly, the simulation results showed that with the appropriate match of the respective parameters, the relative error in the estimated strain can be limited to 0.05 (5%), or below. Consequently, we validated the accuracy of our experimental technique, which, along with its ease and versatility in use, is suitable for standard PE characterization for a wide range of materials used in current technological applications.

Perspectives

The results deduced in this PhD Thesis can pave the way for future work regarding the Co/PMN-xPT/Co and PZT-xFe₃O₄ composites.

Regarding both PMN-xPT and Pb(Zr_{1-x}Ti_x)O₃, it is well known that their phase diagrams consist of experimental data deduced from various techniques (e.g. XRD, neutron diffraction, dielectric spectroscopy), and especially for temperatures $T > 300$ K. Nevertheless, a small percentage of these data originate from measurements of the PE coefficients (d_{ij}). Hence, the temperature dependence of the PE coefficients d_{ij} is an interesting issue. Specifically, it can be

correlated with well-known phase transitions that occur at temperatures $T > 300$ K, e.g. rhombohedral to tetragonal. To this end, we have developed an optical thermoplatform, by means of which we have the capability to record the in-plane strain $S_{zi}(E_{ex,z})$ curves upon controlled variation of the temperature up to the Curie temperature, T_c , (above which the materials are no longer PE), under the application of an external electric field. Accordingly, the temperature variation of the respective d_{zi} ($d_{zi}(T)$) could also be surveyed (see Appendix D). In contrast to the high-temperature regime, to the best of our knowledge, only few data exist in the literature regarding the low-temperature phase transitions of PMN-xPT and $Pb(Zr_{1-x}Ti_x)O_3$, originating almost exclusively from XRD and Raman spectroscopy. In this context, we also have designed and constructed an optical cryochamber for the exploration of PE coefficients, d_{zi} , down to liquid nitrogen temperature ($T=78$ K). In this respect, any possible anomaly that might be detected in the $d_{zi}(T)$ would allow us to probe the underlying crystallographic phase transitions and consequently confirm or even farther enrich the low-temperature phase diagrams (see Appendix D). What is more, irrespectively of the phase diagram studies, the recording of $d_{zi}(T)$ at low temperatures (down 78 K) also allows us to inspect systematically the ‘freezing’ of extrinsic contribution (ferroelectric domain wall motion) that is known to be associated with the decrease of $d_{zi}(T)$.

Concerning Co/PMN-0.30PT/Co, it would be very useful to record its in-plane PE coefficients below room temperature, ideally in the same temperature regime that the EMIs occur ($170 \text{ K} < T < 300 \text{ K}$) in order to study in depth the origin of EMIs that we observed via magnetization measurements. This would be possible with the optical cryochamber mentioned above. Furthermore, analogously to the modulation of PE coefficients of PZT-5% Fe_3O_4 under $H_{ex,z}$ application, it would be interesting to study possible variations of the PE coefficients of Co/PMN-0.30PT/Co under $H_{ex,z}$, as well; in fact, since the magnetostriction of Co and the PE coefficients of PMN-0.30PT are higher than the ones of Fe_3O_4 NPs and PZT, we would expect even more impressive percentage variation in the PE coefficient values.

Concerning the PZT-5% Fe_3O_4 composite, an issue that deserves further investigation is the preparation conditions. In *J. Alloys and Comptd.* **612**, 34 (2014), we have shown that by increasing the sintering temperature of PZT the PE coefficients improve. Hence, for the case of PZT-5% Fe_3O_4 composite, in order to employ higher sintering temperature and simultaneously avoid the transformation of Fe_3O_4 to α - Fe_2O_3 (which leads to lower magnetization and magnetostriction values), it would be very advantageous to prepare the samples under inert atmosphere (e.g. under vacuum). In addition, in correspondence to the reported modulation of the in-plane PE coefficients of PZT-5% Fe_3O_4 under $H_{ex,z}$, a very interesting issue to be studied is the magnetic field-induced modulation in relevant dielectric properties, such as the capacity, a phenomenon that apts technological applications.

Finally, referring exclusively to the technical point of view, an interesting perspective would be the modification of the OM platform employed in our technique so that we can immerse the sample and the lens into oil, with the possibility of simultaneous $E_{ex,z}$ application. This modification would not only improve the OM resolution, but also ensure a better insulating environment for the sample, so that higher $E_{ex,z}$ can be applied to it.

List of Publications

- (1) *Applicability and limitations of an optical microscopy-based local experimental technique for the estimation of the in-plane strain-electric field curves and piezoelectric coefficients*, G. Vertsioti and D. Stamopoulos (submitted for publication).
- (2) *Electric-field control of the remanent-magnetic-state relaxation in a piezoelectric-ferromagnetic PZT-5%Fe₃O₄ composite*, G. Vertsioti, M. Pissas, S. Zhang and D. Stamopoulos, *J. Appl. Phys.* **126**, 044104 (2019).
- (3) *Pronounced and reversible modulation of the piezoelectric coefficients by a low magnetic field in a magnetoelectric PZT-5%Fe₃O₄ system*, G. Vertsioti, S. Zhang and D. Stamopoulos, *Sci. Rep.* **9**, 2178 (2019).
- (4) *On the optimum processing conditions of Pb(Zr_xTi_{1-x})O₃: revealing the mechanisms to increase the piezoelectric coefficients up to 1100 pm/V*, M. Zeibekis, G. Vertsioti and D. Stamopoulos, *J. Phys. D.: Appl. Phys.* **49**, 105304(2016).
- (5) *Degradation of the remanent ferromagnetic state under the action of ferroelectric relaxation processes in Co/(1-x)PMN-xPT/Co hybrids: possible implications on cryogenic and room-temperature applications*, D. Stamopoulos, M. Zeibekis, G. Vertsioti and S. Zhang, *J. Appl. Phys.* **116**, 084304 (2014).

List of Conferences

- (1) *Controlling the piezoelectric coefficients through an external magnetic field in a composite PZT-5%Fe₃O₄ system*, G. Vertsioti and D. Stamopoulos, 14th International Conference of Nanoscience and Nanotechnologies, Thessaloniki, Greece, July 4-7, 2017 (poster).
- (2) *Controlling the relaxation of the remanent magnetization in a composite PZT-5%Fe₃O₄ system*, G. Vertsioti and D. Stamopoulos, E-MRS Fall Meeting, Warsaw, Poland, September 18-21, 2017 (poster).

Appendix A

Digital magnification and length scale: two key ingredients associated with the OM-based PE technique

The conventional OM-based PE technique that we employed in this Thesis focuses on the estimation of dimensional (i.e. length) changes of a PE sample, due to application of an external electric field, $E_{ex,z}$, as described in great detail in subchapter 3.3.1. We briefly recall that we trace the in-plane displacement (let us say along the xy plane) of a characteristic point (CP) of the sample surface, as monitored in real time upon successive variation of $E_{ex,z}$. To this end, two key ingredients should be available: a reliably-defined *length scale* and a useful *magnification*; both should definitely obey the diffraction limit.

Referring to the first ingredient, it is obvious that a calibration sample should be employed. This was preliminary discussed in subchapter 3.3.1. Extra clarifications are given here. Specifically, the calibration sample TGZ3 (NT-MDT Co, Moscow, Russia) is one of those employed in this PhD Thesis for the quantification of the CP's displacements. The specific calibration sample TGZ3 is shown in the inset (i) of Fig. A.1 by means of a SEM image; the width of each stripe and the period of the structure are measured with great precision to be 1.5 μm and 3.0 μm , respectively.

Regarding the second ingredient, *digital magnification*, it is a necessary tool to reveal the displacements of the CP. We note that the PZT compound studied in this Thesis exhibits CP's displacements on the order of 1 μm or even smaller, for typical variations of $E_{ex,z}$ (step of $E_{ex,z}$). In subchapter 3.3.1 we saw that the specific lens (magnification: x10, NA: 0.25) employed in almost all measurements in our OM system (total magnification: x130), has a diffraction-limited resolution with a nominal value $d=1.2 \mu\text{m}$ (for $\lambda=500 \text{ nm}$) that is comparable to the typical dimensional changes of PZT, 1 μm . Hence, in order to reveal information below 1 μm , we use a simple, however efficient, method based on *digital magnification*. By means of this method, we are able to recover information down to the diffraction limit, 0.20 μm , even by using this specific lens (magnification: x10, NA: 0.25). Thus, in order to estimate electric-field driven displacements of the CP with the diffraction-limited resolution of 0.20 μm , we should essentially trace its in-plane position in a sequence of *processed* images obtained from the raw (unprocessed) ones.

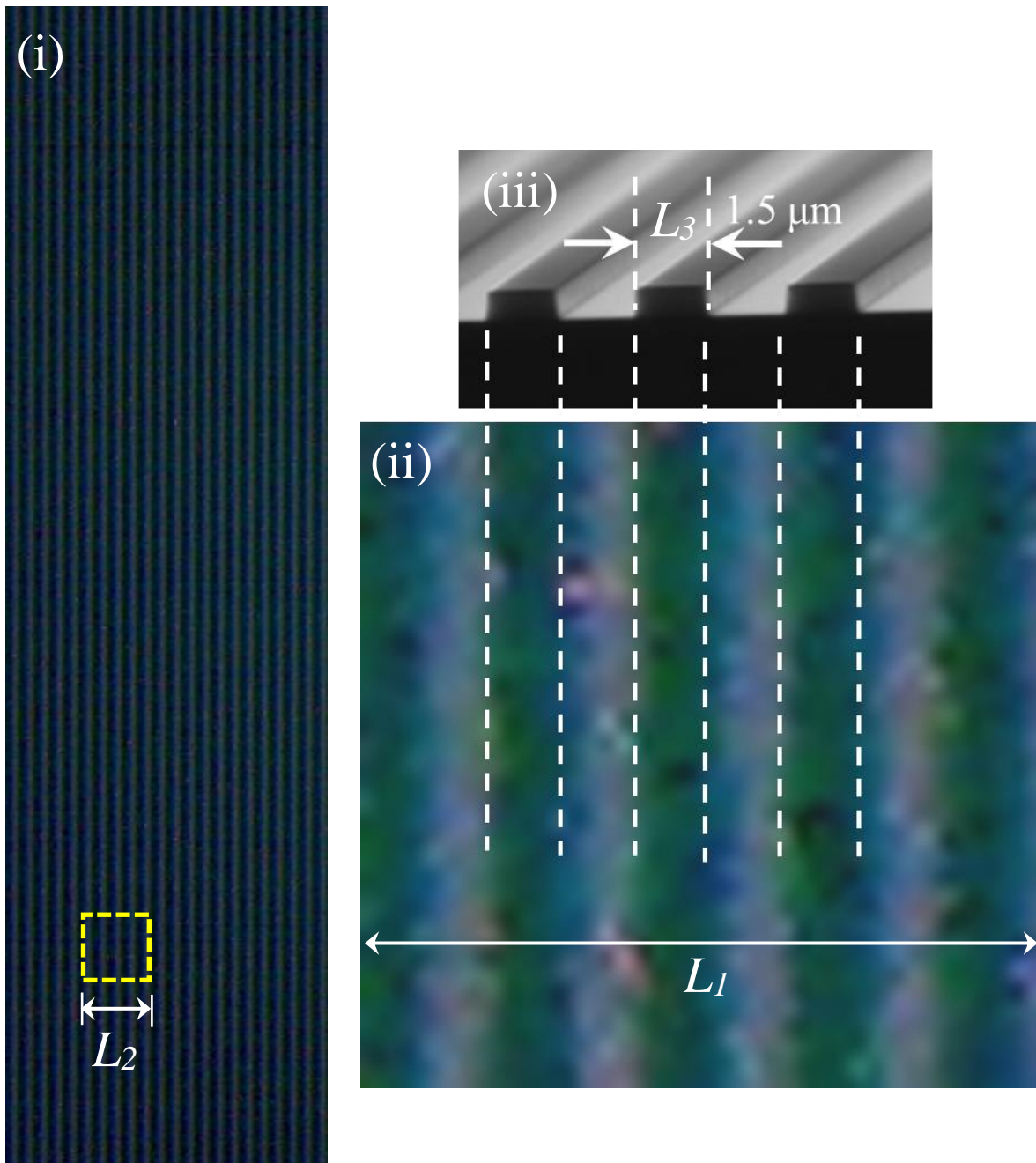


Fig.A.1: (i) Representative part of the raw optical microscopy (OM) image of the calibration sample TGZ3 (total magnification: $\times 130$; objective lens: $\times 10$, camera: $\times 13$), as obtained by means of our OM unit. The dashed yellow square indicates the area selected for cropping. (ii) The cropped and enlarged OM image; the respective digital magnification is determined by the ratio of the latter enlarged to the former cropped images, L_1/L_2 . (iii) SEM image of the calibration sample TGZ3; the width of each stripe is $L_3 = 1.5 \mu\text{m}$, a standard length scale from which the quantification of the CP's displacement is realized.

By processing the raw OM images we refer to two basic actions. First, we *crop* the area of interest down to a minimum permitted size, as determined by two main factors: (i) the image size should be adequately higher than the pixel *per se*, and (ii) the cropped area should certainly include the CP when its maximum displacement is considered for the range of E_{ex} under investigation. Second, we *enlarge* the cropped image up to a maximum permitted size that is limited by the inevitable blurring of the resulted image. After these two actions are completed, we can define the *digital magnification* as the dimensional ratio of the latter enlarged to the former cropped images. We note that these two images should have the same aspect ratio, so that morphological distortion and irregular estimation of digital magnification are avoided. It should also be highlighted that the digital magnification should by no means exceed the so-called *useful magnification* that is limited by the maximum value $\times 1900$ - $\times 2000$ at best, as dictated by the diffraction-limited resolution of $0.20 \mu\text{m}$ [1]. Any extra magnification will cause the so-called *empty magnification* [2] that suffers from excessive blurring without any corresponding increase in resolution.

The aforementioned procedure of image processing is here employed to the raw OM image of the calibration TGZ3 sample, shown in Fig. A.1 as obtained by means of our OM unit (total magnification: $\times 130$ /objective lens: $\times 10$, camera: $\times 13$). First, we crop the area of interest down to a sensible permitted size (as discussed above), as for instance is shown in the inset (ii) of Fig. A.1 with the dashed yellow square. Second, we enlarge the cropped area up to a reasonable permitted size (as discussed above). Accordingly, the digital magnification is given by the ratio of the latter enlarged to the former cropped images, that for the specific case is $L_1/L_2=1600$.

We note that the exact same procedure should be employed to estimate the digital magnification in all raw OM images obtained in every investigated PE sample. This is representatively shown in Figs. A.2(a) and A.2(b) for a PZT sample under $E_{ex,z}=0 \text{ kV/cm}$ and $E_{ex,z}=+8 \text{ kV/cm}$, respectively. The scale bar, $1 \mu\text{m}$, was designated by the digitally magnified image of the calibration sample TGZ3, shown in the inset (ii) of Fig. A.1 ($L_3=1.5 \mu\text{m}$). The CP, or strictly speaking the characteristic feature, is shown with a red arrow in both Figs. A.2(a) and A.2(b). In the insets, Figs. A.1(a.i) and A.1(b.i), we observe that the application of $E_{ex,z}$ has caused not only the expected displacement of the characteristic feature but also an alteration in its shape. Specifically, its shape changes from circular-like (Fig. A.1(a.i)) to elliptical-like (Fig. A.1(b.i)). For this reason, in Figs. A.1(a) and A.1(b), we outlined the spatial limits of the characteristic feature with a red circular and elliptical contour line, respectively. Accordingly, the center of symmetry of the characteristic feature (that now can be called CP) defines its position in each image. The magenta dashed horizontal lines, and the corresponding arrows, denote the length of the displacement of the CP, that is on the order of $0.38 \mu\text{m}$ under $E_{ex,z}=+6 \text{ kV/cm}$.

At this point we should highlight the following: the tracking of the characteristic feature's spatial limits (which basically determines its in-plane displacement) is restrained by the blurring around its periphery, caused by two factors. The first one is the enlargement of the original raw image, which occurs for both the investigated PE (e.g. PZT) and the calibration samples (see insets (a.i), (b.i) of Figs. A.2(a), A.2(b), respectively, and inset (ii) of Fig. A.1). The second one is at play exclusively for the investigated PE sample, since it originates from

the out-of-plane deformation of the sample (let us say along the z-axis), during which its top surface is repositioned at a level slightly different from the original focal plane of the lens. Though these deformations cannot be quantitatively estimated by our technique, for specific $E_{ex,z}$ values they are fairly evident as an additional blurring, as this is shown in Fig. A.2(b) upon application of $E_{ex,z}=+6$ kV/cm. Accordingly, in order to describe and quantify the uncertainty in tracking the characteristic feature's limits, caused by the aforementioned factors, we introduce the term *error in shape delimitation*. From our data, we generally estimate that this error is well below the diffraction limited resolution of our OM unit, $0.20 \mu\text{m}$ (see below for details). However at the worst case scenario, this error marginally equals $0.20 \mu\text{m}$. Accordingly, the error in shape delimitation can range within $0.05 \mu\text{m}$ - $0.20 \mu\text{m}$ (for more details, see Appendix B). Obviously, the higher the PE response of the sample (e.g. when applying a relatively high $E_{ex,z}$), the less significant this error becomes. For instance, in Fig. A.2, the PE response of the sample for $E_{ex,z}=+6$ kV/cm is fairly high, so that the displacement of the CP can be clearly discerned. On the other hand, when the PE response is fairly low (e.g. when applying a relatively low $E_{ex,z}$) the CP's displacement is inevitably almost comparable in size with the error in shape delimitation; as a consequence the estimation of the CP's displacement cannot be trustworthy. Hence, the smallest CP's displacement that confidently surpasses the error in shape delimitation, can be plausibly defined as the resolution associated with processed OM images, R_{OM} . From an abundance of processed images corresponding to PZT samples that we studied (sintered at $T=1000$ °C), we have deduced that $R_{OM}\approx 0.20 \mu\text{m}$; this is representatively shown in Figs. A.3(a) and A.3(b) for $E_{ex,z}=0$ kV/cm and $E_{ex,z}=+3$ kV/cm, respectively.

As expected, the value $R_{OM}=0.20 \mu\text{m}$ equals the classic diffraction-limited resolution of conventional optical microscopy. Hence, by means of this procedure that introduces digital magnification, we manage to recover both useful and reliable information, similar to the one that would have been recorded with a magnification lens of high performance (e.g. $\times 100$, NA: 1.25). Nevertheless, even with the discussed processing procedure of the images obtained with the conventional OM unit that we used in our measurements, we cannot exceed the useful magnification $\times 1900$ - $\times 2000$ and the related resolution of $0.20 \mu\text{m}$, as dictated by the diffraction limit.

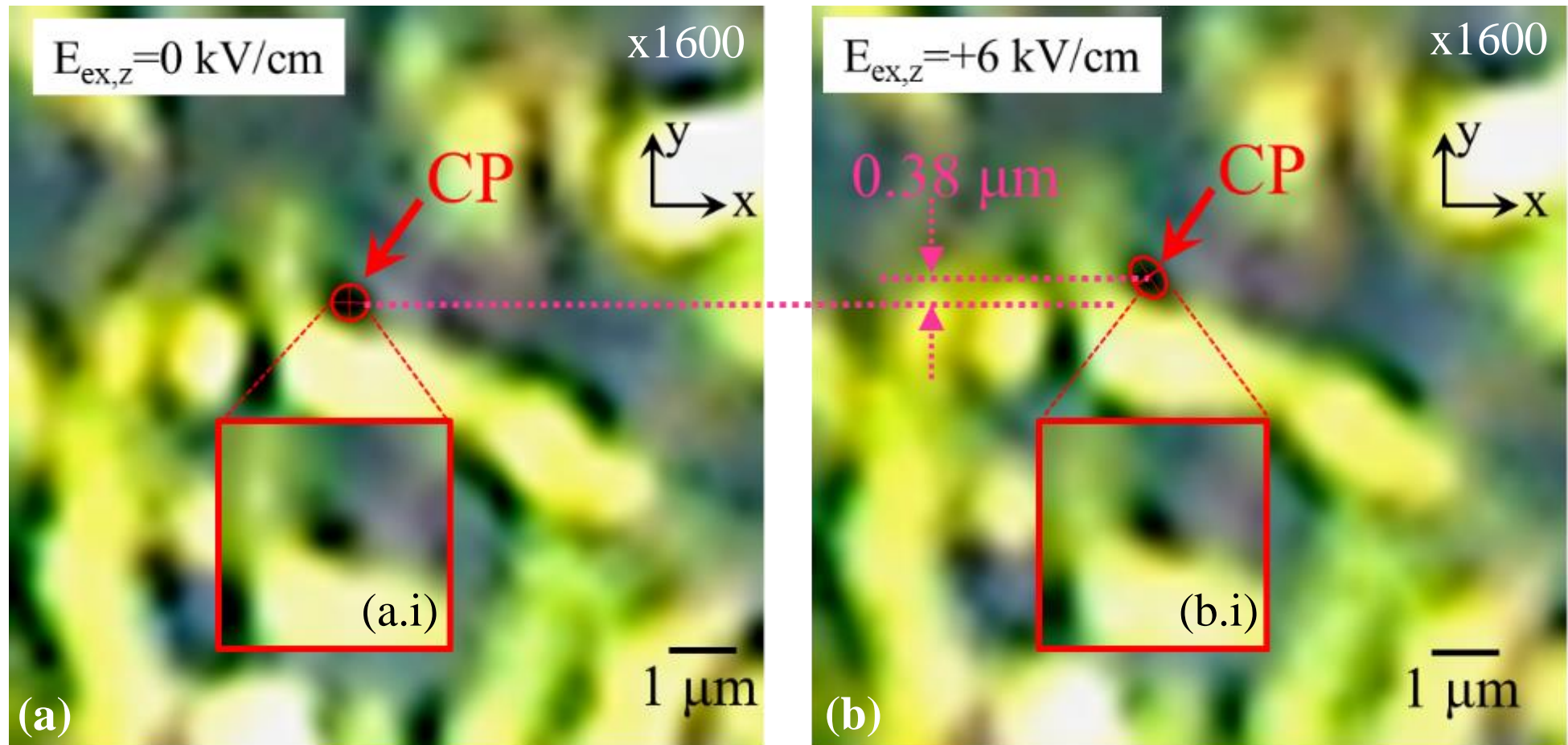


Fig.A.2: (a),(b) Processed optical microscopy (OM) images of a PZT sample at (a) $E_{ex,z} = 0 \text{ kV/cm}$ and (b) $E_{ex,z} = +6 \text{ kV/cm}$. The selected CP is shown with a red arrow in both panels; its shape alters under $E_{ex,z}$ application from a round-like to an elliptical-like shape, as can be discerned in the insets (a.i) and (b.i), respectively. For this reason the spatial limits of the CP are outlined with a red (a) circular and (b) elliptical contour line, along with their respective symmetry axes. The magenta dotted lines and arrows denote the clearly discerned displacement of the CP along y-axis that is on the order of $0.38 \mu\text{m}$. The scale bar designates $1 \mu\text{m}$.

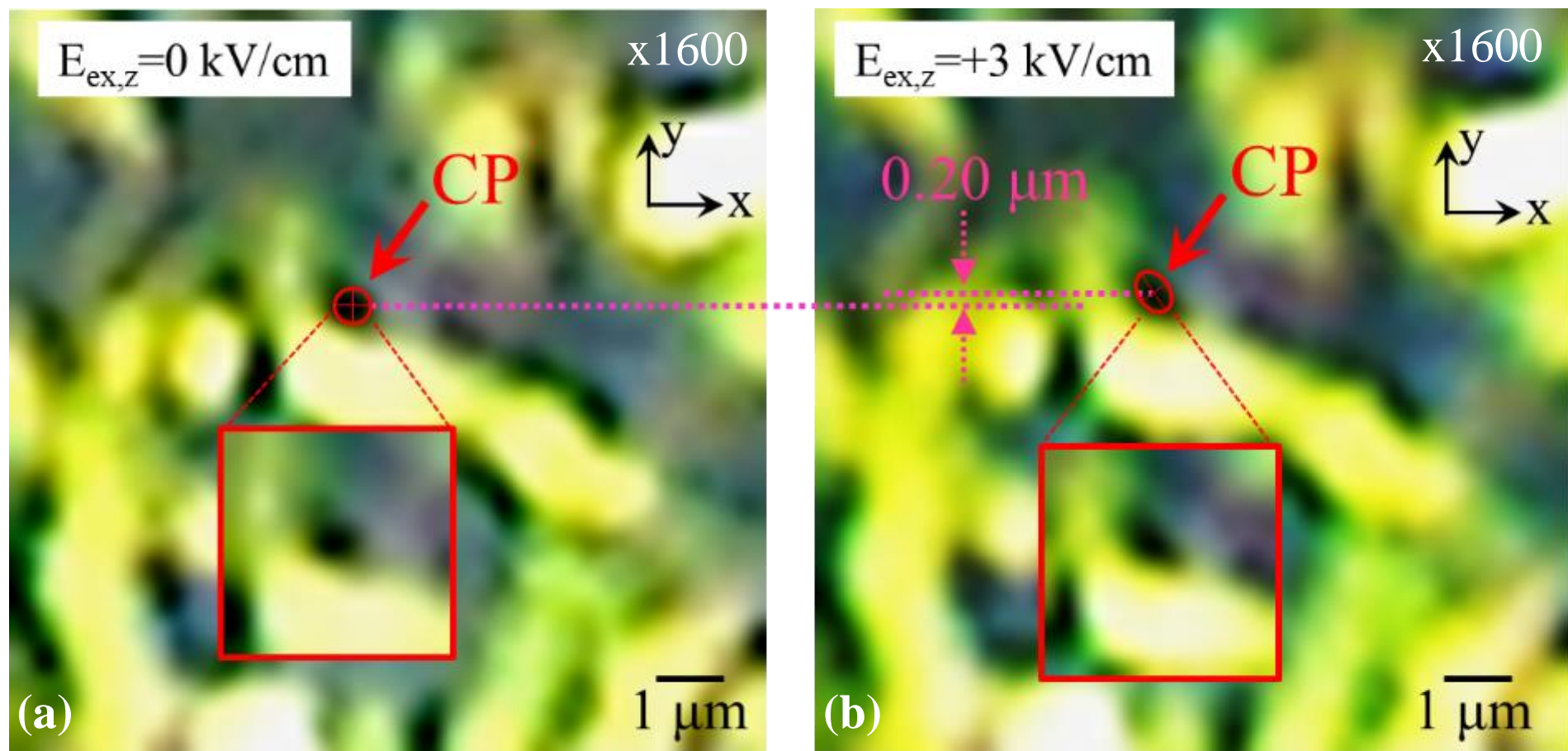


Fig.A.3: (a),(b) Processed optical microscopy (OM) images of a PZT sample at (a) $E_{ex,z}=0$ kV/cm and (b) $E_{ex,z}=+3$ kV/cm. The selected CP is shown with a red arrow in both panels; its shape alters under $E_{ex,z}$ application from a round-like to an elliptical-like shape, as can be discerned in the insets (a.i) and (b.i), respectively. For this reason the spatial limits of the CP are outlined with a red (a) circular and (b) elliptical contour line, along with their respective symmetry axes. The magenta dotted lines and arrows denote the least discerned displacement of the CP along y-axis that is on the order of $0.20 \mu\text{m}$; we stress that $R_{OM}=0.20 \mu\text{m}$, where R_{OM} corresponds to the resolution of the processed image. The scale bar designates

References

- [1] J. A. DeRose and M. Doppler, *Micros. Today* **26**, 20 (2018).
- [2] M. S. Elliot and W. C. K. Poon, *Adv. Colloid Int. Sci.* **92**, 133 (2001).

Appendix B

Propagation of errors in $S(E_{ex,z})$ data: a proof of concept of the OM-based PE technique

This appendix aims in clarifying the propagation of errors in the estimation of the strain-electric field curves, $S(E_{ex,z})$. In this context, let us recall the definition of strain, which is given by the relation shown below:

$$S = \frac{\Delta l}{l} \quad (B.1)$$

where l is the length of a PE sample at $E_{ex,z}=0$ (unstrained state) and Δl is the change in length due to $E_{ex,z}$ application. Also, the electric field is given by the following relation:

$$E_{ex,z} = \frac{V_{ex}}{t} \quad (B.2)$$

where V_{ex} is the external voltage that is applied along the thickness of the sample, t (i.e. along z -axis).

Since S is a function of Δl and l ($S(\Delta l, l)$) and $E_{ex,z}$ is a function of V_{ex} and t ($E_{ex,z}(V_{ex}, t)$), the respective errors, δS and $\delta E_{ex,z}$, should be determined by standard error propagation.

In general, if R is a function of two variables, namely X and Y , written as $R(X, Y)$, then the error of R is obtained by the expression:

$$\delta R = \sqrt{\left(\frac{\partial R}{\partial X} \cdot \delta X\right)^2 + \left(\frac{\partial R}{\partial Y} \cdot \delta Y\right)^2} \quad (B.3)$$

Accordingly, the errors δS and $\delta E_{ex,z}$ of $S(\Delta l, l)$ and $E_{ex,z}(V_{ex}, t)$, respectively, are described by the relations presented below:

$$\delta S = \sqrt{\left(\frac{\partial S}{\partial \Delta l} \cdot \delta \Delta l\right)^2 + \left(\frac{\partial S}{\partial l} \cdot \delta l\right)^2} \quad (B.4)$$

with $\delta \Delta l$, δl the errors of Δl and l , respectively,

and

$$\delta E_{ex,z} = \sqrt{\left(\frac{\partial E_{ex,z}}{\partial V_{ex}} \cdot \delta V_{ex}\right)^2 + \left(\frac{\partial E_{ex,z}}{\partial t} \cdot \delta t\right)^2} \quad (B.5)$$

with δV_{ex} , δt the errors of V_{ex} and t , respectively.

From Eqs. (B.4), (B.5) we can estimate δS and $\delta E_{ex,z}$ by introducing representative values in $\delta \Delta l$, δl and δV_{ex} , δt , respectively.

Regarding $\delta \Delta l$, it is the error in *shape delimitation*. This error is introduced upon image analysis; it refers to the precision that we can survey the spatial limits of a characteristic

feature (see Appendix A). Accordingly, for $\delta\Delta l$ we consider the following representative values $\delta\Delta l=0.05\ \mu\text{m}$, $0.10\ \mu\text{m}$ and $0.20\ \mu\text{m}$. In addition, δl is the error in the measurement of sample's length, using a digital caliper. Thus, for δl we take the nominal error of the digital caliper that we used, that is $\delta l=0.02\ \text{mm}$. Concerning δV_{ex} , it is the output error in the DC-voltage supply unit, $\delta V_{\text{ex}}=0.1\ \text{V}$. Furthermore, δt is the nominal error of the digital caliper (mentioned above), $\delta t=0.02\ \text{mm}$.

In table B1 below we summarize the individual error values $\delta\Delta l$, δl , δV_{ex} and δt . Also, the error values δS and $\delta E_{\text{ex},z}$ that result from Eqs. (B.4) and (B.5) are also presented in bold.

$\delta\Delta l\ (\mu\text{m})$	$\pm 0.05, \pm 0.10, \pm 0.20$
$\delta l\ (\text{mm})$	± 0.02
$\delta V_{\text{ex}}\ (\text{V})$	± 0.1
$\delta t\ (\text{mm})$	± 0.02
δS	$\pm 1\cdot 10^{-5}, \pm 2\cdot 10^{-5}, \pm 4\cdot 10^{-5}$
$\delta E_{\text{ex},z}\ (\text{kV/cm})$	± 0.001

Table B1: Individual error values, $\delta\Delta l$, δl , δV_{ex} and δt , that come into the calculation of δS and $\delta E_{\text{ex},z}$. The resulting values of δS and $\delta E_{\text{ex},z}$ are also presented in bold.

In Fig. B.1 below, we survey the influence of δS and $\delta E_{\text{ex},z}$, presented in Table B1, on representative $S(E_{\text{ex},z})$ data obtained in this PhD Thesis. Specifically, we present the error bars corresponding to δS and $\delta E_{\text{ex},z}$ on $S(E_{\text{ex},z})$ data of PZT samples sintered at $T=1000\ ^\circ\text{C}$ (Figs.B.1(a.i)-(c.i)) and at $T=1180\ ^\circ\text{C}$ (Figs.B.1(a.ii)-(c.ii)); these results have been already discussed in Fig. 4.14 of the subchapter 4.2.1.V. The panels (a)-(c) correspond to $\delta S=\pm 1\cdot 10^{-5}$, $2\cdot 10^{-5}$ and $4\cdot 10^{-5}$, represented with black, red and magenta-colored error bars, respectively (please, note that solid and open blue symbols, constituting the $S(E_{\text{ex},z})$ data, are identical in all panels (a.i)-(c.i) and (a.ii)-(c.ii), respectively). The error bars corresponding to $\delta E_{\text{ex},z}$ are well below the symbol size, and thus not shown in the following Figs.

Firstly, we will discuss the influence of δS on the data of panels (a.i)-(c.i), referring to PZT sintered at $T_{\text{sin}}=1000\ ^\circ\text{C}$. For the best case scenario, $\delta S=\pm 1\cdot 10^{-5}$, shown in panel (a.i), we observe that the black-colored error bars are slightly smaller than the symbol size. For the intermediate case, $\delta S=\pm 2\cdot 10^{-5}$, shown in panel (b.i), the red-colored error bars are comparable to the symbol size, while for the worst case scenario, $\delta S=\pm 4\cdot 10^{-5}$, shown in panel (c.i), the magenta-colored error bars are quite high. Based on these error bars, a grey-shaded bell-shaped curve is employed in order to denote the uncertainty in allocating the specific $E_{\text{ex},z}$ value at which the $S(E_{\text{ex},z})$ peaks occur in each panel; we note that when neglecting the error bars, which is the case of panel (a.i), the peaks occur at $E_{\text{ex},z}=\pm 3.5\ \text{kV/cm}$ for PZT sintered at $T_{\text{sin}}=1000\ ^\circ\text{C}$, as shown in Fig. B.1(a.i) by the thick black arrow. Accordingly, the uncertainty in allocating the peak at the $S(E_{\text{ex},z})$ curves of panels (b.i) and (c.i) extends to 2.5 kV/cm and 4 kV/cm, as indicated by the red and magenta thick horizontal bars, respectively.

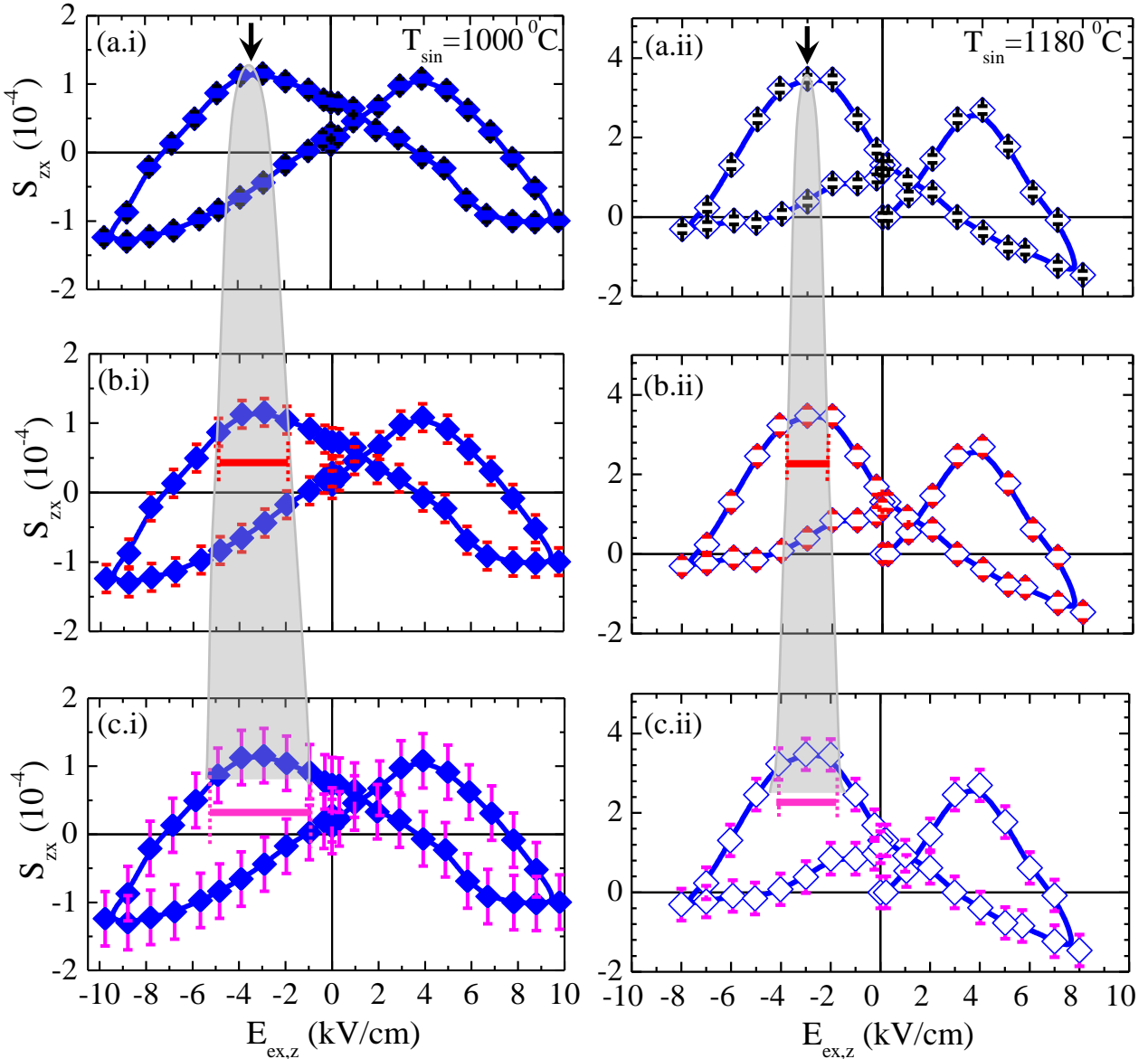


Fig. B.1: $S(E_{ex,z})$ curves for PZT samples sintered at (a.i)-(c.i) $T=1000$ °C and at (a.ii)-(c.ii) $T=1180$ °C. The error bars, δS , take the specific values (i) $\pm 1 \cdot 10^{-5}$, (ii) $\pm 2 \cdot 10^{-5}$ and (iii) $\pm 4 \cdot 10^{-5}$ that refer to an error in shape delimitation, $\delta \Delta l$, (i) ± 0.05 μm , (ii) ± 0.10 μm and (iii) ± 0.20 μm , respectively (see text for details).

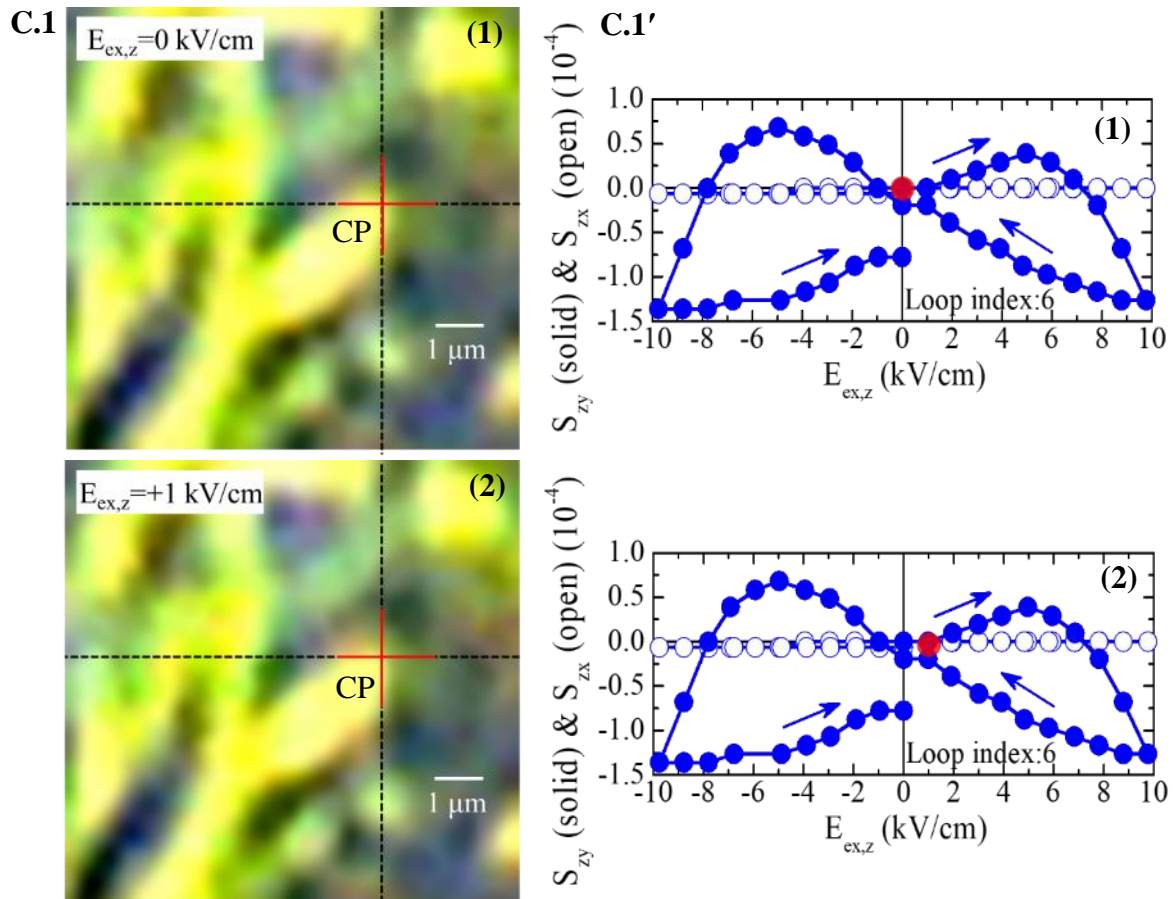
Secondly, we will discuss the influence of δS on the data of panels (a.ii)-(c.ii), referring to PZT samples sintered at $T_{sin}=1180$ °C. The respective samples exhibited noticeably higher PE response compared to the ones sintered at $T_{sin}=1000$ °C. For this reason, we see that the error bars $\delta S = \pm 1 \cdot 10^{-5}$ and $2 \cdot 10^{-5}$ are smaller than the symbol size, as shown in panels (a.ii), (b.ii), and thus can be neglected. Thus, the peaks of $S(E_{ex,z})$ can be determined with almost negligible uncertainty, at $E_{ex,z} = \pm 3$ kV/cm, as shown in panel (a.ii) with a thick black arrow. For the worst case scenario, $\delta S = 4 \cdot 10^{-5}$, shown in panel (c.ii), the error bars are notable, though fairly small. Regarding the $S(E_{ex,z})$ curve of this panel, the uncertainty in allocating its peak extends to 2 kV/cm, as denoted by the grey-shaded bell-shaped curve.

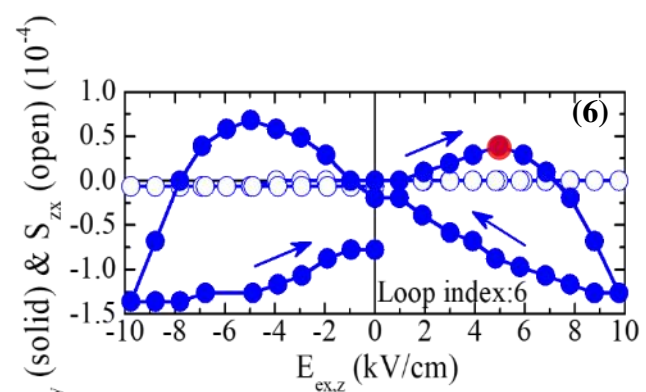
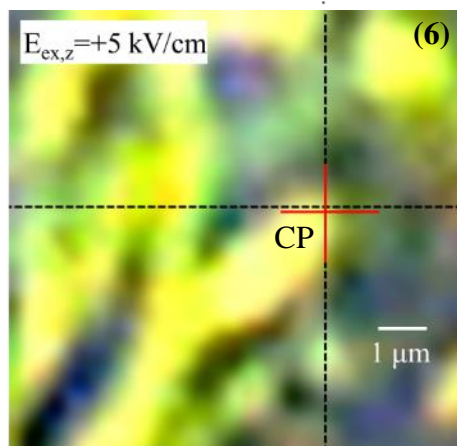
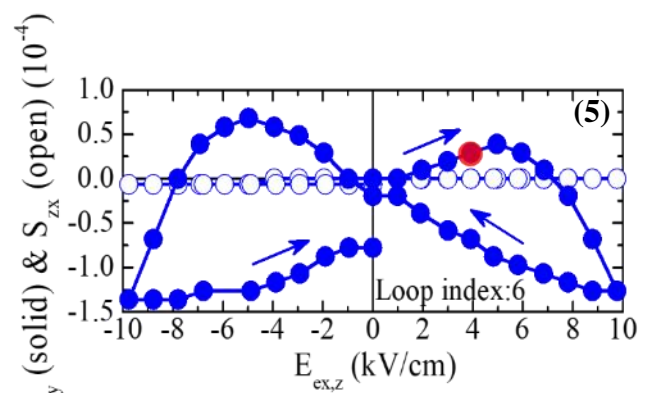
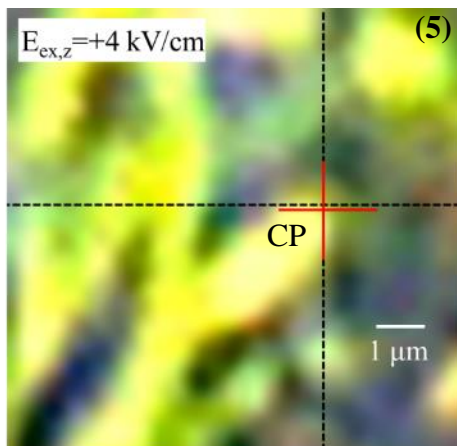
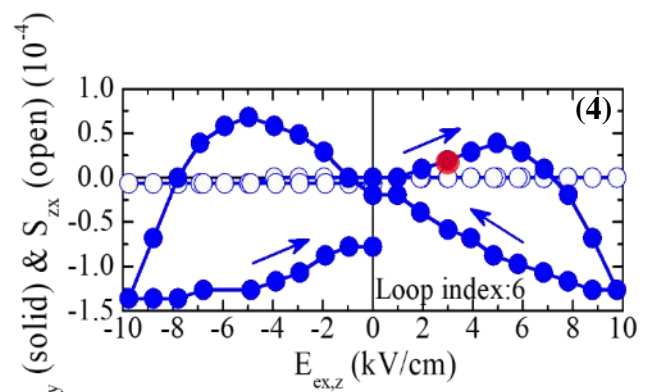
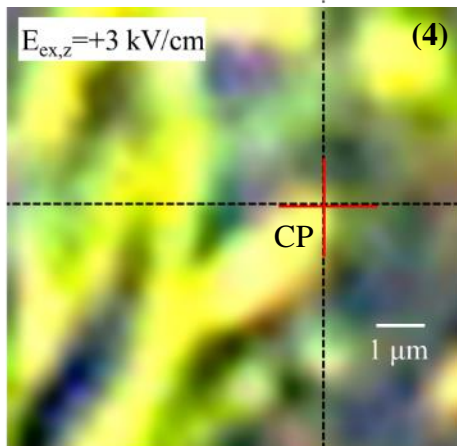
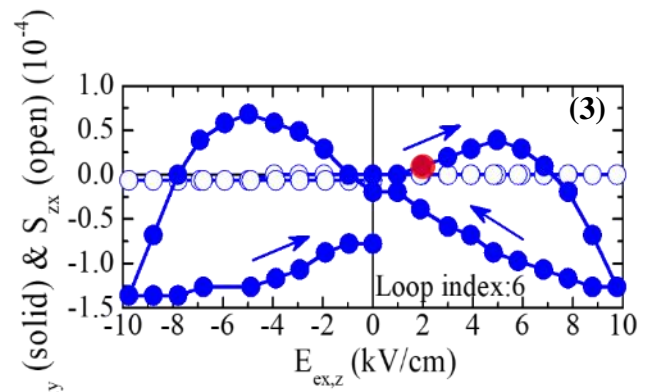
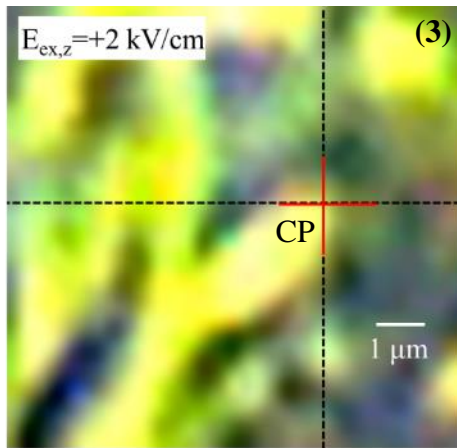
Lastly, we should highlight the following; among the gradually increasing error bars presented with different colors in Figs. B.1(a.i)-(c.i) and B.1(a.ii)-(c.ii), we stress that the

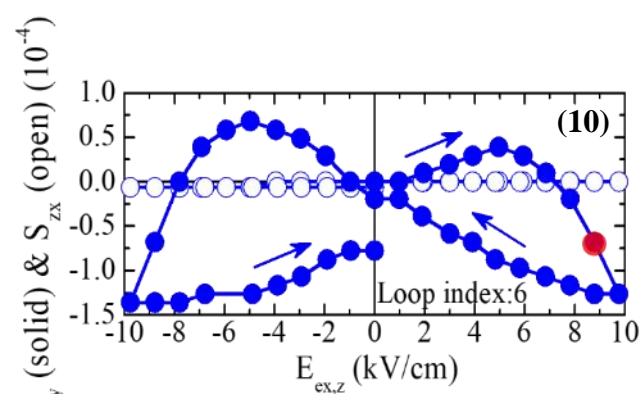
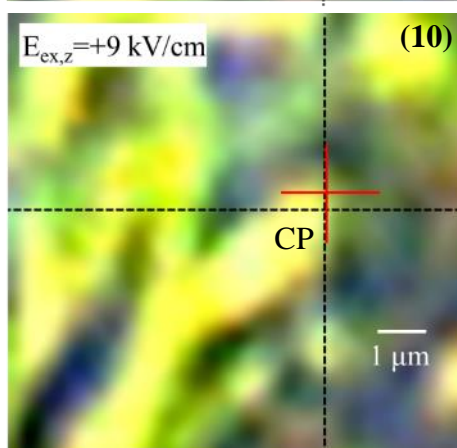
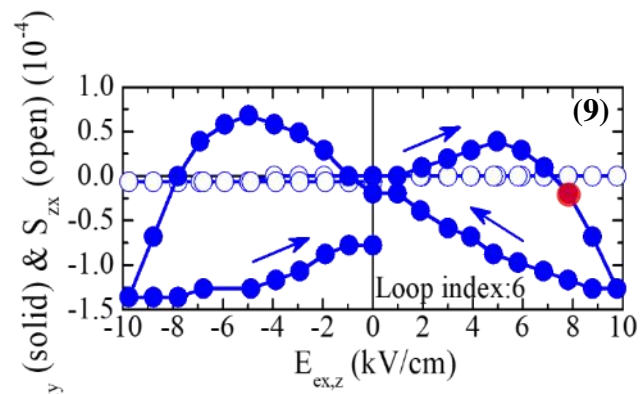
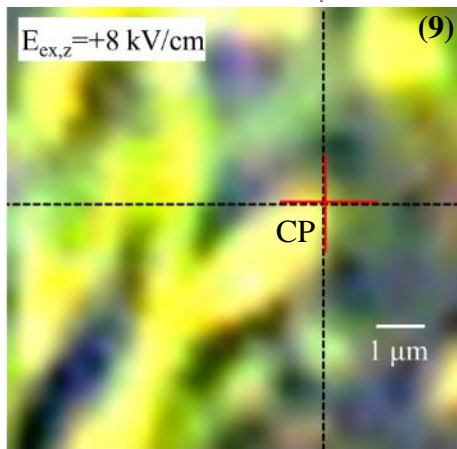
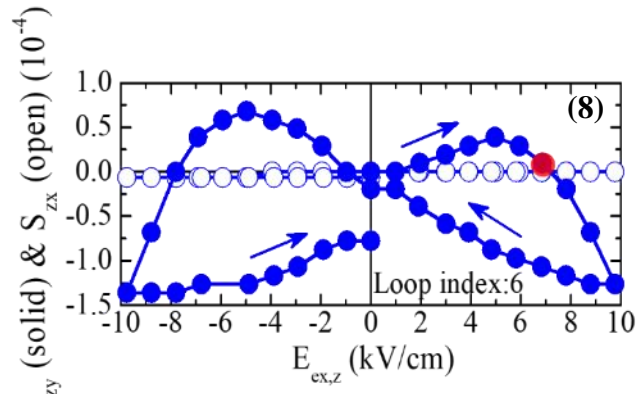
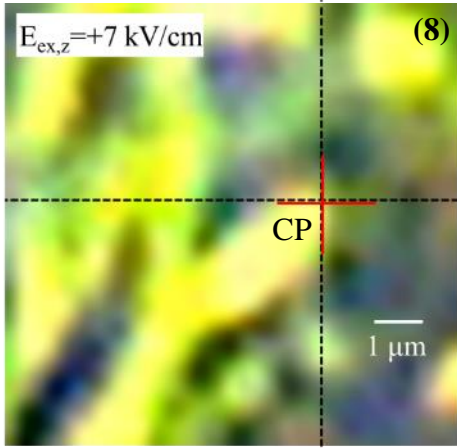
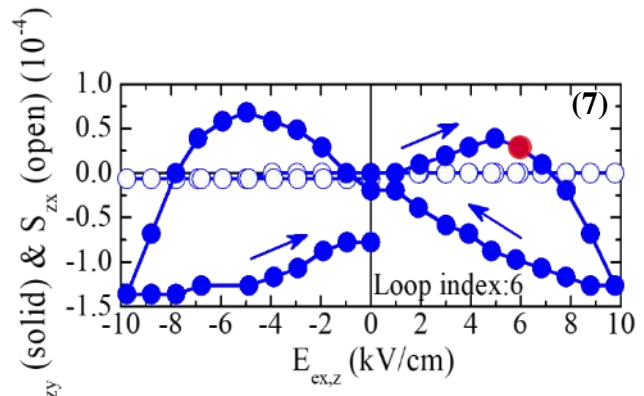
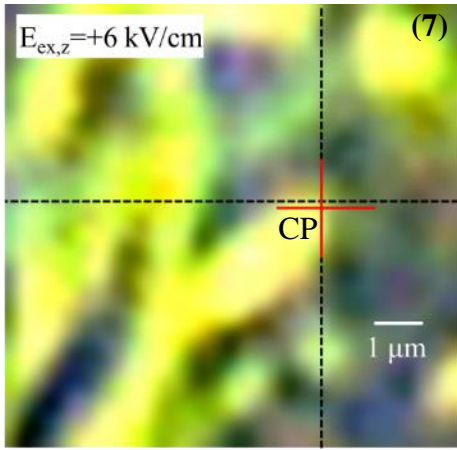
case of $\delta S = \pm 2 \cdot 10^{-5}$ (Figs. B.1(b.i) and B.1(b.ii)) corresponds to the data obtained for PZT samples studied in this Thesis. Specifically, from the Eq. (B.4), above, it is deduced that the value of δS is mainly determined by $\delta \Delta l$, i.e. the *error in shape delimitation* (for details, see Appendix A). In Appendix A, we saw that the minimum CP's deformation that can be confidently measured from a processed OM image, originally obtained by our optical system, is $\Delta l = 0.20 \mu\text{m}$. Accordingly, the respective error in shape delimitation cannot exceed the value $\delta \Delta l = \pm 0.10 \mu\text{m}$; in turn, the corresponding error δS cannot exceed the value $\delta S = \pm 2 \cdot 10^{-5}$.

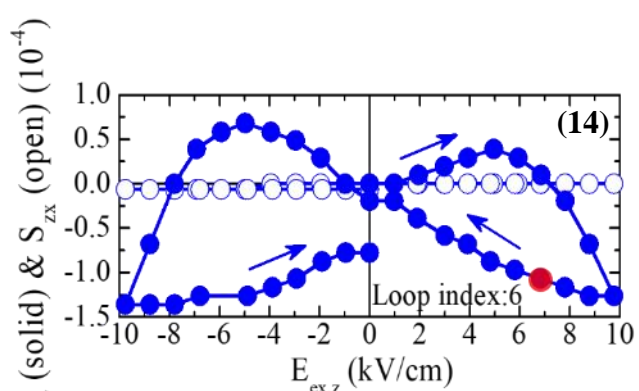
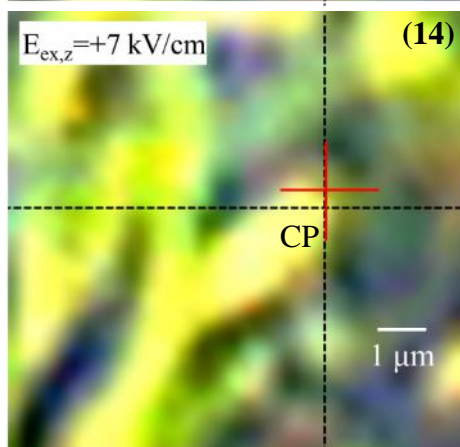
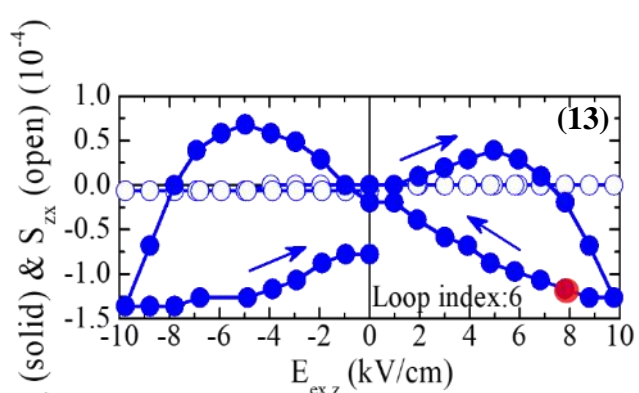
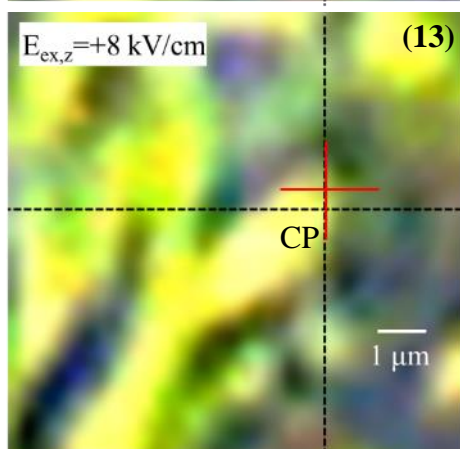
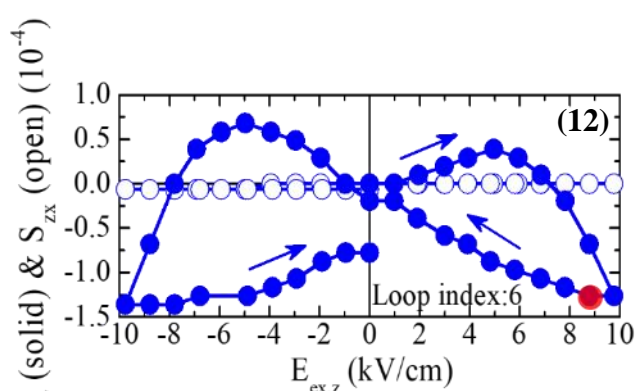
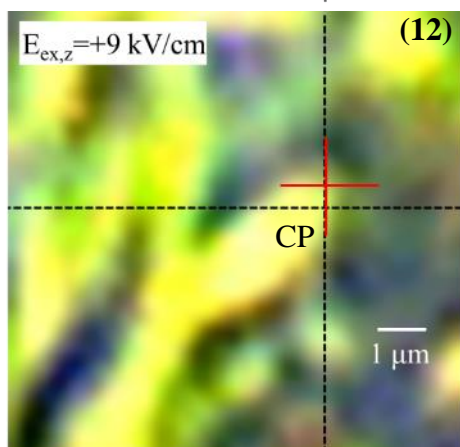
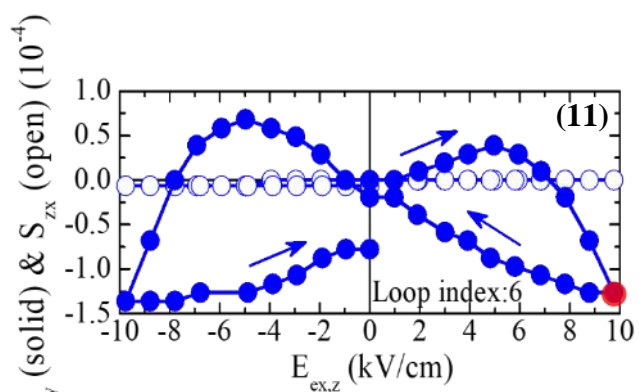
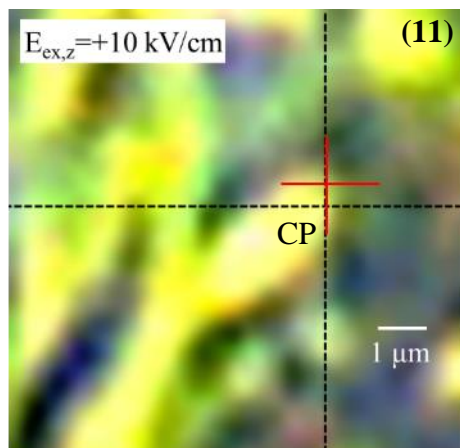
Appendix C: Sequence of representative $S(E_{ex,z})$ data

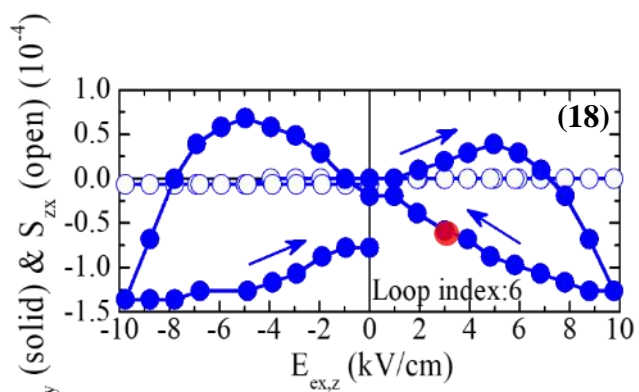
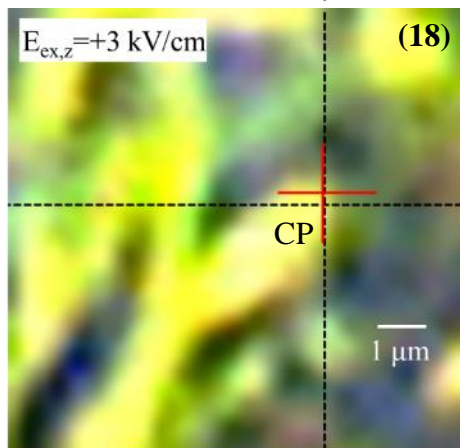
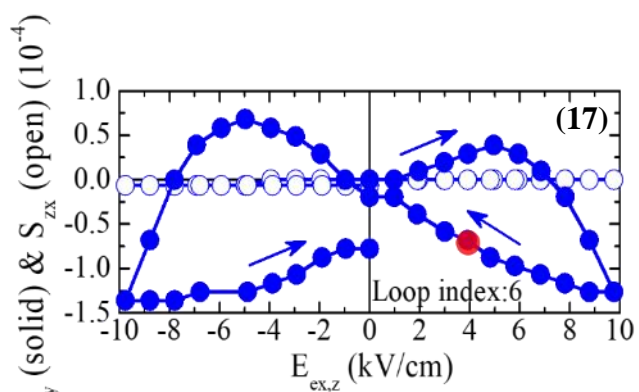
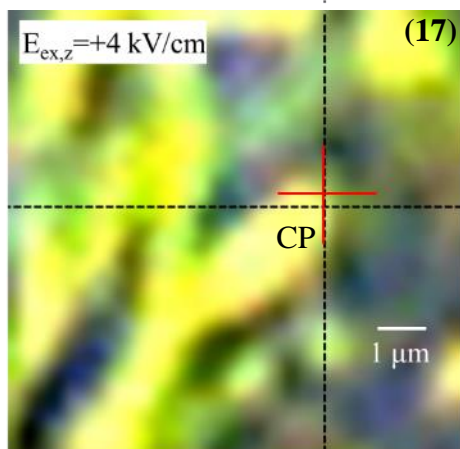
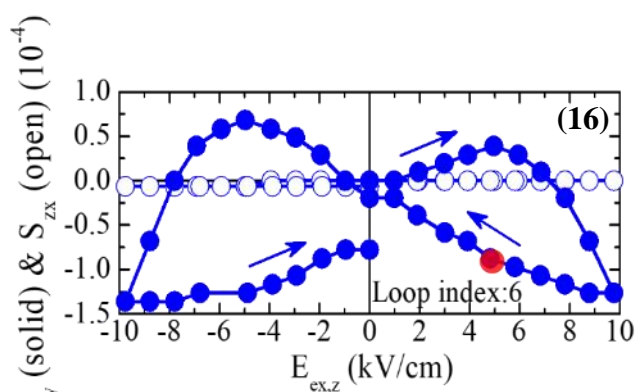
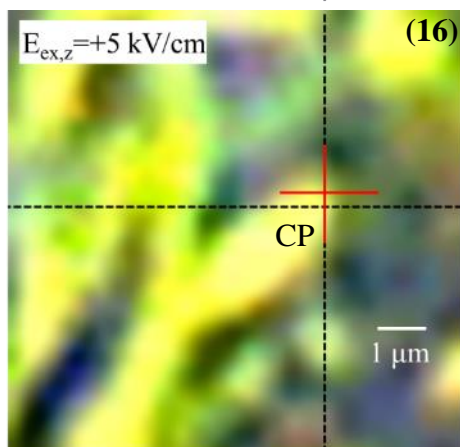
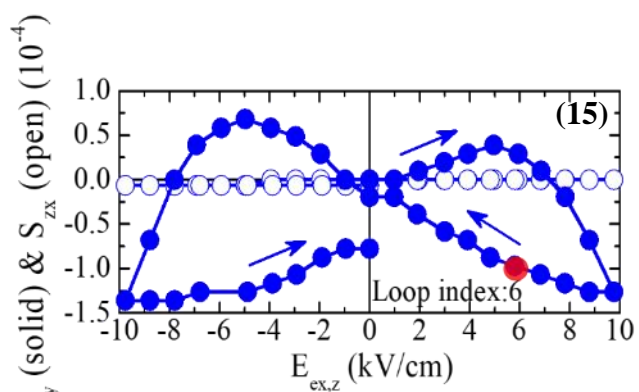
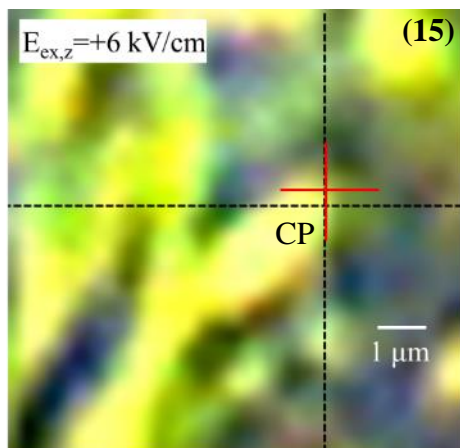
In this appendix we present a typical sequence of processed OM images for a PZT-5%Fe₃O₄ sample, so that the reader gets the general overview on how the entire procedure is accomplished; starting from the cropped and enlarged OM images (see Appendix A for details on image processing), we trace a CP so that we ultimately construct the $S(E_{ex,z})$ curves. This data is also available in the form of animation (see “Representative strain-electric field data” mp4 video file). Each image corresponds to a specific $E_{ex,z}$ value (that falls within ± 10 kV/cm), as shown in Figs. C.1(1)-C.1(40); each one presents the initial position of the CP with an extended black dashed cross. The center of the latter is fixed and serves as the reference point of the initial unstrained state ($E_{ex,z}=0$). On the contrary, the limited solid red cross traces the position of the CP as we vary $E_{ex,z}$ in the following sequence of photographs. Thus, the resulting displacement can be quantified by means of the scale bar that designates 1 μ m (see Appendix A for details on length scale estimation). The specific value of $E_{ex,z}$ is shown in the upper left corner of each image. The deduced $S_{zx}(E_{ex,z})$ and $S_{zy}(E_{ex,z})$ are shown in Figs. C.1'(1)-C.1'(40). By careful observation of this sequence of images we deduce that the displacement along x-axis is at the borderline of -or below- the resolution limit of the processed images ($R_{OM}=0.20$ μ m, see Appendix A), while the ones along the y-axis are well above. Consequently, we completely ignore displacements along x-axis so that almost all data points referring to the respective $S_{zx}(E_{ex,z})$, presented in Figs. C.1'(1)-C.1'(40), are placed to zero. In contrast, $S_{zy}(E_{ex,z})$ obtains clearly non-zero values, denoted by the red solid circle that traces the entire $S_{zy}(E_{ex,z})$ loop in Figs. C.1'(1)-C.1'(40).

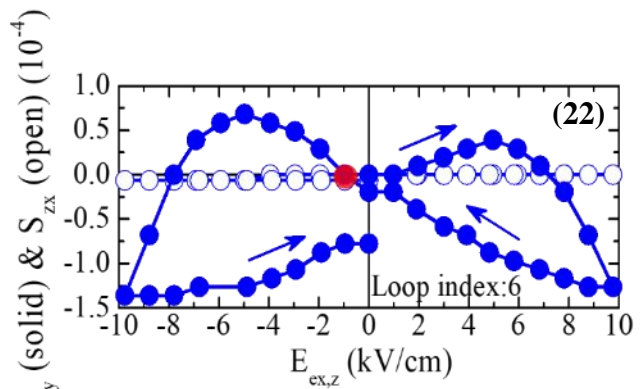
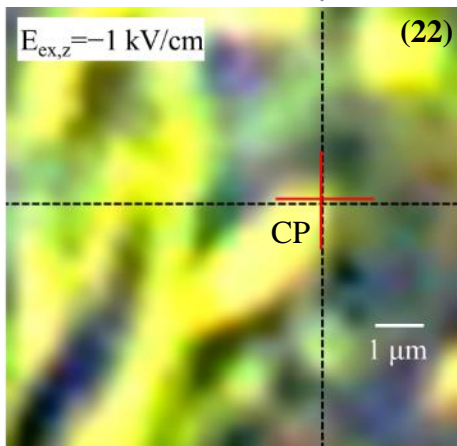
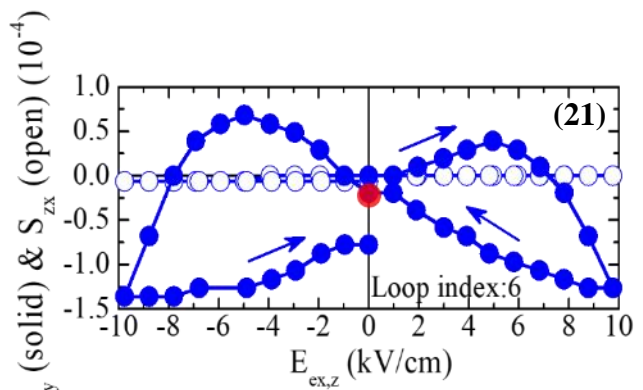
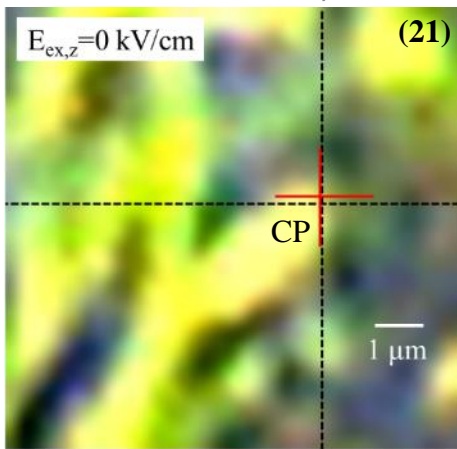
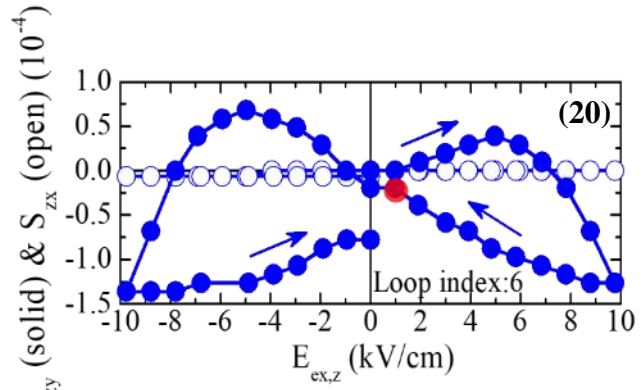
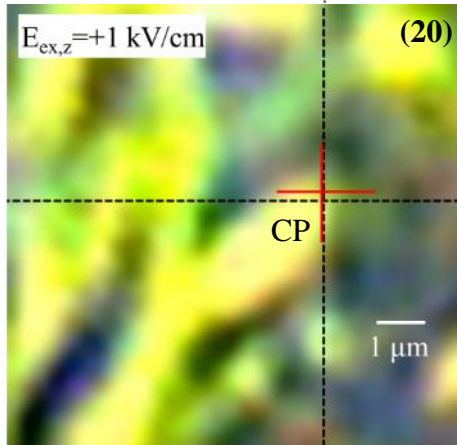
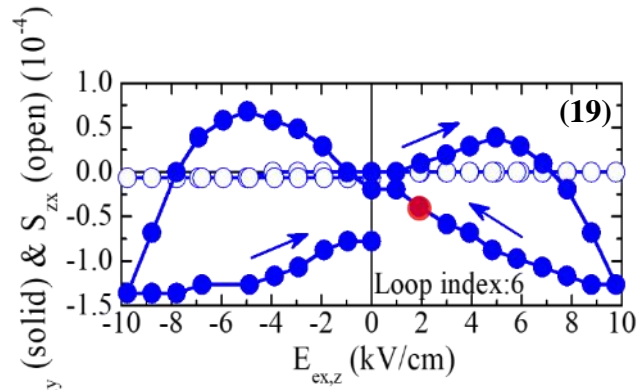
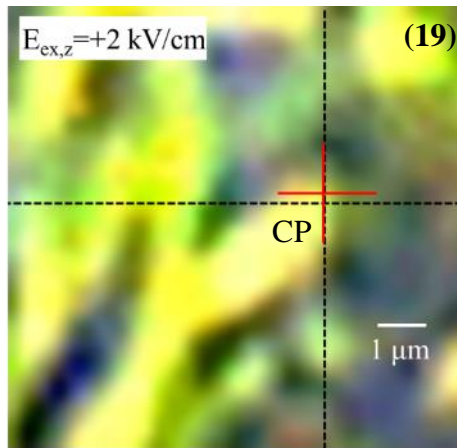


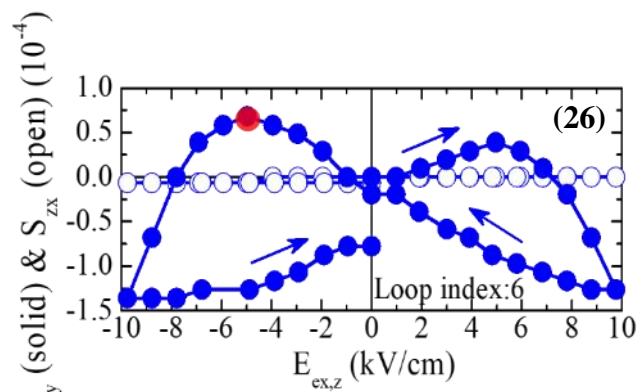
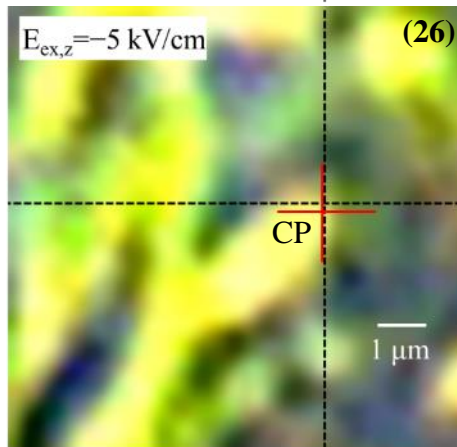
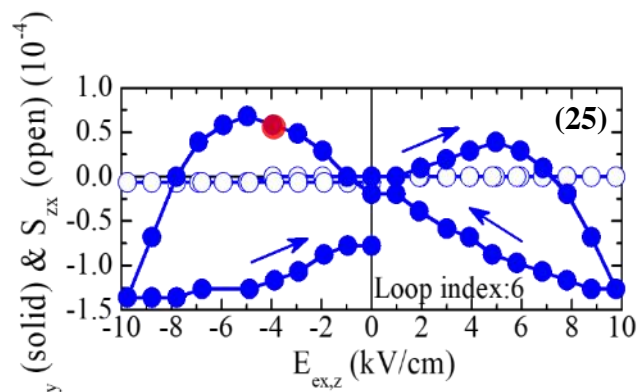
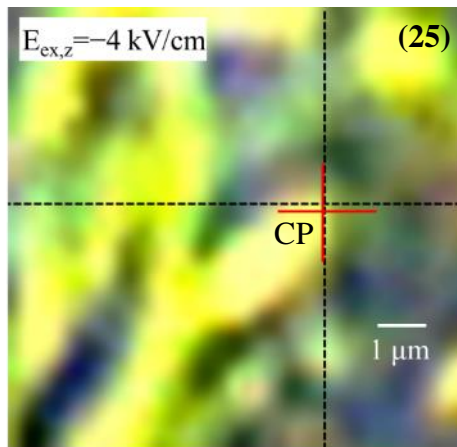
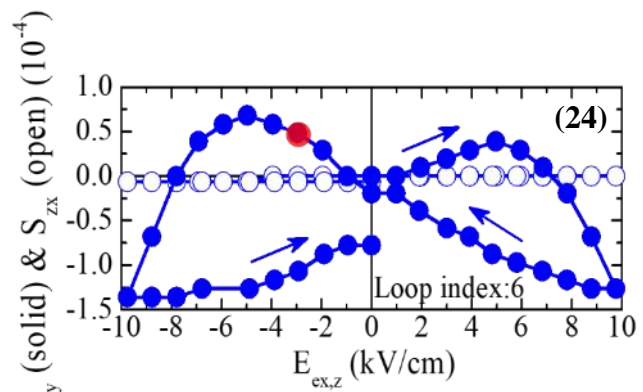
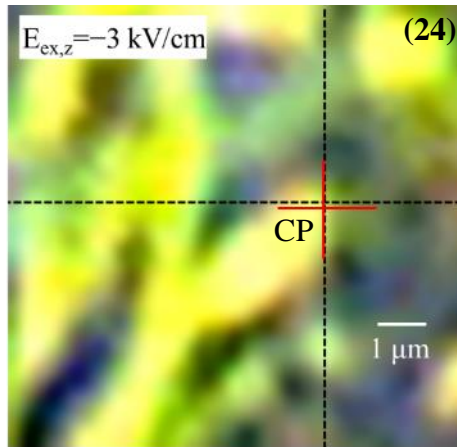
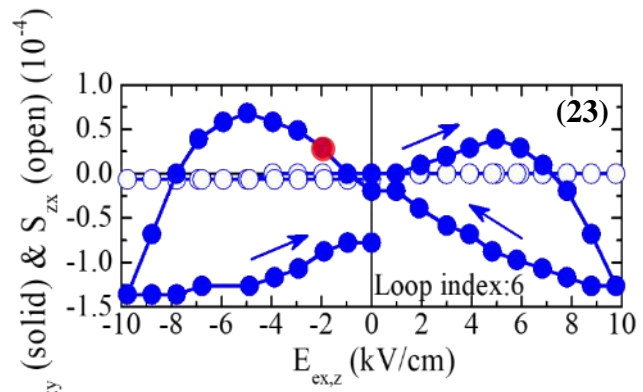
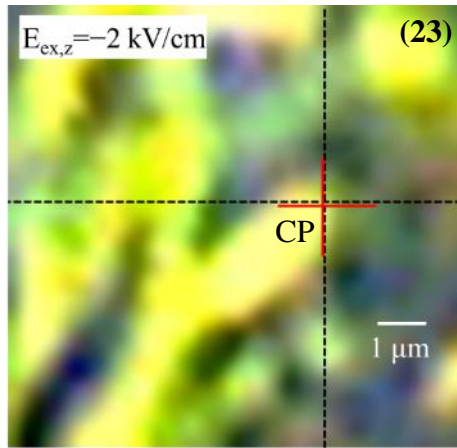


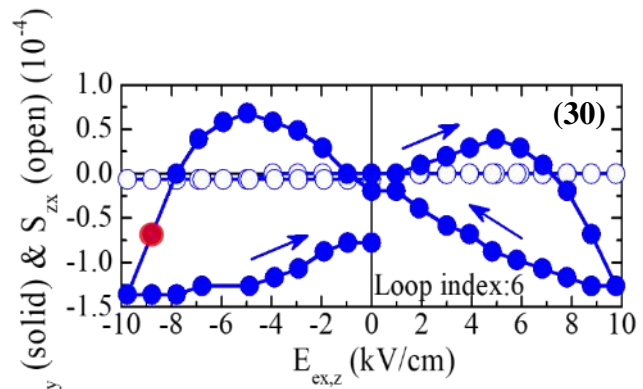
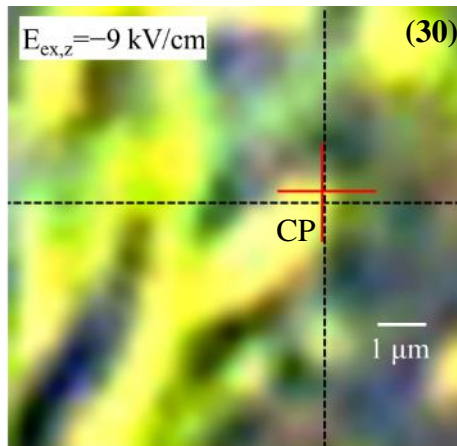
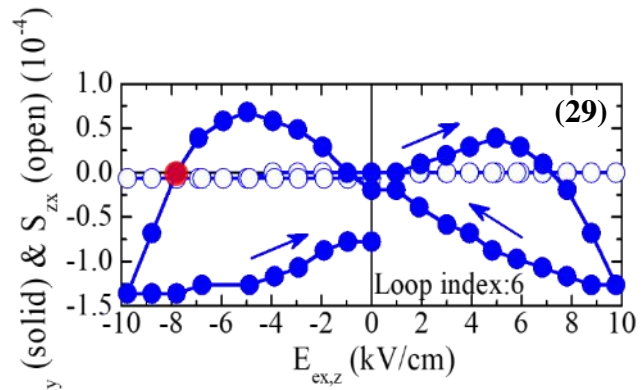
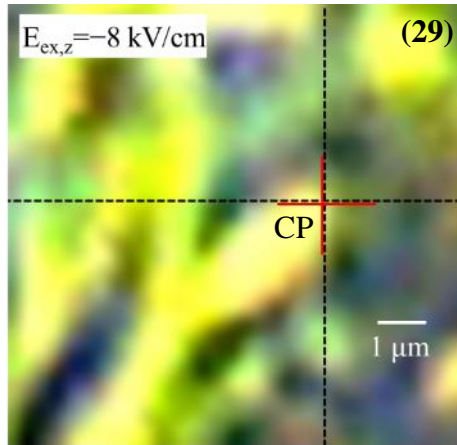
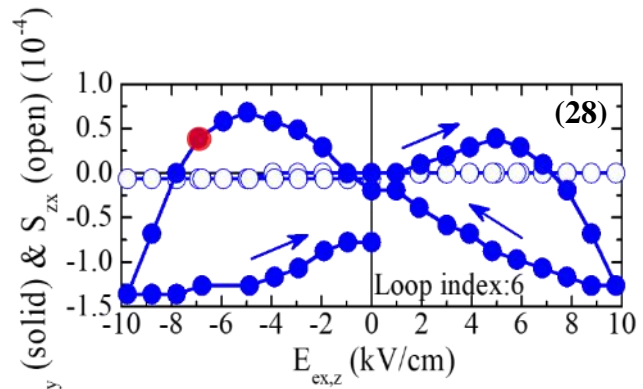
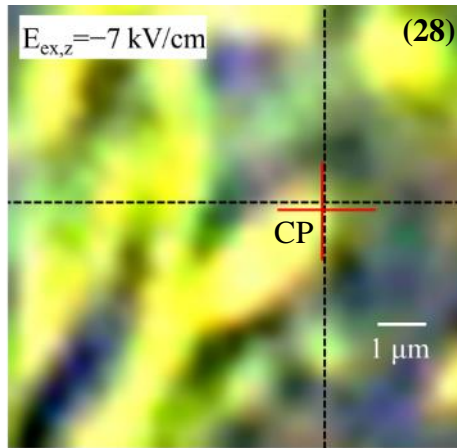
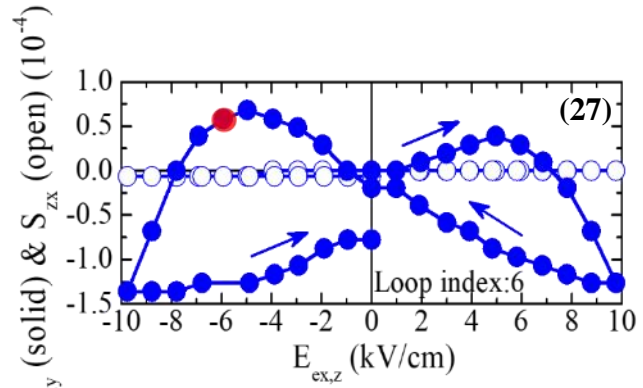
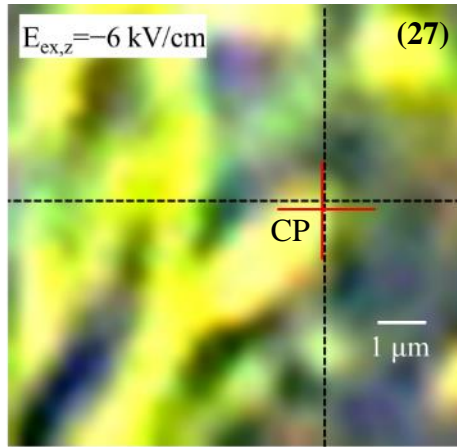


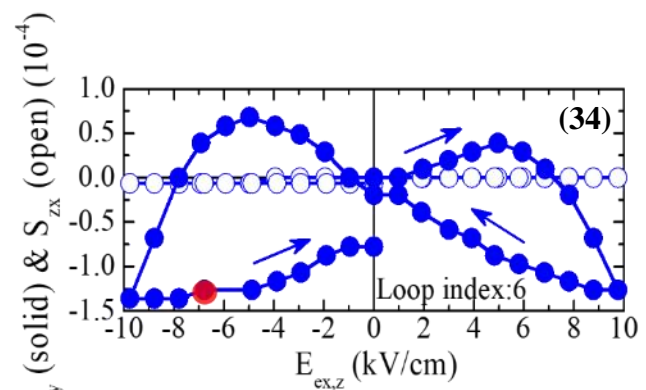
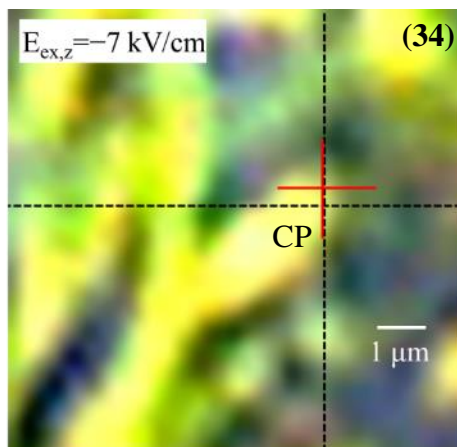
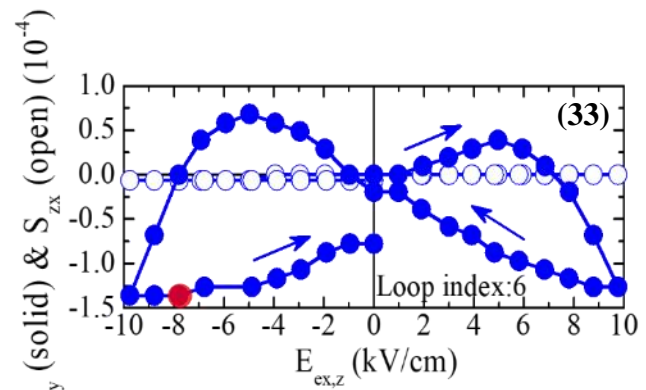
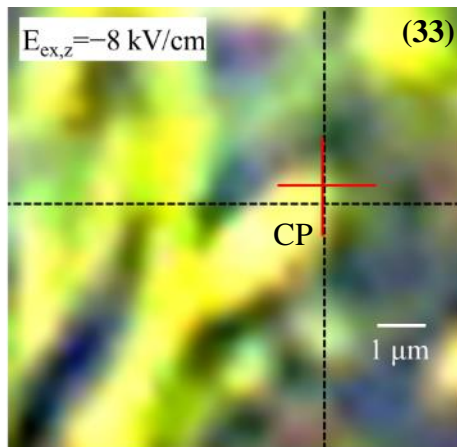
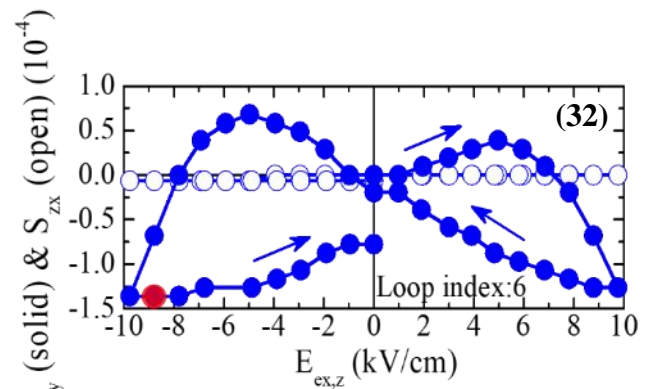
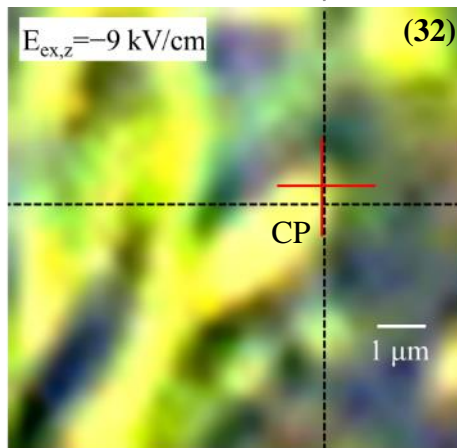
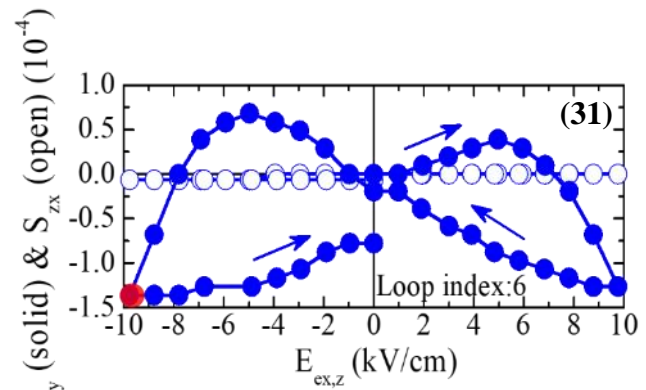
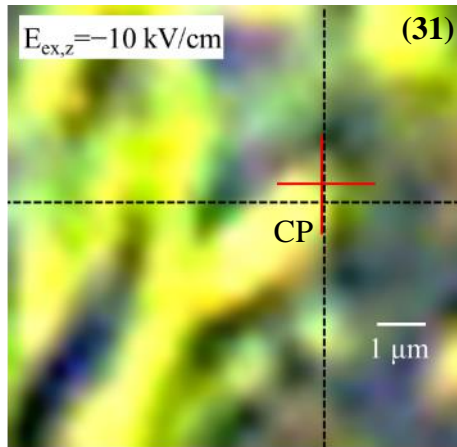


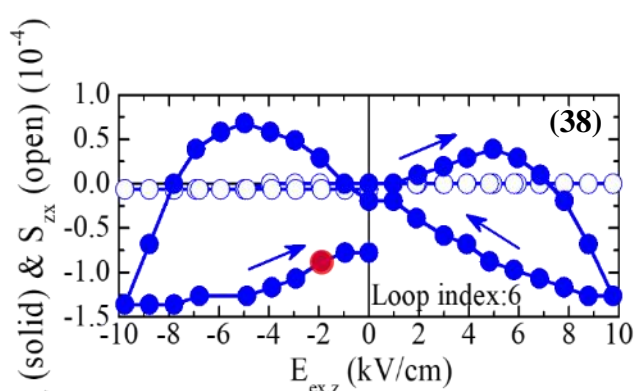
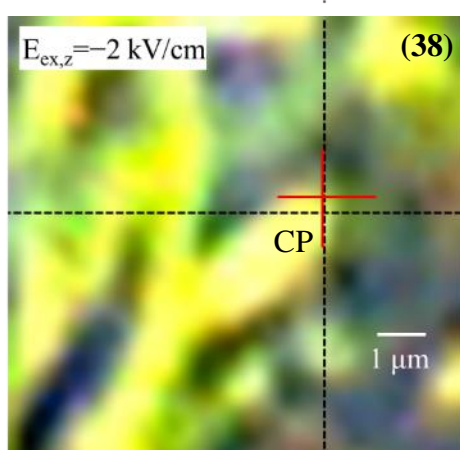
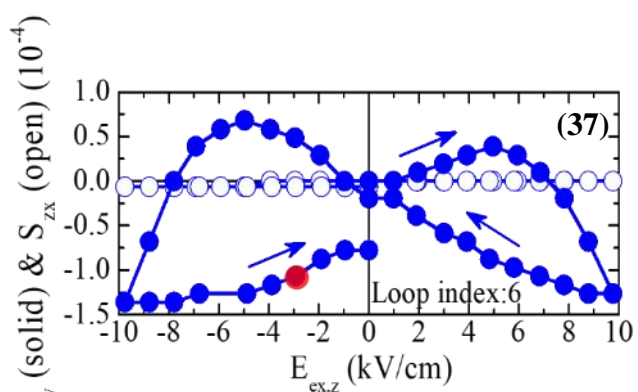
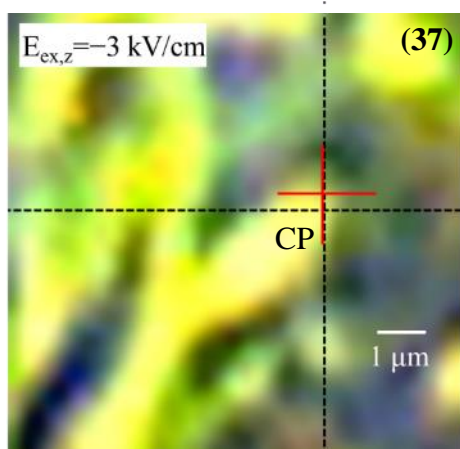
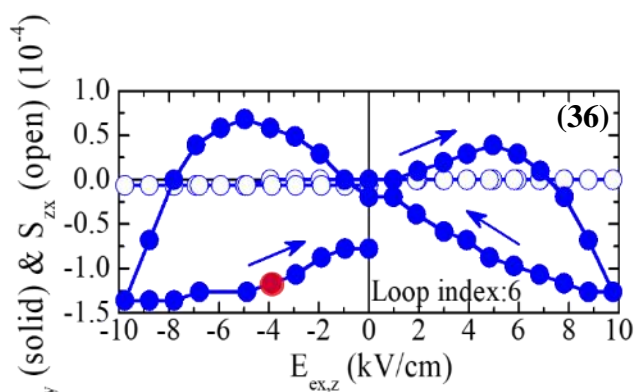
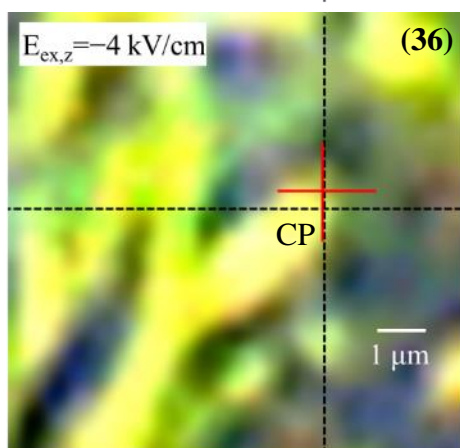
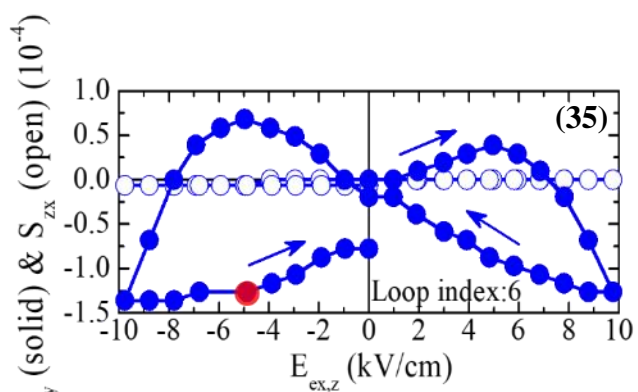
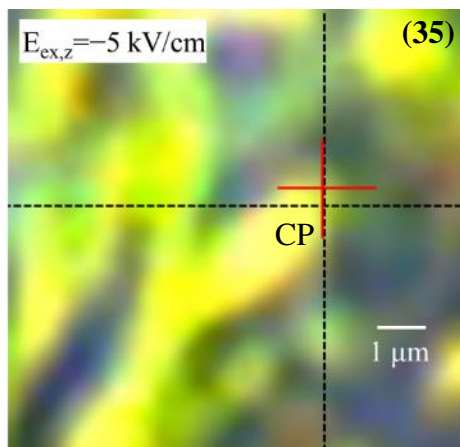












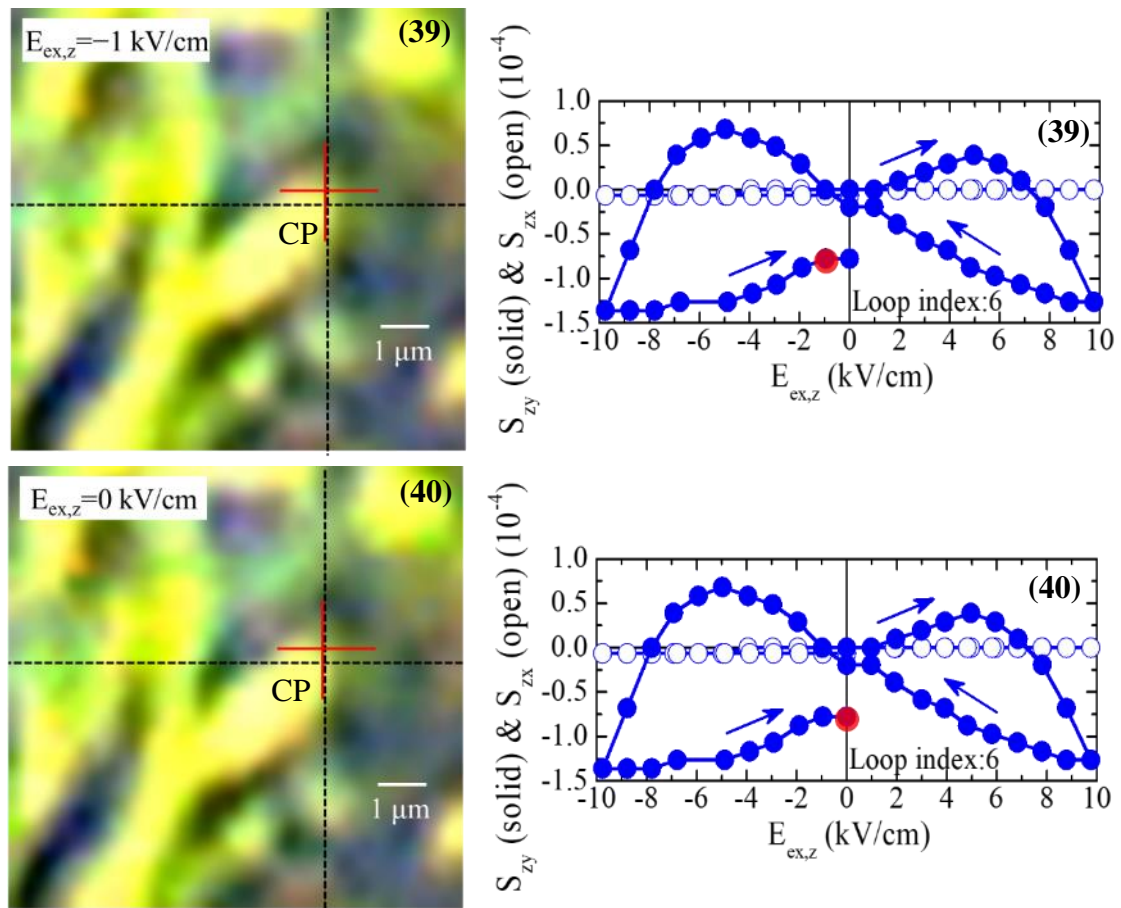


Fig. C.1 (1-40) Sequence of processed OM images upon varying $E_{ex,z}$ within ± 10 kV/cm. In each image the extended black dashed cross shows the initial position of the CP (unstrained sample, $E_{ex,z}=0$ kV/cm). The limited red solid cross traces the position of the CP while varying $E_{ex,z}$. The specific value of $E_{ex,z}$ is shown in the upper left corner, while the scale bar designates $1\mu\text{m}$. **C.1' (1-40)** The deduced in-plane strain values S_{zx} and S_{zy} for each $E_{ex,z}$ are shown with the open and solid blue circles, respectively. The red solid circle traces the entire $S_{zy}(E_{ex,z})$ loop.

Appendix D: Optical cryochamber and thermoplatform for the estimation of the respective low and high temperature piezoelectric coefficients

The phase diagrams of PE materials such as $\text{Pb}(\text{Zr}_{1-x}\text{Ti}_x)\text{O}_3$ and PMN-xPT are constantly being investigated through the decades. Very recently, crucial experimental points were added to the phase diagrams so that the structure of the respective compounds was clarified in terms of their compositional and temperature dependence. These experimental points were deduced from several techniques such as XRD, neutron diffraction and dielectric spectroscopy; nevertheless, only few of these experimental data refer to information on the PE coefficients, d_{ij} . For example, in Fig. D.1, which shows a recent version of the $\text{Pb}(\text{Zr}_{1-x}\text{Ti}_x)\text{O}_3$ phase diagram, focused on the compositional range within $0.39 \leq x(\text{Ti}) \leq 0.54$ and the temperature range within $0 \text{ K} \leq T \leq 700 \text{ K}$ (Cordero et al., Phase Transit. **87**, 255 (2013)), we observe that, in general, only a small number of experimental points (symbols: squares) were deduced from measurements of PE coefficients (G. Arlt, Proceedings of the IEEE, Ultrasonic Symposium., 733 (1990)). By focusing on the low-temperature regime $T < 300 \text{ K}$, in particular, we observe that there are much fewer experimental points compared to $T > 300 \text{ K}$ that are mainly obtained by means of XRD and Raman spectroscopy (symbols: red bars and blue stars). Accordingly, in order to investigate the less studied low-temperature region of the phase diagrams of $\text{Pb}(\text{Zr}_{1-x}\text{Ti}_x)\text{O}_3$ and PMN-xPT (and possibly of other PE materials), we have designed and constructed a preliminary version of an optical cryochamber that gives us the capability of recording the in-plane strain curves, $S_{zi}(E_{ex,z})$ ($i=x,y$), by OM upon controllable variation of temperature down to liquid nitrogen conditions ($T=78 \text{ K}$) with simultaneous application of a desired external electric field, $E_{ex,z}$. By means of this cryochamber the temperature dependence of the respective PE coefficients, $d_{zi}(T)$, can be surveyed. In this respect, any possible anomaly that might be detected in the $d_{zi}(T)$ curves, could fairly be ascribed to crystallographic phase transitions, enabling us to enrich the phase diagram in its low-temperature regime.

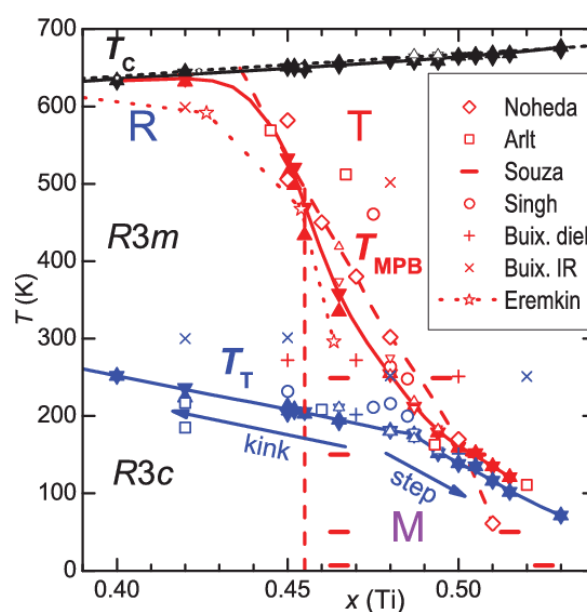


Fig. D.1: Phase diagram of $\text{Pb}(\text{Zr}_x\text{Ti}_{1-x})\text{O}_3$ focused on the compositional range $0.39 \leq x(\text{Ti}) \leq 0.54$ and on the temperature range $0 \text{ K} \leq T \leq 700 \text{ K}$. The different symbols correspond to the different experimental techniques from which the specific points of the phase diagram were deduced (Cordero et al., Phase Transit. **87**, 255 (2013)).

Following a similar approach, in order to extend the investigation of the PE coefficients in the high-temperature regime, $T > 300$ K, we have also developed an optical thermoplatform. By means of this apparatus we have the capability of recording the in-plane strain $S_{zi}(E_{ex,z})$ curves with controllably increasing the temperature up to the Curie value, $T_c \approx 420-450$ K (above which the materials are no longer PE), also under the simultaneous application of a desired $E_{ex,z}$. Hence, possible anomalies in the respective $d_{zi}(T)$ curves could be attributed to the well-known structural phase transitions that occur at temperatures $T > 300$ K, e.g. rhombohedral to tetragonal. Below, we will firstly describe the optical cryochamber, in Part I and, secondly, the optical thermoplatform, in part II.

Part I: Optical Cryochamber

For the sake of discussion, the cryochamber is firstly presented schematically in Figs. D.2 and D.3. Specifically, Figs. D.2(a.i)-(a.iv) present its main parts in side view, while Figs. D.2(b.i)-(b.iv)) show the respective top view, whereas the dimensions are included in all cases. At this point, we note that we will simply describe the different parts of the cryochamber, shown in Figs. D.2(a.i)-(a.iv) and Figs. D.2(b.i)-(b.iv); their exact role will be explained below, in the discussion of Fig. D.3, where the constructed device is presented.

Fig. D.2(a.i) shows the compact lower part that serves as the basis of the cryochamber; it constitutes of two concentric cylinders of appropriate dimensions; a smaller one (1) on top, and a larger one (2) at the bottom. Regarding (1), we observe that it has a recess (3), where an insert, shown in panel (a.i'), can be firmly adjusted. The latter is a cylinder, with a small pin machined on its top flat surface for mounting the sample under investigation (see below) and applying an external voltage for the production of the desired external electric field, $E_{ex,z}$. In addition, the cylindrical insert has two inlets, one on its lateral surface and the other at its bottom. The first inlet serves for mounting one of the two electrodes (let us term it V^-) used for voltage application (4), while the second one hosts the thermometer (5). Regarding the lower part (2), it is the actual basis of the cryochamber. Specifically, the black dashed lines signify the canal that accommodates the leads of the thermometer. The next part, shown in Fig. D.2(a.ii), is a teflon ring-shaped flange/spacer of appropriate dimensions. In this scheme, the lower (panel (a.i)) and the upper (panel (a.iii)) parts are completely thermally isolated. In addition, the ring-shaped flange/spacer is accompanied at both sides by appropriate O-rings so that vacuum shielding can be maintained given that a conventional mechanical pump is used to evacuate the upper part of the cryochamber. Fig. D.2(a.iii) presents the upper part, which is a cap having appropriate dimensions. In this scheme, the upper part forms a shell around (1). Its inner space is the actual chamber that hosts the sample and should be evacuated through an outlet (6), as already discussed above. On the outer surface of the top ring-shaped part a canal is machined where an O-ring is introduced (see Fig. D.2(a.iii) and Fig. D.2(b.iii)). Next, a plexiglass (7) is placed, which serves as the optical window for the observation of the sample under investigation. Also, two metallic pins are installed in the plexiglass ((8), (9)) for applying the external electric voltage (V^- and V^+ , respectively) to the sample for the production of $E_{ex,z}$. Furthermore, the central pin (9), except for voltage application, also serves as the top pin for the mechanical support of the sample in a face-to-face configuration together with the respective aligned pin of the cylindrical insert (see (9) in Fig. D.2(a.iii) and (10) in Fig. D.2(a.i'), respectively). In order to preserve the evacuation of the chamber, a ring-shaped cap

that hosts an O-ring at its bottom surface is placed against the plexiglass, as shown in Fig. D.2(a.iv). Finally, the aforementioned parts are held together with five screws that span the entire cryochamber in the vertical direction.

Once we assemble the cryochamber, we evacuate it by means of a conventional mechanical pump and immerse it into a liquid nitrogen bath, as schematically shown in Fig. D.3. The thermal isolation of the lower and the upper parts of the cryochamber by the teflon flange/spacer ensure the efficient cooling of the small cylinder of the lower part (see also (1) in Fig. D.2(a.i)) and the accompanying cylindrical insert (see also Fig. D.2(a.i')), while the outer cylindrical shell of the upper part remains practically thermally unaffected. In order to decrease/increase the temperature in a controllable way, a heater/resistor is wrapped around the small cylindrical insert of the lower part in alternate orientation, so that magnetic field generation is avoided.

Figs. D.4 show the preliminary version of the optical cryochamber realized on the basis of the design discussed above. Specifically, Figs. D.4(a)-(g) show step by step the assembling of the cryochamber, in top view. These parts, (1)-(10), correspond to the lower part, (1), cylindrical insert, (2), teflon flange/spacer, (3), upper part, (4), plexiglass optical window, (5), and top cap (6). Panel (a) presents all these distinct parts side by side. Panels (b)-(g) show the successive assembling of these parts, (2)-(6), so that the entire optical cryochamber is ultimately realized. We should acknowledge the Machinery group of N.C.S.R. 'Demokritos' for the productive collaboration of the realization of this cryochamber. This device is now adapted to an experimental setup hosted in the 'Laboratory of Microscopy Techniques' at the Department of Physics, N.K.U.A. (see below).

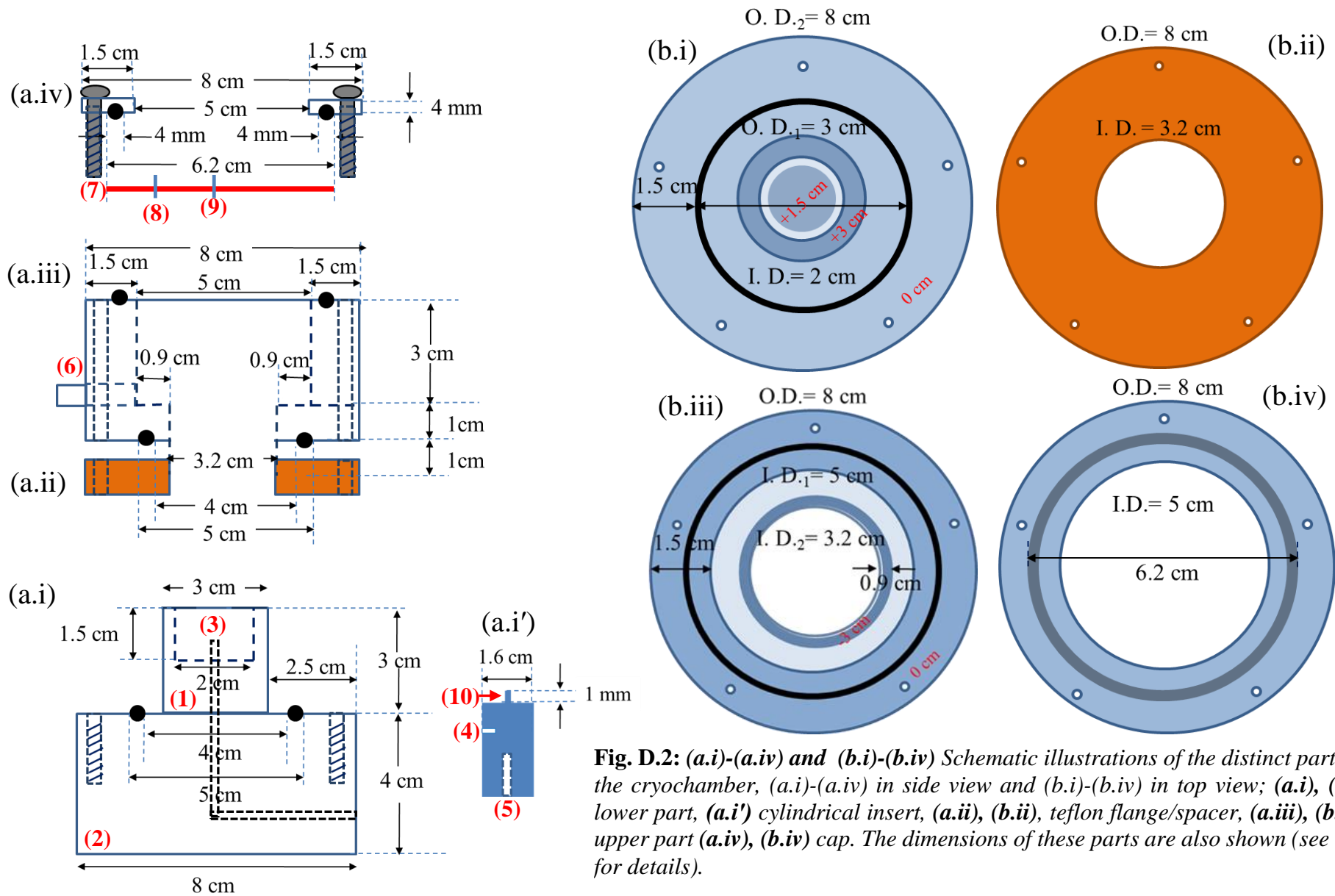


Fig. D.2: (a.i)-(a.iv) and (b.i)-(b.iv) Schematic illustrations of the distinct parts of the cryochamber, (a.i)-(a.iv) in side view and (b.i)-(b.iv) in top view; (a.i), (b.i) lower part, (a.i') cylindrical insert, (a.ii), (b.ii), teflon flange/spacer, (a.iii), (b.iii) upper part (a.iv), (b.iv) cap. The dimensions of these parts are also shown (see text for details).

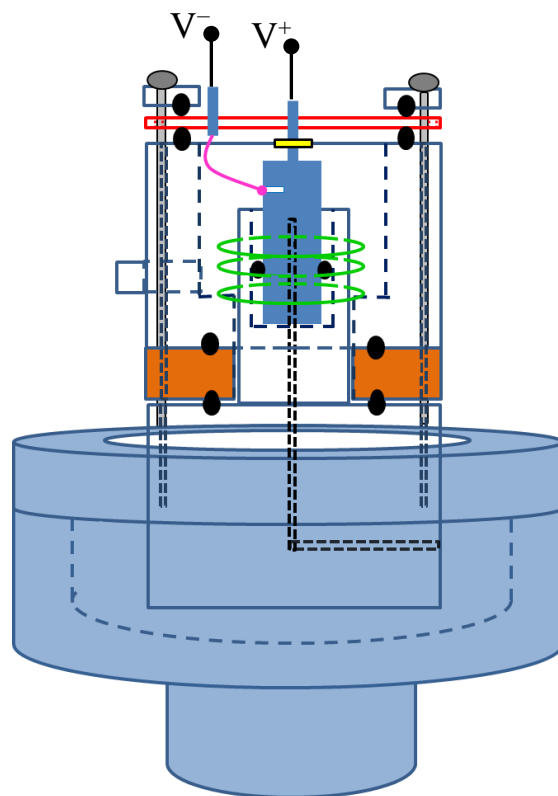


Fig. D.3: Side view of the optical cryochamber immersed into liquid nitrogen bath (see text for details).

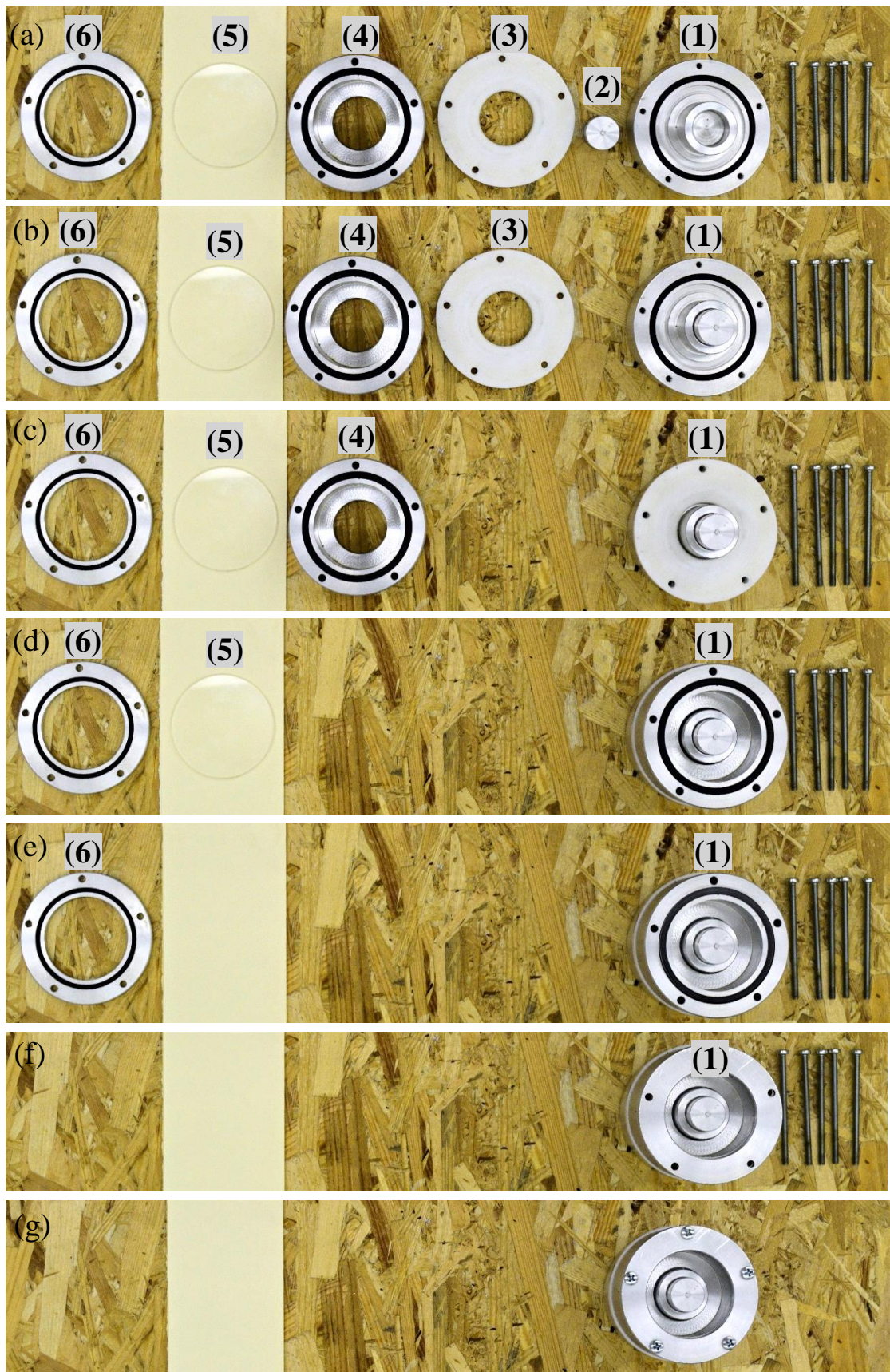


Fig. D.4: (a)-(g) Step by step assembling of the cryochamber, in top view. (1)-(10) Distinct parts of the cryochamber: (1) aluminum lower part, (2) aluminum cylindrical insert, (3) teflon flange/spacer, (4) aluminum upper part, (5) plexiglass optical window, (6) aluminum cap (see text for details).

Part II: Optical thermoplatform

The optical thermoplatform is presented at first schematically in Figs. D.5(a), below. Its design is similar to the one employed in this Thesis (see subchapter 3.3.1 of the main text), with some new features that render it appropriate for operation in the temperature region $300\text{ K} < T < 470\text{ K}$.

Specifically, the basis of the thermoplatform is the cubic-shaped lower part (1). A small pin (2) is machined on its top surface for mounting the sample under investigation (yellow square-shaped plate) and for applying an external voltage (let us term it V^-) for the production of the desired external electric field, $E_{\text{ex},z}$. Also, a hole of square cross-section is manufactured throughout (1) so that a heater/ceramic resistor (3) can be hosted. Next, a quartz glass is placed over the sample, serving as the optical window for observation with OM. We choose quartz over a conventional glass, since the latter is not tolerant at temperatures above $T=373\text{ K}$. Furthermore, since quartz is a bad thermal conductor, it also serves as a thermal reflector; considering that the sample surface is much smaller than the aluminium frame, we can assume that the sample temperature is held constant. The quartz glass hosts a pin feedthrough, the lower part of which, (4), is in contact with the sample. In fact, both pins (2-bottom) and (4-top) serve for applying the external electric voltage (V^- and V^+ , respectively) to the sample for the production of $E_{\text{ex},z}$ and for its mechanical support in a face-to-face configuration, allowing the sample to deform freely in all direction under the application of $E_{\text{ex},z}$. Furthermore, a cap of appropriate dimensions (5), hollow at its center, is placed against the quartz glass, as shown in Fig. D.5(a). The aforementioned parts are held together with two screws that span the thermoplatform in the vertical direction. Finally, in order to fix the thermoplatform tightly onto the microscope stage (see Fig. 2.9 (a) of subchapter 3.3.1 of the main text) a teflon base (6) is screwed onto the lower part of the platform. We employ teflon, since it is resistant to high temperatures up to 523 K (melting point: 595 K) and it creates thermal insulation between the platform and the stage. A photo of the thermoplatform is shown in Fig. D.5(b). We should acknowledge the Machinery group of N.C.S.R. ‘Demokritos’ for the productive collaboration of the realization of this thermoplatform.

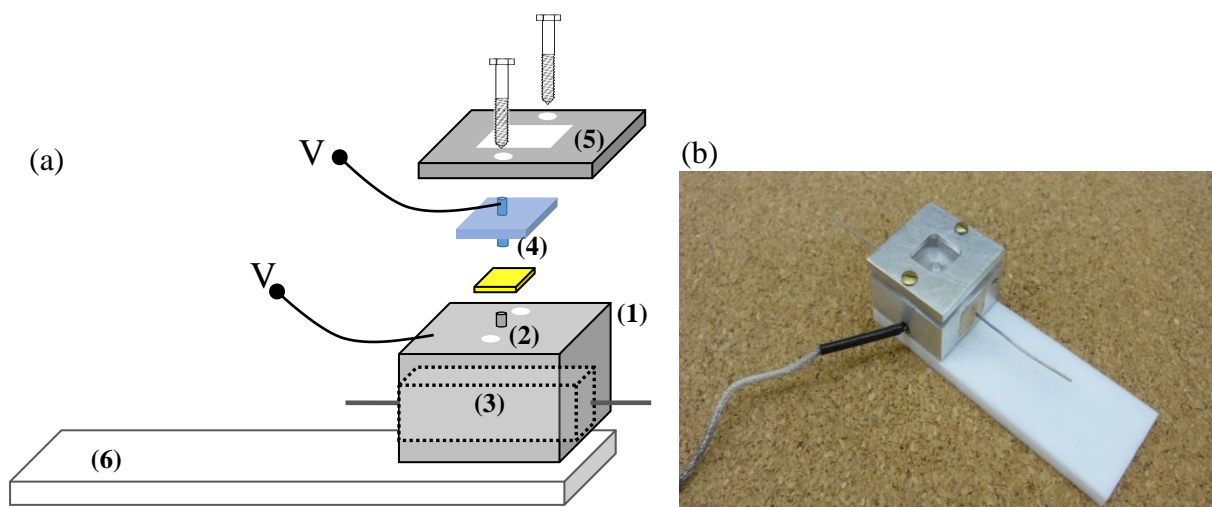


Fig. D5: (a) Schematic illustration presenting in perspective view the assembling of the thermoplatform. (1)-(6) Distinct parts of the thermoplatform: (1) lower part, (2) bottom pin, (3) heater/ceramic resistor, (4) top pin, (5) cap, (6) teflon base (see text for details). (b) Photo of the optical thermoplatform

Part III: Experimental setup including the optical cryochamber and thermoplatform

The experimental setup of the optical cryochamber and thermoplatform is shown in panel (a). Specifically, it consists of an OM (Celestron (1)) supported by a digital camera (Celestron (2)), a desktop PC (3), a high-voltage supply (Keithley Instruments (4)) for the application of the external electric field, $E_{ex,z}$, a mechanical pump (5), a conventional digital thermometer (TELE (6)) and an spiral-shaped tube (7). Finally, a low-voltage supply (QJE (not shown)) is used for feeding the heater/resistor. The spiral-shaped tube can be wrapped tightly around the cryochamber, serving as an alternative way of cooling via the flow of nitrogen. Notice that the monitor presents the edge of the disc-shaped sample where the border between the Au-coated and Au-free regimes is clearly visible. This Au-free edge zone is needed to prevent from possible electric arc during application of high voltages. Panel (b) shows a close-up of the cryochamber hosting a disk-shaped Au-coated PZT sample. Panel (c) focuses on the sample. The red dashed rectangles in all panels denote the sample surface/area. The entire experimental setup is hosted in the ‘Laboratory of Microscopy Techniques’ at the Department of Physics, N.K.U.A.

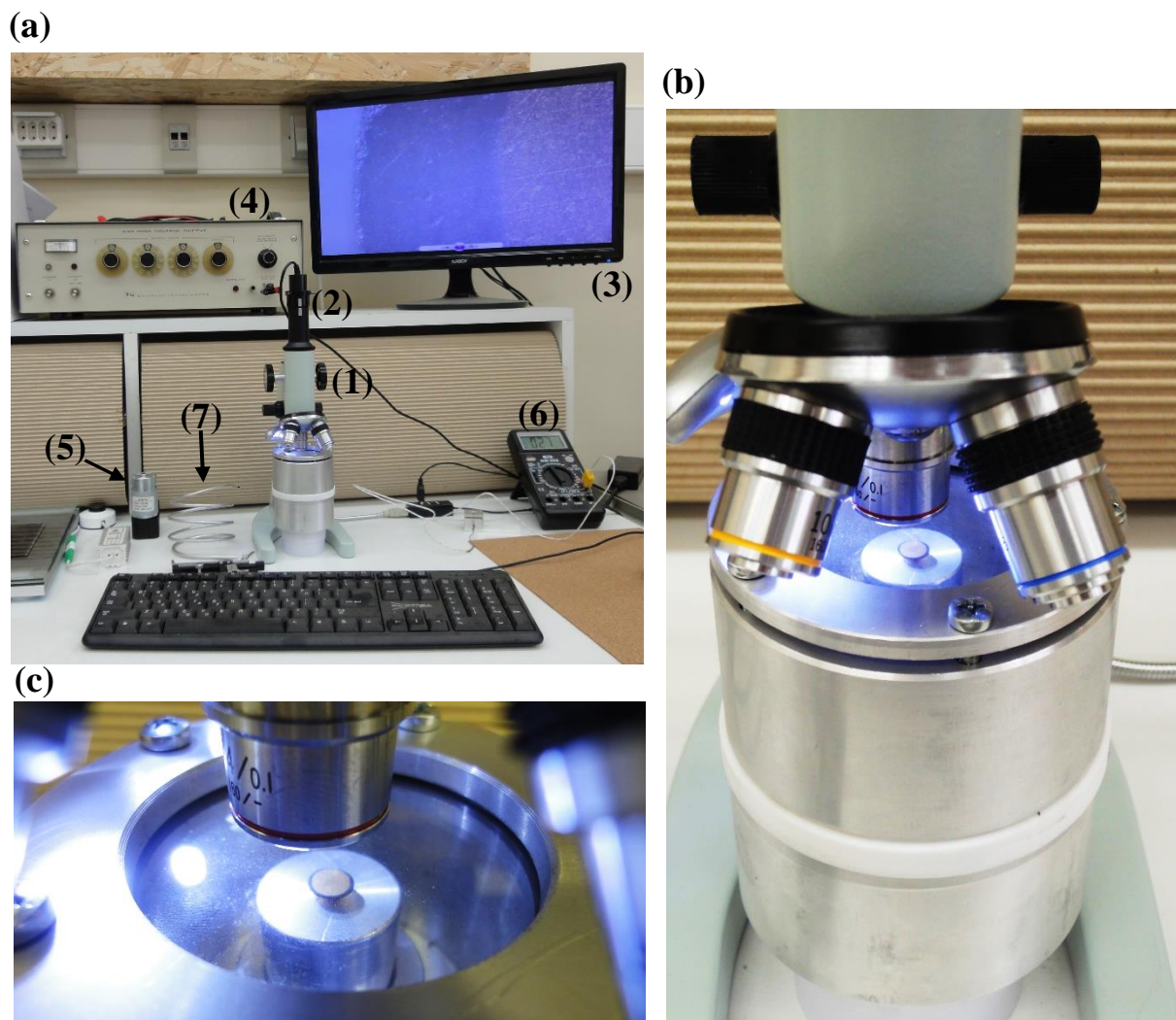


Fig. D6: (a) Entire experimental setup of the optical cryochamber and thermoplatform. (b) Close up of the cryochamber hosting a disc-shaped Au-coated PZT sample for OM investigation at cryogenic conditions. (c) Detail of the cryochamber and sample.